New insights into Late Albian – Turonian paleoceanography and climate evolution from high resolution analysis of drill cores in the Tarfaya Basin, southern Morocco

Dissertation

In fulfillment of the requirements for the degree “Dr. rer. nat.”

of the Faculty of Mathematics and Natural Sciences

at Kiel University

Submitted by

Sebastian Beil

Kiel, 2018

Referent: Prof. Dr. Wolfgang Kuhnt

Koreferent: Prof. Dr. Klaus Wallmann

Tag der Disputation: 12.07.2018

Zum Druck genehmigt:

Die Dekanin: Prof. Dr. Natascha Oppelt

Eidesstattliche Erklärung

Hiermit erkläre ich, Sebastian Beil, dass die vorliegende Dissertation „*New insights into Late Albian – Turonian paleoceanography and climate evolution from high resolution analysis of drill cores in the Tarfaya Basin, southern Morocco* “, abgesehen von der Beratung durch meine akademischen Lehrer, in Form und Inhalt meine eigene Arbeit darstellt.

Ich habe weder Teile, weder im ganzen noch zum Teil, an keiner anderen Stelle im Rahmen eines Prüfungsverfahrens vorgelegt. Teile dieser Arbeit wurden zur Veröffentlichung in Fachzeitschriften eingereicht oder sind in Vorbereitung hierzu.

Diese Arbeit ist unter Einhaltung der Regeln zur guten wissenschaftlichen Praxis der Deutschen Forschungsgemeinschaft (DFG) entstanden.

Kiel, den 01.06.2018

_____

Sebastian Beil

Acknowledgements

This thesis and the research presented in it would not be possible without the advice, support and help of many people. First I want to thank my PhD-advisors, Prof. Dr. Wolfgang Kuhnt and Dr. Ann Holbourn, for giving me the opportunity to work on this exciting and amazing project. Their advice and support helped me to develop a deeper understanding of controlling processes and mechanisms under different climatic boundary conditions in earth history. Without their knowledgeable improvements of the manuscripts presented here, this thesis would not be as meaningful as it is. I am also grateful to the SFB754 community for the funding of my project and the scientific input from different disciplines.

My further thanks goes to various colleagues I had the honor to work with during the different stages of my PhD-candidature. Mohamed Aquit taught me all the preparation strategies for the Cretaceous material and was extremely helpful with advice and discussions about the Cretaceous world. I am also indebted to Marcus Regenberg and Elena Lo Giudice Capelli for insightful discussions about Quaternary climatology and their guidance with Mg/Ca-thermometry. Dieter Garbe-Schönberg and Samuel Müller were never tired of debasting the various aspects of XRF-scanning and –data-evaluation and Nils Andersens advice was important for understanding isotope systems and their measurements. The phosphorus manuscript would have not been possible without the tireless help of Julian Oxmann and Florian Scholz in adapting Quaternary analysis methods for Cretaceous material. I also thank Dörte Mikschl and Karen Bremer for their indispensible support in solving pervasive problems during my various studies.

The patience of my fellow PhD-students from the Marine Micropaleontology Sven Balmer, Janika Jöhnck, Karlos Guilherme Diemer Kochhann, Julia Luebbers and Renjie Pei is also highly appreciated. Thanks for all the discussions that gave me valuable insight into various aspects of paleoenvironmental reconstructions during different periods of earth history.

I also want to thank my parents, Marlen Beil and Rudolf Beil, for their patience and the possibility of pursuing a scientific career. My close friends Felix Rosenow and Claudia Wittwer did a perfect job in reminding me that Geology is significant but that there are a variety of different things that are also important. And last but definitely not least I want to express my deepest gratitude to Felicitas Esch for constantly challenging me, my ideas, priorities and worldviews. Keeping an open mind is difficult with a lot of well-defined tasks and problems. Having someone who compensates over-focus and narrow ideas is therefore not only essential for everyday life but also crucial to remain curious and to hunt for new ideas and solutions.

Abstract

The Cretaceous with extremely high atmospheric pCO_2 is one of the warmest periods in the Phanerozoic, providing an endmember to test climate models. Repeated periods of widespread dysoxic / anoxic conditions (Oceanic Anoxic Events; OAEs) were characterized by enhanced burial of organic matter and different degrees of marine faunal turnovers, that can be seen as extreme equivalents for the already observed trend of expanding Oxygen Minimum Zones (OMZ) in modern oceans caused by anthropogenic climate warming. One of the largest OAEs occurring at the Cenomanian / Turonian boundary is OAE2. This thesis presents results from Core SN°4 drilled in the Tarfaya Basin (SW Morocco). This continuous record spanning the time from the late Albian to early Turonian allowed 1) to reconstruct climatic and paleoceanographic variability during this period in the Tarfaya Basin, 2) to unravel climate processes and biospheric changes during the onset of OAE2 and 3) to study phosphorus dynamics during the Cenomanian and early Turonian.

Sedimentary deposits from the upper Albian to lower Turonian are characterized by prominent cyclicities in Natural Gamma Ray and XRF-scanning derived Log(Zr/Rb) and thus permitted frequency analysis and comparison with orbital cyclicities. Based on sedimentation rates of 4.5-6 cm/kyr from the late Albian to middle Cenomanian and 8-9 cm/kyr for the late Cenomanian and early Turonian a total length of the Cenomanian of 4.8 ±0.2 Myr was calculated. Intensive upwelling started in the Tarfaya Basin already in the latest Albian, further intensifying following the mid-Cenomanian event (MCE) and during the onset of OAE2. Both events are of equal duration and share common characteristics implying common controlling mechanisms and climate-carbon

cycle feedbacks. Prominent sequence boundaries during both events witness major sea level falls. Intense oxygen depletion by enhanced primary productivity during both event are evidenced by low XRF-scanning derived Log(Mn/S), high C_{org}/N_{total} and increased organic matter content.

A high-resolution study of the onset of OAE2 with stable isotopes, content of organic matter and carbonates, XRF-derived Log-ratios and linescan data showed highly dynamic behavior of the ocean-climate-system already preceding OAE2. Two preceding minima in $\delta^{13}C_{org}$ were probably related to the injection of isotopically light carbon into the atmosphere. The main increase of $\delta^{13}C_{org}$ lasting ~100 kyr and probably coinciding with a minimum in eccentricity (400 kyr cycle) is interrupted by a transient plateau. It is characterized by a maximum in $\delta^{13}C_{carbonate}$ and located on top of a virtually terrigenous-free, carbonatic interval and interpreted as the transgressive surface of the last major Cenomanian sea level cycle. Sedimentation of terrigenous material, carbonate and organic matter and the isotopic composition of carbonate and organic material are strongly influenced by obliquity forcing. Maximum enrichment of organic carbon is determined for the latest part of the main $\delta^{13}C_{org}$ increase, contemporaneous with the first of 3 increases in $\delta^{18}O$ interpreted as the first cooling step of the Plenus Cold Event. Timing suggests a triggering by periodic drawdown of atmospheric pCO_2 in response to enhanced organic carbon burial during intervals of low obliquity and eccentricity forcing. The globally recognized extinctions of the upper thermocline dwelling foraminiferal species *Rotalipora greenhornensis* and *Rotalipora cushmani* are coinciding with the first and third cooling event, related to the periodic elimination of the respective habitat by obliquity paced intensification and expansion of the oxygen minimum zone

causing increasingly anoxic conditions in the photic zone accompanied by ocean acidification.

The study of phosphorus dynamics during the Cenomanian and early Turonian revealed a strong sea level influence on concentrations of total (P_{total}), aluminium-iron- (AlFeP) and calcium-bound (CaP) phosphorus and CaP/AlFeP with maxima at 221 and 104 m during the onset of the MCE and OAE2 coinciding with condensed intervals deposited during sea level high stands of Ce2.1 and Ce5. The background level for this interval argues for redox-induced sink-switching between the different phosphorus speciations inside the sedimentary column. This process enriches phosphorus relative to organic material as evidenced by C_{org}/P_{react} and N_{total}/P_{react} significantly below the Redfield ratio C:N:P of 106:16:1. This changes during the MCE and OAE2 when, during the positive carbon isotope excursions, C_{org}/P_{react} and N_{total}/P_{react} increase by a factor of 3 and 5, resulting from phosphorus release from the sediments under decreasing bottom water redox conditions. Enhanced primary productivity driven by redox-induced phosphorus leakage from the sediments is likely during OAE2, as the first maximum in C_{org}/P_{react} and N_{total}/P_{react} immediately precedes the period of maximum organic matter (TOC) accumulation.

Zusammenfassung

Die Kreide zeichnet sich als eine der wärmsten Perioden des Phanerozoikums durch signifikant höhere atmosphärische CO_2-Konzentrationen aus, was sie zu einem idealen Vergleichsobjekt für Klimamodellierungen macht. Wiederholt auftretende Ozeanische Anoxische Events (OAEs) sind gekennzeichnet durch weiträumige dysoxische / anoxische Bedingungen, welche sich in einer starken Anreicherung organischen Kohlenstoffes in marinen Sedimenten, häufig begleitet von Aussterbeereignissen, wiederspiegeln. Diese Ereignisse können als extreme Äquivalente des sich bereits heute zu beobachtenden Trends der Expansion der Sauerstoff-Minimum-Zonen (OMZ) infolge der globalen Klimaerwärmung angesehen werden. Das OAE2 an der Cenomanium-Turonium-Grenze ist eines der bedeutendsten dieser Events. Im Rahmen dieser Dissertation wurde der Bohrkern SN°4 aus dem Tarfaya Becken (SW Marokko) untersucht. Dieser kontinuierliche Sedimentkern besteht aus offen marinen Ablagerungen der mittleren Kreise vom oberen Albium bis zum unteren Turonium und gestattete: 1) die Rekonstruktion von klimatischen und ozeanographischen Änderungen dieser Zeit, 2) eine hoch aufgelöste Studie klimatischer und sedimentärer Variabilität während der Anfangsphase des OAE2 und begleitender Umwälzungen in der Biosphäre und 3) die Rekonstruktion von Änderungen im Phosphorhaushalt während des Cenomaniums und unteren Turoniums.

Sedimentabfolgen vom oberen Albium bis zum unteren Turonium zeichnen sich durch prominente Periodizitäten vor allem in Bohrlochmessdatensatz der natürlicher Gammastrahlung (NGR) und der auf Röntgenfluoreszenzmessung basierenden Log(Zr/Rb)-Daten aus. Die Korrelation

mit orbitalen Periodizitäten ergab eine Sedimentationsrate von 4.5-6 cm/kyr für das obere Albium bis mittlere Cenomanium und 8-9 cm/kyr für das obere Cenomanium und untere Turonium und somit eine kumulative Länge des Cenomaniums von 4.8 ±0.2 Myr. Eine Intensivierung der Auftriebsströmung fand im Tarfaya Becken bereits im späten Albium statt und verstärkte sich weiter nach dem Mittel-Cenomanischen Event (MCE) und während der Anfangsphase des OAE2. Beide Events weisen vergleichbare Charakteristika und Länge auf, was auf analoge Ursachen und Kopplungsmechanismen von Klima und Kohlenstoff-Kreislauf schließen läßt. Eine weitere Gemeinsamkeit sind prominente Sequenzgrenzen infolge eustatischer Meeresspiegelschwankungen. Eine aufgrund verstärkter Primärproduktion reduzierte Sauerstoffsättigung spiegelt sich in einer Reduktion der auf Röntgenfluoreszenzmessungen basierenden Log(Mn/S)-Daten, einem Anstieg von C_{org}/N_{total} und einem erhöhten Anteil organischen Materials wieder.

Ein hochgradig dynamisches Verhalten des Ozean-Klima-Systems bereits vor Einsetzen des OAE2 beeinflusst Stabile Isotope, den Gehalt organischen Kohlenstoffs, den Karbonatgehalt, röntgenfluoreszenzmessungsbasierte Log- und linescan-Daten. Zwei dem OAE2 vorrausgehende $\delta^{13}C_{org}$-Minima sind wahrscheinlich auf eine Anreicherung von vulkanogenem CO_2 zurückzuführen. Der für das OAE2 charakteristische steile Anstieg in $\delta^{13}C_{org}$ dauerte ~100 kyr und fällt wahrscheinlich in eine Periode minimaler Exzentrizität (400 kyr Zyklus). Unterbrochen ist er durch eine kurze Plateau-Phase, geprägt durch ein Maximum in $\delta^{18}O$, am Top eines karbonatreichen, fast terrigen-freien Intervalls, welche durch die Transgressionsoberfläche des letzten großen Meeresspiegelzyklusses den Cenomaniums verursacht wurde. Ein insgesamt

starker Einfluss des Obliquitäts-Zyklus prägte die Sedimentation von terrigenem, karbonatischem und organischem Material und die isotopische Zusammensetzung von Karbonaten und organischem Material. Die maximale Anreicherung an organischem Kohlenstoff fällt in den letzten Teil des $\delta^{13}C_{org}$-Anstieges, unmittelbar vor das erste Maximum des OAE2, während der ersten der 3 positiven Exkursionen in $\delta^{18}O$. Interpretiert werden diese als schrittweise Abkühlungen des Plenus Kalt-Events. Dies impliziert eine periodische Reduktion atmosphärischen pCO_2s infolge verstärkter Einlagerung von organischem Kohlenstoff in marine Sedimente während Phasen reduzierten Obliquitäts- und Exzentrizitäts-Einflusses auf das solare Strahlungsbudget. In die erste und dritte dieser Abkühlungsphasen fällt das Aussterben der Foraminiferenarten *Rotalipora greenhornensis* und *Rotalipora cushmani*, vermutlich infolge einer periodischen, Obliquitäts-gesteuerten Expansion und Intensivierung der Sauerstoffminimumzone in Kombination mit Ozeanversauerung, welche den Lebensraum in der tieferen Thermokline eleminierte.

Die Phosphor-Speziierung während des Cenomaniums und frühen Turoniums zeigt einen starken Einfluss globaler Meeresspiegelschwankungen auf Konzentrationen des gesamten (P_{total}), Aluminium-Eisen- (AlFeP) und Kalzium-gebundenem (CaP) Phosphors, sowie CaP/AlFeP. Maximale Anreicherungen während der initialen Phasen von MCE und OAE2 (221 und 104 m) wurden als Kondensationshorizonte der Meeresspiegelhochstände von Ce2.1 und Ce5 identifiziert. Die generell niedrige Konzentration von AlFeP und ein niedriges Verhältnis CaP/AlFeP impliziert intensives, früh-diagenetisches, Redox-Milieu-kontrolliertes Recycling zwischen den verschiedenen Phosphor-Reservoirs innerhalb der Sedimente. Die relative Anreicherung von Phosphor

zeigt sich auch in, im Vergleich zum Redfield-Verhältnis C:N:P von 106:16:1, erniedrigten C_{org}/P_{react} und N_{total}/P_{react}. Dies ändert sich nur mit Einsetzen des MCE und OAE2, wenn parallel zur $\delta^{13}C_{org}$-Exkursion sich diese Verhältnisse um den Faktor 3 beziehungsweise 5 erhöhen. Interpretiert wird dies als der Einfluss einer zunehmend reduzierenden Wassermasse, welche die Freisetzung von Phosphor aus den Sedimenten gestattet. Im Falle des OAE2s kann von einer zusätzlichen, Phosphor-bedingten Verstärkung der Primärproduktion ausgegangen werden, da die ersten Maxima in C_{org}/P_{react} und N_{total}/P_{react} unmittelbar vor der maximalen Anreicherung an organischem Kohlenstoff gemessen wurden.

Structure of the thesis

Chapter 1 presents the main objectives of the thesis that are the basis for the studies conducted in the framework of chapters 2-4. It also includes the level of knowledge of the studied time interval and the sampled sediment core.

Oceanographic and climatic changes during the recovered time interval in Core SN°4 are presented in ***Chapter 2***. Reconstructions are based on stable isotope records ($\delta^{13}C_{org}$, $\delta^{13}C_{carbonate}$, $\delta^{18}O_{carbonate}$), XRF-core-scanning derived Log-ratios and discrete measurements of carbonate and organic matter content. Frequency analysis was performed an XRF-derived Log(Zr/Rb) and the borehole-log-dataset NGR to reconstruct sedimentation rates and to estimate the cumulative duration of the Cenomanian. This chapter is entitled "*New insights into Cenomanian paleoceanography and climate evolution from the Tarfaya Basin, southern Morocco*", by S. Beil, W. Kuhnt, A. E. Holbourn, M. Aquit, S. Flögel, E. H. Chellai and H. Jabour, and was published in *Cretaceous Research*.

Chapter 3 contains the high-resolution study of the structure of and environmental variability during the onset of OAE2 based on $\delta^{13}C_{org}$, $\delta^{13}C_{carbonate}$ and $\delta^{18}O_{carbonate}$, organic matter and carbonate content, XRF-derived Log-ratios and high-resolution sampling of biostratigraphic samples. It is entitled "*Unraveling the onset of Cretaceous Oceanic Anoxic Event 2 in an extended sediment archive from the Tarfaya-Laayoune Basin, Morocco*", by W. Kuhnt, A. E. Holbourn, S. Beil, M. Aquit, T. Krawczyk, S. Flögel, E. H. Chellai, and H. Jabour, and was published in Paleoceanography.

Chapter 4 includes the new phosphorus speciation record for the Cenomanian and early Turonian and the comparison with environmental proxies presented in *chapter 1*. It is entitled "*Variability of phosphorus concentrations and*

speciations across the mid- Cenomanian Event and Oceanic Anoxic Event 2 in the Tarfaya Basin (SW Morocco)".

Chapter 5 includes general conclusions of the thesis and opens new questions for future research and compilative studies.

All references are compiled into the chapter ***References***.

In ***Appendix A*** the entire range of measured elements are plotted according to the different tube-voltage settings.

Appendix B contains the assembled core images derived by linescanning covering the entire Cretaceous interval of Core SN°4 and the separate images of the individual Sections.

Table of contents

List of Figures

1. Introduction

2. New insights into Cenomanian paleoceanography and climate evolution from the Tarfaya Basin, southern Morocco

3. Unravelling the onset of Cretaceous Oceanic Anoxic Event 2 in an extended sediment archive from the Tarfaya-Laayoune Basin, Morocco

4. Phosphorus concentrations and speciations across the mid-Cenomanian Event and Oceanic Anoxic Event 2 in the Tarfaya Basin (SW Morocco)

List of tables

2. New insights into Cenomanian paleoceanography and climate evolution from the Tarfaya Basin, southern Morocco

4. Phosphorus concentrations and speciations across the mid-Cenomanian Event and Oceanic Anoxic Event 2 in the Tarfaya Basin (SW Morocco)

Chapter 1:

Introduction

1. Introduction

1.1 The Cretaceous period in the geological time scale

The Cretaceous was always one of the focal points of geological and paleontological research, but despite centuries of stratigraphic refinement the durations of individual stages are still under debate, complicating reconstruction of environmental variability. Traditional and highly precise dating is based on radiometric methods. Of importance for Mesozoic strata are methods based on $^{40}Ar/^{39}Ar$ and U/Pb isotopes (Gradstein et al., 2012). As both methods require volcanic minerals for exact age dating, the presence of ash or effusive layers is essential. Correlation of these horizons within the sedimentary column and between different localities worldwide is realized with magneto- and / or biostratigraphy. The global distribution of frequently occurring volcanogenic layers in combination with characteristic, in many cases global, evolutionary changes of both macro- and microfossils in the Upper Cretaceous allowed the establishment of a reliable and precise age scale for the time interval starting with the Cenomanian. Prominent examples are the Cenomanian-Turonian-boundary at 93.9 Ma bracketed by radiometric ages from Western interior bentonites at 93.79 and 93.96 Ma (Meyers et al., 2010) and the Maastrichtian-Danian boundary with ^{40}Ar-^{39}Ar-ages of 66 Ma (Husson et al., 2011). More complex is age dating and correlation for the Lower Cretaceous with only sporadic intercalations of datable horizons and a higher degree of provincialism of both macro- and microfauna worldwide (Gradstein et al., 2012, chapter 27). Age calibration of interjacent events and biozones is achieved by

cyclostratigraphy that requires continuous sedimentary sequences characterized by the imprint of orbital cyclic pattern.

Precise time calibration is hampered by the absence of a definite orbital solution for time periods older than 50 Ma (Laskar et al., 2004, 2011a, 2011b). Therefore, estimates of the duration of the Cenomanian stage vary widely between 4.4 Ma (Scott et al., 2009; Scott 2014) and 6.6 Ma presented in the Geological Time Scale 2012 (GTS2012; Fig. 1.1; Gradstein et al., 2012) and GTS2016 (Ogg et al., 2016). A solution to resolve time differences in Mesozoic sediments is the extraction of orbital frequencies and conversion into durations by comparing frequency ratios. This approach is considered valid for time intervals older than 50 Ma and offers the chance to refine chronologies in older sediments (e.g., Berger et al., 1992; Meyers and Sageman, 2007). This strategy was also applied to calibrate durations of stages and derive absolute ages for the Lower Cretaceous (Gradstein et al., 2012, chapter 27). The Albian spans, for example, according to cyclostratigraphic analysis of Grippo et al. (2004) and Huang et al. (2010), 12.45 Myr with the lower boundary calibrated at 113 Ma. The Aptian lower boundary was placed at 126.3 Ma after calculating a duration of 13.3 Myr (Huang et al., 2010). Both boundaries were calculated relative to the Cenomanian-Albian boundary that is essential for the calibration of Lower Cretaceous ages.

1.2 The late Albian to early Turonian climatology

The Cretaceous and in particular the Cenomanian and Turonian stages represent one of the warmest periods of the Phanerozoic. The broad trend of the

climate evolution is from a cold greenhouse during the Albian to the warm greenhouse of the Cenomanian and Turonian (Kidder and Worsley, 2010, 2012). The more recent compilation of O'Brien et al. (2017) of different temperature proxies ($\delta^{18}O$ of planktic foraminifera and TEX_{86}; Fig. 1.1) presented a more heterogeneous picture with pronounced short-term variability (0.1 – 1 Myr) and an extended period of cooler sea surface temperatures during the middle Cenomanian. Maximum sea surface temperatures for the last 150 Ma were identified for the period of the uppermost Cenomanian and lower Turonian encompassing the Oceanic Anoxic Event 2 (OAE2).

The OAE2 at the Cenomanian-Turonian boundary was classified by Kidder and Worsley (2010, 2012) as one of the Haline Euxinic Acidic Thermal Transgression (HEATT) episodes with hothouse conditions, widespread anoxia (Fig. 1.2) and intensive burial of organic matter (Schlanger and Jenkyns, 1976) on a global scale. The general warming trend towards the Cretaceous Thermal Maximum during the uppermost Cenomanian and lower Turonian (O'Brien et al., 2017) was accompanied by a major 2nd-order transgression that produced the highest sea levels of the Cretaceous and possibly the entire Phanerozoic during the earliest Turonian, when epicontinental seas were covering large parts of the continents (Haq 2014). This highstand is the overall culmination of the second order supercycle UZA2 of Haq et al. (1987, 1988).

Multiple causes are suggested for observed short-term sea level changes during the Cretaceous. Evidences for glaciations and therefore potentially glacio-eustatically caused sea level changes are reported during various parts of the Early and Late Cretaceous (Sames et al., 2016). More enigmatic is the Hot Greenhouse phase at the Cenomanian-Turonian-boundary with high

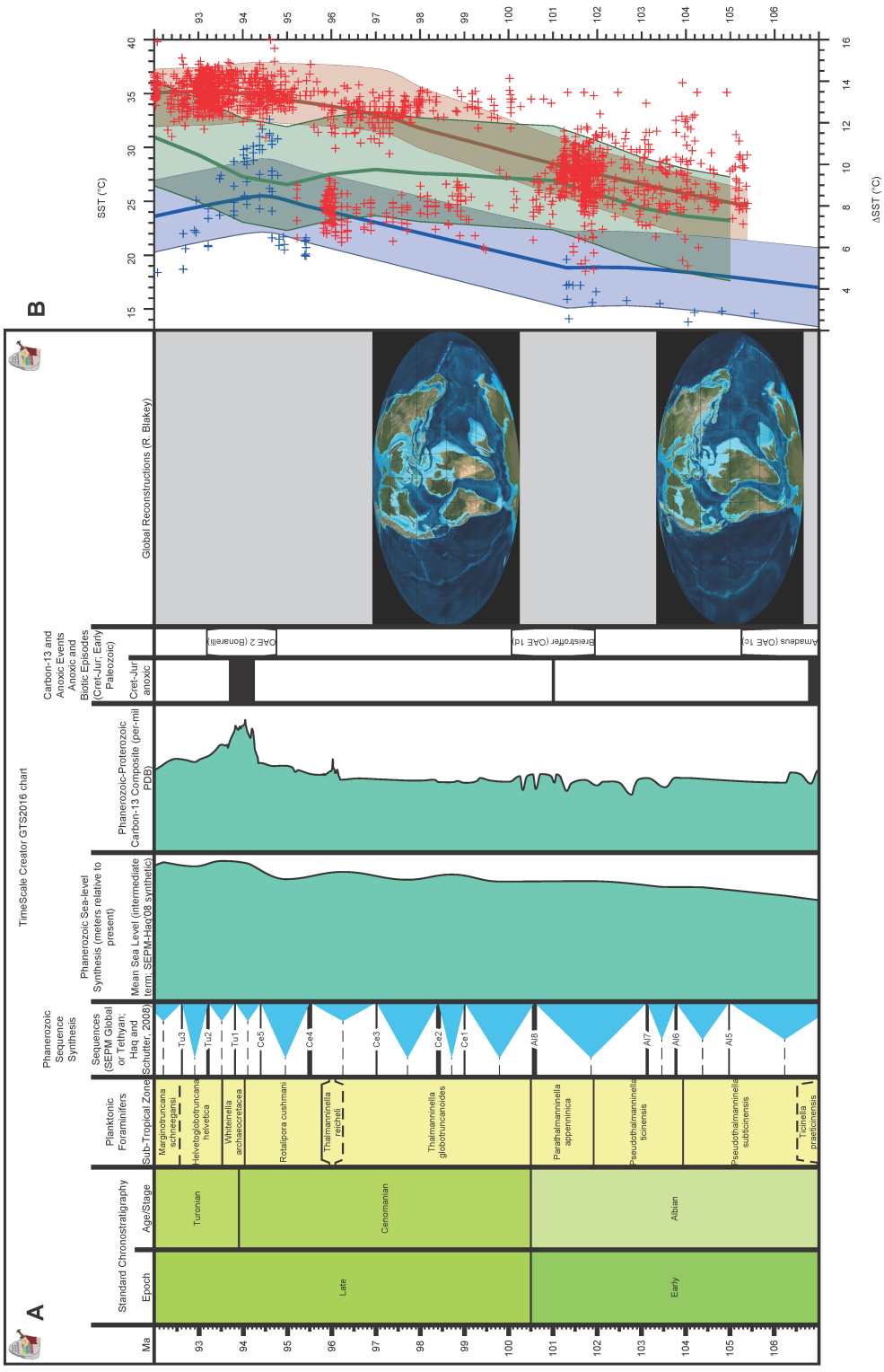

Figure 1.1: Chronology, paleogeography and paleoclimatology of the Albian to Turonian interval. **A.** Chronology and Chronostratigraphy from Gradstein et al., 2012 with Epoch representing the official subdivision of the Cretaceous; Phanerozoic sequences synthesis and Phanerozoic Sea-

level synthesis revised from Haq 2014; Carbon-isotope-compilation after Jarvis et al. (2006) until 100 Ma and Gale et al. (2011) for the older interval; Late Precambrian to Recent globes by Ron Blakey (https://deeptimemaps.com/global-series-thumbnails/), based on Chris Scotese's reconstructions (at http://www.scotese.com). The diagram was created with TSCreator - visualization of enhanced Geologic Time Scale 2004 database (Version 6.8; 2016) James Ogg (database coordinator) and Adam Lugowski (software developer) http://www.tscreator.org. **B.** Global mean paleotemperature reconstruction (TEX_{86} and $\delta^{18}O$) for high latitude in red, low latitudes in blue and gradient between high- and low latitudes in green from O'Brien et al. (2017). Discrete data points indicated as colored crosses, LOESS smoothed trends as bold colored lines and calibration error as bright area.

temperatures (Kidder and Worsley, 2010, 2012; O'Brien et al., 2017) when stable polar ice shields seem to be improbable (Sames et al., 2016). For this scenario the alternative model of aquifer-eustasy (Hay and Leslie, 1990, Sames et al., 2016) was proposed. During ice-free periods an enhanced hydrological cycle and the added ice-free areas available for temporary ground water storage would enable the storage of additional water on land causing sea level falls. These reserves would be drained during periods with weakened hydrological cycles and decreased transport of moisture towards the continents (Hay and Leslie, 1990, Sames et al., 2016). In contrast, modeling results suggest that at least ephemeral ice shields would be possible during "cold" orbital configurations even at atmospheric CO_2 levels considered for this period (Floegel et al., 2011, Hay and Floegel, 2012). New records are required to draw conclusions about the nature of sea level variations during different periods of the Cretaceous greenhouse world. The reconstruction $\delta^{18}O$-trends from excellently preserved,

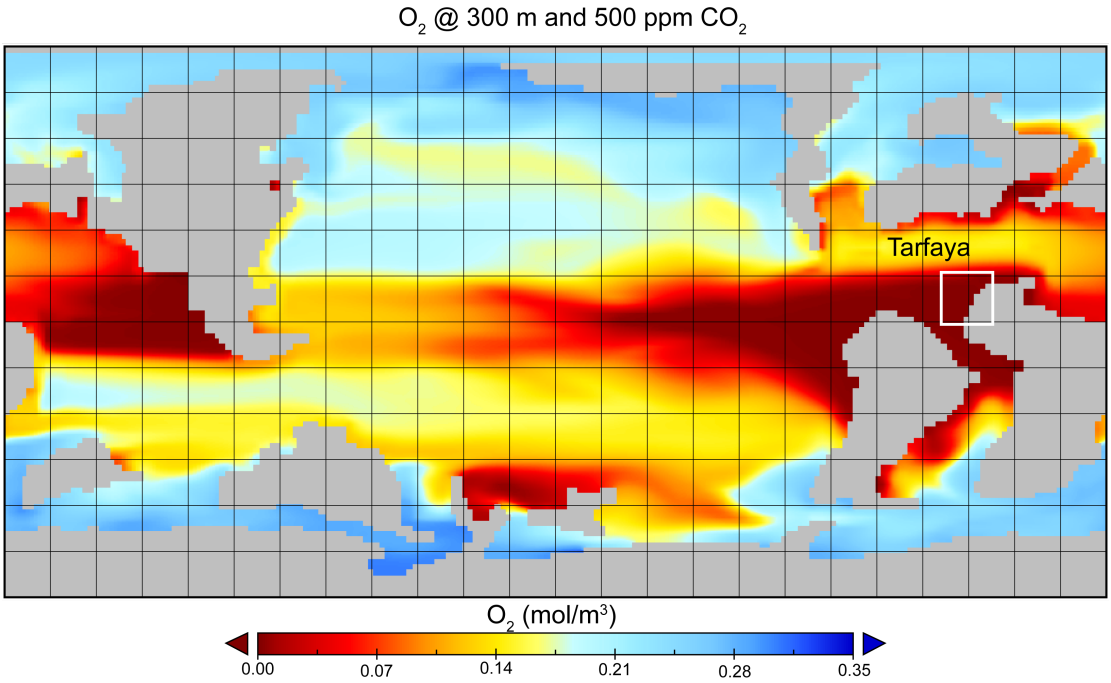

Figure 1.2: Modeled global extent of dysoxic / anoxic conditions in 300 m water depth. Oxygen concentration in mol/m³. Model calculation with the University of Victoria Intermediate Complexity Earth System Climat. Model (UVic, Weaver et al., 2001) with 500 ppm CO_2 and Cenomanian-Turonian boundary conditions. Approximate position of the Tarfaya Basin as part of the Tarfaya-Laayoune Basin indicated by black box. (from Beil et al., 2018)

glassy, planktic foraminifera are necessary for comparison with high-resolution reconstructions of sea level variability to exactly determine sign and phasing of $\delta^{18}O$ changes in relation to sea level lowstands. A glacio-eustatic control on sea level would be characterized by a negative relationship with an increasing oxygen isotope signal coupled to sea level decreases in contrast to aquifereustatic changes that exhibit a positive correlation (Wendler and Wendler, 2016). Only a limited amount of studies exists for a few regions worldwide (e.g., Jordan: Wendler and Wendler, 2016; Tanzania: Wendler et al., 2016), supportive of aquifer eustasy. A global coverage is essential to minimize the influence of regional control on sea level variability (e.g., isostasy). Additional

records from the same locations of TEX_{86} for paleotemperatures reconstruction (Schouten et al., 2002, 2003), sterane-hopane-ratio to evaluate the maturity of organic matter (Maxkenzie et al., 1980; Seifert and Moldowan, 1986), clumped isotopes as paleotemperature proxy to detect early diagenetical recrystallization (Ghosh et al., 2006; Eiler, 2007; Eiler et al., 2009) and BIT index for fluviatil freshwater influence (Hopmans et al., 2004) would detect alternative controls of the $\delta^{18}O$-signal.

1.3 Carbon isotope events during the late Albian to early Turonian interval

The Mesozoic era is punctuated by large carbon isotope excursions (CIE) of global extent (Fig. 1.1) in many sedimentary archives characterized by organic carbon enrichments (Schlanger and Jenkyns, 1976; Jenkyns 1980). One of the largest of these events is OAE2 at the Cenomanian/Turonian-boundary, also recognized as a time of faunal turnover of several marine groups including planktic foraminifera (e.g., Kaiho et al., 2014). Consensus exists about the global extent of OAE2 and characteristic large burial rates of organic carbon reflected in total organic carbon (TOC) enrichments recorded in many sedimentary archives in various regions (e.g., Germany (Voigt et al., 2008); Italy (Tsikos et al., 2004); Jordan (Wendler et al., 2014); Demerara Rise (Friedrich et al., 2006); Western Interior Seaway (Bowman and Bralower, 2006); Kerguelen Plateau (Dickson et al., 2017)). Climatic changes such as the Plenus Cold Event (e.g., Gale and Christensen, 1996; Jarvis et al., 2011; Jenkyns et al., 2017; Kuhnt et al., 2017) are commonly interpreted as a direct consequence of enhanced burial of organic matter.

OAE2 is characterized by widespread anoxic conditions (Fig. 1.2), enabling or enhancing organic carbon preservation at the sea floor. Deteriorating redox conditions were not confined to bottom water, but were locally influencing even upper water masses with evidences of euxinic conditions in the photic zone in the Tarfaya Basin (Kolonic et al., 2005). Still under intense debate are triggering factors and the nature of feedback process during OAE2. Suggested mechanisms are e.g. enhanced fertilization of shallow marine basins caused by enhanced weathering (Poulton et al., 2015) or redox induced release of nutrients (e.g. phosphorus) from the sediments (Mort et al., 2007, 2008). Mounting evidences for example by Os-isotopes (Du Vivier et al., 2014) suggest a triggering of OAE2 by the emplacement of the Caribbean or the Ontong-Java Large Igneous Province (Turgeon and Ceaser, 2008). Extensive studies during the last decades (e.g., Kuhnt et al., 2005, 2009; Meyers et al., 2012a) helped to identify successive phases in the evolution of OAEs and attempted to resolve their timing in relation to orbital pacing.

Besides these large-scale carbon cycle disturbances evidence for the repeated occurrence of additional smaller scale events is emerging. Especially the mid-Cenomanian Event (MCE) moved into research focus (Paul et al., 1994; Mitchell et al., 1996; Jarvis et al., 2001, 2006; Voigt et al., 2004; Gale et al., 2008; Giraud et al., 2013) during the last decades motivated by growing evidence for its global character. Records covering the MCE in appropriate resolution to compare characteristics with OAE2 or to resolve the timing of different phases are still sparse. Therefore many question remain: Is the MCE comparable in phasing and timing of environmental changes to OAE2? Are triggering factors and preconditions of the ocean-atmosphere system comparable? Is the response of

the global carbon cycle similar? Can the MCE be interpreted as a precursor event in a Cenomanian environment predisposed for perturbations of the global carbon cycle?

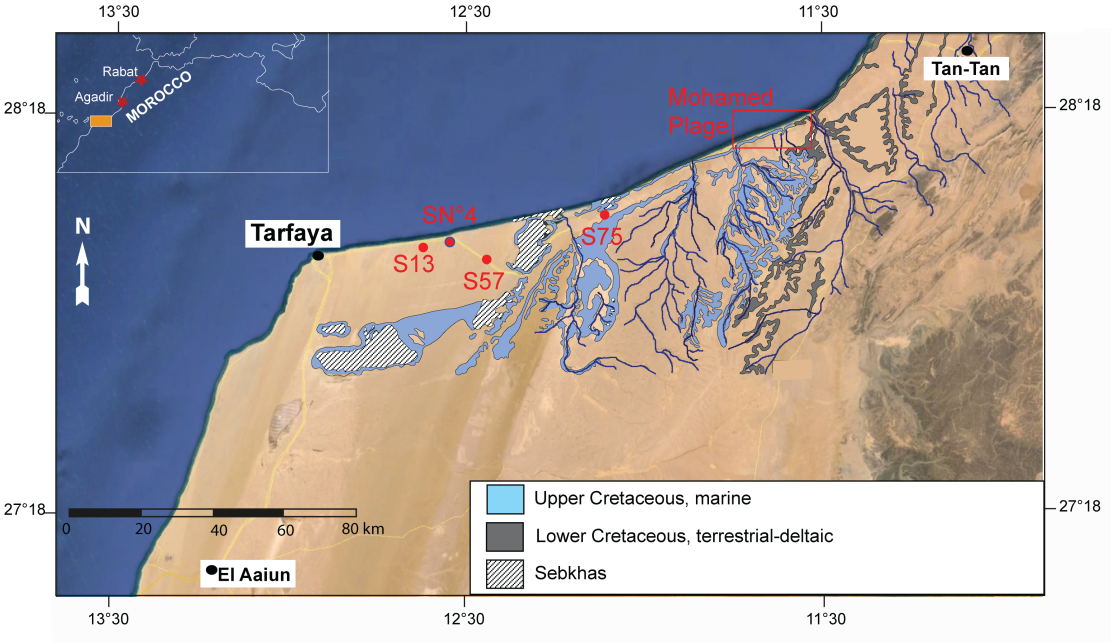

Figure 1.3: Location of drill-site of Core SN°4. Also indicated is the proximal outcrop section Mohamed Plage and the drill sites for Shell/ONAREP Cores S13, S57 and S75. (modified from Auqit et al., 2016)

1.4 The Tarfaya Basin and Core SN°4

This study is based on the continuous 350 m long drilled sediment Core SN°4 spanning the period from the upper Albian to lower Turonian recovered in 2009 close to the paleo-depocenter near the village of Tarfaya (Kuhnt et al., 2001) in the central part of the Tarfaya Bain, SW Morocco (Fig. 1.3). The Tarfaya Basin is located in the northwestern part of the stable Sahara Craton positioned during the Upper Cretaceous at the southern subtropical margin of the Western Tethys. The opening of the North Atlantic initiated the continues subsidence of the basin since the Triassic (Ranke et al., 1982; Wiedmann et al., 1978, 1982; El

Khatib et al., 1995, 1996) resulting in the accumulation of more than 700 m of Upper Cretaceous sediments. With ~2% of the global excess organic carbon burial during OAE2, the Tarfaya Basin, encompassing only ~0.05% of the Cenomanian sea floor, was one of the hotspots of global organic carbon burial (Kuhnt et al., 2017). Environmental changes influencing the export of organic carbon into the sediments should have global repercussions.

The continuous record of Core SN°4 offers the opportunity to reconstruct environmental variability in high resolution and for comparison and correlation with various localities in disparate basins. It further allows the analysis of orbital variability and the comparison to orbital solutions to refine the Cenomanian chronology.

Cyclostratigraphy of the latest Cenomanian and early Turonian in Core S13 exhibited distinct Milankovitch cyclicity in logging data with prominent obliquity and eccentricity cycles expressed in fluctuations of carbonate and organic carbon content and corresponding variability of density and natural gamma ray logs (Leine 1986; Kuhnt et al., 1997; Meyers et al., 2012a). Complete Cenomanian sea-level cycle reconstructions based on outcrops bio- and lithostratigraphy were achieved on several continents, including the Indian Cauvery Basin (Gale et al., 2002), the North American Western Interior Basin (Gale et al., 2008), the North European Anglo-Paris Basin (Gale et al., 2008), the shallow part of the Tarfaya Basin (Kuhnt et al., 2009), and the Vocontian Basin in SE France (Grosheny 2006). However, a complete Cenomanian core and logging record in continuous pelagic sediments with planktic biostratigraphy control that would allow orbital calibration in a resolution beyond the 405 kyr long eccentricity cycle still remains a challenge.

Previous work on the Cenomanian of the Tarfaya basin was focused on the outcrop section Mohamed Plage or cores drilled for oil shale exploration (e.g. S13, S57, S75). The proximal paleoposition of the Mohamed Plage section permitted the construction of a high-resolution sea level curve for the Tarfaya basin (Kuhnt et al., 2009) but impedes continuous reconstructions due to hiatuses especially during the onset of OAE2 and during early and middle Cenomanian sea level lowstands (Kuhnt et al., 2009). The most complete, distal core S13 drilled by ONAREP did not recover the base of the Cenomanian (Kuhnt et al., 2009), with logging restricted to the upper Cenomanian (Leine 1986, Kuhnt et al., 1997). Later commercial wells (i.e. S57 and S75) by Shell were focused on the organic rich blackshales and were terminated close to the onset of OAE2 (Leine 1986).

The new Core Tarfaya SN°4 presented in this study is geographically located between S13 and S57 / S75 covering the period between early Turonian and the late Albian *Planomalina buxtorfi* zone with full core recovery and wireline logging. The Core SN°4 thus presents the unique opportunity for a continuous reconstruction of the Cenomanian environment and correlation of major carbon cycle perturbations such as OAE2 and the MCE with orbital stratigraphy,

The record encompasses XRF-derived elemental ratios, phosphorus speciation, stable isotope and carbon content measurements permitting the reconstruction of paleoenvironmental changes during a major transgressional phase from the upper Albian through the Cenomanian into the Turonian (Haq 2014) that culminates in the encroachment of the Oxygen Minimum Zone (OMZ) on the shelf and the establishment of stable dysoxic / anoxic conditions during

OAE2 (Kuhnt et al., 2017) during a 3rd order sea level highstand (Haq et al., 1987, 1988). The record of Core SN°4 enables not only the reconstruction of changes on the northwest African shelf but also provides hints to the climatological variability within the source area of the deposited sediments. The correlation with the land section of Mohamed Plage provides the opportunity for comparison with a proximal record and correlation to an adjacent sea level record (Kuhnt et al., 2009). The continuous character of the sedimentation for SN°4 allows to discern additional sequence boundaries within hiatuses in or above the exposed strata in Mohamed Plage. Utilizing the organic carbon isotope record enables us to expand of the West African Atlantic Margin isotope record back in time and to correlate this record with other localities.

Being one of the global hotspots of organic matter burial during the late Cenomanian and early Turonian (Kolonic et al., 2005) the onset of these oxygen depleted conditions are important for the understanding of the Cenomanian-Turonian greenhouse world and the development of CIEs. Previous low-resolution studies of the Tarfaya basin suggest a late early Cenomanian age for the onset of blackshale deposition that peaks during OAE2 at the Cenomanian-Turonian boundary. However, a precise timing (on orbital timescales) of the onset and evolution of these upwelling conditions remained elusive.

1.5 Research questions and objectives

The following research questions will be explored in this thesis:

1) How variable was the climate-ocean system during the late Albian to early Turonian and when did dysoxic / anoxic conditions start in the Tarfaya Basin?
2) What are the similarities and differences of the different carbon isotope excursions recorded in upper Albian to lower Turonian deposits?
3) How long was the duration of the Cenomanian stage and what is the timing of events during this period?
4) What is the detailed shape of the OAE2 carbon isotope excursion and how did the enhanced marine carbon burial during this period influence the climatic system and the biosphere?
5) How did the phosphorus cycle evolve during the Cenomanian: Did it change during periods of enhanced primary productivity and anoxia associated with periods of major carbon cycle disturbances?

The main approaches of this thesis to answer these research questions are:

1) To reconstruct depositional and climatic variability from the late Albian to early Turonian, mainly based on XRF-derived and sedimentological data (*chapter 2 and 4*).
2) To evaluate high resolution organic and bulk carbonate isotope records and investigate their relation to carbonate oxygen isotope records and sedimentological data as proxies for climatic and oceanographic variability (*chapter 2 and 3*).

3) To extract orbital cyclicities from sediment records with prominent periodicities to derive sedimentation rates for different parts of the Cenomanian and calculate of the duration of the Cenomanian stage (*chapter 2*).
4) To reconstruct the detailed structure of the OAE2 $\delta^{13}C$ excursion by comparing bulk carbonate and organic $\delta^{13}C$ and to compare it with global climatic changes using $\delta^{18}O_{carbonate}$ and with regional oceanographic changes using organic matter content.
5) High-resolution correlation of the extinction events of the planktic foraminiferal species *Rotalipora greenhornensis* and *Rotalipora cushmani* to the carbon isotope record (*chapter 3*).
6) To create and interpret a phosphorus speciation record for the Cenomanian and early Turonian to reconstruct redox shifts and the onset of ocean fertilization by phosphorus leakage from the sediments (*chapter 5*).

Chapter 2:

New insights into Cenomanian paleoceanography and climate evolution from the Tarfaya Basin, southern Morocco

Sebastian Beil, Wolfgang Kuhnt, Ann E. Holbourn, Mohamed Aquit, Sascha Flögel, El Hassane Chellai, Haddou Jabour

Published in:

Cretaceous Research, 84, 451-473, doi: 10.1016/j.cretres.2017.11.006.

New insights into Cenomanian paleoceanography and climate evolution from the Tarfaya Basin, southern Morocco

Sebastian Beil[1], Wolfgang Kuhnt[1], Ann E. Holbourn[1], Mohamed Aquit[1,2], Sascha Flögel[3], El Hassane Chellai[4] and Haddou Jabour[5]

[1]Institute of Geosciences, Christian-Albrechts-University, Ludewig-Meyn-Str.10-14, D-24118 Kiel, Germany

[2]OCP S.A., Direction de Recherche et Développement, Recherche Géologique, 46300 Youssoufia, Morocco

[3]GEOMAR Helmholtz-Zentrum für Ozeanforschung Kiel, Ozeanzirkulation und Klimadynamik, Paläo-Ozeanographie, Wischhofstr. 1-3, D-24148 Kiel, Germany

[4]Department of Geology, Faculty of Sciences Semlalia, Cadi Ayyad University, Marrakech, Morocco

[5]ONHYM, Office National des Hydrocarbures et des Mines, 5, Avenue Moulay Hassan, BP99 Rabat 10000, Morocco

Correspondence to: S. Beil (Sebastian.Beil@ifg.uni-kiel.de

Keywords: Oceanic Anoxic Event 2 (OAE2), mid-Cenomanian Event (MCE), Cenomanian, Cyclostratigraphy, Oxygen Minimum Zone (OMZ)

Highlights:

- Complete upper Albian to early Turonian climate archive in drilled core from Tarfaya Basin
- Eccentricity pacing of mid Cretaceous OAE isotope excursions
- MCE and OAE2 associated with climate cooling and sea level fall

Abstract

A 325 m long continuous succession of uppermost Albian to lower Turonian pelagic (outer shelf) deposits was recovered from a new drill site in the central part of the Tarfaya Basin (southern Morocco). Natural gamma ray wireline logging, carbonate and organic carbon content, bulk carbonate and organic carbon stable isotopes and X-ray fluorescence (XRF)-scanner derived elemental distribution data in combination with planktonic foraminiferal biostratigraphy indicate complete recovery of the Cenomanian Stage. This exceptional sediment archive allows to identify orbitally driven cyclic sedimentation patterns and to evaluate the pacing of climatic events and regional environmental change across the Albian-Cenomanian boundary (ACB), the mid-Cenomanian Event (MCE) and Oceanic Anoxic Event 2 (OAE2) in the latest Cenomanian. The deposition of organic-rich sediments in the Tarfaya Basin, likely driven by upwelling of nutrient-rich water masses, started during the latest Albian and intensified in two major steps following the MCE and the onset of OAE2. The duration and structure of the MCE and OAE2 carbon isotope excursions exhibit striking similarities, suggesting common driving mechanisms and climate-carbon cycle feedbacks. Both events were also associated with eustatic sea level falls, expressed as prominent sequence boundaries in the Tarfaya Basin. Based on the 405 kyr signal imprinted on the Natural Gamma Ray (NGR) and XRF-scanner derived Log(Zr/Rb) records, we estimate the duration of the Cenomanian Stage to be 4.8 ±0.2 Myr.

2.1. Introduction

Orbital control on greenhouse climate and sea level changes was previously associated with the 405 kyr eccentricity cycle and linked to well-documented fourth order sequences in marine sedimentary successions (e.g. Gale et al., 2008). An orbital control on these regularly paced cycles implies that they are not primarily caused by regional changes in subsidence or volcanic events, which occur episodically and are essentially non-cyclic in nature. A recent study suggested that Mesozoic greenhouse eustatic sequences and stable isotope records show a strong imprint of the ~2.4 Myr modulation of eccentricity cycle, implying that orbital forcing exerted a major control on sea level variations and on the carbon cycle in a greenhouse world (Boulila et al., 2011). These authors proposed that low insolation during minima in the ~2.4 Myr eccentricity modulation promoted Antarctic ice sheet expansion, which caused global sea level falls, expressed as sequence boundaries in the stratigraphic record. These climatic events were associated with perturbations of the global carbon cycle and gave rise to widespread deposition of organic-carbon rich sediments and carbon isotope excursions.

The late Albian to early Turonian interval provides an excellent case to test this hypothesis since it encompasses three major paleoceanographic events expressed as positive $\delta^{13}C$ excursions (the Albian-Cenomanian boundary excursion, the mid-Cenomanian Event and the latest Cenomanian OAE2). The $\delta^{13}C$ curve over these intervals is delineated by distinctive, globally correlated excursions in orbitally tunable sedimentary successions from several continents (Gale et al., 1999, 2002, 2008; Kuhnt et al., 2009). Most of the records are based on composites of correlated outcrop sections, which have high quality

biostratigraphic control and allow detailed sedimentological observations. However, continuously cored and logged drill cores that cover this time interval without major stratigraphic hiatuses in pelagic outer shelf environments are still extremely rare. Such continuous records are essential for detailed correlation of isotopic, oxygenation and sediment flux oscillations on a global scale and for resolution of late Albian to early Turonian climate, sea level and paleoceanographic evolution.

The chronostratigraphy of the Cenomanian Stage is still a matter of intense debate, despite a well established biostratigraphic framework based on planktonic foraminifers, calcareous nannoplankton and cosmopolitan ammonite taxa, in addition to carbon isotope stratigraphy and cyclostratigraphy. Gale (2007), Gale et al. (1999, 2002, 2008) and Kuhnt et al. (2009) used planktonic foraminifers, ammonites and carbon isotope stratigraphy to correlate Cenomanian eustatic sequences from southeast India, southern England, the US Western Interior and Morocco. Assuming that these sea level oscillations are driven by the long eccentricity (405 kyr) cycle in the Milankovitch frequency band, these authors came to the conclusion that the Cenomanian Stage encompasses 11 ±1 eccentricity cycles, corresponding to a duration of the Cenomanian Stage of 4.4 ±0.4 Myr. This estimate is in agreement with a study including sequence stratigraphy, cosmopolitan dinoflagellate biostratigraphy and ammonite biostratigraphy that correlates the base of the Cenomanian with the Clay Spur Bentonite Bed radiometrically dated at 97.88 ±0.69 Ma in the Western Interior, resulting in an age of 97.13 Ma for the base of the Cenomanian and a duration of just over 4 Myr for the Cenomanian Stage (Scott et al., 2009; Scott, 2014). However, this is in sharp contrast to the widely used Geological

Timescale 2012 (Gradstein and Ogg, 2012), which approximates the duration of the Cenomanian Stage to 6.6 ±0.6 Myr, based on Ar/Ar dates of bentonites in the Western Interior and Japan.

A key to integrate Cenomanian biostratigraphic events, cyclostratigraphy and carbon isotope stratigraphy lies in resolving the chronostratigraphic position of the globally recognized mid-Cenomanian carbon isotope excursion in relation to the well-established chronology across the Cenomanian-Turonian boundary and, thus, determine the duration of the late Cenomanian. Based on the dating of Obradovitch (1993), Gale et al. (2008) assigned a radiometric age of 95.78 ±0.61 Ma to a bentonite bed within the Thatcher Limestone Member, associated with the first $\delta^{13}C$ peak of the mid-Cenomanian carbon isotope excursion, which places the mid-Cenomanian event 2 Myr before or, in agreement with the cyclostratigraphy of Gale (2007), five long eccentricity cycles below the Cenomanian-Turonian boundary. However, high precision U-Pb zircon ID-TIMS dating of a late-middle Cenomanian bentonite in the Western Canada Foreland Basin, which correlates with the "X" bentonite of the US Western Interior (dated by Obradovitch with 94.93 ±0.53 Ma), yielded an age of 95.87 ±0.10 Ma (Barker et al., 2011). This dating suggests that the sanidine Ar/Ar ages of Obradovitch (1993) are considerably too young and that the time interval between the Cenomanian-Turonian boundary and the first peak of the mid-Cenomanian $\delta^{13}C$ excursion corresponds to ~2.8 Myr or seven long eccentricity cycles.

In this study, we analyze a 350 m continuously cored research well, which was drilled in December 2009 close to the depocenter of the Tarfaya-Laayoune Atlantic Margin Basin (southern Morocco), referred to in this work as the Tarfaya

Basin. During the Albian to early Campanian, the Tarfaya Basin was located at the southeastern margin of the Central North Atlantic, forming an unrestricted embayment (e.g. Ranke et al., 1982; Patriat and Labails, 2006) within the Western Tethys that recorded not only regional variability but also global environmental changes in the marine realm.

Continuous subsidence resulted in the deposition of more than 700 m of Upper Cretaceous sedimentary rocks. The 325 m long Cretaceous interval recovered in Core SN°4 spans the lower Turonian to uppermost Albian (Vraconian). Earlier research (Kuhnt et al., 1990; Kolonic et al., 2005) and new model simulations (Fig. 2.1) indicate that the upper water column at this location was highly depleted in oxygen and was located within one of the global hotspots of organic matter burial during the late Cenomanian and early Turonian. This continuous record provides a unique opportunity to reconstruct the variability of a hemipelagic outer shelf sedimentary environment in high to intermediate temporal resolution (typically 1 cm spacing or ~200 year temporal resolution for the XRF-scanner records, and 40 cm spacing or ~5-8 kyr for discrete analysis of stable isotopes) and to gain new insights into Cenomanian and early Turonian climate evolution. This sediment archive can also be correlated with regional records from more proximal settings (Kuhnt et al., 2009), thus providing better constraints on the Cenomanian sea level history of the Tarfaya Basin in comparison to the global eustatic curve.

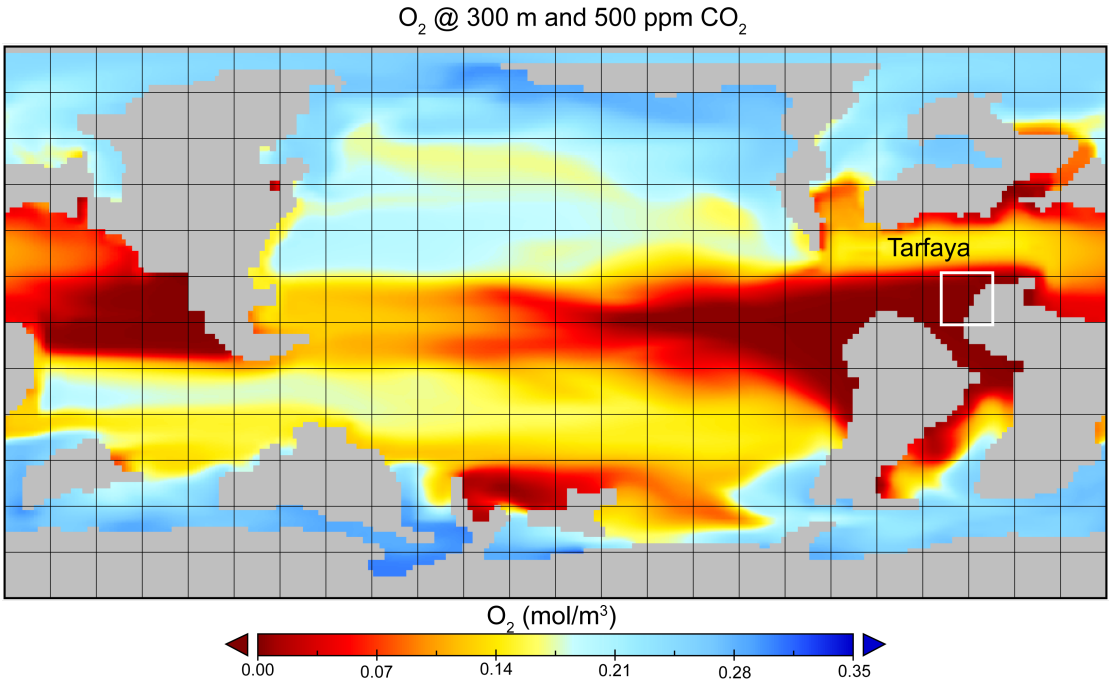

***Figure 2.1*:** Location of Tarfaya Basin within the modeled "hotspot" of Late Cetaceous tropical anoxia. Oxygen concentration (mol/m^3) in 300 m water depth, calculated with the University of Victoria (UVic) Intermediate Complexity Earth System Climate Model (Weaver et al., 2001) with 500 ppm pCO_2 and Cenomanian/Turonian boundary conditions.

2.2. Material and Methods

2.2.1 Core Tarfaya SN°4

Core Tarfaya SN°4 (N 27° 59' 46.4'', W 12° 32' 40.6'') was drilled with the assistance of ONHYM (National Office of Hydrocarbons and Mines of Morocco) in December 2009, ~40 km east of the town of Tarfaya, close to the road to Tan Tan. Core SN°4 is located between previously drilled wells S13 and S57/S75 (Fig. 2.2). The most complete exploration well S13, drilled in the 1970s by ONAREP close to the town of Tarfaya, did not recover the base of the Cenomanian and wireline logging was restricted to the Turonian and uppermost Cenomanian. Oil shale exploration wells (e.g. S57 and S75) drilled subsequently by Shell (Leine,

1986) focused on organic rich black shales and were terminated at the onset of OAE2.

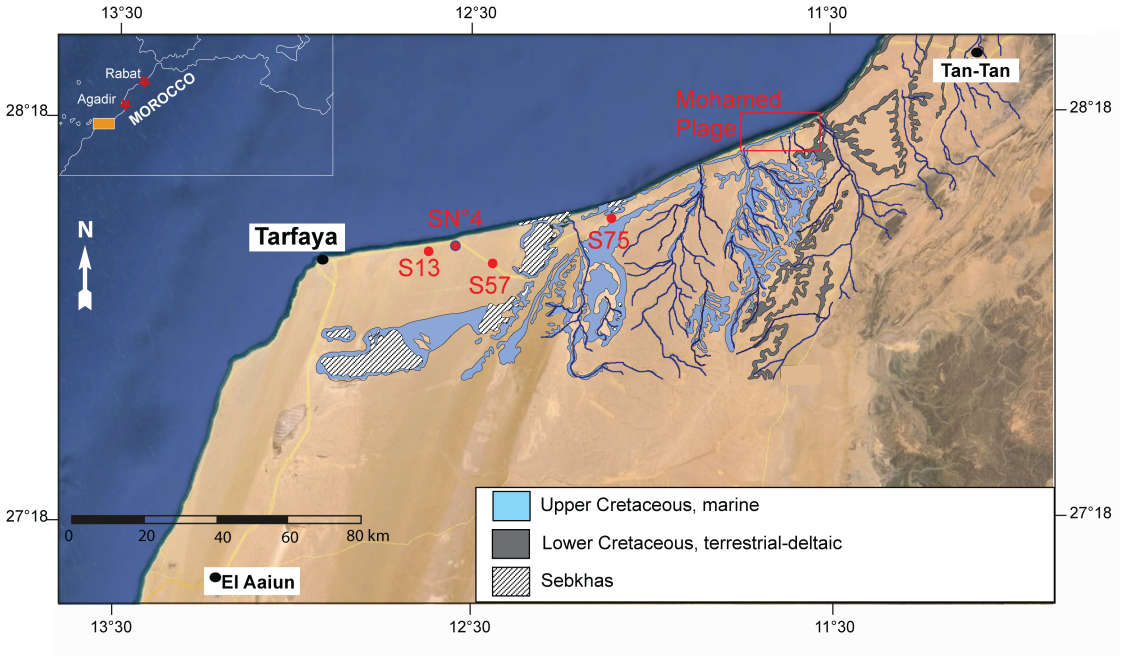

Figure 2.2: Location of coring site SN°4 in relation to Shell/ONAREP Cores S13, S57, S75 and the outcrop section at "Mohamed Plage" (modified from Aquit et al., 2016)

A Salzgitter WD3500 hydraulic drilling system with metal core barrels (section length 3.05 m) and seawater as drilling liquid was used to recover Core SN°4. Each section was divided in segments of ~80 cm length, which were sealed in plastic sleeves. The diameter of the cores was 88 mm for the upper 120 m and 68 mm for the lower part down to the bottom at 350.2 m. Individual segments were cut with a Kaufmann-Titan diamond rock saw into working and archive halves. A few segments, which were too fragile to be sawed, appear as gaps in the linescan and XRF-scanner records. A new depth scale was created to compensate for discrepancies between cumulative section lengths measured during drilling (referred to as driller's depth) and cumulative segment lengths measured during

XRF-scanning (Supplementary Material Table S2.1). For plotting analytical results and time series analysis the new depth scale was used.

2.2.2 Wire-line logging, Natural Gamma Ray

Wireline logging was carried out by Geoatlas Laayoune between 23 and 28 December 2009 immediately after the drilling operations were completed. The following suite of logging tools was used: (1) Natural Gamma Ray (NGR), values are given in counts per second (cps) as API (American Petroleum Institute) radioactivity units with a vertical resolution of 10 cm, (2) Caliper Log, (3) Downhole P- and S-wave velocity logging, (4) Normal Resistivity 16”N, 64”N, (5) Electric Log in mono-electrode and lateral configuration (RES), (6) Conductivity and resistivity of fluids, (7) Temperatures (absolute and differential), (8) Electromind Optical Televiewer Probe (OPTV). The walls of the hole were not covered with a metal casing and logging depth is recorded relative to the surface with a precision of ±0.1 m. However, the OPTV logging was carried out immediately after drilling and the strong turbidity and dispersed sediment in the drilling fluid did not allow to obtain high quality images.

2.2.3 Time series analyses

Harmonic analysis was performed using the astrochron-package (Meyers et al., 2012a) for R (R Core Team, 2017). For Evolutive Harmonic Analysis (EHA), the *eha*-function of the astrochron-package (Meyers et al., 2012a) with a window of 25 m and a step-size of 0.1 m for NGR and 0.01 m for the linearly interpolated and detrended Log(Zr/Rb) dataset was used in the frequency range between 0 and 1 cycles/m. Spectral analysis was performed with the *mtmML96*-function

(Patterson et al., 2014) of astrochron, an implementation of the robust red noise MTM analysis of Mann and Lees (1996).

2.2.4 Biostratigraphy

Samples for biostratigraphy (10-120 g) were taken every ~5-10 m, dried, crushed and then treated for 3 to 5 days with the alcoholic solution of anionic tensides REWOQUAT W 3690 PG by REWO-Chemie (Steinau, Germany). Soaked samples were, then, washed with a 63 µm sieve, dried and sieved into the size fractions 63-150, 150-250, 250-630 and >630 µm. The size fraction 250-630 µm was used for the identification of planktonic foraminifers and foraminiferal biozones were defined following the zonation of Robaszynski and Caron (1995) with modifications across the Albian/Cenomanian boundary based on a detailed re-investigation of the Global Boundary Stratotype Section and Point (GSSP) for the base of the Cenomanian Stage at Mont Risou, France (Petrizzo et al., 2015). These recent investigations of the boundary stratotype now allow to discriminate a brief interval between the last occurrence of the late Albian *Planomalina buxtorfi* and the first occurrence of the early Cenomanian marker *Thalmanninella globotruncanoides* (which we lumped with *Thalmanninella brotzeni*), which is characterized by the occurrence of *Thalmanninella gandolfii* (Petrizzo et al., 2015). The sampling grid was subsequently refined to constrain the zonal boundaries.

2.2.5 Carbonate content, total organic carbon and nitrogen

Between 8 and 10 mg of pulverized and homogenized sample material (sampling grid is identical with $\delta^{13}C_{org}$ measurements) was sealed twice in tin

capsules for Total Carbon (TC) and Nitrogen (N) measurements. The same amount was twice weighed into silver capsules and decarbonized with 0.25N hydrochloric acid (HCL) before sealing for Total Organic Carbon (TOC) measurements. Both sets of samples were measured with a Carlo Erba Proteinanalyzer NA1500 at Geomar Helmhotz Centre for Ocean Research (Kiel). For calibration and monitoring of longterm stability, different weights of Acetanilid (10.36% N, 71.09% C) and a certified soil standard BSTD1 (0.216% N, 3.5% C) were weighed and measured. Total Inorganic Carbon (TIC) were calculated as TIC=(TC-TOC)*8.3333. A total of 352 discrete samples were measured along the core for TOC, N and carbonate content. As carbonate data show a good correlation (R^2 = 0.69) with XRF-scanner derived Log(Terr10/Ca) values, Log(Terr10/Ca) was used to continuously track changes of carbonate content in high resolution along the core.

2.2.6 Stable isotopes ($\delta^{18}O$, $\delta^{13}C_{carbonate}$, $\delta^{13}C_{org}$)

Stable isotope measurements of bulk carbonate were conducted on samples of 1 cm thickness with a spacing of 40 cm between 23 and 193 m and of 120 cm between 193 and 251 m. The interval spanning the onset of OAE2 (98–115 m) was additionally analyzed with a spacing of 2 cm by Kuhnt et al. (2017). Before grinding with an agate mortar, sample surfaces were carefully cleaned to avoid contamination by drilling mud. Measurements were performed at the Leibniz Laboratory for Radiometric Dating and Stable Isotope Research (Christian-Albrechts-University, Kiel) on the Finnigan MAT 251 and 253 with Carbo-Kiel-autosampler for automated individual acid treatment of carbonate samples. Longterm accuracy is ±0.05‰ for $\delta^{13}C_{carbonate}$ and ±0.08‰ for $\delta^{18}O$. For

the calibration of results, two standards of the National Institute Bureau of Standards and Technology (Gaithersburg, Maryland, US) NBS 20 and NBS 19 and an internal standard were used. Results are reported as $\delta^{18}O$ and $\delta^{13}C_{carbonate}$ on the PeeDee belemnite (PDB) scale.

Sample intervals for organic carbon $\delta^{13}C_{org}$ analyses vary between ~1.6 m over the interval 23 to 65 m, ~40 cm over the interval 65 to 115.2 m, ~100 cm over the interval 115.2 to 250 m and ~120 cm over the interval 250 to 350 m. Approximately 1 to 3 mg of sample material was surface cleaned and ground. Samples were decarbonatized with 10% HCL and agitated until visible reaction stopped. Subsequently, 25% HCL was added for the dissolution of dolomitic material and samples were agitated overnight. After at least 12 hours of exposure, samples were five times neutralized with deionized water followed by decanting. Finally, samples were dried at 40°C, ground and measured with a Flash EA 2000 elemental analyser coupled online to a ThermoFinnigan Delta V Plus mass spectrometer at the GeoZentrum Nordbayern (Erlangen). Results are reported as $\delta^{13}C_{org}$ on the V-PDB (Vienna PDB) scale. For control of accuracy, an internal standard calibrated to the international standards USGS 40 and USGS 41 was measured. Measurement accuracy is ±0.06‰ (1σ).

2.2.7 XRF-scanner derived elemental ratios, Linescan imaging and RGB records

A second generation Avaatech X-ray fluorescence (XRF) scanner at the Christian-Albrechts-University, Kiel was used to scan segments after polishing with fine-grained sand paper and covering with 4 µm thick Ultralene foil. Scanning was performed in 1 cm intervals with a vertical slit of 1 cm and a

horizontal slit of 1.2 cm. Three different tube voltage settings for 10, 30 and 50 kV were used (scanning parameter and scanned elements in Supplementary Material Table S2.2). Some segments were too fragile to be scanned and appear as gaps in the XRF record. Raw spectra were converted into element counts with the iterative least-square package "WIN AXIL batch" from Canberra Eurisys and the voltage-specific Kiel models. For the analysis logarithmic ratios of elemental counts were used to eliminate method-specific effects such as matrix effect or variation in rock density (Weltje and Tjallingii, 2008).

Linescan data were acquired from the polished surface of working halves with the Jai CV-L107 3 CCD color linescan camera installed in the Avaatech XRF-scanner at the Christian-Albrechts-University, Kiel. The camera is equipped with a Dichroic RGB beam-splitter prism (RGB-channels at 630, 535 and 340 nm) followed by 3 sensors with 2048 pixel. The downcore resolution is 143 ppcm. L*, a* and b* were calculated from the digital RGB-images.

2.2.8 Numerical modeling

Modeling was performed with the UVic Earth System Climate Model (UVicESCM), which consists of an ocean general circulation model (Modular Ocean Model, Version 2) coupled to a vertically integrated two dimensional energy-moisture balance model of the atmosphere, a dynamic-thermodynamic sea-ice model, a land surface scheme, a dynamic global vegetation model and a sediment model. The model is driven by seasonal variations in solar insolation at the top of the atmosphere and seasonally varying wind stress and wind fields (after Flögel et al., 2005). The coupled model has a resolution of 2° in longitude and 2° in latitude and conserves energy, water and carbon to machine precision

without the use of flux adjustment (Meissner et al., 2012 and references therein). The physical components of the model are described in Weaver et al. (2001).

2.3. Results

2.3.1 Wireline logging (Natural Gamma Ray)

The NGR dataset (Fig. 2.3) is characterized by a longterm decrease from an average of 99.3 cps (lowermost 30 m) to 53.7 cps (uppermost 30 m). Pronounced short-term cyclicity with high amplitude fluctuations is evident in the NGR logging record between 25 m (top of Cretaceous sedimentation overlain by ~25 m Moghrabien) and 120 m below surface (Fig. 2.3). This upper part of the record can be easily correlated to published density and NGR records of previously drilled Tarfaya wells, in particular Cores S13, S57, and S75 for which biostratigraphic and cyclostratigraphic frameworks are available (Kuhnt et al., 1997, 2005; Tsikos et al 2004; Meyers et al., 2012a). A wavelet power spectrum over the interval 25 to 125 m indicates an increase in sedimentation rate at ~84 m within the upper part of cycle 3 (following the cycle scheme of Kuhnt et al., 1997) (Fig. 2.3), which is close to the biostratigraphically defined Cenomanian-Turonian boundary (Tsikos et al., 2004; Kuhnt et al., 2005, 2017). The increase in sedimentation rates from ~6-7 to ~8-9 cm/kyr is reflected by an increase in the wavelength of the most robust cycle (corresponding to 405 kyr long eccentricity) from ~28 to ~32 m and an increase in the wavelength of the shortest prominent cycle (corresponding to 38 kyr obliquity) from ~2-3 to ~3-4 m (Fig. 2.3).

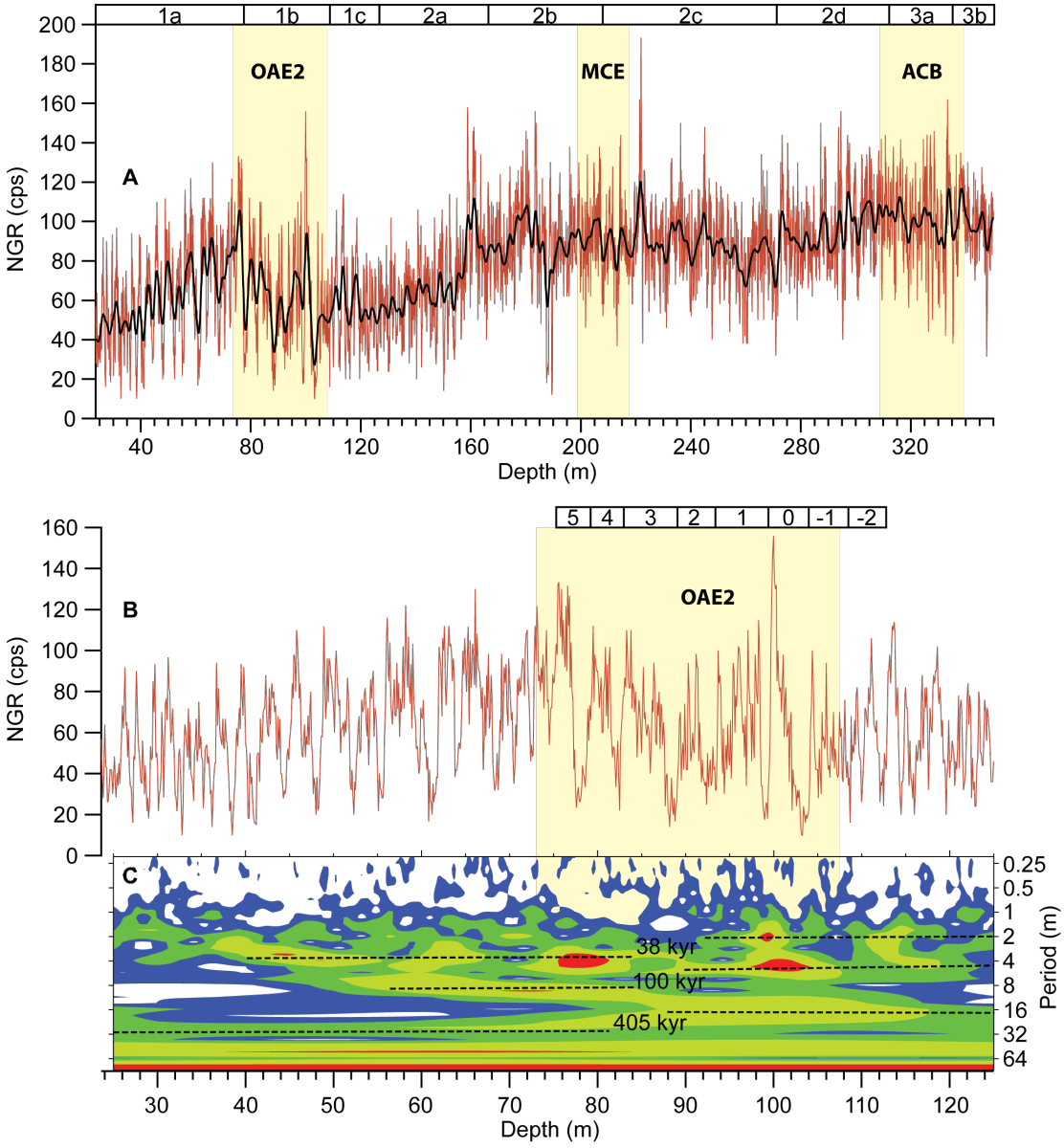

Figure 2.3: Natural Gamma Ray logging record of Core SN°4. **A.** Complete record with smooth interpolation using a Stineman function, numbers refer to lithological subunits. **B.** Upper 125 m of NGR analyzed with wavelet power spectrum, numbers refer to sedimentary cycles following the numbering scheme of Kuhnt et al. (1997). **C.** Wavelet spectrum of NGR calculated following Torrence and Compo (1998), using the software available at URL: http://atoc.colorado.edu/research/wavelets. Main periodicities referring to long eccentricity (405 kyr) and obliquity (38 kyr) are marked with black dotted lines, estimated sedimentation rates fluctuate at ~6-7 cm/kyr for the part below 84 m and at ~8-9 cm/kyr above 84 m. Note the decrease in spectral power below ~120 m core depth.

2.3.2 Core description, carbonate content, TOC and XRF-scanner based estimates of terrigenous components

The core was subdivided into 3 main lithological units and 9 subunits based on visual description (Fig. 2.4A and 2.4B), carbonate and organic carbon measurements and XRF-scanner derived Log(Terr10/Ca)-data (Fig. 2.5A).

2.3.2.1 Unit 1 (23.6 to 126.8 m)

Unit 1 is characterized by low terrigenous content and cyclic fluctuations in organic carbon vs. carbonate-rich intervals, forming couplets of 3 m ±0.3 m thickness. Unit 1 is subdivided into 3 subunits, based on carbonate content, organic carbon and bedding rhythm:

Subunit 1a extends from Section 12, Segment 1, 0 cm (23.6 m) to Section 32, Segment 2, 42 cm (77.53 m). It consists of brown to dark brown marlstones alternating with lighter brownish limestones. Subunit 1a exhibits prominent variations in XRF-derived Log(Terr10/Ca), considered a proxy for terrigenous input which is negatively correlated to $CaCO_3$-content, with generally higher mean (-1.2916, StDev = 0.2426) than the underlying subunit. Discrete measurements (n=59) give a mean carbonate content of 61% and an average TOC-content of 7.4%. The lower boundary of Subunit 1a at 77.53 m was defined at the base of a light brownish limestone bed with a sharp contact to the underlying dark brown marlstone, correlative to the center of cycle 5 in the scheme of Kuhnt et al. (1997) (Fig. 2.4B).

Subunit 1b reaches from Section 32, Segment 2, 42 cm (77.53 m) to Section 42, Segment 3, 34 cm (108.79 m). It consists of brownish to light brownish marly limestones and marlstones with intercalated black shales and is

characterized by marked lithologic changes between dark and light layers. It also exhibits a large small-scale variability (StDev = 0.2404) in Log(Terr10/Ca), but with lower average values (mean = -1.4693) than the underlying and overlying subunits. Average carbonate content is 71% and mean TOC content is 9.3%

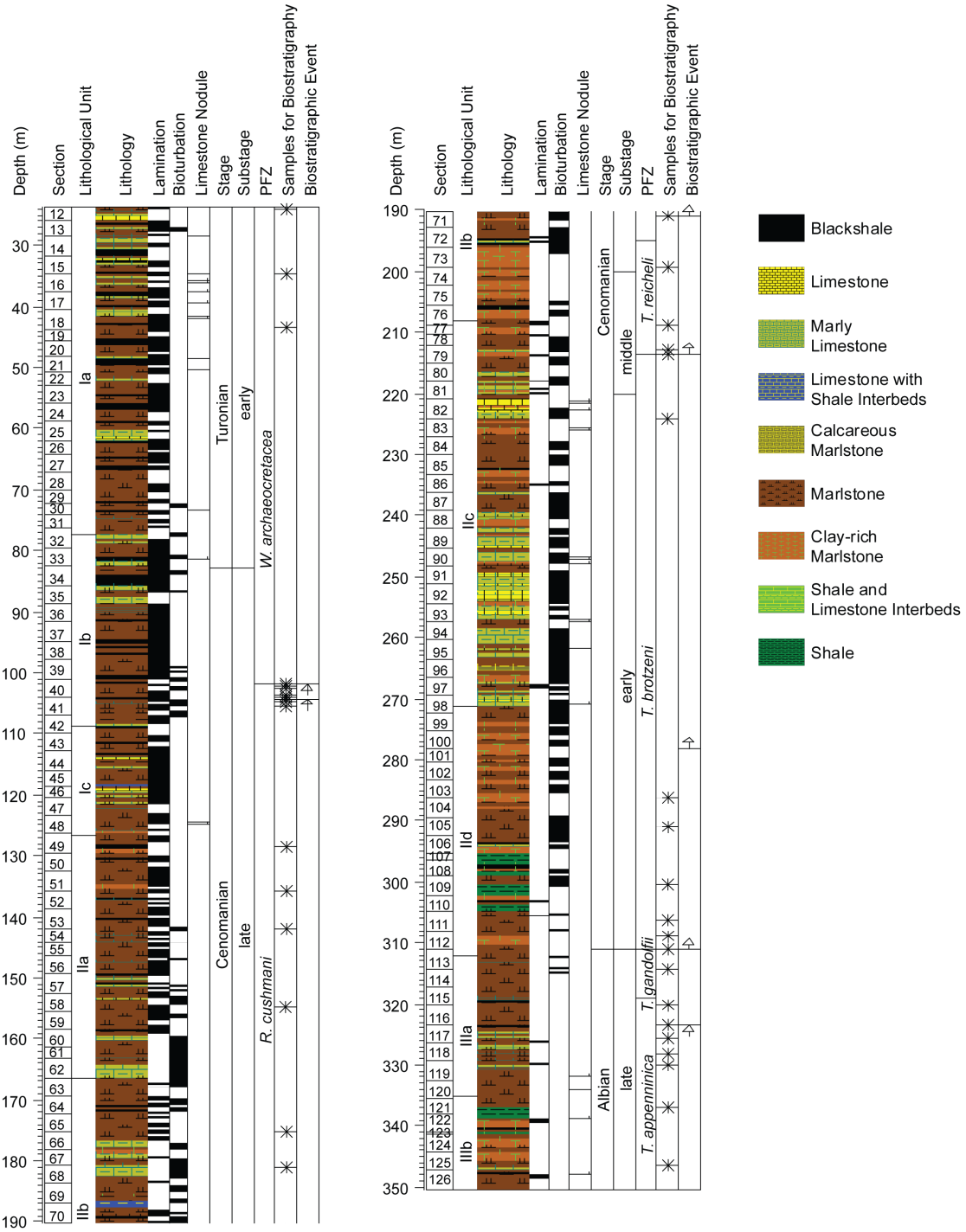

Figure 2.4A: Lithology, biostratigraphy and chronostratigraphy of Core SN°4

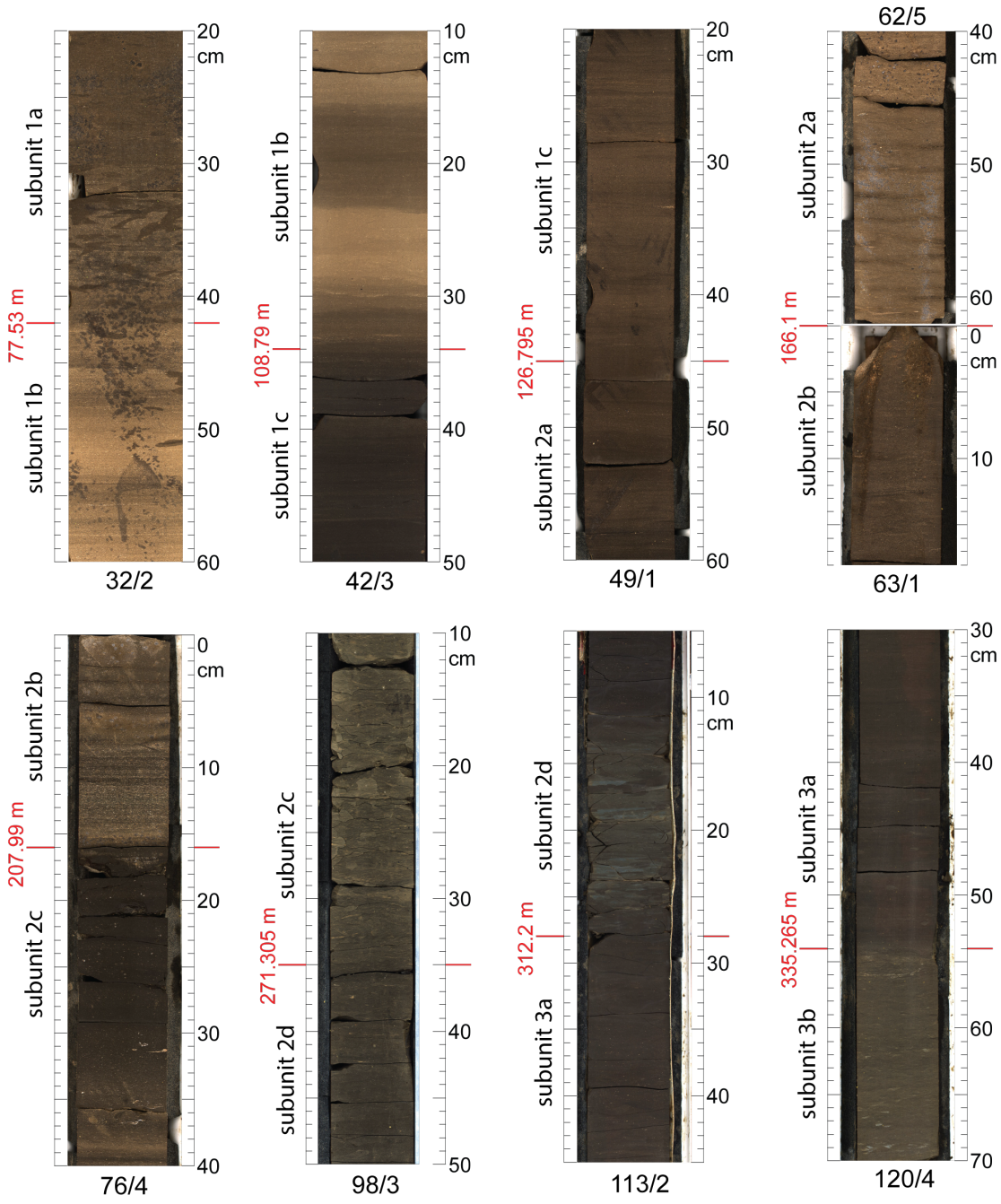

Figure 2.4B: Lithological boundaries between subunits in Core SN°4. Number in red indicates depth of lithological boundary. Section and segment number are given below each photo.

(n=72). This subunit corresponds to the interval of main organic carbon accumulation in the Tarfaya Basin (termed "zone riche" in the 1970s by oil shale exploration geologists from Shell and ONAREP). Subunit 1b includes the globally recognized OAE2, which is characterized by a prominent positive carbon isotope

excursion. The base of Subunit 1b is defined by a distinct lithologic change from light brownish marly limestone to dark laminated shales correlative to the base of cycle 1 in the scheme of Kuhnt et al. (1997) (Fig. 2.4B).

Subunit 1c ranges from Section 42, Segment 3, 34 cm (108.79 m) to Section 49, Segment 1, 45 cm (126.80 m). It consists of brownish marly limestones and marlstones that are partly (intervals of over 1 m thickness) laminated (mm-scale) and also show a large high frequency variability (StDev = 0.2510) of Log(Terr10/Ca) (mean = -1.2473). Average carbonate content (64%) and average TOC (6.3%) are lower than in Subunit 1b (n=28). A distinct trend towards lower terrigenous input and higher carbonate and organic carbon contents is evident within Subunit 1c and orbital-scale cyclicity is poorly developed. The boundary to the underlying Unit 2 is gradual, the two units mainly differ in the proportion of terrigenous input, which is substantially higher in Unit 2 (Fig. 2.4B).

2.3.2.2 Unit 2 (126.8 to 312.2 m)

Unit 2 is mainly characterized by an elevated proportion of the terrigenous component and lower carbonate and organic carbon percentages. Carbonate contents increase stepwise from the bottom to the top of the unit. We subdivided Unit 2 in 4 subunits, mainly based on the relative importance of the terrigenous and biogenic (carbonate and organic carbon) components. The globally recognized carbon isotope event MCE is situated close to the lithological boundary between Subunits 2b and c.

Subunit 2a extends between Section 49, Segment 1, 45 cm (126.795 m) and Section 63, Segment 1, 0 cm (166.41 m). It consists of brownish marly

limestones to marlstones with intercalations of lighter limestones, laminated intervals and black shales with a maximum thickness of 40 cm. Medium scale variability is increased (StDev = 0.2836) around an elevated mean in Log(Terr10/Ca) of -1.0365. Average TOC concentrations decrease to 4.8% with mean carbonate content of 64% (n=34). The base of Subunit 2a is placed at the transition between brighter marly limestones above to darker, more clay-rich marlstones below (Fig. 2.4B).

Subunit 2b extends from Section 63, Segment 1, 0 cm (166.41 m) to Section 76, Segment 4, 16 cm (207.99 m). It is composed of brownish marlstones that become enriched in clays and show increasing Log(Terr10/Ca) towards the base and overall increasing carbonate content from ~30 to ~70% towards the top. The middle part between 176 m and 183 m includes lighter intervals with higher carbonate content. Intercalated are intervals of marly limestones, up to 70 cm thick, and laminated intervals with a maximum thickness of 40 cm. Average TOC-concentrations are in the range of 4.2% (n=35). The base of Subunit 2b correlates with an abrupt change from brighter marlstones above to darker blackshales below.

Subunit 2c ranges from Section 76, Segment 4, (207.99 m) to Section 98, Segment 3, 35 cm (271.31 m). It consists of lighter brownish to greyish calcareous marlstones and marly limestones, up to 30 cm thick, with lighter limestones. The top of Subunit 2c is generally darker and the variability in Log(Terr10/Ca) is lower (StDev = 0.2692, mean = -0.5217) than in the lower part. The boundary to Subunit 2d is characterized by an abrupt decrease in clay content evident by the transition from greenish marlstones above to brownish

marlstones below (Fig. 2.4B). Mean carbonate content is 45% and mean TOC is 2.2% (n=56).

Subunit 2d ranges from Section 98, Segment 3, 35 cm (271.31 m) to Section 113, Segment 2, 28 cm (312.2 m). It consists of greyish to greenish-brownish clay-rich marlstones and is generally darker than underlying Subunit 3a. Intervals of up to 2 m are characterized by higher Log(Terr10/Ca) due to enrichment of clays. The upper boundary of this subunit corresponds to an abrupt decrease in clay content, whereas the lower boundary is marked by an abrupt increase in clay content. Subunit 2d is characterized by small-scale variability (StDev = 0.1861, mean = -0.1373) of Log(Terr10/Ca), low average carbonate content of 27% and low mean TOC of 1.9%. The contact to the underlying Unit 3 is characterized by the abrupt end of intense visible bioturbation at the top of Unit 3 (Fig. 2.4B).

2.3.2.3 Unit 3 (312.2 to 350.2 m)

Unit 3 is characterized by large changes in terrigenous sediment supply expressed in high variability of carbonate contents between <20 and >70%. The unit consists mainly of brownish to greenish-brownish marlstones with intercalations of clay-rich marlstones and claystones. Intensely bioturbated or laminated intervals are rare. Unit 3 is subdivided into 2 subunits, mainly based on changes in terrigenous content.

Subunit 3a ranges from Section 113, Segment 2, 28 cm (312.2 m) to Section 120, Segment 4, 54 cm (335.265 m). It is characterized by an abrupt increase in terrigenous material and consists of brownish, calcareous marlstones that are generally lighter with a higher carbonate content of 46% (n=19) and

decreased Log(Terr10/Ca) (mean = -0.6270) compared to the underlying Subunit 3b. A darkening upward trend in color is observed. TOC is slightly higher than in the underlying and overlying units with an average of 3.7%. The lower boundary to Subunit 3b is positioned at the transition between intensively bioturbated light grey marlstones below and dark grey to black, partly laminated marlstones above (Fig. 2.4B).

Subunit 3b extends from Section 120, Segment 4, 54 cm (335.265 m) to the bottom in Section 126, Segment 5, 7 cm (350.34 m). It consists of dark brown to greenish-brown marlstones with intercalations of marly limestones to limestones and finely laminated intervals with a thickness of up to 20 cm in the lower part. The increase in Log(Terr10/Ca) reflects increasing clay content from the bottom to the top of the subunit. Average carbonate content (36%) and TOC (2.2%, n=13) is lower than in Subunit 3a.

2.3.3 Planktonic foraminiferal biostratigraphy

The top of the Cretaceous interval at 23.6 m in Core SN°4 falls within the *Whiteinella archaeocretacea* zone of Robaszynski and Caron (1995) and is, therefore, of latest Cenomanian to earliest Turonian age (Fig. 2.4A). The FO of the lower Turonian marker *Helvetoglobotruncana helvetica* appears to be globally diachronous (Gale et al., 1993) and its appearance is delayed in the Tarfaya Basin (Kuhnt et al., 2005). Thus, we assume that the upper part of the *Whiteinella archaeocretacea* zone recorded in SN°4 is already well within the lower Turonian. We place the transition between the *Whiteinella archaeocretacea* and *Rotalipora cushmani* zones at 101.8 m (between 101.70 and 101.89 m) in Core SN°4 based on the last occurrence of *Rotalipora cushmani* at 101.89 m. The

boundary between the *Rotalipora cushmani* and *Thalmanninella reicheli* zone is located at ~195 m (between 191.08 and 199.43 m). The lower limit of the *Thalmanninella reicheli* and upper boundary of the *Thalmanninella brotzeni* zone is at ~213.6 m (between 213.49 and 213.69 m). The first occurrence of *Thalmanninella globotruncanoides,* which we lumped with *Thalmanninella brotzeni,* is in Section 113, Segment 1, 0-4 cm at 311.13 m. This datum defines the base of the Cenomanian in the GSSP at Mount Risou (Petrizzo et al., 2015). The *Thalmanninella gandolfii* zone (partial range zone between the first occurrence of *Thalmanninella gandolfii* and *Thalmanninella globotruncanoides*) is included in the latest Albian. The boundary between the *Thalmanninella gandolfii* and *Thalmanninella appenninica* zone, which is also characterized by the last occurrence of *Planomalina buxtorfi* is placed at ~319 m (between 314.23 and 323.5 m) (Fig. 2.4B).

2.3.4 Organic carbon (C_{org}) content and C/N ratio

TOC varies between 0.2 and 20.5% (Fig. 2.5B). The lowermost part of the core (350.34–235 m) is characterized by low TOC and low variability (average 1.9%, StDev 0.98%), except for a substantial increase in TOC (average 4.3%) between 334.5 and 319.7 m. In the overlying interval (235–115 m), TOC increases to an average of 4.3%, followed by a further increase (average 6.9%) until 105 m. Highest TOC of 20.5% is measured in the interval from 105 to 83.5 m, where variability is highest (average 10.3%, StDev 4.9%). TOC exhibits a decreasing trend in the remaining part of the core (Fig. 2.5B).

The atomic ratio (C/N ratio, Fig. 2.5B) of organically bound carbon (C_{org}) against total nitrogen content measured on bulk material fluctuates around 15

below 236 m, except for two intervals with increased ratios between 259 and 271 m (average of 21) and between 319 and 335 m (average of 20.5). Above 236 m, the C/N ratio shows a gradual increase, reaching an average of 36 in the uppermost 10 m. This longterm trend is interrupted by an interval with larger fluctuations reaching values of ~43.5 between 115 and 85 m, which corresponds to OAE2.

2.3.5 Isotope stratigraphy ($\delta^{13}C_{org}$ excursions)

Carbon isotope values (Fig. 2.5B) of organic matter vary between -29.24 and -24.24‰. A background level of ~28.5‰ or lower is determined above 250 m. This background level is punctuated by two prominent isotope excursions at 224–196 m (MCE) and at 107–65 m (OAE2). Both events are characterized by a short negative excursion and a steep increase culminating in two peaks divided by a transient decrease to lower values. The OAE2 $\delta^{13}C_{org}$ maxima are centered at 103.22 m (-24.20‰) and at 99.80 m (-24.31‰). The MCE exhibits $\delta^{13}C_{org}$ maxima at 211.99 m (-27.28‰) and 206.07 m (-26.80‰). Apart from their different amplitude (1.7‰ for the MCE and 4.3‰ for OAE2), both isotope events differ in the relative length of their plateau phase. OAE2 exhibits a longer lasting plateau after the second $\delta^{13}C_{org}$ peak before values gradually return to background levels. OAE2 additionally shows a third peak at the end of the plateau at 88.7 m with a maximum of -25.1‰. The relative extent of the recovery phases is also different, with a much faster return to background levels after the MCE.

A third lower amplitude excursion corresponding to the Albian-Cenomanian boundary event (ACB) occurs in the lower part of the core starting

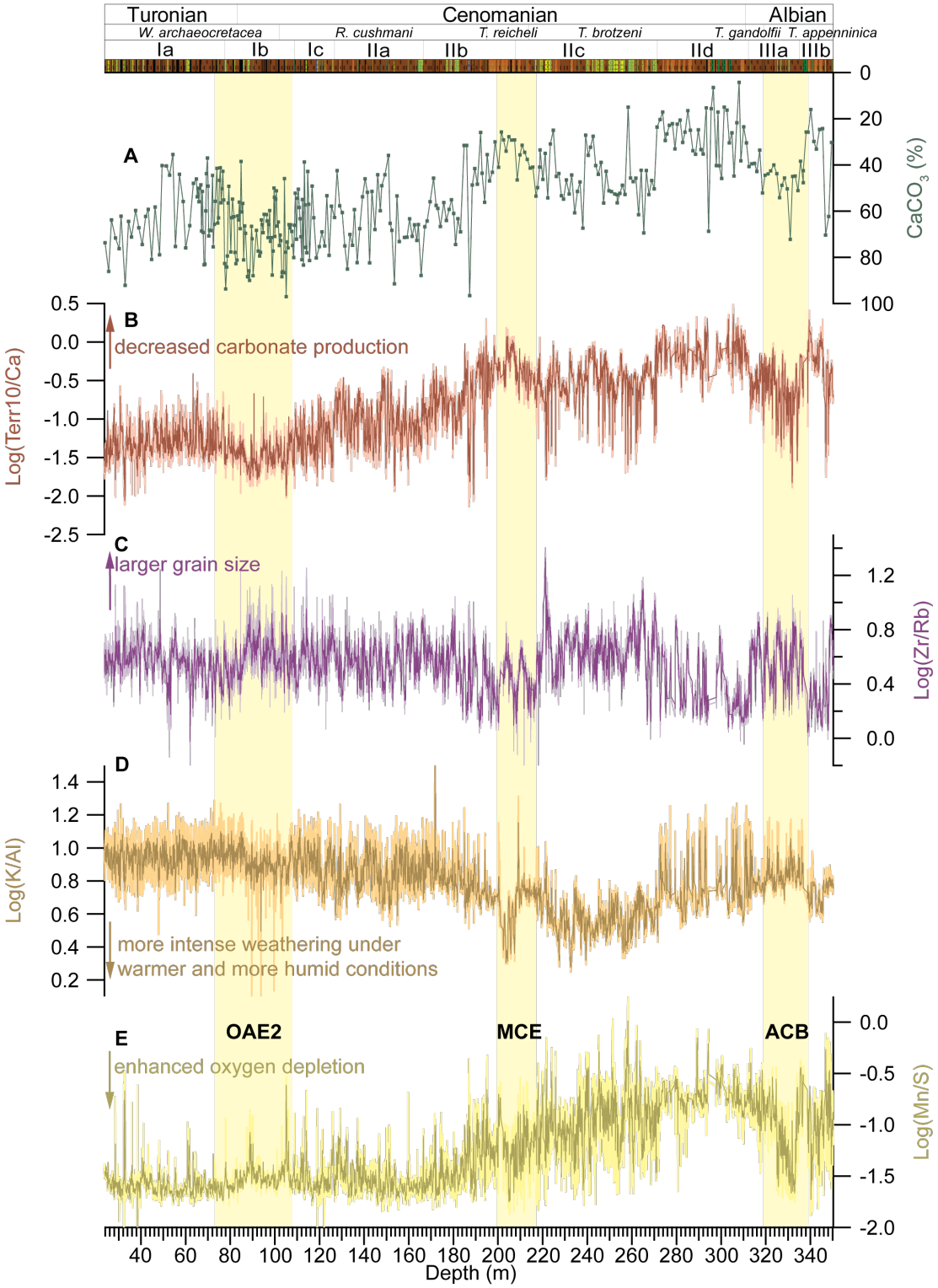

Figure 2.5A: Paleoenvironmental proxy records from Core SN°4: **A.** carbonate content (%), **B.** XRF-derived Log(Terr10/Ca) interpreted as proxy for terrigenous input, **C.** XRF-derived Log(Zr/Rb) interpreted as grain size variability, **D.** XRF-derived Log(K/Al) representative of variations of the clay mineral assemblage and **E.** XRF-derived Log(Mn/S) interpreted as redox-

proxy for water column conditions. Column at the top represents lithology, chrono- and biostratigraphy.

with a sharp increase at 339 m from a late Albian background mean of -28.2‰ to a maximum value of -27.1‰, followed by a stepwise decrease to -28.1‰ at 318.5 m. Although the amplitude of the carbon isotope excursion marking the ACB is only in the range of ~1‰, it is associated with an interval of TOC enrichment and Log(Mn/S) depletion indicating an anoxic phase.

2.3.6 Bulk carbonate $\delta^{18}O$

Oxygen isotope values (Fig. 2.5B) vary between -5.5 and -2.28‰ with high amplitude short-term variability. Higher values occur predominantly between 251 and 106 m with an average of -3.64 ‰ and variations between -4.94 and -2.28‰. The upper part of the record between 106 and 23 m is characterized by lower values with an average of -4.12‰ (-5.65 to -2.28‰), following a decrease that coincides with the $\delta^{13}C_{org}$ increase marking the onset of OAE2. Positive excursions are recorded during OAE2 (starting at 102.73 m) of ~1.37‰ and during the MCE (starting at 209.83 m and culminating at 206.07 m) of ~0.7‰.

The cross plot of bulk carbonate $\delta^{18}O$ against $\delta^{13}C$ over the interval analyzed for stable isotopes does not reveal any significant correlation (Supplementary Material Figure S2.3), supporting the interpretation of longterm trends as primary features (Nelson and Smith, 1996). A detailed discussion of high frequency variability of bulk stable isotopes for the OAE2 interval is included in Kuhnt et al. (2017).

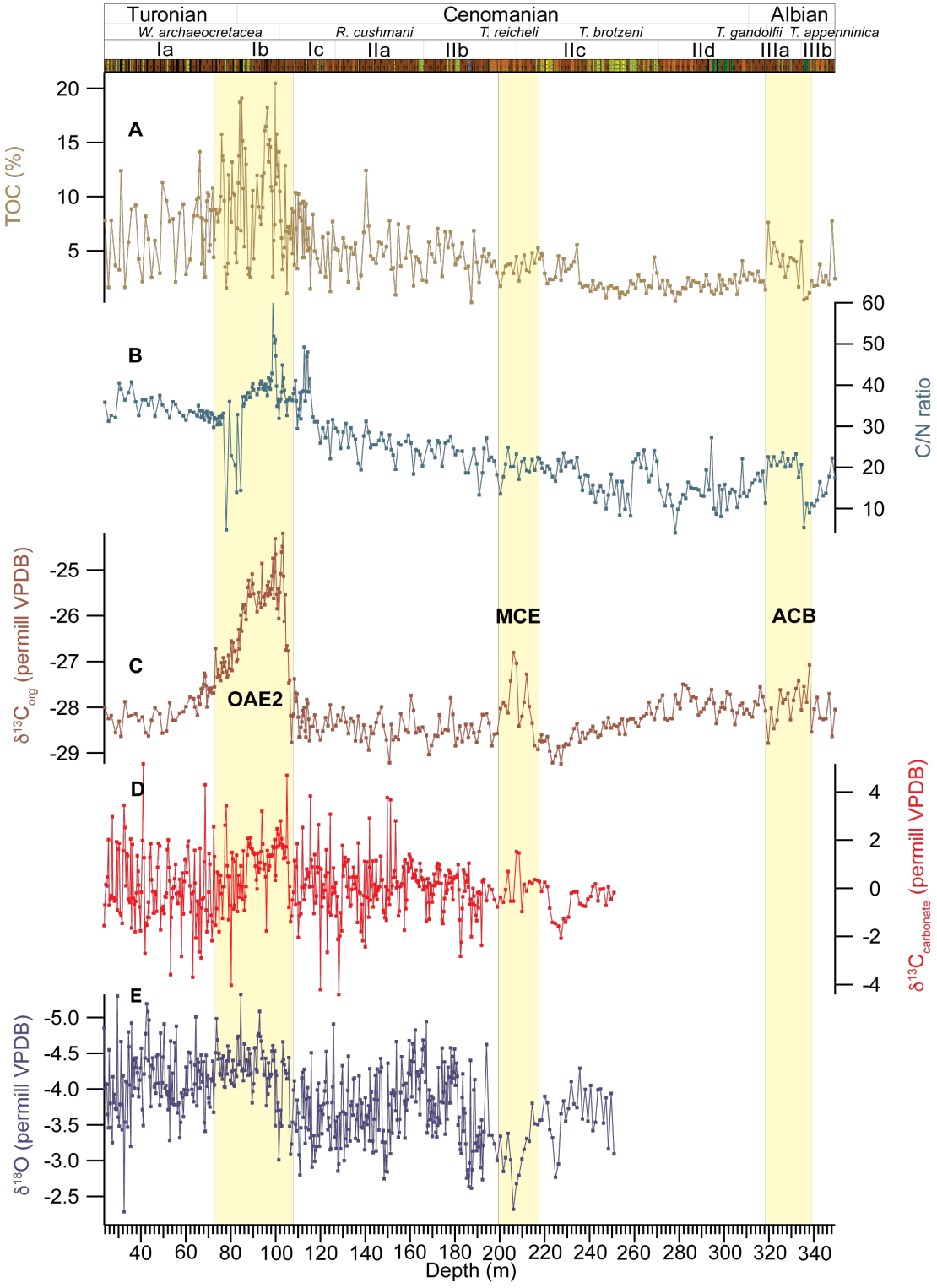

Figure 2.5B: Paleoenvironmental proxy records from Core SN°4: **A.** TOC (%), **B.** C_{org}/N_{total}-ratio measured on bulk material, **C.** $\delta^{13}C_{org}$, **D.** $\delta^{13}C_{carbonate}$ and **E.** $\delta^{18}O$. Column at the top represents lithology, chrono- and biostratigraphy.

2.3.7 XRF-scanning derived elemental ratios

We used four records of elemental ratios to characterize variations in terrigenous input, proximity to the sediment source, clay mineral composition and weathering in the source area and redox conditions at the sediment surface.

2.3.7.1 Log(Terr10/Ca)

The elements Al, Fe, K, Si and Ti generally have a terrigenous origin, especially in hemipelagic settings (Peterson et al., 2000; Calvert and Pedersen, 2007; Mulitza et al., 2008; Tisserand et al., 2009; Govin et al., 2012). Tests of marine organism contribute most of the calcium in the form of calcium carbonate. The logarithmic ratio of the sum of Al, Fe, K, Si and Ti normalized against Ca (Log(Terr10/Ca)) is, thus, used as a proxy for terrestrial clastic material vs. marine biogenic carbonate (Fig. 2.5A).

In Core SN°4, values vary between -2.14 and +1.68 (Fig. 2.5A). Below 196.62 m (Subunits 3b to 2b), Log(Terr10/Ca) is characterized by increased variability and overall higher values (>0.75). This is followed by a two-step decline with a largest decrease occurring up to 166.41 m (Subunit 2b) and a smaller decrease up to 108.79 m (Subunits 2a and 1c). The interval above 108.79 m shows large variability around a near constant average (<-1).

2.3.7.2 Log(Zr/Rb)

The element Zr is almost exclusively found in the heavy mineral zirconium within sediments. Alumosilicates and their weathering products (clays) are the main source for Rb. According to Calvert and Pedersen (2007) high Log(Zr/Rb) ratios (sediments relative enriched in Zr) coincide with large

grain sizes due to the high density of zircons, which can only be transported in conjunction with comparatively large grains of less dense minerals (alumosilicates and quartz grains). In this study, Log(Zr/Rb) is interpreted as an indicator of grain size changes in the terrigenous component due to changes in the proximity of the sediment source, likely associated with sea level changes.

In Core SN°4, Log(Zr/Rb) varies between -0.82 and 1.41 (Fig. 2.5A). Despite the large variability, Log(Zr/Rb) shows a clear cyclicity of ~4 m especially in the lower part of the core below 196 m (Fig. 2.5A). Log (Zr/Rb) varies in antiphase with Log(Terr10/Ca) between 348 and 337 m and between 312 and 275 m, indicating extended periods of predominantly fine grained terrigenous discharge. Above 196.62 m, short-term fluctuations in Log (Zr/Rb) decrease in amplitude with longterm averages of ~0.6 between 196.62 and 86 m and of ~0.55 above 86 m.

2.3.7.3 Log(K/Al)

Log(K/Al) (Fig. 2.5A) has been widely used as a proxy for the mineralogical composition of clay assemblages (Weaver, 1967, 1989; Niebuhr, 2005). We interpret Log(K/Al) as reflecting variations in the amount of potassium-rich illite in the clay mineral assemblages, which is controlled by variations of the weathering intensity in the source area (Calvert and Pedersen, 2007). Silicate weathering under warm conditions with sufficient supply of water is characterized by a continuous breakdown of the crystal structure of feldspars and a depletion of potassium in comparison to aluminum. Potassium-enriched clay minerals in the tropics, thus, indicate relatively dry conditions in the source area.

In Core SN°4, the log-ratio of K/Al varies between 0.3 and 1.3 except for a few brief intervals with extreme potassium enrichment or depletion (Fig. 2.5A). As for Log(Zr/Rb), Log(K/Al) exhibits high amplitude variability with a wavelength of >~4 m in the lower part of the core (>196.62 m). The lowermost interval (270-350 m) also shows characteristic minima in Log(K/Al) around 275-312 m and 337-348 m. Between 202 and 270 m, Log(K/Al), unlike Log(Zr/Rb), shows a pronounced longterm minimum (mean values ~0.6) that ends with a marked increase at 202 m. Above 202 m, Log(K/Al) shows a stepwise increase in average values from 0.85 between 202 and 87 m to 0.95 between 87 and 23 m. This stepwise trend is paralleled by a decrease in amplitude recorded in decreasing standard deviation from 0.132 (202–87 m) to 0.099 (above 87 m).

2.3.7.4 Log(Mn/S)

The main factor controlling Log(Mn/S) (Fig. 2.5A) is deep water oxygenation and the redox state at the sediment-water-interface, as manganese (Mn) is insoluble under oxic conditions, but soluble under reducing conditions (Landing and Bruland, 1980; Bruland, 1983). As shown by Brumsack (2006), Mn is generally depleted in modern and Cretaceous sediments underneath upwelling zones. Sulfur content is mainly influenced by the degree of pyritization in normal pelagic sediments, which is to a certain degree controlled by the TOC content and reactivity of the organic matter (Rachold and Brumsack, 2001). Sediments depleted in sulfur in combination with a low organic matter content are indicative of well-oxygenated bottom water conditions (Rachold and Brumsack, 2001). Log(Mn/S) is, therefore, interpreted as an indicator for bottom water oxygenation with an increased ratio indicative of better ventilated bottom water.

In Core SN°4, Log(Mn/S) generally varies between -2 and 0, except for a few levels enriched with pyrite crystals (Fig. 2.5A). Between 350 and 320 m, Log(Mn/S) fluctuates from -1.2 to -1.6 with an interval of sustained lower values (~-1.5) between 333 and 326 m. The interval 320–273 m is characterized by higher values (>-1) and lower amplitude variability. Between 273 and 185 m, Log(Mn/S) exhibits a longterm decrease in values and amplitude. In the upper part of the core (185–23 m), Log(Mn/S) displays relatively low amplitude variability, oscillating around a mean of ~-1.6.

2.3.8 Cyclostratigraphy based on NGR logging and XRF-scanner elemental ratios

Cycles with a wavelength of >100 m were removed from the NGR dataset using the *astrochron*-function *noKernel* (Meyers et al., 2012a). EHA of the filtered NGR data reveals strong cyclicity with high amplitude variability in the upper part of the core between 60 and 110 and lower amplitude variability over the intervals 150 to 230 m and 280 to 337.5 m (Fig. 2.6, Supplementary Material Figure S2.4). Within the high amplitude interval between 60 and 110 m, a highly significant peak (confidence level (CL) > 95%) is determined by spectral analysis (Table 2.1) with frequency of 0.2474 cycles/m (wavelength 4.04 m). Additional significant peaks (CL > 90%) are at 0.03198 (31.33 m) and 0.47087 (2.12 m) cycles/m. Power-maxima at 0.14765 (6.77 m), 0.33121 (3.02 m) and 0.70231 (1.42 m) cycles/m are not statistically significant.

The XRF-scanner derived Log(Zr/Rb) shows strong cyclicity below 200 m (Fig. 2.7). The record above ~200 m exhibits considerably lower amplitude variability. We restricted the spectral analysis of the Log(Zr/Rb) record to the

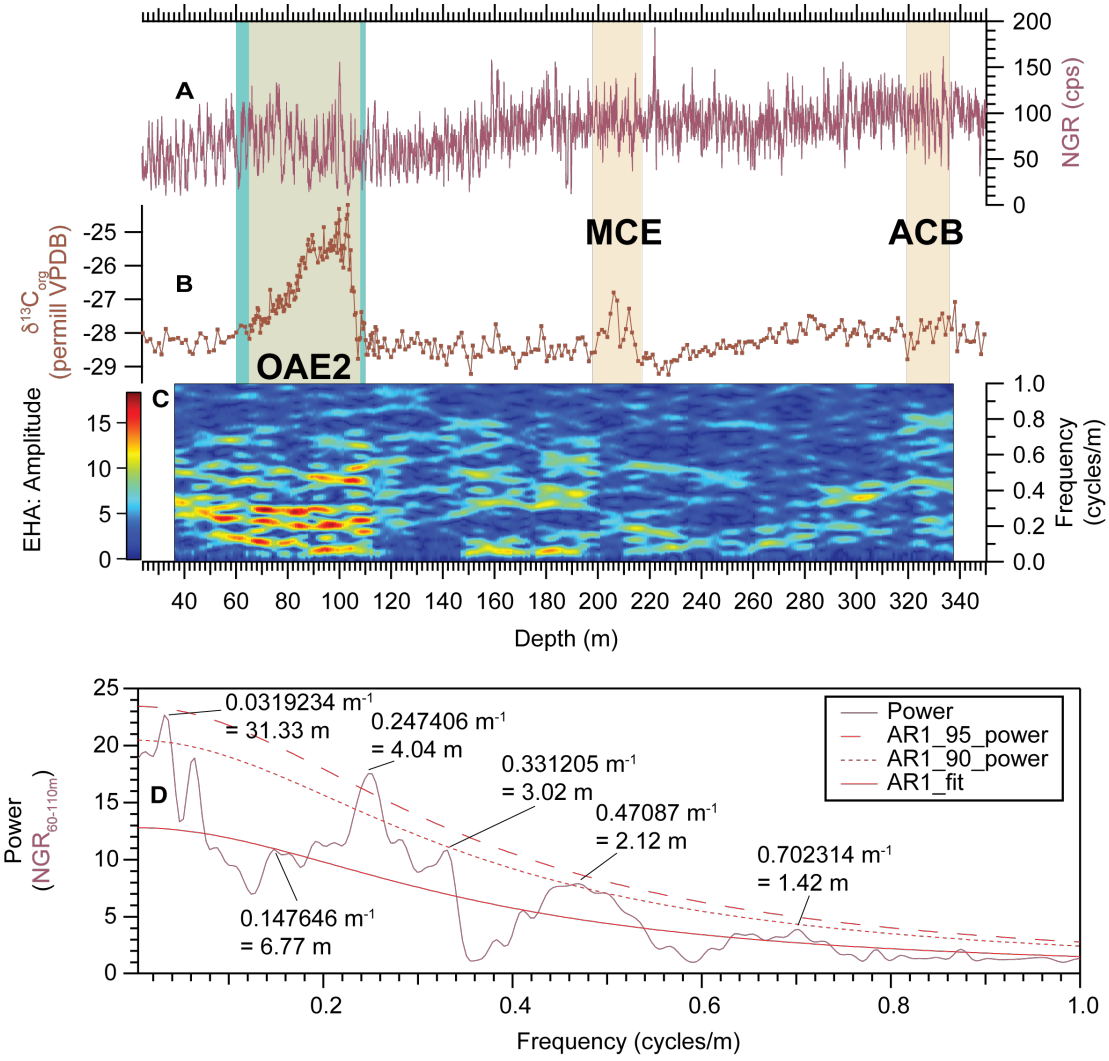

Figure 2.6: Frequency analysis of Natural Gamma Ray (NGR) from SN°4 bore hole log data. **A.** NGR dataset. **B.** $\delta^{13}C_{org}$, **C**. EHA, **D.** mtmML96 power spectrum of NGR over depth interval 60 to 110 m highlighted in turquoise encompassing OAE2 calculated with Astrochron (Meyers et al., 2012a). For interpretation of marked peaks in power spectrum see Table 2.1.

interval between 200 and 350 m, which exhibits the strongest signal. Low frequency cycles with a wavelength of >100 m detected mainly in the lower part of the core were removed using a Gaussian kernel in the astrochron-function *noKernel* (Meyers et al., 2012a). Spectral analysis of Log(Zr/Rb) indicates statistically highly significant (>99, 95 and 90 % confidence level) spectral peak at periodicities of 46.96, 21.47, 14.45 and 9.16 m, related to fluctuations in the

Table 2.1: Comparison of detected frequencies in Core SN°4 NGR (60 – 110 m) and orbital cycles from orbital solutions La04 (Laskar et al., 2004), La10 (Laskar et al., 2011a) and La11 (Laskar et al., 2011b). Orbital terms in brackets denote statistically not significant frequencies (CL<90%). E1: long eccentricity, E2, E3: short eccentricity, O1, O2: obliquity and P1, P2: precession.

NGR in SN°4 (60–110 m)				Extracted frequencies from Laskar et al. (2004, 2011a, 2011b)		
Frequency (cycles/m)	Wave-length (m)	Confidence level (%)	Ratio	Orbital term	Wave-length (kyr)	Ratio
0.031923 (0.025-0.039)	31.33	>90	1	E1	405.49	1
0.14765 (0.139-0.172)	6.77		0.22	(E3)	96.79	0.24
0.24741 (0.240-0.259)	4.04	>95	0.13	O1	48.24	0.12
0.33121 (0.320-0.335)	3.02		0.10	(O2)	37.64	0.09
0.47087 (0.462-0.479)	2.12	>90	0.07	P1	22.46	0.06
0.70231 (0.690-0.710)	1.42		0.05	(P2)	18.33	0.05

Table 2.2: Detected frequencies of Log(Zr/Rb) in Core SN°4 (200 – 350 m) and orbital cycles extracted from orbital solutions La04 (Laskar et al., 2004), La10 (Laskar et al., 2011a) and La11 (Laskar et al, 2011b). E1: long eccentricity, E2, E3: short eccentricity, O1, O2: obliquity and P1, P2: precession.

Log(Zr/Rb) in SN°4 (200–350 m)				Extracted frequencies from Laskar et al. (2004, 2011a, 2011b)		
Frequency (cycles/m)	Wave-length (m)	Confidence level (%)	Ratio	Orbital term	Wave-length (kyr)	Ratio
0.02130 (0.011-0.031)	46.96	>99				
0.04658 (0.044-0.048)	21.47	>95		E1	405.49	1
0.06921 (0.059-0.071)	14.45	>90		E1	405.49	1
0.10914 (0.106-0.116)	9.16	>90		heterodyne E2/3-E1		
0.19032 (0.171-0.215)	5.25			E2+E3	127.14 96.79	0.31 0.24
0.31809 (0.305-0.321)	3.14			O1	48.24	0.12
0.62686 (0.602-0.640)	1.60			O2	37.64	

grain density and grain size of the terrigenous component (Fig. 2.7). Additional peaks centered at 5.3 m (0.19032 cycles/m), 3.1 m (0.31809 cycles/m) and 1.6 m (0.62686 cycles/m) (Table 2.2) are statistically less significant (CL<90%).

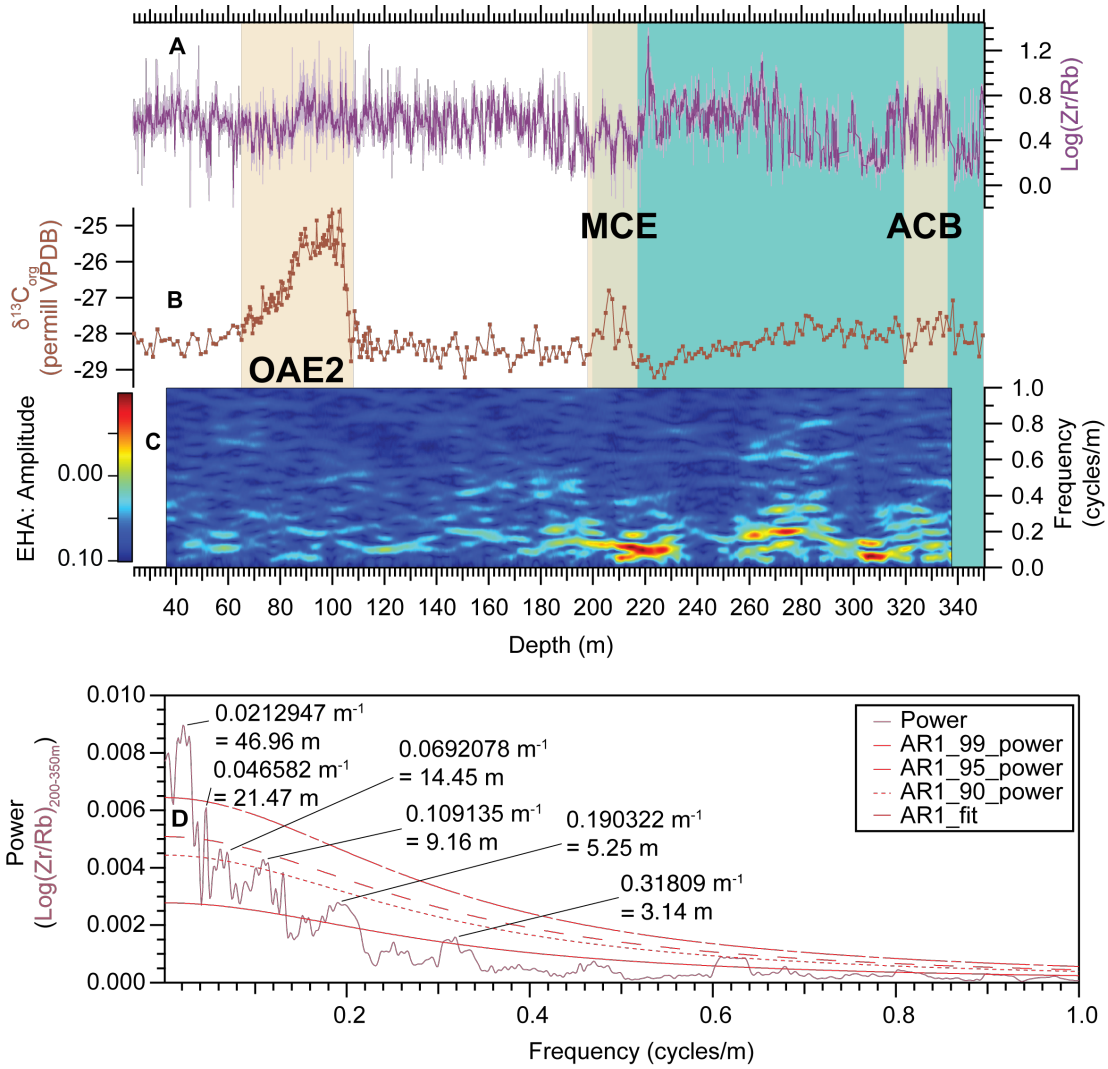

Figure 2.7: Frequency analysis of XRF scanner derived proxy data. **A.** Log(Zr/Rb) time series. **B.** $\delta^{13}C_{org}$, **C.** EHA calculated over entire core. **D.** mtmML96 power spectrum of Log(Zr/Rb) calculated over interval 200 to 350 m highlighted in turquoise with Astrochron (Meyers et al., 2012a). Dotted lines in power spectrum indicate 90, 95 and 99% confidence intervals. For interpretation of marked peaks in spectrum see Table 2.2.

2.4. Discussion

2.4.1 Late Albian-early Turonian orbital variability

Despite decades of research, a definitive orbital solution for the time period older than 40 Ma still remains elusive. The solution of Laskar et al. (2004, La04) includes the full orbital parameter set of precession, obliquity and eccentricity, but is only valid for the last 40 Ma. Laskar et al. (2011a) published a more extended solution with four different options, but it was limited to eccentricity (Fig. 2.8). Furthermore, these authors stressed that due to the chaotic behavior of the inner solar system and limitations in the knowledge of the tidal dissipation effect, shorter orbital periodicities (precession and obliquity) could not be extended beyond the scope of the La04 solution. Thus, further refinements of orbital solutions need to be based on comparisons with sedimentological records (Laskar et al., 2011b). Only periodicities caused by the interactions of planets in the outer planetary system are stable enough to allow a projection into the deeper past (Laskar et al., 2011a, 2011b). However, the long modulation of eccentricity with a wavelength of 405 kyr was considered to be stable and valid for paleoceanographic reconstructions (Laskar et al., 2004, 2011a, 2011b, Fig. 2.8), even for periods of 100 Ma and beyond. Although the chaotic character governing the motion of celestial bodies of the inner solar system and especially the motion of large asteroids may prevent the calculation of a definitive orbital solution for periods beyond the Cenozoic (Laskar et al., 2011b), the relative ratio of different frequencies are still suitable for deeper time intervals (Berger et al., 1992). These ratios can be used for the analysis of power spectra of sedimentary sequences (e.g., Meyers and Sageman, 2007).

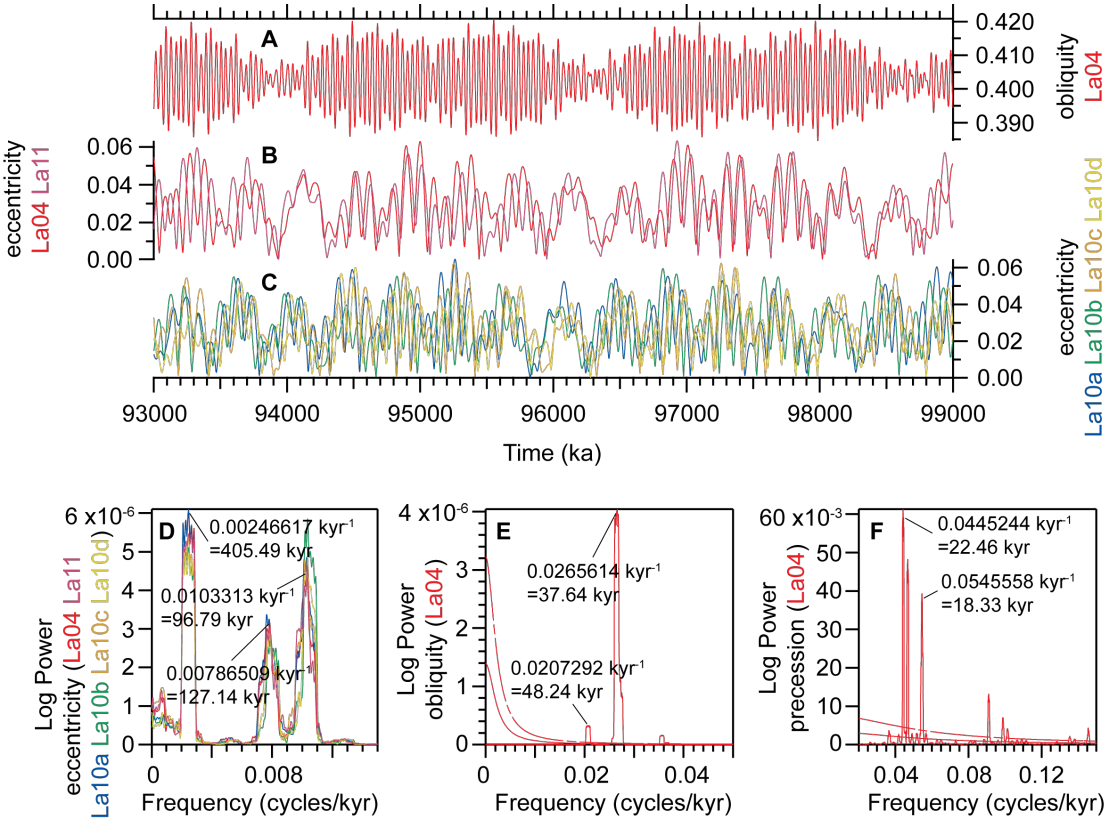

Figure 2.8: Examples for potential orbital configurations during late Albian to early Turonian from Laskar et al. (2004 (**A**, **B**), 2011a (**C**) and 2011b (**B**)). Due to the chaotic behavior of the inner solar system, power spectra of the displayed curves can only be used to extract wavelengths for the main periodicities of **D** eccentricity (405.49 (E1), 127.14 (E2), and 96.79 kyr (E3)), **E** obliquity (48.24 (O1) and 37.64 kyr (O2)) and **F** precession (22.46 (P1) and 18.33 kyr (P2)).

2.4.2 Identification of orbital periodicities in NGR and Log(Zr/Rb) records

Prominent cycles in NGR over the interval 60 to 110 m in Core SN°4, which encompasses OAE2, allow analysis and correlation of power maxima with distinct frequencies (Fig. 2.6 and Table 2.1), based on the ratio between the respective orbital wavelengths extracted from the orbital solutions La2004, 2010a-d and 2011 (Laskar et al., 2004, 2011a and 2011b). Highly significant peaks correlate to long eccentricity (E1) with wavelength of 31.33 m, to obliquity

(O1) with wavelength of 4.04 m and to precession (P1) with wavelength of 2.12 m. Additional peaks interpreted as short eccentricity (E3) with wavelength of 6.77 m, O2 with wavelength of 3.02 m and P2 with wavelength of 1.42 m support this interpretation. The calculated sedimentation rate based on the long eccentricity cycle (405 kyr) is 7.7 cm/kyr. This agrees well with the calculated sedimentation rates of 8.47 and 6.07 cm/kyr for nearby Core S13 in the Tarfaya Basin (Meyers et al., 2012a).

Strong cyclicities in Log(Zr/Rb) below 200 m (Fig. 2.7) permitted further analysis in the lower part of the core. The correlation with orbital frequencies extracted from the La2004 (precession, obliquity and eccentricity) and La2010/2011 solutions (eccentricity) reveals the most significant frequencies between 14.45 m and 21.47 m wavelength, which corresponds to 321 and 477 kyr respectively and, thus, represents the long (405 kyr) eccentricity cycle. The relatively broad double peak is most likely caused by changes in sedimentation rate within the analyzed window of 200 to 350 m. Thus, the average 405 kyr cycle has a wavelength of 18 m (frequency of 0.055 cycles/m) assuming an average 4.5 cm/kyr sedimentation rate with sedimentation rates varying between 3.6 and 5.3 cm/kyr. Obliquity cycles vary between 1.6 and 3.14 m, depending on sedimentation rates and varying spectral power of the 38 and 48 kyr obliquity cycles (Table 2.1). The short eccentricity cycle has a relatively consistent wavelength of ~5.25 m (corresponding to 117 kyr at average sedimentation rate of 4.5 cm/kyr). Based on an average sedimentation rate of 4.5 cm/kyr for the interval between 200 and 350 m, the duration of the lower Cenomanian (thickness of 120 ±10 m) is estimated to be 2.66 ±0.2 Myr.

The strongest and most significant frequency in the NGR data occurs between 60 and 110 m (frequency of 0.24741 cycles/m, 4.04 m wavelength) and corresponds to O1 (48.54 kyr) (Fig. 2.6), implying a strong obliquity forcing on depositional processes, even at low latitudes during the late Cenomanian. However, the mechanism translating obliquity forcing into a signal imprinted on low latitude sediments remains enigmatic. Possible processes may include mean annual insolation in the tropics, which decreases with higher obliquity, and obliquity-driven changes in the insolation gradient between high and low latitudes, which enhances seasonal atmospheric heat and moisture transfer between high and low latitudes, especially in a supergreenhouse world. Recently, Laurin et al. (2015) suggested an alternative mechanism, albeit effective only on longer timescales. These authors used modeling in comparison with proxy data to reproduce the 1.2 Myr obliquity modulation during the Late Cretaceous, based on non-linear responses of high-latitude (e.g. peats, permafrost, methane hydrates) and global (euxinic basins, soils) carbon reservoirs to insolation forcing. These authors suggested that destabilization of these reservoirs in combination with reconfiguration of the global circulation strongly influenced the global marine carbon cycle.

A general characteristic of the EHA of NGR (Fig. 2.6) is the unusually strong cyclicity signal during OAE2. In contrast, the upper part of the MCE interval (195-210 m) is characterized by a muted orbital signal (Supplementary Material Figure S2.4). The orbital signal between the ACB and the early phase of the MCE including the first $\delta^{13}C_{org}$ maximum remains weak. Assuming that bottom water dysoxia or anoxia facilitates the preservation of the original orbital signal in sediments due to the lack of bioturbation, the low TOC-content

measured for the MCE suggests an attenuation of the signal by bioturbation and therefore at least dysoxic conditions at the sea floor. An alternative explanation is that the sea level fall connected to the sequence boundaries Ce2.1 and Ce3 (chapter 4.6) are responsible for considerable short-term changes in sedimentation rates, which would obliterate clear orbital patterns in the sedimentary record.

The general stronger response to orbital forcing during OAE2, as detected with EHA, may be caused by enhanced preservation of the cyclic sedimentary structure due to reduced bioturbation and predominance of laminated deposits. Further possible influences on the response to orbital forcing include high frequency fluctuations in sea level and pCO_2 or a generally higher response of the Oxygen Minimum Zone (OMZ) to organic carbon flux at higher deep water temperatures. Sea level would control transport distance of deposited sediments, smooth short-term variability with increasing sea level and decreasing proximity and, therefore, transfer power from short-term to longer term periodicities. Global warming under increasing atmospheric pCO_2 may have, thus, intensified the imprint of orbital variability by modifying intermediate water oxygenation and sediment input.

2.4.3 Evolution of bottom water oxygenation, organic matter accumulation and paleoproductivity

Changes in bottom water oxygenation and organic matter accumulation are approximated from TOC, C/N and Log(Mn/S). Lower Cenomanian deposits (between 273 and ~320m) in Core SN°4 are generally characterized by high Log(Mn/S), and low TOC (<3 %), indicative of relatively well ventilated bottom

water conditions (Fig. 2.5). In the latest Albian (below ~320 m), higher TOC values (3-8%) and lower Log(Mn/S) values (in the range of -1.2 to -1.6 with strong fluctuations in the lower part) indicate more dysoxic/anoxic conditions in the water column. In particular the interval 333–326 m, where Log(Mn/S) is consistently lower (fluctuating around -1.5, comparable to values in the upper Cenomanian/Turonian), corresponds to a transient period of anoxia and elevated organic matter accumulation. A coeval increase in organic matter (TOC fluctuating at ~5%) supports the interpretation of oxygen-depleted conditions promoting improved preservation of organic matter during this interval.

Log(Mn/S) exhibits an extended transitional phase between ~185 m and 273 m with strongly fluctuating Log(Mn/S) and a consistent decrease in mean values from ~-1.0 to ~-1.5. This transitional trend in Log(Mn/S) is paralleled by TOC, which increases from a running mean of ~2 to ~5%. Above ~185 m, Log(Mn/S) becomes more stable around a mean of -1.5 and high amplitude fluctuations (>–1.3) become rare transient events. We interpret this evolution as indicative of the establishment of an increasingly stable OMZ during a long transitional phase between 185 and 273 m. This transition towards less oxygenated conditions may have been facilitated by a regional sea level rise that promoted impinging of the OMZ on the shelf. The interval <185 m is characterized by prevailing anoxic bottom water conditions with only transient oxygenation events. The establishment of a stable late Cretaceous OMZ in the latest Cenomanian/early Turonian is a common feature along the West African Margin (e.g., Holbourn et al., 1999). However, our data suggest that the transition towards an upwelling-related oxygen depleted depositional environment started earlier (in the middle part of the early Cenomanian at 273 m in Core SN°4) in the

Tarfaya Basin and resulted in consistent deposition of organic-rich sediments since the end of the middle Cenomanian (~185 m). Although both the upper Albian and OAE2 are characterized by elevated TOC in the Tarfaya Basin, the MCE is not characterized by exceptional changes in oxygenation or TOC accumulation at a time when the "background" oxygen depletion and resulting organic matter preservation were already elevated in the Tarfaya Basin.

2.4.4 Mid-Cenomanian Event (MCE): A precursor to OAE2?

The MCE, originally defined in the chalk successions of northwestern Europe (Paul et al., 1994), was subsequently identified in different ocean basins and is now considered a global event (Mitchell et al., 1996; Mitchell and Carr, 1998; Jarvis et al., 2001, 2006; Coccioni and Galeotti, 2003; Voigt et al., 2004; Gale et al., 2008; Hardas et al., 2012; Giraud et al., 2013). In Core SN°4, the MCE is characterized by a positive carbon isotope excursion with an increase in $\delta^{13}C_{org}$ of ~1.7‰ and a characteristic double peak within the *T. reicheli* Zone. A $\delta^{13}C_{org}$ minimum immediately precedes the main positive shift (Fig. 2.5). These features show striking similarities to the shape of the $\delta^{13}C_{org}$ curve across OAE2, which was studied at higher resolution in SN°4 by Kuhnt et al. (2017). The SN°4 records also indicate that the duration of the early phase (negative excursion, main increase and double peak) of the MCE and OAE2 isotope events was comparable, taking into account differences in sedimentation rate (7-8 cm during OAE2 and ~4 cm during the MCE). In both cases, the duration of this early phase corresponds to one long (405 kyr) eccentricity cycle, suggesting that the onset and early development of the MCE and OAE2 were orbitally modulated.

The MCE and OAE2 both exhibit short-lived increases in $\delta^{18}O$ following the initial $\delta^{13}C_{org}$ increase. The $\delta^{18}O$ increase during OAE2 was attributed to a massive atmospheric CO_2 drawdown through organic matter burial (e.g. Jarvis et al., 2011), which resulted in global cooling, as indicated by different proxies in various basins (e.g. Forster et al., 2007; Pearce et al., 2009; Barclay et al., 2010). A sustained cooling phase that may have even resulted in ephemeral glaciations in Antarctica, was also suggested for the MCE based on a bulk carbonate $\delta^{18}O$ increase in combination with sequence stratigraphic evidence for a high-amplitude sea level fall (Stoll and Schrag, 2000; Miller et al., 2003, 2005). A significant cooling during the MCE was determined from brachiopod shells from the mid-latitudinal shelf of Europe by Voigt et al. (2004). These authors hesitated to relate the cooling with ephemeral glaciations because the coolest temperatures were determined within a bed identified as a transgressive surface, preferring the alternative explanation of a major re-organization of shelf sea circulation. A temperature minimum expressed as a $\delta^{18}O$ maximum, also occurs above a transgressive surface in Core SN°4 (Fig. 2.9), although initial cooling started significantly earlier following the first $\delta^{13}C_{org}$ peak within the MCE. Maximum cooling coincided with the second $\delta^{13}C_{org}$ peak, as in the Contessa record (Stoll and Schrag, 2000), but unlike the Salder record (Voigt and Hilbrecht, 1997). The widespread occurrence of these events thus suggests a supra-regional or even global character rather than a regional re-organization of shelf circulation.

The “mid-Cenomanian glaciation hypothesis” was subsequently challenged by isotope records of glassy planktonic and benthic foraminifers that did not indicate a measurable ice volume signal in $\delta^{18}O$ records across the MCE

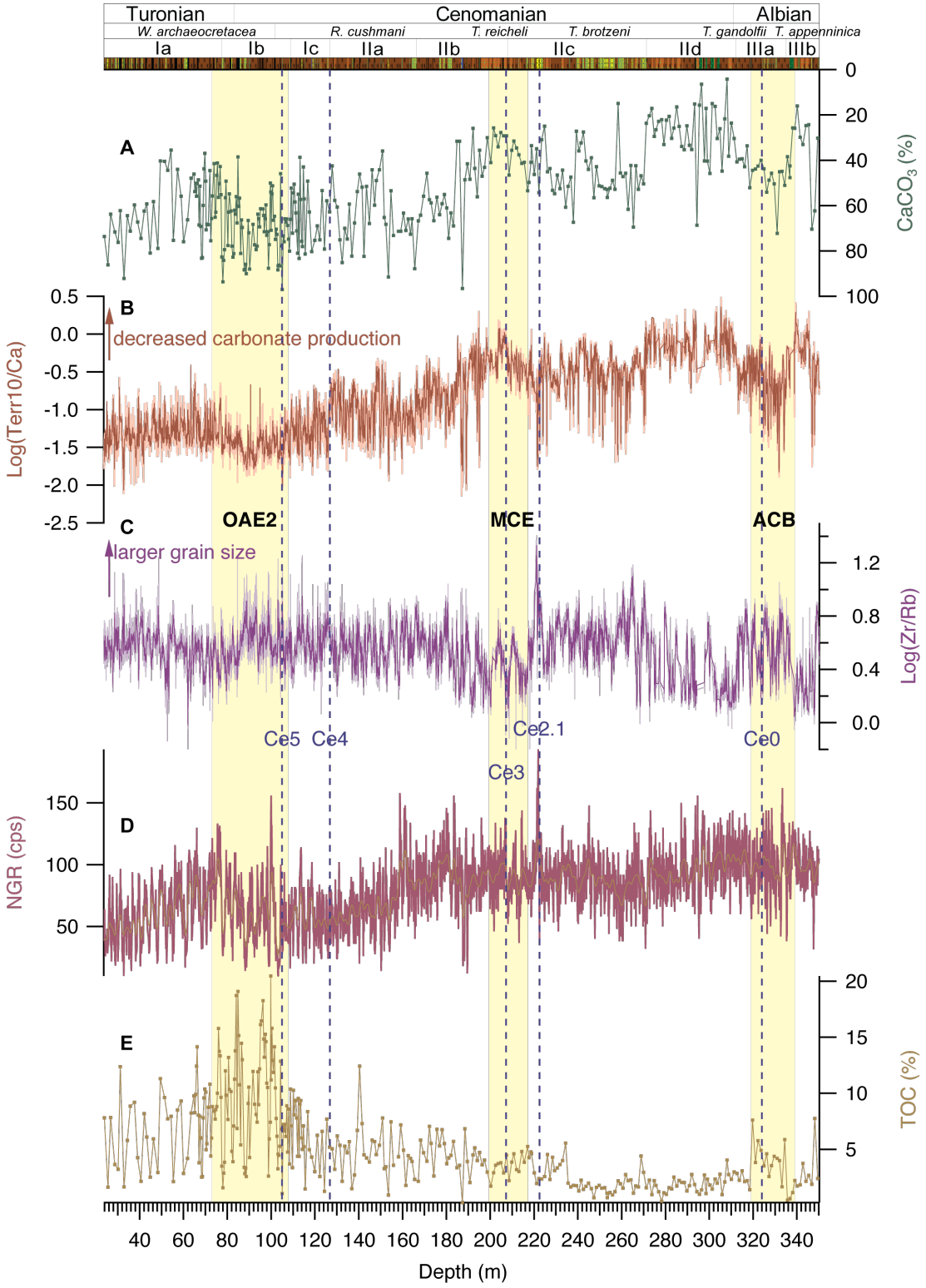

Figure 2.9: Sea level influenced paleoenvironmental proxies from Core SN°4: **A.** carbonate content (%), **B.** XRF-derived Log(Terr10/Ca) interpreted as proxy for terrigenous input, **C.** XRF-derived Log(Zr/Rb) interpreted as grain size variability, **D.** NGR (cps) and **E.** TOC (%). Vertical lines mark transgressive surfaces with corresponding sequences after Gale et al., (2002).

(Moriya et al., 2007; Ando et al., 2009). However, the isotopic composition of Antarctic ice in the Cretaceous greenhouse world must have been relatively close to or even heavier than that of modern "warm" Greenland ice (in the order of -25 to -30‰ in contrast to today's Antarctic ice $\delta^{18}O$ of -55‰, Lhomme et al., 2005). Thus, even the waxing and waning of sizable ice caps with a sea level effect in the order of 20-30 m (half of the modern Antarctic ice shield) would probably not be detectable in Cretaceous marine $\delta^{18}O$ records.

Apart from striking similarities, there are also differences between the MCE and OAE2. In particular, the amplitude and shape of the $\delta^{13}C_{org}$ excursion as well as the organic carbon burial rates differ markedly. In contrast to the characteristic plateau and gradual $\delta^{13}C_{org}$ decrease in the later stage of OAE2, the end of the MCE carbon isotope excursion is relatively abrupt and $\delta^{13}C_{org}$ returns rapidly to background level. However, the similarities in the carbon isotope record and associated sedimentation patterns during the onset of the MCE and OAE2 suggest comparable triggering mechanisms and climate-carbon cycle feedbacks during the two events, although the duration and amplitude of the initial CO_2 release from volcanic exhalations and the amount of ^{12}C sequestered through organic carbon burial probably were considerably lower during the MCE than during OAE2.

In contrast to that of the MCE, the OAE2 $\delta^{18}O$ record additionally shows a pronounced temperature increase towards a stable global Turonian temperature optimum, which is approximately in phase with the $\delta^{13}C_{org}$ increase (Clarke and Jenkyns, 1999; Wilson et al., 2002). Based on osmium isotope data, Turgeon and Ceasar (2008) and Du Vivier et al. (2014) suggested that this global temperature

increase was related with volcanic exhalations of the Columbia-Caribbean Large Igneous Province. Modeling studies (e.g. Flögel et al., 2011) further supported the notion of volcanogenic CO_2-induced warming into the Cenomanian-Turonian climate optimum.

2.4.5 Timing of $\delta^{13}C$ excursions and duration of the Cenomanian Stage

In Core SN°4, the initial $\delta^{13}C$ increases defining the onset of the three main anoxic events are located at 107 m (OAE2), 217 m (onset of the MCE) and 339 m (ACB), resulting in depth differences of 110 m between OAE2 and the MCE and of 122 m between the MCE and the ACB. Mean sedimentation rates for these intervals, estimated from the dominant orbital cycles (from 14.45 to 21.47 m for the 405 kyr long eccentricity cycle), are between 3.6 and 5.3 cm/kyr, with an overall average of 4.5 cm/kyr in the lower part of the core and typically 7.7 cm/kyr (31.33 m for a 405 kyr long eccentricity cycle) in the upper part of the core during OAE2. Changes in the frequency spectrum and signal amplitude in the EHA of NGR indicate a change in sedimentation rates at a depth of ~120 m (Fig. 2.6). Decreasing Log(Terr10/Ca) and increasing carbonate content also point to higher accumulation rates of carbonate (Fig. 2.5A). An increase in primary production and biogenic flux is also evident in the TOC record, which registers a marked increase above ~120 m. For an estimate of the time interval between the onset of the MCE and OAE2 we use the sedimentation rate of 7.7 cm/kyr, characteristic of enhanced carbonate/organic carbon accumulation, for the depth between 107 and 120 m, which results in a duration of ~0.17 Myr for this 13 m interval. The remaining 97 m (between 120 and 217 m) were deposited at an average sedimentation rate of 4.5 cm/kyr, in ~2.16 Myr adding

up to a total duration of ~2.33 Myr for the interval between OAE2 and the MCE, which is close to the modulation of the long eccentricity cycle (~2.4 Myr).

The time difference between the MCE onset (217 m) and the ACB (339 m) calculated with sedimentation rates of ~4.5 cm/kyr corresponds to 2.71 Myr, which is again within the range of the 2.4 Myr modulation of the long eccentricity cycle. Together these estimates suggest a duration of ~4.8 Myr for the Cenomanian Stage, since the ACB with a duration of one 405 kyr eccentricity cycle still falls into the latest Albian and the main part of OAE2 with approximately the same duration occurs in the Cenomanian. A minimal tuning approach using calculated sedimentation rates is presented in Supplementary Material Figure S2.5. Filtering for 405-kyr-cyclicity resulted in 11 long eccentricity cycles in agreement with Gale et al. (1999). These results support the estimated duration of the Cenomanian Stage suggested by Gale et al. (1999) and are in contrast to the significantly longer duration proposed by Gradstein et al. (2012).

2.4.6 Correlation of Cenomanian eustatic sea level records

Previous studies of sedimentary successions in the Tarfaya Basin included sequence stratigraphic interpretations of sedimentary features in outcrop sections situated in the more proximal part of the basin (Kuhnt et al., 2009; Aquit et al., 2013, 2015). These studies identified sequence boundaries and transgressive surfaces as important sequence stratigraphic features for interbasinal correlations of past sea level changes (Haq, 2014) and tentatively correlated them to the Cenomanian eustatic sea level reconstruction of Gale et al. (2002, 2008). Transgressive surfaces (TS) form the first significant flooding

surface at the onset of a transgressive sequence. The TS develops, when the increase in accommodation space outpaces the rate of sediment supply, thus forming the base of the transgressive systems tract (TST). A TS is often characterized by well cemented carbonate surfaces or hard grounds, which are commonly perforated by burrowing organisms.

In shallow shelf sedimentary systems or areas with low sediment supply, where falling sea level and/or lowstand facies is not usually preserved above the sequence boundary, the TS falls together with the sequence boundary (SB). Following this approach, Kuhnt et al. (2009) interpreted the characteristic nodular limestone beds in the more proximal section at Mohamed Plage as transgressive and merged the TS and SB at the base of these limestone beds. However, in the more distal Core SN°4, we consider that the relatively coarse grained carbonate beds or nodules in this deeper environments represent lowstand deposits between the SB and the TS. Sedimentary rocks across and immediately overlying the TS are commonly coarse-grained and winnowed by waves or tidal currents in deeper marine settings. These features are recognizable in our continuous XRF-scanner records by peaks in the Log(Zr/Rb) that are accompanied by low Log(Terr10/Ca), whereas high Log(Terr10/Ca) are more typical for fine-grained clay mineral deposition. On the NGR curve, a TS typically consists of a relatively abrupt increase in NGR associated with deposition of organic rich shales during the transgressive system tract above the TS.

Following these criteria, we identified five major TS within the sedimentary succession of Core SN°4 (Fig. 2.9 and Supplementary Material Figure S2.6):

(1) A major TS is recognized at 105 m within the onset of OAE2, which is correlative to sequence boundary Ce5 in the nomenclature of Gale et al. (2008). In Core SN°4, it is typically represented by the bioturbated surface on top of a prominent limestone bed and overlying organic-rich marlstones.

(2) The lithological change towards more carbonate rich and clay/organic lean rocks at the base of Subunit 1c in Core SN°4 corresponds to an abrupt change from organic rich to carbonate rich deposits at ~207 m in Core S13, which was previously correlated to sequence boundary Ce4 (Kuhnt et al., 2009). Although there is no sharp boundary in Core SN°4, an initial change in TOC and carbonate content occurs between 139 and 140 m, followed by a second major change (mainly expressed in the carbonate/terrigenous ratio) at the lithological boundary between Subunits 1c and 2a at 126.80 m.

(3) The most prominent TS within the Cenomanian sea level record is associated with Ce3 and was previously identified at Folkestone (Anglo-Paris Basin) and Pueblo, Colorado (Gale et al., 2008). At these locations, Ce3 is located at the base of the Thatcher Limestone in the center of the $\delta^{13}C_{org}$ trough between the two peaks of the carbon isotope excursion and coincides with a major sequence boundary, which forms a characteristic intensely bioturbated hard ground. In the Mohammed Plage section, Ce3 is prominently expressed as the boundary between greenish-gray claystones characterized by extremely low TOC and a nodular limestone bundle at the base of the *T. reicheli* zone (Kuhnt et al., 2009). This TS falls within a period of minimal sedimentation rates within the proximal setting of Mohamed Plage (Kuhnt et al., 2009), indicating sediment transport into more distal parts of the Tarfaya Basin.

In Core SN°4, Ce3 at 207.3 m is characterized by the intercalation of light, laminated carbonate rich layers with shell debris, indicating bottom current activity, within a sequence of dark marlstones (Fig. 2.10A). The NGR logging data show an abrupt increase across the TS, corresponding to the facies change to transgressive organic rich shales. Log(Zr/Rb) and Log(Terr10/Ca) exhibit an increase in grain size within the lowstand carbonate layers, followed by a decrease in grain size and higher clay content above the TS.

(4) A prominent TS (Ce2.1) defined by higher Log(Zr/Rb) and NGR is located between 222 and 223 m in the uppermost part of the *T. brotzeni* Zone, close to the onset of the MCE (Fig. 2.10B). This TS is coeval with a first small $\delta^{13}C_{org}$ increase prior to the MCE onset and at ~25 m below Ce3.

(5) The transgressive surface at the base of the Cenomanian (Ce0) is located at a maximum in Log(Zr/Rb) at 324 m, close to the top of the ACB.

2.4.7 C/N ratio and stoichiometry of organic matter indicating water column dysoxia/anoxia and paleoproductivity

The C_{org}/N_{total} ratios (Fig. 2.5B) in Core SN°4 are on average higher by a factor of 5 than the present day Redfield ratio (Redfield, 1942) of 6.6 representative for marine phytoplankton or average values of ~5 in organic-carbon-poor sediments (Bouloubassi et al., 1999). Diagenetic effects that would change the signal by a factor of up to 10 are not known today and the unusually high C/N ratios can be assumed to represent original variability (Meyers 1989, 2006). Two possible explanations were presented by Meyers (1989, 2006): (1) recycling of organic matter within the water column and uppermost cm of sediments under suboxic or anoxic conditions or (2) input of terrestrial organic

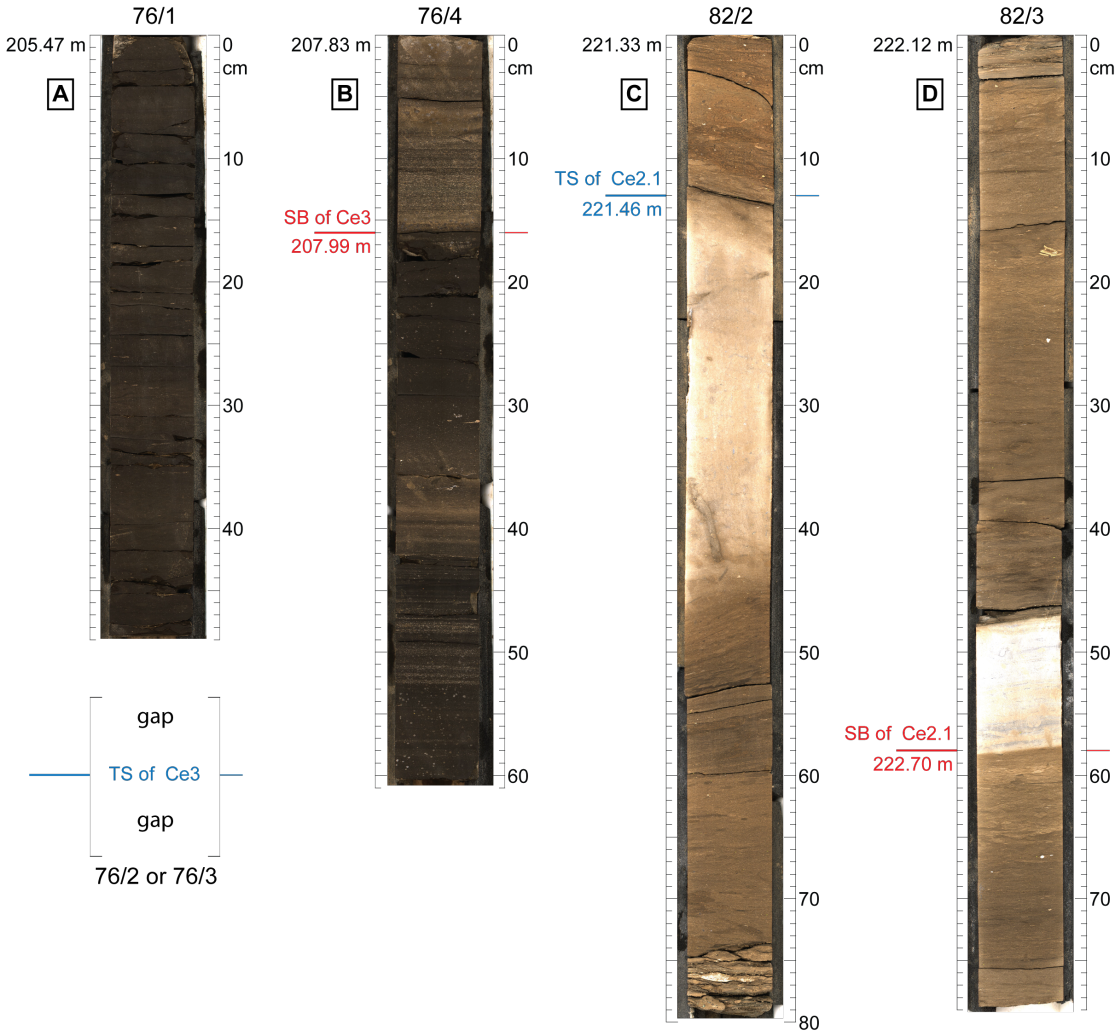

Figure 2.10A: Facies change across Ce2.1 and Ce3 in Core SN°4. **D.** Nodular carbonate beds with overlying coarse flaser-laminated marlstones correspond to Ce2.1. **B.** Organic-rich black shales with increased clay mineral content correspond to Ce3. Laminated carbonate rich intervals with small-scale erosional base indicate current redeposition (Ce3). Black shale deposition indicates a subsidence-related deeper environmental setting during Ce3 than during Ce2.1. Sequence boundaries (SB) are marked in red, the transgressive surface of Ce2.1 in blue.

material rich in cellulose. Rock Eval data from parallel cores in the Tarfaya Basin showed a predominance of kerogen types I and II with organic matter mainly consisting of alginite and bituminite that indicate a marine origin (Kuhnt et al., 2001), which excludes a terrestrial source for the N-rich organic matter. Van Mooy et al. (2002) concluded that modes of organic matter recycling differed

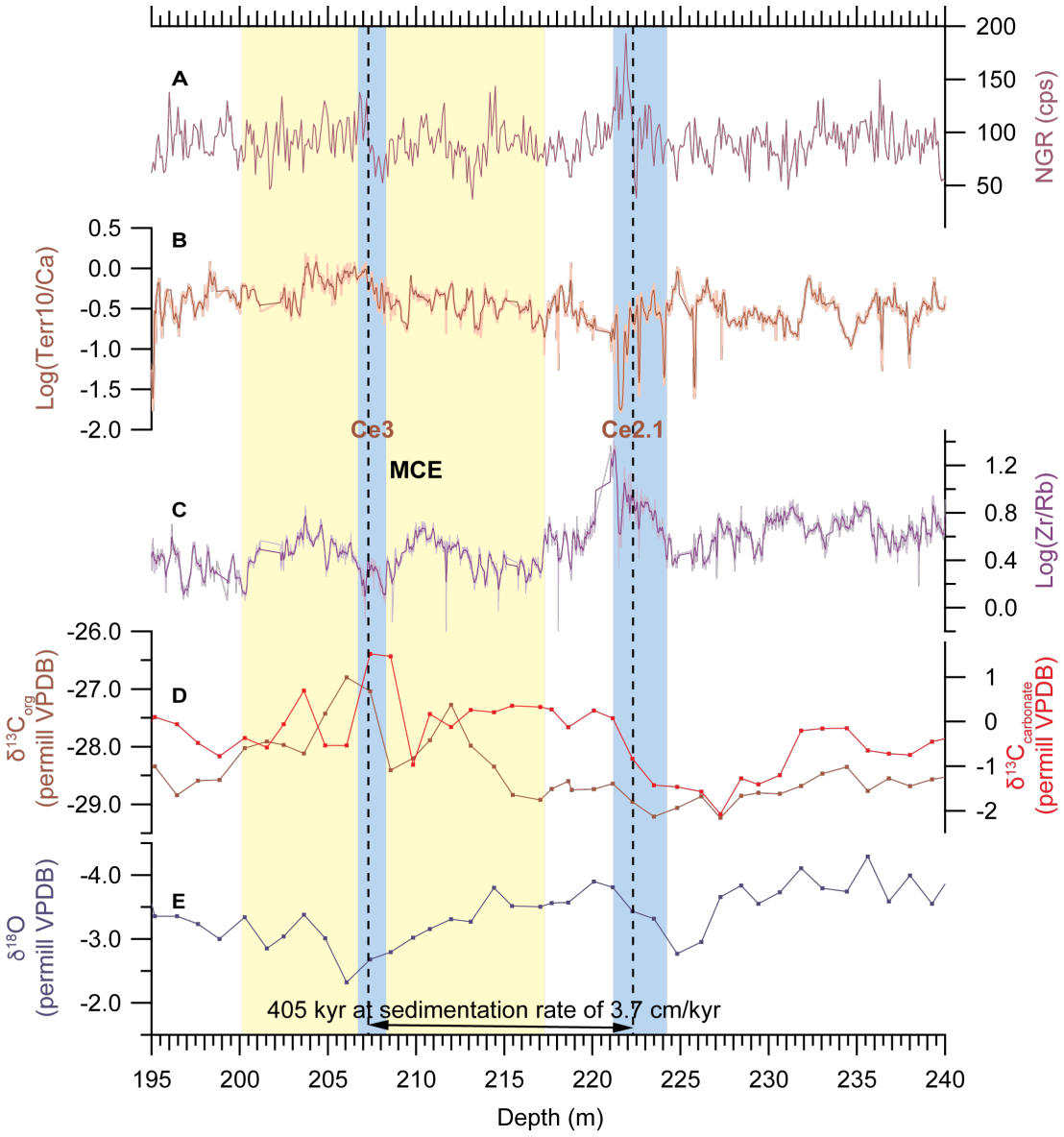

Figure 2.10B: Transgressive surfaces (TS) correlative to Ce2.1 and Ce3 in Core SN°4. Note increases in Log(Zr/Rb) below TS and distinct increases in NGR at TS. Ce2.1 and Ce3 are associated with global $\delta^{13}C$ increases. Blue shading marks sea level lowstands. Dotted lines mark TS. Yellow shading marks MCE interval. **A.** NGR in cps. **B.** XRF-derived Log(Terr10/Ca) interpreted as proxy for terrigenous input. **C.** XRF-derived Log(Zr/Rb) interpreted as grain size variability. **D.** $\delta^{13}C_{org}$. and $\delta^{13}C_{carbonate}$ **E.** $\delta^{18}O$.

between oxic and anoxic conditions. Suboxic microbial degradation and denitrification in the water column and at the sea floor preferentially disintegrate amino acids rich in N and lead to elevated C/N ratios. In contrast,

post-depositional diagenetic processes result in relative enrichment of N in organic matter and lowered C/N ratios (Müller, 1977; Waples and Sloan, 1980).

The relative depletion of N in the SN°4 sedimentary rocks, therefore, indicates suboxic or anoxic conditions within the water column or in the sediments during the sedimentation. A link to high productivity related anoxia is supported by increased C/N values in Mediterranean sapropels (Bouloubassi et al., 1999) and by generally increased values during mid-Cretaceous OAEs (Meyers et al., 2006). Twichell et al. (2002) used the C/N-ratio as proxy for elevated productivity on account of the coupling between increased productivity and water column redox state. The signal seems to be linked to the adaptation of heterotrophic organisms to dysoxic or anoxic conditions. Following this approach, periods with drastically increased C/N-ratio in Core SN°4 represent intervals of exceptionally increased productivity, in particular prior and during OAE2. This early increase in primary production may have been restricted to the northwest African shelf, which was subject to wind-driven upwelling since the early Cenomanian.

Enrichment of barium preceding and accompanying the initial $\delta^{13}C_{org}$ increase of OAE2 in the proximal Mohamed Plage section was interpreted by Mort et al. (2008) as a productivity increase stimulated by enhanced nutrient input from transgressive flooding of low altitude desert areas. Seismic offshore data indicate an open shelf setting for the Late Cretaceous Tarfaya Basin (e.g. Ranke et al., 1982; Patriat and Labails, 2006) rather than a restricted basin. The global extent of enhanced productivity and water column oxygen depletion is further supported by the occurrence of coeval elevated phosphorus mass accumulation rates in European (Tethys) and North American (Western Interior

Seaway) sections (Mort et al., 2007). These authors interpreted the initial peak in phosphorous accumulation as the result of increased productivity preceding globally enhanced organic carbon burial during OAE2.

2.5. Conclusions

A high-resolution analysis of a 325 m long continuous sedimentary succession recovered in Core SN°4 from the Tarfaya Basin reveals that terrigenous input as well as carbonate and organic carbon production rates were primarily controlled by a longterm transgressive trend from the late Albian to early Turonian. Three positive carbon isotope excursions are identified in the $\delta^{13}C_{org}$ record: OAE2 in the latest Cenomanian, the MCE during the mid-Cenomanian and the ACB. The most prominent Cenomanian transgressive surface separating two third-order eustatic sea level cycles, SB Ce3 (Haq et al., 1987) is identified close to the second peak of the MCE carbon isotope excursion. Sequence boundary Ce3 coincides with a fundamental change in cyclic sedimentation pattern and marks the onset of a longterm trend in increasing carbonate and organic carbon productivity. Low Log(Mn/S) ratios as well as elevated TOC and C/N ratios indicate intense oxygen depletion during OAE2 and the ACB, which we relate to enhanced primary production during these events. Mean sedimentation rates are 4.5–6 cm/kyr for the late Albian to middle Cenomanian (200–350 m) and 8-9 cm/kyr for the late Cenomanian to early Turonian. Based on EHA analyses of eccentricity and obliquity signals in the NGR wireline logging data and the XRF-scanner derived Log(Zr/Rb), we estimate the duration of the Cenomanian Stage to be 4.8 ±0.2 Myr.

2.6. Acknowledgements

We thank Nils Andersen (Leibniz Laboratory for Radiometric Dating and Stable Isotope Research, Kiel) and Michael Joachismki (GeoZentrum Nordbayern, Friedrich-Alexander Universität Erlangen-Nürnberg) for stable isotope measurements, Dieter Garbe-Schönberg and Samuel Müller (Institute of Geosciences, Kiel) for advice with X–ray fluorescence scanning, and Bettina Domeyer (GEOMAR) for technical help with the CHN Analyzer. RWE Dea AG in cooperation with the Office National des Hydrocarbures et des Mines, Morocco, enabled drilling SN°4 in the framework of the Atlantic Margin Integrated Basin Analysis Project. This research was funded by the German Research Council (DFG) in the framework of SFB 754, TP A7. We gratefully acknowledge two anonymous reviewers for comments and suggestions that significantly improved the manuscript.

2.7. Supplementary Material

for

New insights into Cenomanian paleoceanography and climate evolution from the Tarfaya Basin, southern Morocco

Sebastian Beil[1], Wolfgang Kuhnt[1], Ann E. Holbourn[1], Mohamed Aquit[1,2], Sascha Flögel[3], El Hassane Chellai[4] and Haddou Jabour[5]

[1]Institute of Geosciences, Christian-Albrechts-University, Ludewig-Meyn-Str.10-14, D-24118 Kiel, Germany
[2]OCP S.A., Direction de Recherche et Développement, Recherche Géologique, 46300 Youssoufia, Morocco
[3]GEOMAR Helmholtz-Zentrum für Ozeanforschung Kiel, Ozeanzirkulation und Klimadynamik, Paläo-Ozeanographie, Wischhofstr. 1-3, D-24148 Kiel, Germany
[4]Department of Geology, Faculty of Sciences Semlalia, Cadi Ayyad University, Marrakech, Morocco
[5]ONHYM, Office National des Hydrocarbures et des Mines, 5, Avenue Moulay Hassan, BP99 Rabat 10000, Morocco

Contents of this file:

Supplementary Material Table S2.1: Sections lengths and composite depth scale for Core SN°4.

Section	Segment	Segment length original (cm)	adjusted Segment length in crumbled segments (cm)	top of section (m) (driller depth)	composite depth scale (Top of segments m)
12	1	15.5	15.5	23.6	23.6
	2	78	78		23.755
	3	74	74		24.535
	4	27	27		25.275
13	1	54	54	25.8	25.8
	2	64.5	64.5		26.34
	3	67.5	67.5		26.985
	4	78	78		27.66
	5	18	18		28.44
14	1	47	47	28.6	28.62
	2	75	75		29.09
	3	69	69		29.84
	4	71	71		30.53
15	1	67	67	31.6	31.6
	2	80	80		32.27
	3	60	60		33.07
	4	76	76		33.67
16	1	59	59	34.6	34.6
	2	82	82		35.19
	3	79	79		36.01
	4	79	79		36.8
17	1	72	72	37.6	37.6
	2	71.5	71.5		38.32
	3	76	76		39.035
	4	67	67		39.795
	5	15.5	15.5		40.465
18	1	53.5	53.5	40.6	40.62
	2	72.5	72.5		41.155
	3	69	69		41.88
	4	70	70		42.57
	5	26	26		43.27
19	1	39	39	43.6	43.6
	2	76	76		43.99
	3	78	78		44.75
20	1	75	75	45.5	45.53
	2	72	72		46.28
	3	63	63		47
	4	65.5	65.5		47.63
21	1	81	81	48.3	48.3
	2	80	80		49.11
	3	76.5	76.5		49.91
22	1	73	73	50.6	50.68
	2	75.5	75.5		51.41
	3	60	60		52.165
23	1	72	72	52.8	52.8
	2	77	77		53.52
	3	71	71		54.29
	4	73	73		55
24	1	74	74	55.8	55.8
	2	73	73		56.54
	3	77	77		57.27
	4	71.5	71.5		58.04
	5	16	16		58.755
25	1	56	56	58.9	58.915
	2	75	75		59.475
	3	69	69		60.225
	4	71	71		60.915
	5	25.5	25.5		61.625
26	1	59	59	61.9	61.9
	2	82	82		62.49
	3	76	76		63.31
26/27	4/1	80	80		64.07
27	1/2	52	52	64.9	64.87
	2/3	73.5	73.5		65.39
	3/4	66.5	66.5		66.125
	4/5	31.5	31.5		66.79
28	1	77	77	67	67.105
	2	76	76		67.875
	3	74	74		68.635
	4	77	77		69.375
29	1	77	77	70.1	70.145
	2	76	76		70.915
	3	75	75		71.675
30	1	82	82	72.3	72.425
	2	77	77		73.245

Section	Segment	Segment length original (cm)	adjusted Segment length in crumbled segments (cm)	top of section (m) (driller depth)	composite depth scale (Top of segments m)
66	1	81	81	175.5	175.345
	2	76	76		176.155
	3	76	76		176.915
	4	42	42		177.675
67	1	64	64	178.3	178.095
	2	68	68		178.735
	3	74	74		179.415
	4	44	44		180.155
68	1	60	60	180.8	180.595
	2	68	68		181.195
	3	73	73		181.875
	4	73	73		182.605
	5	41.5	41.5		183.335
69	1	31	31	184	183.75
	2	77	77		184.06
	3	73	73		184.83
	4	69	69		185.56
	5	66	66		186.25
70	1	82	82	187.1	186.91
	2	71	71		187.73
	3	82	82		188.44
	4	80	80		189.26
71	1	73	73	190.2	190.06
	2	65	65		190.79
	3	78.5	78.5		191.44
	4	69.5	69.5		192.225
72	1	73	73	193	192.92
	2	76	76		193.65
	3	77	77		194.41
	4	79	79		195.18
	5	12	12		195.97
73	1	77	77	196.1	196.09
	2	83	83		196.86
	3	81	81		197.69
	4	79	79		198.5
74	1	80	80	199.2	199.29
	2	69	69		200.09
	3	76	76		200.78
	4	76	76		201.54

Section	Segment	Segment length original (cm)	adjusted Segment length in crumbled segments (cm)	top of section (m) (driller depth)	composite depth scale (Top of segments m)
75	1	74	74	202.3	202.3
	2	78	78		203.04
	3	83	83		203.82
	4	82	82		204.65
76	1	74	74	205.4	205.47
	2	79	79		206.21
	3	83	83		207
	4	84	84		207.83
77	1	76	76	208.5	208.67
	2	71	71		209.43
78	1	45	45	209.9	210.14
	2	78.5	78.5		210.59
	3	72.5	72.5		211.375
79	1	79	79	211.9	212.1
	2	80	80		212.89
	3	73	73		213.69
	4	73	73		214.42
80	1	78	58.5	215	215.15
	2	71.5	71.5		215.735
	3	83	83		216.45
	4	71	71		217.28
81	1	64	64	218.1	217.99
	2	81	81		218.63
	3	75	75		219.44
	4	63	47.5		220.19
	5	46	34.5		220.665
81	1	64	64	218.1	217.99
	2	81	81		218.63
	3	75	75		219.44
	4	63	47.5		220.19
	5	46	34.5		220.665
82	1	32	32	221.2	221.01
	2	79	79		221.33
	3	79	79		222.12
	4	74	74		222.91
	5	56	56		223.65
83	1	72	72	224.3	224.21
	2	77	58		224.93
	3	79	79		225.51
	4	80	80		226.3

Section	Segment	Segment length original (cm)	adjusted Segment length in crumbled segments (cm)	top of section (m) (driller depth)	composite depth scale (Top of segments m)
104	1	80	80	286.3	286.225
	2	78	78		287.025
	3	77	77		287.805
	4	79	79		288.575
105	1	79	79	289.4	289.365
	2	79	79		290.155
	3	78	78		290.945
	4	81	81		291.725
106	1	77	77	292.5	292.535
	2	75	75		293.305
	3	61	61		294.055
107	1	75	75	295.5	295.5
	2	22	22		296.25
108	1	54	54	296.5	296.47
	2	78	78		297.01
	3	77	77		297.79
	4	58	58		298.56
109	1	80	80	299.4	299.14
	2	69	69		299.94
	3	73	73		300.63
	4	71	71		301.36
	5	17	17		302.07
110	1	62	62	302.3	302.24
	2	79	79		302.86
	3	75	56.5		303.65
	4	79	59.5		304.215
	5	17	17		304.81
111	1	50	50	305.3	304.98
	2	80	80		305.48
	3	76	76		306.28
	4	68	68		307.04
	5	38	38		307.72
112	1	79	79	308.3	308.1
	2	74	74		308.89
	3	82	82		309.63
	4	68	68		310.45
113	1	79	79	311.3	311.13
	2	82	82		311.92
	3	81	81		312.74
	4	68	68		313.55
114	1	77.5	77.5	314.3	314.23
	2	77	77		315.005
	3	81	81		315.775
	4	66	66		316.585
115	1	83	83	317.3	317.245
	2	75	75		318.075
	3	65.5	65.5		318.825
	4	73.5	73.5		319.48
116	1	80	80	320.3	320.215
	2	74.5	74.5		321.015
	3	72	72		321.76
	4	62	62		322.48
	5	33	33		323.1
117	1	78	78	323.3	323.43
	2	77	77		324.21
	3	79	79		324.98
	4	70	70		325.77
118	1	78	78	326.3	326.47
	2	76	76		327.25
	3	69.5	69.5		328.01
	4	74	74		328.705
119	1	73	73	329.3	329.445
	2	80	80		330.175
	3	76	76		330.975
	4	70	70		331.735
120	1	77	77	332.3	332.435
	2	75	75		333.205
	3	77	77		333.955
	4	70	70		334.725
121	1	72	72	335.3	335.425
	2	73.5	73.5		336.145
	3	67.5	67.5		336.88
	4	54	54		337.555
122	1	75	56.5	338.3	338.095
	2	74	74		338.66
	3	78	78		339.4
	4	69	69		340.18
123	1	59	44.5	340.9	340.87

Section	Segment	Segment length original (cm)	adjusted Segment length in crumbled segments (cm)	top of section (m) (driller depth)	composite depth scale (Top of segments m)
124	1	72	72	341.6	341.315
	2	68	68		342.035
	3	66	66		342.715
	4	75.5	75.5		343.375
125	1	75.5	75.5	344.3	344.13
	2	69	69		344.885
	3	63	63		345.575
	4	77	58		346.205
	5	37.5	37.5		346.785
126	1	76	76	347.1	347.16
	2	78	78		347.92
	3	78	78		348.7
	4	79	79		349.48
	5	9	7		350.27
				350.2	350.34

adjusted segment lengths in crumbled sections

Supplementary Material Table S2.2: Settings for the Avaatech X-ray fluorescence core scanner (2nd generation) and detected elements

Tube voltage setting	**Scanning parameter**	**Elements**
10 kV	10 kV, 750 µA, 10 s, no filter	Al, Si, P, S, Cl, K, Ca, Ti, V, Cr, Mn, Fe, Rh
30 kV	30 kV, 1500 µA, 20 s, Pd-thick filter	Ni, Cu, Zn, Br, Rb, Sr, Zr, Pb
50 kV	50 kV, 2000 µA, 20 s, Cu-filter	Fe, Ni, Br, Rb, Sr, Zr, Rh_Area, Ag, Sn, Te, I, Ba

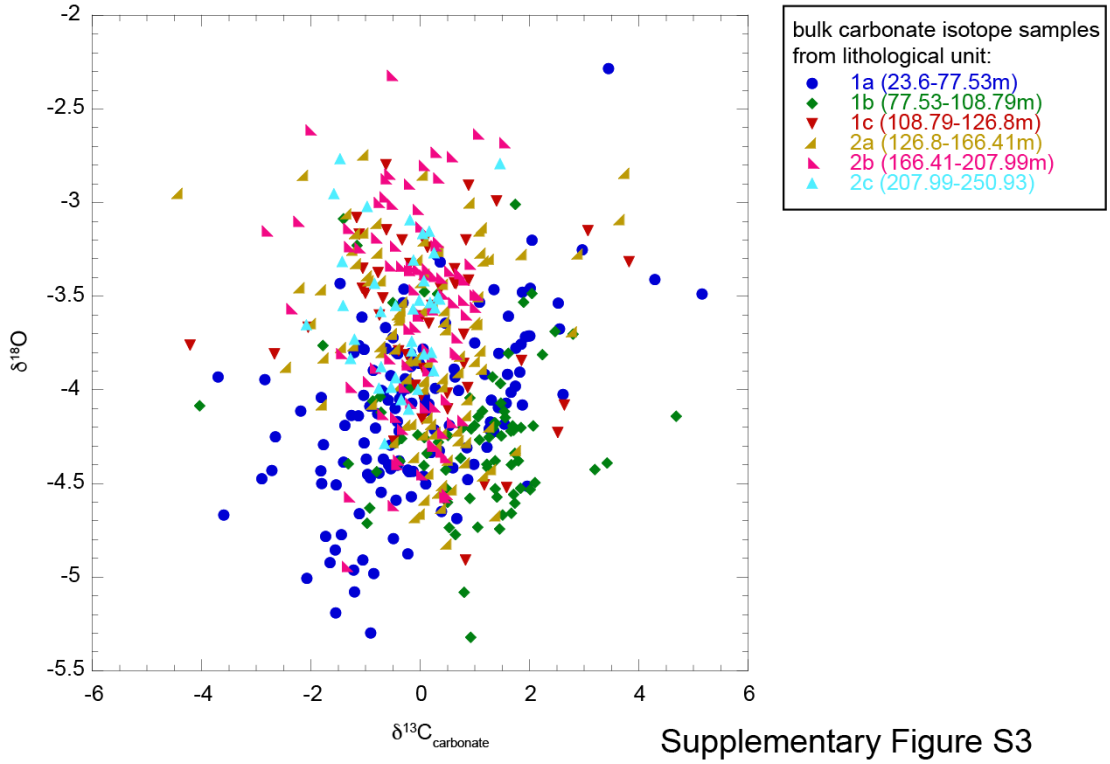

Supplementary Material Figure S2.3: Crossplot of stable isotope measurements ($\delta^{13}C$ against $\delta^{18}O$) on bulk material grouped according to the respective lithological unit

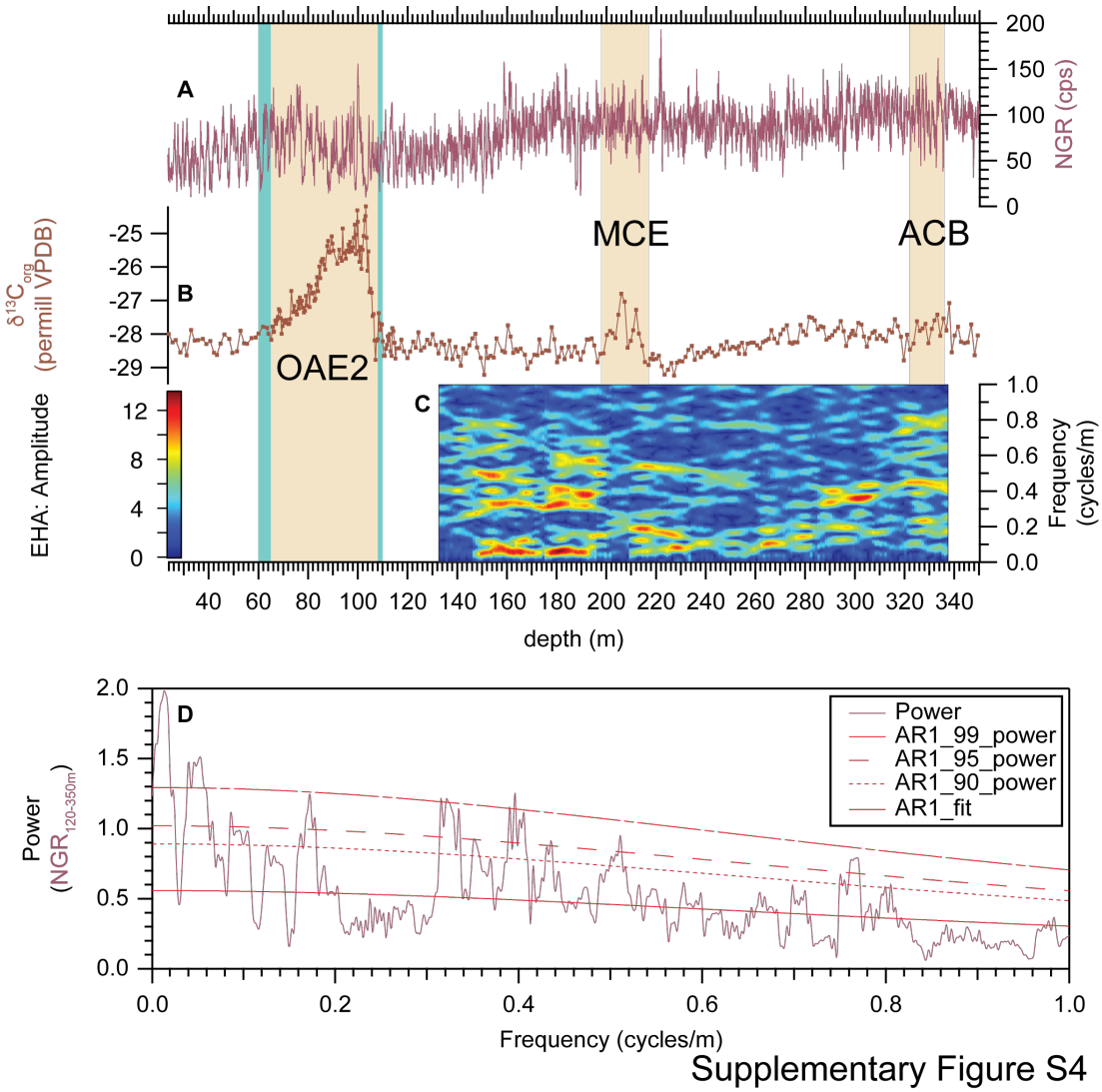

Supplementary Figure S4

Supplementary Material Figure S2.4: EHA-analysis of Natural Gamma Ray (NGR) for the depth interval 120 – 350 m excluding the high amplitude variability of OAE2. **A** NGR (cps), **B** $\delta^{13}C_{org}$ (permill VPDB), **C** EHA-Amplitude of NGR between 120 and 350 m and **D** Frequency spectrum extracted with *mtmML96*-function of *astrochron* for the depth interval 120 – 350 m, red lines in spectrum indicating AR1 red noise fit and 90, 95 and 99% confidence level.

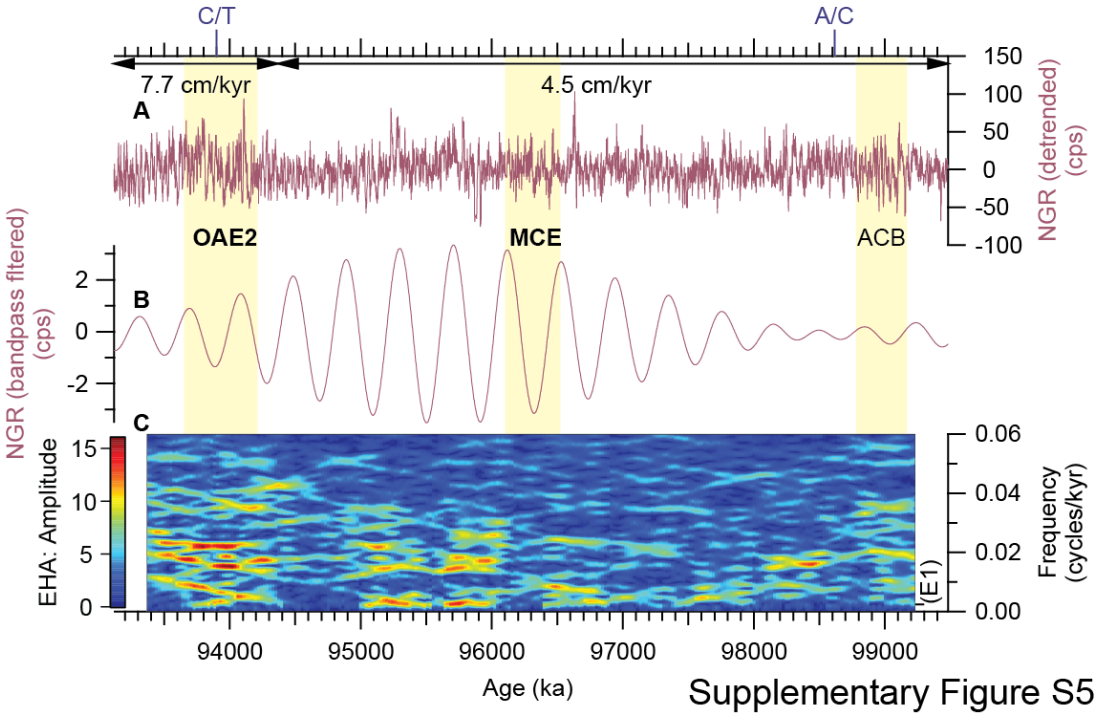

Supplementary Material Figure S2.5: EHA-analysis with astrochron (Meyers et al., 2012a) of Natural Gamma Ray (NGR). **A** Calculated sedimentation rates (presented at the top) were used to translate the NGR-data (cps) into the depth domain. The record was anchored at the Cenomanian/Turonian-boundary (C/T) with an age of 93900 ka. A/C marks the Albian/Cenomanian-boundary determined by foraminiferal biostratigraphy in Core SN°4. All marked intervals represent time-translated intervals from Core SN°4. **B** Bandpass-filtered NGR-record using a Gaussian windows centered around 0.0023 cycles/kyr to compensate for uncorrected drift in sedimentation rate. **C** EHA-Amplitude of NGR with E1 marking the frequency of the 405 kyr cycle.

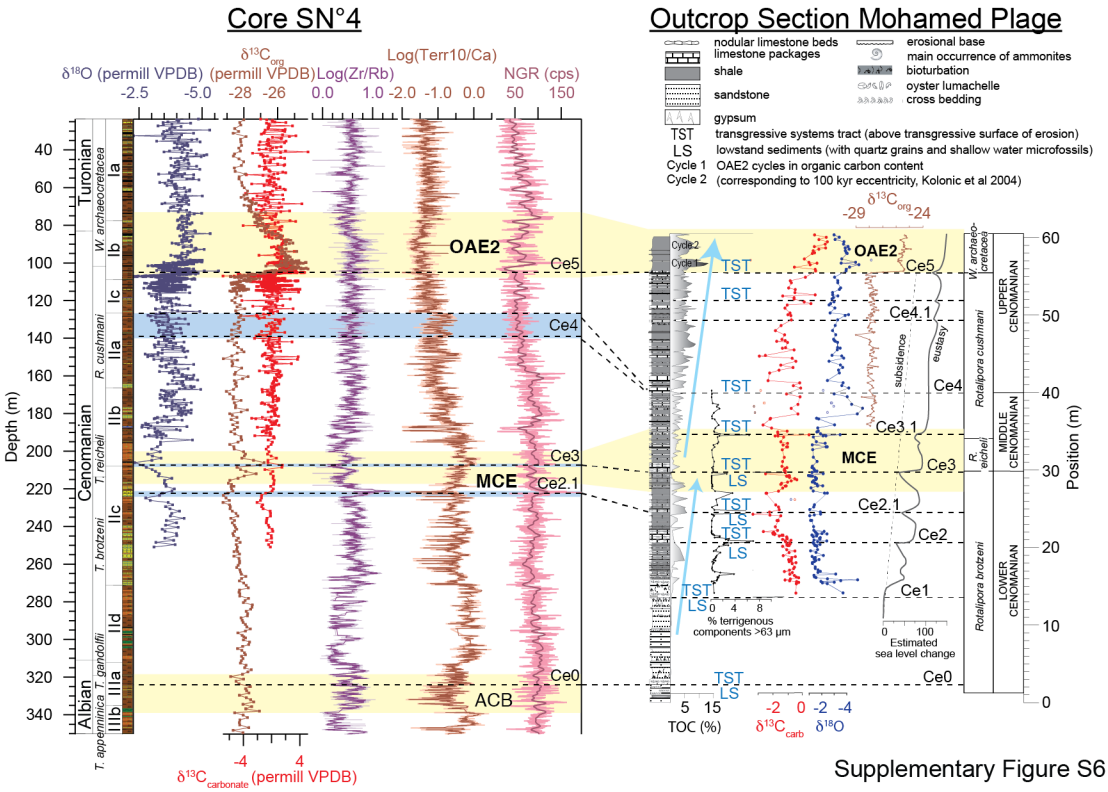

Supplementary Figure S6

Supplementary Material Figure S2.6: Correlation of hemipelagic Core SN°4 with proximal Outcrop Section Mohamed Plage (after Kuhnt et al., 2009). Carbon Isotope Events OAE2, MCE and ACB highlighted in yellow. Sequence Boundaries Ce0, Ce2.1, Ce3, Ce4 and Ce5 marked with dashed lines.

Chapter 3:

Unravelling the onset of Cretaceous Oceanic Anoxic Event 2 in an extended sediment archive from the Tarfaya-Laayoune Basin, Morocco

Wolfgang Kuhnt, Ann E. Holbourn, **Sebastian Beil**, Mohamed Aquit, Tim Krawczyk, Sascha Flögel, El Hassane Chellai, Haddou Jabour

Published in:

Paleoceanography, 32, 923–946. doi: 10.1002/2017PA003146.

Unravelling the onset of Cretaceous Oceanic Anoxic Event 2 in an extended sediment archive from the Tarfaya-Laayoune Basin, Morocco

Wolfgang Kuhnt[1], Ann E. Holbourn[1], Sebastian Beil[1], Mohamed Aquit[1,2], Tim Krawczyk[1], Sascha Flögel[3], El Hassane Chellai[4] and Haddou Jabour[5]

[1]Institute of Geosciences, Christian-Albrechts-University, Ludewig-Meyn-Str.10-14, D-24118 Kiel, Germany

[2]OCP S.A., Direction de Recherche et Développement, Recherche Géologique, 46300 Youssoufia, Morocco

[3]GEOMAR Helmholtz-Zentrum für Ozeanforschung Kiel, Ozeanzirkulation und Klimadynamik, Paläo-Ozeanographie, Wischhofstr. 1-3, D-24148 Kiel, Germany

[4]Department of Geology, Faculty of Sciences Semlalia, Cadi Ayyad University, Marrakech, Morocco

[5]ONHYM, Office National des Hydrocarbures et des Mines, 5, Avenue Moulay Hassan, BP99 Rabat 10000, Morocco

Keywords: paleoclimate, Cretaceous; Oceanic Anoxic Event

Highlights:

- The onset of OAE2, which corresponds to a two-stepped increase in $\delta^{13}C$spanning ~100 kyr, is preceded by negative carbon isotope excursions
- A three-stepped transient climate cooling with intermittent brief anoxicepisodes occurred in the latest stage of the main $\delta^{13}C$ increase

- Two major extinction events of thermocline dwelling planktonic foraminifers were closely linked to intensifications of the OMZ

Abstract

We investigated the onset and development of Cretaceous Oceanic Anoxic Event 2 (OAE2) in a newly drilled core (SN°4) from the Tarfaya Basin (southern Morocco), where this interval is unusually expanded. High-resolution (cm-scale equivalent to centennial) analysis of bulk organic and carbonate stable isotopes and of carbonate and organic carbon content in combination with XRF scanner derived elemental distribution reveal that the ocean-climate system behaved in a highly dynamic manner prior to and during the onset of OAE2. Correlation with the latest orbital solution indicates that the main carbon isotope shift occurred during an extended minimum in orbital eccentricity (~400 kyr cycle). Shorter term fluctuations in carbonate and organic carbon accumulation and in sea level related terrigenous discharge were predominantly driven by variations in orbital obliquity. Negative excursions in organic and carbonate $\delta^{13}C$ preceded the global positive $\delta^{13}C$ shift marking the onset of OAE2, suggesting injection of isotopically depleted carbon into the atmosphere. The main $\delta^{13}C$ increase during the early phase of OAE2 in the late Cenomanian was punctuated by a transient plateau. Maximum organic carbon accumulation occurred during the later part of the main $\delta^{13}C$ increase and was associated with climate cooling events, expressed as three consecutive maxima in bulk carbonate $\delta^{18}O$. The extinctions of the thermocline dwelling keeled planktonic foraminifers *Rotalipora greenhornensis* and *Rotalipora cushmani* occurred during the first and last of these cooling

events and were likely associated with obliquity paced, ocean-wide expansions and intensifications of the oxygen minimum zone, affecting their habitat space on a global scale.

3.1. Introduction

Global $\delta^{13}C$ increases in the marine and terrestrial carbon reservoirs, related to enhanced marine productivity and carbon burial (e.g. Arthur et al., 1988), are associated with the two most intense Cretaceous Oceanic Anoxic Events (OAEs): the Selli Event or OAE1a in the early Aptian (~122 Ma) and the Bonarelli Event or OAE2, in the late Cenomanian (~94 Ma). Numerous stable isotope records across OAE2 in Atlantic and Tethyan pelagic successions, characterized by low to intermediate sedimentation rates, depict the onset of the event as continuous positive 2.5‰ (marine carbonate carbon) to 4.5‰ $\delta^{13}C$ (marine organic carbon) shifts, followed by a characteristic double peak of high $\delta^{13}C$ values and a plateau of several 100 kyr duration before $\delta^{13}C$ values return to background levels (e.g. Tsikos et al., 2004). The environmental boundary conditions and triggering mechanisms leading to the onset of OAEs remain, however, challenging issues.

A massive injection of isotopically depleted carbon, triggering a major disturbance in the terrestrial and marine carbon cycle and ultimately leading to widespread anoxia and/or acidification in the ocean, is a plausible scenario for Cretaceous OAEs, Paleogene and Neogene global ocean warming events (Larson and Erba, 1999; Storey et al., 2007; Holbourn et al., 2015). Distinctive negative carbon isotope excursions that have been related to degassing of ^{13}C depleted volcanogenic CO_2 often precede the main positive carbon isotope shifts in the earliest part of these warming events. Recently, osmium isotope records indicated a synchronous decrease in $^{187}Os/^{186}Os$ at the onset of OAE2, suggesting that volcanic degassing from the Caribbean Large Igneous Province were the source of the unradiogenic osmium (Turgeon and Ceaser, 2008; Du Vivier et al.,

2014). However, negative excursions preceding OAE2 have so far not been reported from most of the OAE2 records (i.e. Tsikos et al., 2004; Erbacher et al., 2005), except in records from shallow shelf sections in Wunstorf, northern Germany (Voigt et al., 2008) and Oued Mellegue, Tunisia, (Nederbragt and Fiorentino, 1999), where sharp negative spikes were recorded at the base of the OAE2 carbon isotope excursion. In southern Mexico (Elrick et al., 2009), a combined stratigraphic and $\delta^{13}C$ study of expanded platform carbonates revealed that the main positive shift was preceded by two extended negative excursions, showing similarities to the negative excursions at the onset of OAE1a in expanded sections of shelf carbonates within the Provence platform (Lorenzen et al., 2013). However, evidence for negative carbon isotope excursions preceding the characteristic global $\delta^{13}C$ increases associated with the main Cretaceous OAEs remains ambiguous, partly due to incomplete or condensed marine sedimentary records in the earliest stage of OAEs. One possibility is that the absence or spiky character of negative carbon isotope excursions at the onset of OAE2 in deep water sections may be caused by the presence of hiatuses or by condensed sedimentation, related to a sea level maximum within this interval. Furthermore, the conventional sampling resolutions for "high-resolution" stable isotope records, ranging between 10 cm and 1 m, may be insufficient to resolve negative excursions in laminated sediments, characterized by extremely low sedimentation rates.

Organic and carbonate carbon isotope values across OAE2 exhibit two main characteristics: (1) marine organic $\delta^{13}C_{org}$ was significantly lighter (-24 to -28‰ vs. VPDB) than in equivalent Miocene to modern organic carbon rich strata (-16 to -23‰) (Dean et al., 1986); (2) in contrast, bulk marine $\delta^{13}C_{carbonate}$, which,

today, is approximately in equilibrium with near-surface dissolved inorganic carbon (DIC) of -1 to 1‰, was considerably heavier during the Cenomanian-Turonian (in the range of 2 to 4.5‰). A long-held view is that higher pCO_2 levels may explain lighter marine $\delta^{13}C_{org}$ values in Earth's climate history (Hayes et al., 1999; Dean et al., 1986) and that changes in marine $\delta^{13}C_{org}$, when normalized against the $\delta^{13}C$ of contemporary DIC or bulk carbonate $\delta^{13}C_{carbonate}$, may be an indicator of changes in pCO_2 levels (Kump and Arthur, 1999; Jarvis et al., 2011). In particular, the main positive $\delta^{13}C$ shift at the onset of OAE2 (~4‰ in $\delta^{13}C_{org}$ vs. only 2.5‰ in $\delta^{13}C_{carbonate}$) would correspond to a major pCO_2 reduction and reflect a significant drawdown of atmospheric CO_2 (Barclay et al., 2010). The relationship between $\Delta\delta^{13}C_{carbonate\text{-}organic}$ and atmospheric pCO_2 levels has been recently used to explain a distinct cooling event, which immediately follows the initial $\delta^{13}C$ shift at the onset of OAE2, the so-called "Plenus Cold Event" (Gale and Christensen, 1996; Jarvis et al., 2011; Jenkyns et al., 2017).

Bulk and organic $\delta^{13}C$ curves spanning OAE2 were previously generated in expanded sedimentary successions from outcrop sections and exploration wells S13, S57 and S75 in the Tarfaya Atlantic Margin Basin, Southern Morocco (Kuhnt et al., 1990; 1997; Tsikos et al., 2004; Kuhnt et al., 2005; Aquit et al., 2013). Previous studies of orbital cyclicity and biostratigraphy in cored exploration wells revealed that the obliquity signal of the Milankovitch frequency band is most prominent in the record of organic matter and carbonate accumulation across the Cenomanian-Turonian boundary (Kuhnt et al., 1997; Meyers et al., 2012a). These studies, in combination with stable isotope and organic matter accumulation records (Kuhnt et al., 1990, 2005; Tsikos et al.,

2004, Kolonic et al., 2002, 2005; Schönfeld et al., 2015) also showed that the Tarfaya Basin has potential for high-resolution supra-regional stratigraphic correlation of carbon and oxygen isotope records. Moreover, fluctuations of intermediate water oxygenation during the OAE2 were intially correlated to a Milankovitch framework and the duration of these events assessed on millennial time scales (Kuhnt et al., 1997, 2005; Meyers et al., 2012a). However, these earlier studies of orbital cyclicity during OAE2 in the Tarfaya Basin mainly used relatively low-resolution wireline-logging data and/or focused on the main $\delta^{13}C$ increase, plateau and recovery rather than on the onset of OAE2. Since these older commercial wells were targeted for black shale exploration, the recovered cores were not suitable for continuous high-resolution sediment logging and the cored material did not fully recover the onset of OAE2 below the organic carbon-rich zone.

To address these shortcomings, a new complete sediment record of OAE2 was recently drilled in the most distal and expanded part of the Tarfaya Basin in southern Morocco (Core SN°4). A detailed description and stratigraphic analysis of the upper Albian to Turonian sedimentary succession in Core SN°4 are provided in a separate study. Here, we focus on the late Cenomanian interval (98 to 115 m), which allows unprecedented insights into sedimentation patterns, environmental and geochemical changes prior to and during the early onset of OAE2. Specifically, we present high-resolution isotopic and elemental data that contribute to a better understanding of the temporal relationship and feedback mechanisms between CO_2 exhalation, climate evolution and the response of the carbon and nutrient cycle during the onset and development of OAE2.

3.1.1 Tarfaya-Basin

The Tarfaya Basin extends along the west coast of Africa at latitudes 29 to 22°N and is bounded by the Anti-Atlas mountain chain in the northeast, the Reguibat shield in the east, the Mauritanide chain in the south and the Atlantic Ocean in the west (Fig. 3.1). The post-Triassic extensional structures and subsidence of the basin are related to the opening of the Atlantic Ocean (Ranke et al., 1982; Wiedmann et al., 1978, 1982; El Khatib et al., 1995, 1996). Distinctive sedimentary successions are Lower Cretaceous clastic deposits of deltaic or fluvial origin (TanTan Formation) and Upper Cretaceous organic-rich pelagic limestones and marls (Lebtaina Formation, Ratschiller, 1970). Previous paleo-water depth estimates for the mid-Cretaceous Tarfaya basin range between 100 and 300 m (Kuhnt et al. 1986, 2009). These expanded sedimentary successions were deposited at the northwestern margin of the stable Sahara platform and are unconformably overlain by relatively thin sequences of Cenozoic marginal marine sediments (Choubert et al., 1966).

Approximately 700 m of Upper Cretaceous laminated biogenic sediments, mainly consisting of calcareous nannoplankton, dispersed biogenic silica, planktonic foraminifers and marine organic matter were deposited in the Tarfaya Basin, with sedimentation rates exceeding 10 cm/kyr in the depocenter of the basin near the town of Tarfaya (Leine et al., 1986; Kuhnt et al., 1997, 2001, 2005). These sediments exhibit some of the world's highest accumulation rates of marine organic matter for the Cenomanian and Turonian stages, allowing investigation of paleoceanographic and climate events on a centennial to millennial time scale resolution, comparable to the resolution of Pleistocene paleoclimatic archives.

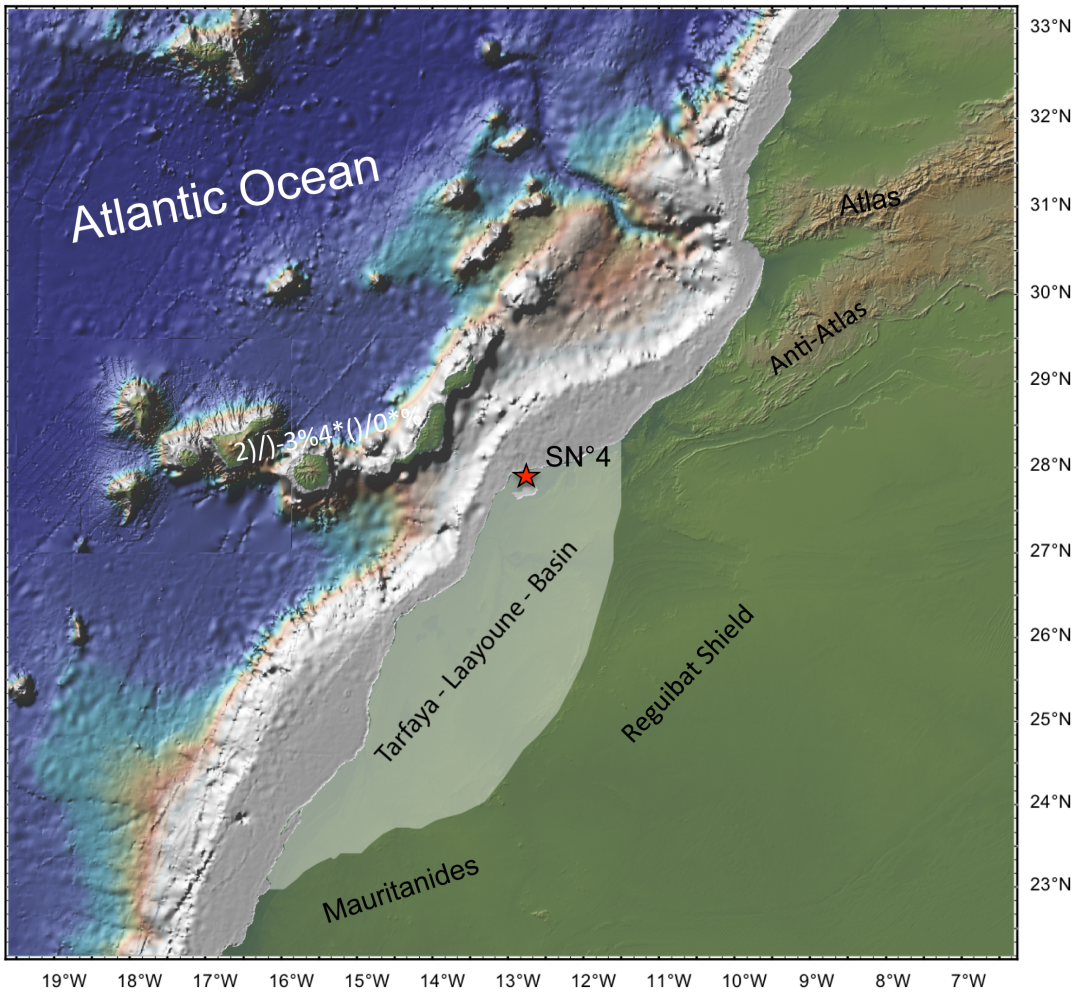

Figure 3.1: Location of Core SN°4 in Tarfaya Basin. Map was generated with GeoMapApp (http://www.geomapapp.org), using topography and bathymetry from Global Multi-Resolution Topography synthesis (Ryan et al., 2009).

The estimated areal extent of the Tarfaya Basin ranges from 53 753 km^2 (Elbatal et al., 2010) to 124 821 km^2 (http://www.onhym.com/en/minerals-laboratory/39-en/petroleum/ 205-tarfaya-lagwira-basin.html) and to as much as 170 000 km^2 (Leine 1986), depending on the definition of its southern margin and consideration of its offshore extent. This huge area and the extremely high accumulation rates of organic carbon during OAE2 indicate that the Tarfaya Basin was an extensive carbon sink at that time, even on a global scale. Kolonic et

al. (2005) calculated an annual burial of ~6 x10^{10} mols C per year for the Tarfaya Basin during OAE2, which corresponds to ~2% of the overall global excess organic carbon burial in an area equivalent to only ~0.05% of the Cenomanian ocean floor. Major changes in organic carbon accumulation in the Tarfaya Basin and its even larger extension to the South, the Senegal-Casamance offshore basin, thus, likely had direct repercussions on the global carbon cycle and $\delta^{13}C$ budget.

3.2. Material and Methods

3.2.1 Tarfaya Core SN°4: High-resolution record of OAE 2 onset

Drill core Tarfaya SN°4 was recovered with the assistance of ONHYM (National Office of Hydrocarbons and Mines of Morocco) in December 2009 close to the main road from TanTan to Tarfaya, ~40 km east of the town of Tarfaya (27° 59′ 46.4′′N, 12° 32′ 40.6′′W). A total of 350 m of sediment were recovered with a Salzgitter WD3500 hydraulic drilling system. Metal core barrels of 3.05 m length with a diameter of 8.8 cm were used in the upper part of the hole (from 0 to 120 m) and with a diameter of 6.8 cm in the lower part. Drilled sections of ~3.05 m were divided into segments (~80 cm), which were inserted into plastic sleeves and sealed to avoid desiccation, then stored in wooden boxes for transport. The coring scheme of sections and segments for the studied interval (98-115 m) is provided in Supplementary Figure 3.1 and core photographs of each segment are provided in Supplementary Figures 3.2A-F. Segments were subsequently split into archive and working halves with a Kaufmann-Titan diamond rock saw. Coring at this site achieved 100% recovery without coring gaps. Detailed lithological description, core logging data and intermediate-

resolution (~40 cm) organic carbon and stable isotope records over the entire Cretaceous succession are provided in a separate study. The positive carbon isotope excursion associated with OAE2 extends between ~60 and 107 m in SN°4. High-resolution XRF scanning (1 cm spacing) and analysis of carbonate, organic carbon and stable isotopes (2 cm spacing) between 98 and 115 m provide unprecedented resolution over the onset and early development of OAE2 in the Tarfaya Basin.

3.2.2 Wire-line logging

Wire-line logging of Core SN°4 was performed by Geoatlas Laayoune using a Century geophysical well logging system with a natural gamma ray (NGR) sensor. Walls of the hole were not covered with a metal casing and logging depth is recorded relative to the surface with a precision of ±0.1 m. NGR-measurements (10 cm spacing) are reported in counts per second (cps) as API (American Petroleum Institute) radioactivity units.

3.2.3 X-ray fluorescence (XRF) core scanning

Elemental composition of the sediment was analyzed on the working half core surfaces, using a second generation Avaatech X-ray fluorescence core scanner at the Institute of Geosciences, Christian-Albrechts-University in Kiel. The core surface was polished with fine-grained sand paper, cleaned with distilled water and covered with a 4 µm thick Ultralene plastic film to avoid contamination and to protect the detector. Measurements were taken continuously at 1 cm intervals with a downcore slit size of 10 mm over 1 cm^2. Tube voltage settings of 10, 30 and 50 kV were used with sampling times of 10 s.

Raw data spectra were transferred into area counts per seconds (Acps) using the iterative least square software (WIN AXIL) from Canberra Eurisys. Results are reported in logarithms of elemental ratios, which are mostly normally distributed and provide the most easily interpretable signals of relative changes in chemical composition downcore and minimize the risk of measurement artefacts from variable signal intensities and matrix effects (Weltje and Tjallingii, 2008; Rothwell and Croudace, 2015). Variations in the abundance of the major elements K, Fe, Ti, Si and Al are used to reconstruct changes in the terrigenous component (Peterson et al., 2000; Haug et al., 2001; Mulitza et al., 2008; Tisserand et al., 2009; Govin et al., 2012). We normalized these records against Ca, mainly derived from the biogenic carbonate of marine organisms, and expressed the ratio of terrestrial derived elements vs. marine carbonate as Log((Al+Ti+Fe+K+Si)/Ca) or Log (Terr/Ca). Additionally, we used Log(Zr/Rb) as an indicator of grain density and size in the terrigenous component due to changes in the proximity of the sediment source and or bottom current intensity which both are commonly associated with sea level changes. The element Zr is almost exclusively found in the heavy mineral zirconium in sediments, while Rb is mainly replacing K in clay minerals. High Log(Zr/Rb) ratios coincide with large grain sizes due to the high density of zircons, which can only be transported over larger distances by stronger currents together with comparatively large grains of other minerals such as quartz and carbonates.

3.2.4 Line scan and RGB measurements

Line scan measurements (resolution of 143 pixel per 1 cm or 70 µm per pixel) and photographs were acquired on the polished surface of oriented cores

with a Jai CV-L107 3 CCD color line scan camera with 3 sensors of 2048 pixels and dichroic RGB beam splitter prism (RGB channels at 630 nm, 535 nm and 450 nm). Color measurement in L*a*b* units are derived from RGB digital images.

3.2.5 Stable isotope analysis of bulk carbonate

A total of 640 samples (2 and 5 cm spacing) were analyzed for stable isotopes of bulk carbonate. Measurements were made with Finnigan MAT 251 and MAT 253 mass spectrometers at the Leibniz Laboratory for Radiometric Dating and Stable Isotope Research at the Christian-Albrechts University in Kiel. The instruments are coupled online to a Carbo-Kiel device for automated CO_2 preparation of carbonate samples. Samples were reacted by individual acid addition. The systems have an accuracy (on the delta scale) of ±0.05‰ for carbon and ±0.08‰ for oxygen isotopes. Results were calibrated using the National Institute Bureau of Standards and Technology (Gaithersburg, Maryland) carbonate isotope standard NBS 20, internal standards and NBS 19 and are reported as $\delta^{18}O_{carbonate}$ and $\delta^{13}C_{carbonate}$ on the Vienna PeeDee belemnite (V-PDB) scale.

3.2.6 Stable carbon isotope analysis of organic matter

Carbon isotope analyses of organic carbon were performed for 340 samples (5 cm resolution) at the GeoZentrum Nordbayern with a Flash EA 2000 elemental analyser connected online to ThermoFinnigan Delta V Plus mass spectrometer. Approximately 2 g of sediment were ground in an agate mortar and decarbonatized with 10% HCL until visible reaction stopped. Subsequently, 25% HCL was added for the dissolution of dolomitic material and the sample

agitated overnight. After at least 12 hours of exposure, samples were five times rinsed with deionized water, decanted, and dried at 40°C. All carbon isotope values are reported in the conventional δ-notation in permil relative to V-PDB (Vienna-PDB). Accuracy and reproducibility of the analyses were checked by replicate analyses of laboratory standards calibrated to international standards USGS 40 and 41. Reproducibility was ±0.04‰ (1σ).

3.2.7 Micropaleontology

Micropaleontological samples from bituminous marls with high organic matter content were crushed and processed using an alcoholic solution of anionic tensides (REWOQUAT by REWO-Chemie, Steinau, Germany), which helped to break down indurated samples. Around 50 g of dry sediment from each sample was washed over a 63 µm sieve, dried below 40°C, and then sieved into 63-150, 150-250 and 250-630 µm fractions. Planktonic foraminifers from the 250-630 µm fraction were picked and the main biostratigraphic datums within this interval (extinction of *Rotalipora greenhornensis* and extinction of *Rotalipora cushmani*) were identified at a sample resolution of ~10 cm.

3.2.8 Determination of total organic carbon (TOC) and carbonate

For the measurement of total organic carbon and carbonate, we used a Carlo Erba elemental analyzer, which analyzes total carbon, nitrogen and sulphur in solid samples. The analytical method is based on the complete and instantaneous oxidation of the sample by „flash combustion“, which converts all organic and inorganic substances into combustion products. The resulting combustion gases pass through a reduction furnace and are swept into the

chromatographic column by a carrier gas (helium). The gases are separated in the column and detected by a thermal conductivity detector (TCD), which gives an output signal proportional to the concentration of the individual components of the mixture. Freeze dried samples were ground in an agate mortar and depending on the carbon concentration, 3 to 20 mg of sediment were weighed into a tin cup for TOC measurement. Organic carbon was determined after removing carbonate carbon by acidification with 0.25N hydrochloric acid. For each set of samples (n=50) standards and blanks were measured. Each sample was run as a duplicate and for long-term precision calculation an internal standard was measured in each set.

3.3. Results

3.3.1 Lithology

Most of the upper Cenomanian to lower Turonian organic-rich marlstones in Core SN°4 are laminated, indicating that environmental conditions in the Tarfaya Basin fulfilled the following essential requirements for lamination (Kemp, 1996): (1) short-term variability in sediment supply and physical or chemical conditions resulting in compositional changes and (2) unusual environmental conditions to preserve the laminated sediment fabric from bioturbational mixing. In the Tarfaya Basin, strongly dysoxic to anoxic conditions prevailed at the seafloor and apparent bioturbational mixing is restricted to distinct horizons in the late Cenomanian (Fig. 3.2A-C). However, the nature of the variability that produced compositional changes in the laminated sediments remains somewhat enigmatic. Visible lamination mainly corresponds to thin

light, carbonate-rich layers, largely composed of planktonic foraminiferal tests, and dark organic-rich layers, consisting of kerogen, fine grained carbonate (coccoliths) with clay minerals as a minor component. The fabric of individual laminae is commonly irregular, lense-shaped and erosional contacts and even rip-up clasts are common. These features indicate active sediment redistribution by bottom currents and/or internal waves or climatic (storm) events (Kuroda et al., 2005), resembling sea floor conditions in some modern upwelling zones (e.g., Peruvian upwelling, Schönfeld et al., 2015, Erdem et al., 2016).

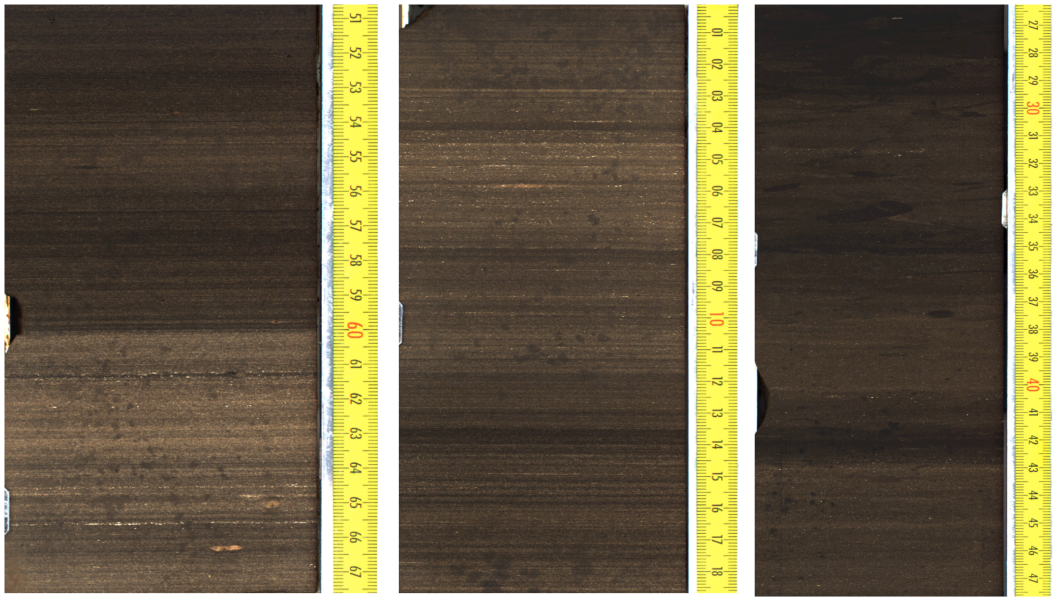

Section 39, Segment 3 Section 39, Segment 4 Section 40, Segment 2

Figure 3.2A: Typical sediment types prior to onset of OAE2 in Core SN°4. Irregular erosive contacts indicating current activity at ocean-floor (Section 42, Segment 1, 0-20 cm). Ripple lamination (Section 44, Segment 3, 20-22 cm) and irregular flaser laminated intervals (Section 44, Segment 3, 38-43 cm) indicate active bottom currents.

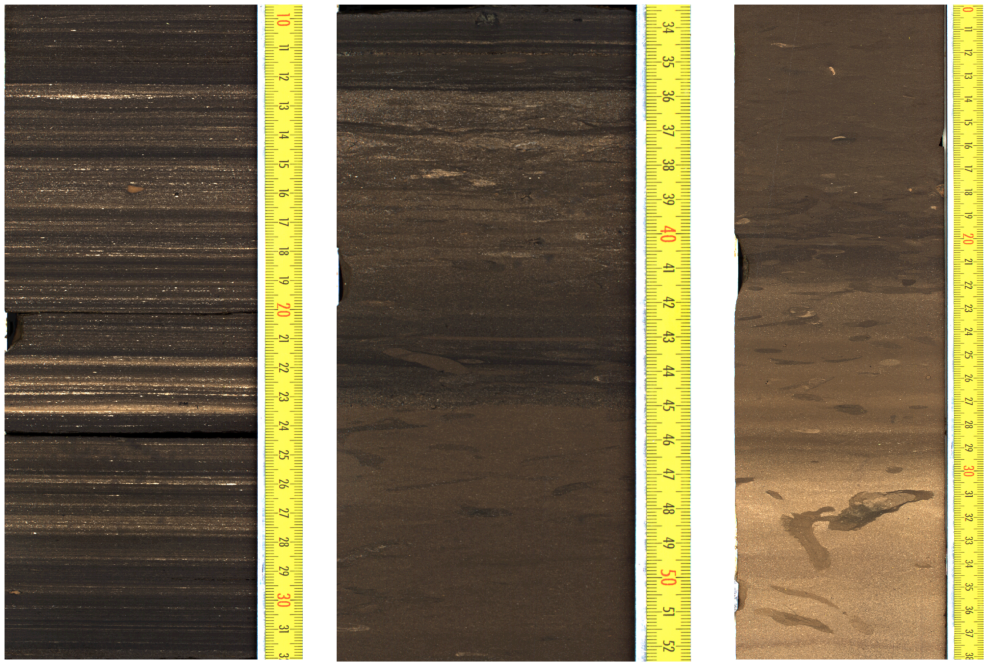

Section 41, Segment 1 Section 41, Segment 1 Section 41, Segment 2

Figure 3.2B: Typical sediment during onset of OAE2 in Core SN°4. Dark and light laminated marlstones with irregular thicknesses of laminae (Section 41, Segment 1, 10-32 cm). Flaser-laminated strongly bioturbated sediments (Section 41, Segment 1, 34-52 cm). Note that dark interval at 43-44 cm is characterized by unusually high P content (81.3 ppm) and low C/P ratio (1.8), indicating unusual enrichment of nutrients. Last occurrence of *R. greenhornensis* occurs at 41-43 cm, whereas sample at 31-32 cm only contains *R. cushmani* and sample residue mainly consists of phosphatic fish debris. Transition of homogenous limestone to bioturbated dark gray marlstone, corresponding to transgressive surface (TS) at ~105 m (Section 41, Segment 2, 30 cm).

The interval corresponding to the onset of OAE2 in Core SN°4 is characterized by high lithological variability, ranging from dark brown laminated carbonate-rich marlstones, to homogenous or bioturbated light brown limestones (Fig. 3.2A-C). The size and shape of bioturbation traces point to near sediment surface grazing by a burrowing macrofauna such as gastropods,

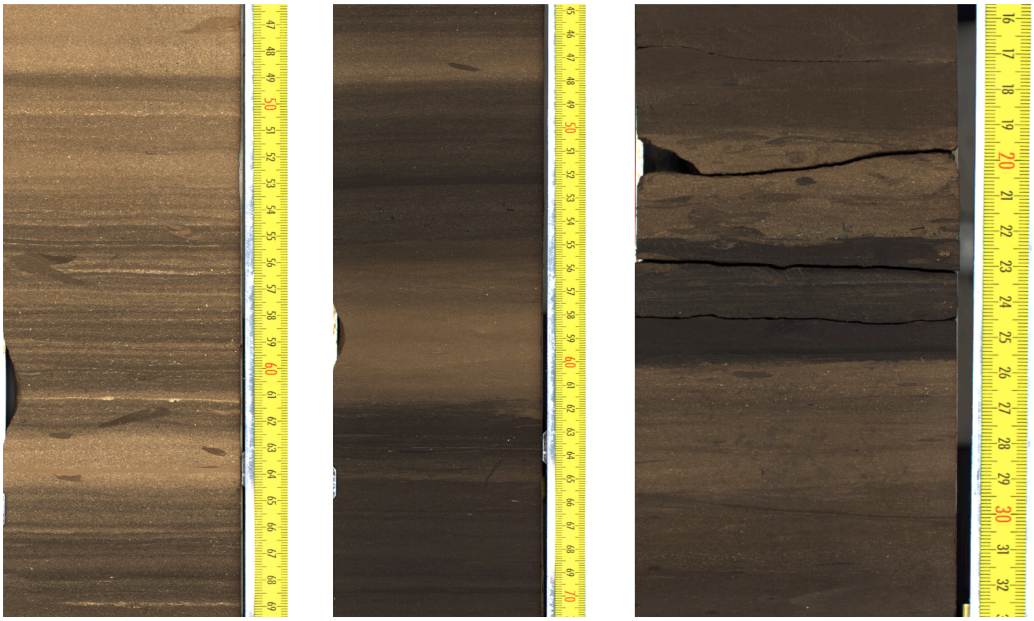

Section 41, Segment 2 Section 41, Segment 3 Section 41, Segment 4

Figure 3.2C: Typical sediment during early development of OAE2 in Core SN°4. Dark and light laminated marlstones with irregular thicknesses of laminae. (Section 39, Segments 3 and 4). Flaser-laminated strongly bioturbated sediments (Section 40, Segment 2).

starfish and crabs, for which oxygen is a strongly limiting factor to deeply penetrate the oxygen minimum zone in modern upwelling systems (Mosch et al., 2012). Upper Cenomanian sediments below the onset of OAE2 (115-107 m) commonly exhibit sedimentary features indicating submarine current activity, including ripple laminations, flaser lamination, and irregular erosive contacts (Fig. 3.2A). The initial onset of OAE2 (107-105 m) is composed of laminated dark organic-rich marls, which grade into a distinct homogenous limestone layer, marking the middle of the initial positive OAE2 carbon isotope shift at ~105 m core depth. This limestone bed is clearly bioturbated at the top, indicating condensed sedimentation and the bed is overlain by brownish marlstones with

intense bioturbation (Fig. 3.2B). This bioturbated interval is finally capped by laminated marlstones (103.97–104.33 m) with distinct mm-scale dark organic-rich and light carbonate-rich layers (Fig. 3.2B). However, the thickness of laminae is very irregular and they are often laterally discontinuous, suggesting that they may result from winnowing by submarine currents rather than represent varved sediments of seasonally or interannually changing biogenic or terrigenous fluxes. The upper part of the studied succession (97.8 to 103.97 m) consists mainly of dark, laminated marlstones with only few intervals of lighter, more calcareous intercalations, which still have preserved lamination (Fig. 3.2C).

3.3.2 Chronology

The chronology is based on the cyclostratigraphic framework of Meyers et al. (2012a), which was developed using evolutive harmonic analysis of the bed-resolution density log of well Tarfaya S13 (Leine et al., 1986; Kuhnt et al., 1997) with the following astronomical target periodicities from Laskar et al. (2011): 405 kyr, 127 kyr and 97 kyr for eccentricity, 49 kyr and 38 kyr for obliquity and 22 kyr and 18 kyr for precession (Meyers et al., 2012a, Ma et al., 2014). In the interval between cycles -2 and cycle 3, all target periodicities are represented in the Tarfaya sediment record with a probability of 90% or more (Meyers et al., 2012a). We derived the age model for Core SN°4 by tuning the gamma ray log to the bed-resolution density record of well S13 (Meyers et al., 2012a) using 21 tiepoints (Fig. 3.3). We adjusted the Cenomanian/Turonian boundary (top of cycle 3) with the first occurrence of the calcareous nannoplankton species *Quadrum gartneri* (Tsikos et al., 2004) to the new Ar/Ar-age of the C/T boundary

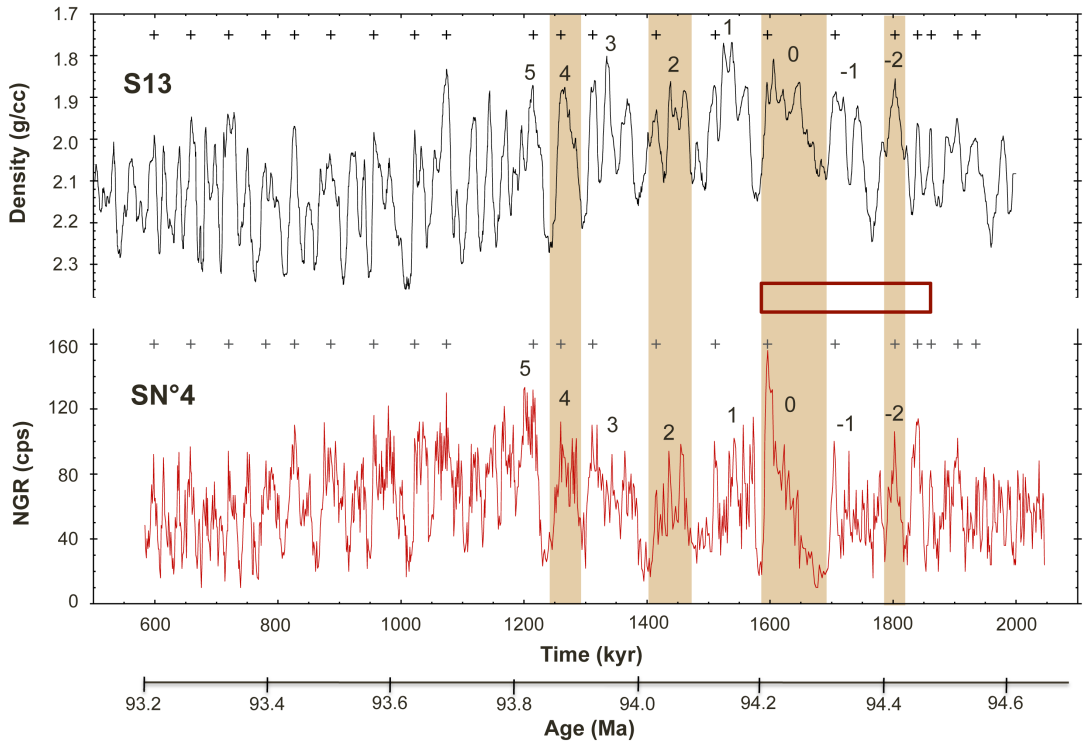

Figure 3.3: Correlation of Core SN°4 natural gamma ray log (NGR) to density log of Shell/ONAREP well S13 (Kuhnt et al., 1997) using age model of Meyers et al. (2012a, b). Age correlation tie points are marked by crosses. Numbers of cycles -2 to 5 refer to the numbering scheme of Kuhnt et al. (1997). Red box indicates onset and development of OAE2.

in the Western Interior Basin of 93.90 Ma (Meyers et al., 2012b) (Fig. 3.4). Sedimentation rates generally range between 4 and 9 cm/kyr with a mean of 7 cm/kyr from 93.2 to 94.6 Ma. Sedimentation rates decrease to 4-7 cm/kyr during the onset of OAE2 (94.4 to 93.9 Ma) and increase to 7-9 cm/kyr at the Cenomanian/Turonian boundary (93.9 Ma). In a recent study of the cyclostratigraphy of Cretaceous OAEs, based on the sedimentary record of the Umbrian Apennines, the onset of OAE2 was tuned to a 405 kyr eccentricity maximum (Batenburg et al., 2016). This interval of increased variability in seasonality follows a prolonged period of low seasonal extremes associated with a 2.4 Myr eccentricity minimum. Following this approach, Batenburg et al.

(2016) came to the conclusion that the eccentricity maximum at 94.17±0.15 Ma is the likely candidate for an orbital trigger of OAE2, although they could not exclude the preceding eccentricity maximum at ~94.57 Ma as a possible timing for the onset of OAE2, which would be in agreement with our tuning approach.

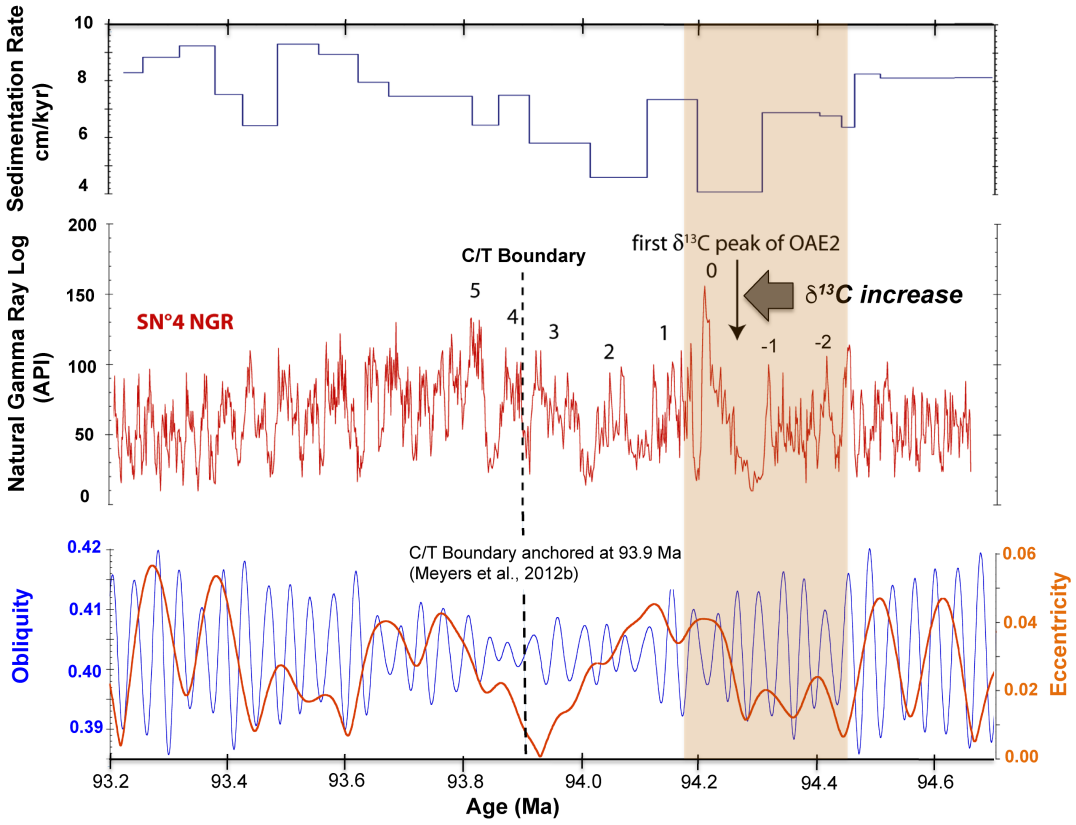

Figure 3.4: Sedimentation rates and NGR cycles in Core SN°4 following orbitally tuned age model of Meyers et al. (2012a) and orbital solution of Laskar et al. (2004). Numbers of cycles -2 to 5 refer to the numbering scheme of Kuhnt et al. (1997).

3.3.3 High-resolution carbonate and organic carbon isotope records of OAE2

3.3.3.1 High variability in $\delta^{13}C_{carbonate}$

The late Cenomanian $\delta^{13}C_{carbonate}$ record in Core SN°4 is characterized by five sharp positive excursions, centered at 114, 112, 109.5, 108.3 and 105 m. Except for the excursion at 109.5 m, these excursions coincide with intervals of light, homogenous or bioturbated sediments with high carbonate content and low TOC (Fig. 3.5), indicating relatively well-oxygenated bottom water conditions and reduced primary productivity. The $\delta^{13}C_{carbonate}$ peaks at 114, 108.3 and 109.5 m are also represented in the $\delta^{13}C_{org}$ record, indicating short-lived positive excursions preceding the main $\delta^{13}C$ increase of OAE2. In particular the $\delta^{13}C_{carbonate}$ peak centered at 109.5 m, which coincides with the first $\delta^{13}C_{org}$ increase, is not related to a major change towards carbonate-rich lithology and, thus, appears unaffected by changes in carbonate components or early diagenetic cementation. The re-occurrence of these $\delta^{13}C_{carbonate}$ peaks and their spacing at ~2 m intervals with sedimentation rates between 7 and 4 cm/kyr suggest that the pacing of these events is controlled by orbital obliquity. The last and most intense of these events (at 105 m) occurs in the middle of the main $\delta^{13}C_{carbonate}$ shift from long-term averages of -0.5 to + 2‰ between 107 and 104 m, which coincides with the $\delta^{13}C_{org}$ shift from -28.5 to -24.5‰.

3.3.3.2 Negative carbon isotope excursions prior to the onset of OAE2

A remarkable feature of the SN°4 $\delta^{13}C$ record is a pronounced negative excursion in $\delta^{13}C_{carb}$ (minimum of ~-4‰) and $\delta^{13}C_{org}$ (minimum of -28.9‰) between 107.8 and 106.8 m, which precedes the main positive shift

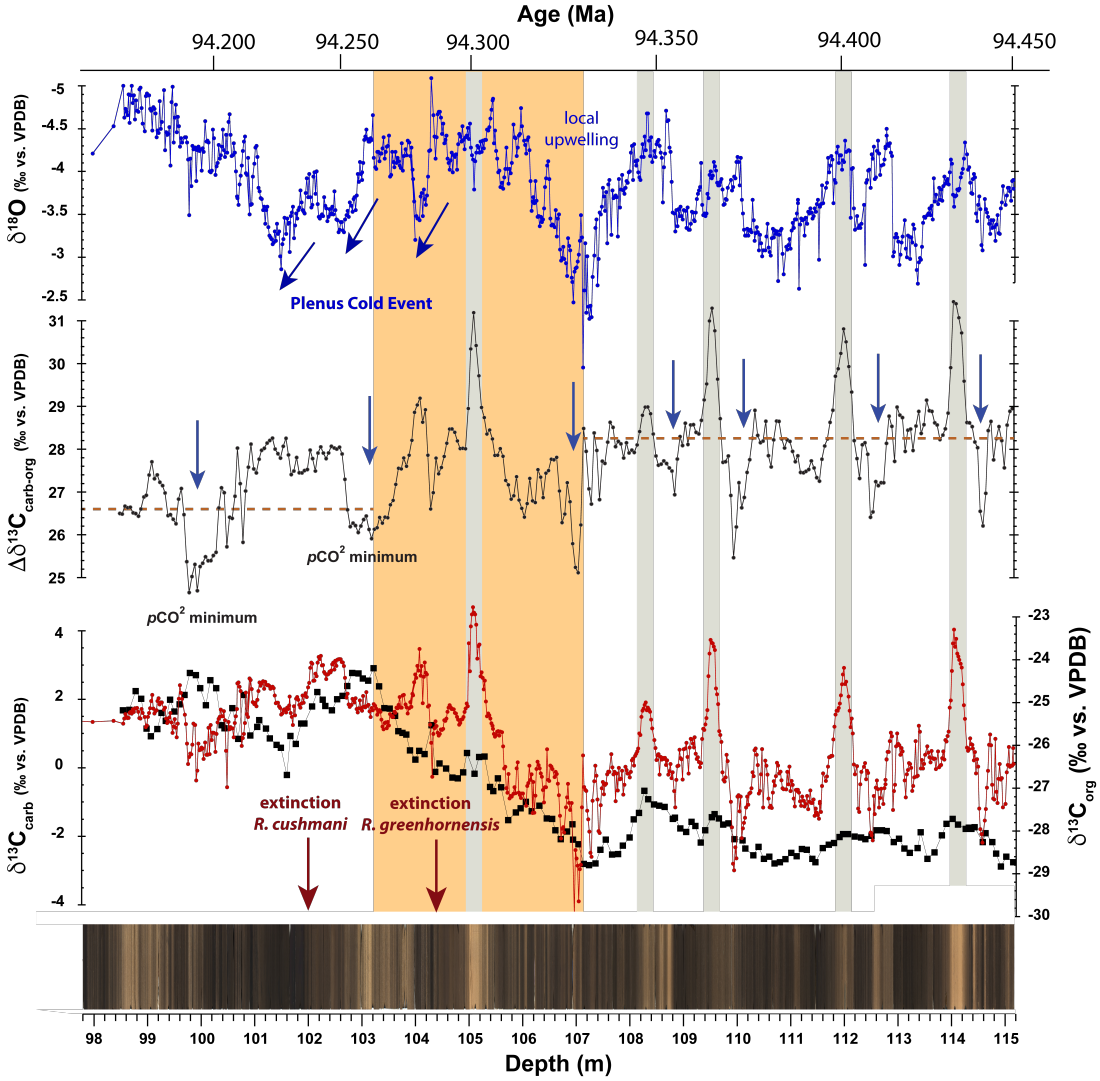

Figure 3.5: Line scan photographs and high-resolution organic carbon and bulk carbonate carbon isotope records ($\delta^{13}C_{org}$ and $\delta^{13}C_{carbonate}$) spanning the onset and development of OAE2 in Core SN°4. Yellow shading marks main $\delta^{13}C_{org}$ increase, which defines onset of OAE2. Gray shading highlights local maxima in $\delta^{13}C_{carbonate}$ related to periodic breakdowns of Tarfaya upwelling system. $\Delta\delta^{13}C_{(carbonate\text{-}org)}$ is strongly driven by diagenetically enhanced high variability in $\delta^{13}C_{carbonate}$, but reflects in its general trend global decrease of $\Delta\delta^{13}C_{(carbonate\text{-}org)}$ during main positive carbon isotope excursion and ensuing atmospheric pCO_2 minima and cooling events ("Plenus Cold Event"). Brown dashed lines indicate average $\Delta\delta^{13}C_{(carbonate\text{-}org)}$ before (~28.2‰) and after (~26.6‰) main $\delta^{13}C_{org}$ increase (carbon burial event). Blue arrows mark pCO_2 minima, apparently paced by orbital obliquity.

characterizing OAE2 (Fig. 3.5). This interval consists mainly of dark, commonly laminated marlstones with intermediate TOC values between 5 and 10%, as in underlying upper Cenomanian organic-rich intervals. In addition, $\delta^{18}O$ values are unusually high, which may indicate enhanced local upwelling of relatively cool, saline water masses. This negative $\delta^{13}C$ trough was preceded by an initial increase in $\delta^{13}C_{org}$ with a peak in both $\delta^{13}C_{org}$ (~-27 ‰) and $\delta^{13}C_{carb}$ (~2‰) centered at 108.3 m, which was associated with a decrease in bulk $\delta^{18}O$ values.

3.3.3.3 Punctuated main $\delta^{13}C$ increase

The main positive shift in $\delta^{13}C_{org}$ from 28.5 to 24.5‰, which defines the onset of OAE2, occurs between 107 and 103 m in Core SN°4 (Fig. 3.5). The duration of this main shift can be calculated as ~80-100 kyr (4 m sediment thickness at sedimentation rates of 4-5 cm/kyr), which corresponds to the duration of two obliquity or one short eccentricity cycle. Moreover, the main $\delta^{13}C$ increase was punctuated, close to its midpoint (105 m), by a plateau in organic $\delta^{13}C_{org}$ and a distinct peak in bulk carbonate $\delta^{13}C_{carbonate}$. The double-peak in $\delta^{13}C_{org}$, characteristic of the early part of OAE2 in the Tarfaya Basin and global record (Tsikos et al., 2004; Kuhnt et al., 2005; Erbacher et al., 2006), occurs at 103 and 100 m in Core SN°4. Within this interval, two $\delta^{13}C_{carbonate}$ maxima are centered at 102.5 and 101 m. Following these maxima, a plateau in both $\delta^{13}C_{carbonate}$ (fluctuating between ~1.5 and 2‰) and $\delta^{13}C_{org}$ (~-25‰) begins above 100 m.

3.3.3.4 Decrease in $\Delta\delta^{13}C_{(carbonate\text{-}org)}$ during the carbon isotope shift at the onset of OAE2

The difference between $\delta^{13}C_{carbonate}$ and $\delta^{13}C_{org}$ ($\Delta\delta^{13}C_{(carbonate\text{-}org)}$), which has been suggested to be an indicator of atmospheric/upper ocean pCO_2 concentrations (Jarvis et al., 2011, 2013), is overall lower after the main positive carbon isotope shift (mean of 27.43‰ between 98.5 and 103 m) than before (mean of 28.24‰ between 107 and 115.2m) (Fig. 3.5). It reaches an overall minimum at ~100 m, following the peak "Plenus Cold Event" and the extinction of *R. cushmani*. This general pattern is in accordance with previous observations (Jarvis et al., 2011) that $\Delta\delta^{13}C_{(carbonate\text{-}org)}$ and atmospheric pCO_2 decreased during the "Plenus Cold Event". Moreover, the evidence for pCO_2 drawdown during the initial parts of the two main OAE2 $\delta^{13}C_{org}$ excursions based on stomatal index (Barclay et al., 2010) closely match the two major drawdowns interpreted from the $\Delta\delta^{13}C_{(carbonate\text{-}org)}$ record in SN°4 (Supplementary Figure 3.3). However, this overall trend is strongly overprinted by intense fluctuations in $\delta^{13}C_{carbonate}$ in the Tarfaya record. These fluctuations are probably caused by periodic breakdowns of the local upwelling system, reflected in substantially increased $\delta^{13}C_{carbonate}$, possibly combined with some early diagenetic effects in the carbonate-rich sediments characterizing these events.

3.3.4 $\delta^{18}O$ fluctuations during OAE2

The bulk carbonate $\delta^{18}O$ record spanning the onset and development of OAE2 exhibits an overall decreasing trend, punctuated by transient episodes of elevated $\delta^{18}O$. Peak warmth is reached during the OAE2 $\delta^{13}C$ plateau ($\delta^{18}O$ of ~-

5‰ at ~99 m), whereas the lowest $\delta^{18}O$ values prior to the OAE2 onset are in the range of -4 to -4.5‰ (Fig. 3.5). The most prominent, transient $\delta^{18}O$ increase corresponds to the "Plenus Cold Event" (Gale and Christensen, 1996), which follows the first carbon isotope maximum of OAE2. In Core SN°4 the "Plenus Cold Event" is expressed as a stepwise $\delta^{18}O$ increase, consisting of three consecutive $\delta^{18}O$ maxima at 101.5, 103 and 104 m interrupted by short warming episodes. The highest $\delta^{18}O$ values (>2.5‰) in the upper Cenomanian of Core SN°4, however, occurred just before the main carbon isotope increase at 107 m in the center of the negative carbon isotope excursion preceding the onset of OAE2. The globally recognized "Plenus Cold Event", which is stratigraphically located within the trough between the first and the second peak of the global OAE2 $\delta^{13}C_{org}$ record (Jarvis et al., 2011), is clearly identified in the high-resolution SN°4 $\delta^{18}O$ curve. It is developed as a three-stepped increase in $\delta^{18}O$, which has so far not been recognized in other records.

3.3.5 Carbonate content, TOC and organic matter accumulation rates

Between 115 and 105 m, TOC values remain relatively low compared to peak OAE2 values, fluctuating around a mean of 6.7% with standard deviation of 2.6%, with a minimum of 1.1% and maximum of 12.7% (Fig. 3.6). In the same interval, the carbonate content exhibits an increasing trend, which is mainly reflected by an increase in the minimum values from just over 30% between 114 and 115 m to 60-70% between 105 and 106 m. Above 105 m, the variability, average and maximum values in TOC increase substantially, reaching a mean of 9.4% (3.7% standard deviation) with maximum values of >20% (Fig. 3.6). This

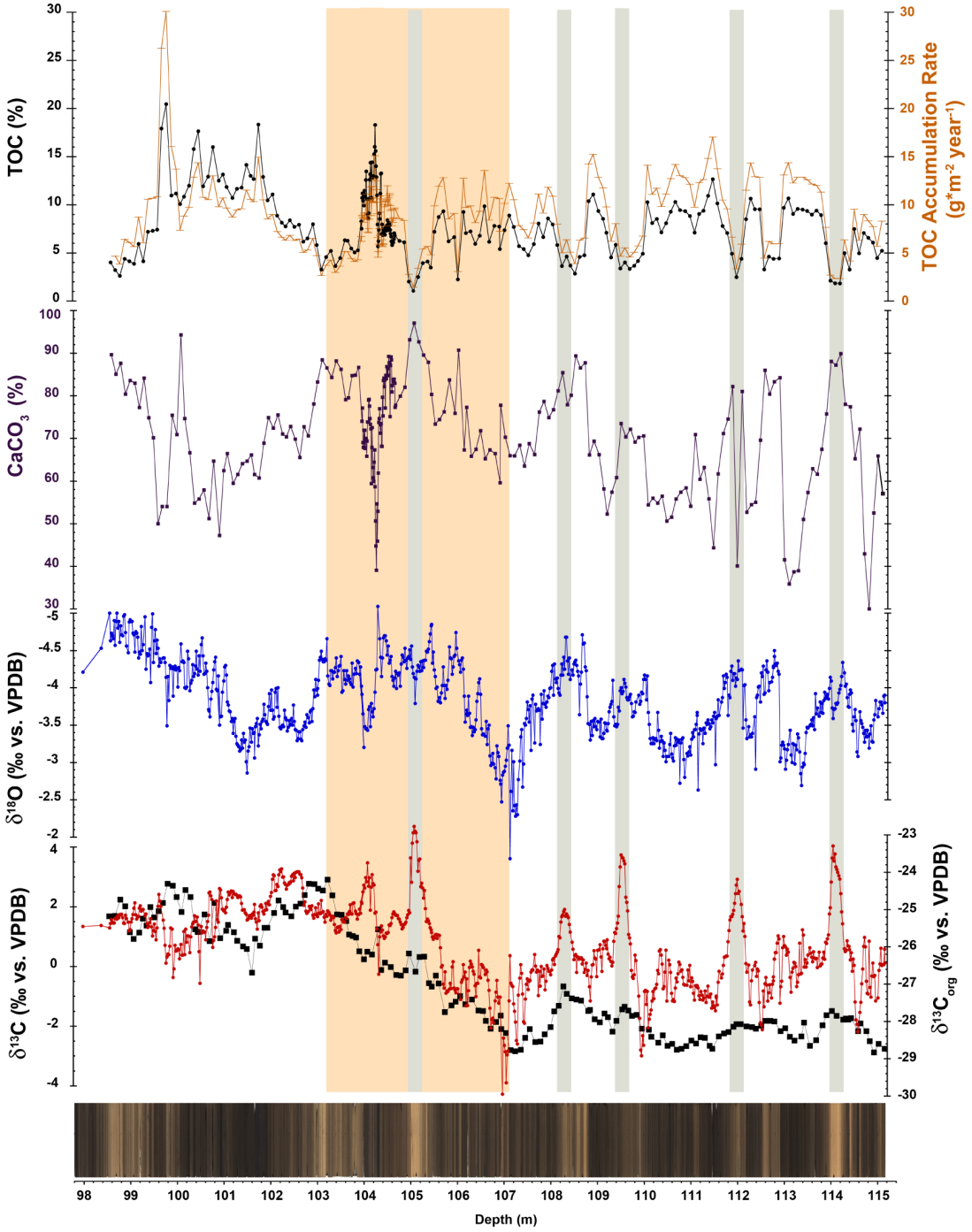

Figure 3.6: High-resolution $CaCO_3$ and TOC records spanning onset and development of OAE2 in Core SN°4. Line scan and stable isotope records are given for stratigraphic orientation. Yellow shading marks interval of $\delta^{13}C_{org}$ main increase, which defines onset of OAE2; gray shading highlights local maxima in $\delta^{13}C_{carbonate}$.

stepped increase in TOC variability, average and maxima parallels the increase in $\delta^{13}C_{org}$ towards the first peak of the OAE2 carbon isotope excursion. However TOC accumulation rates in the Tarfaya Basin do not exhibit a dramatic increase at the onset of OAE2 and highest accumulation rates are reached after the second $\delta^{13}C$ peak (Schönfeld et al., 2015).

3.3.6 XRF-scanner derived estimates of terrigenous supply

Twelve major increases in Log(Zr/Rb) and carbonate can be discriminated in Fig. 3.7. Increases in Log(Zr/Rb) marking increases in grain density and size are associated with coeval decreases in fine-grained terrigenous material (Log(Al/Ca) and Log(K/Ca)), reflecting abundance of elements mainly bound to clay minerals) (Fig. 3.7). These increases in carbonate grains and coarse terrigenous flux and decreases in clay mineral flux are likely related to falling sea level, shifting the coastline seawards and promoting re-suspension and winnowing transport of fine grained terrigenous material by bottom currents and transport to deeper parts of the basin. The most prominent increases in Log(Zr/Rb) and carbonate occurred at ~114.3, ~108.8, ~105.3 and ~103.9 m. The striking changes from carbonate-rich layers with coarse terrigenous components to black shales with fine-grained terrigenous content, expressed in a subsequent increase of Log(Al/Ca) and Log(K/Ca) at these levels are interpreted as transgressive surfaces (TS), overlain by laminated organic-rich sediments indicating intensification of upwelling.

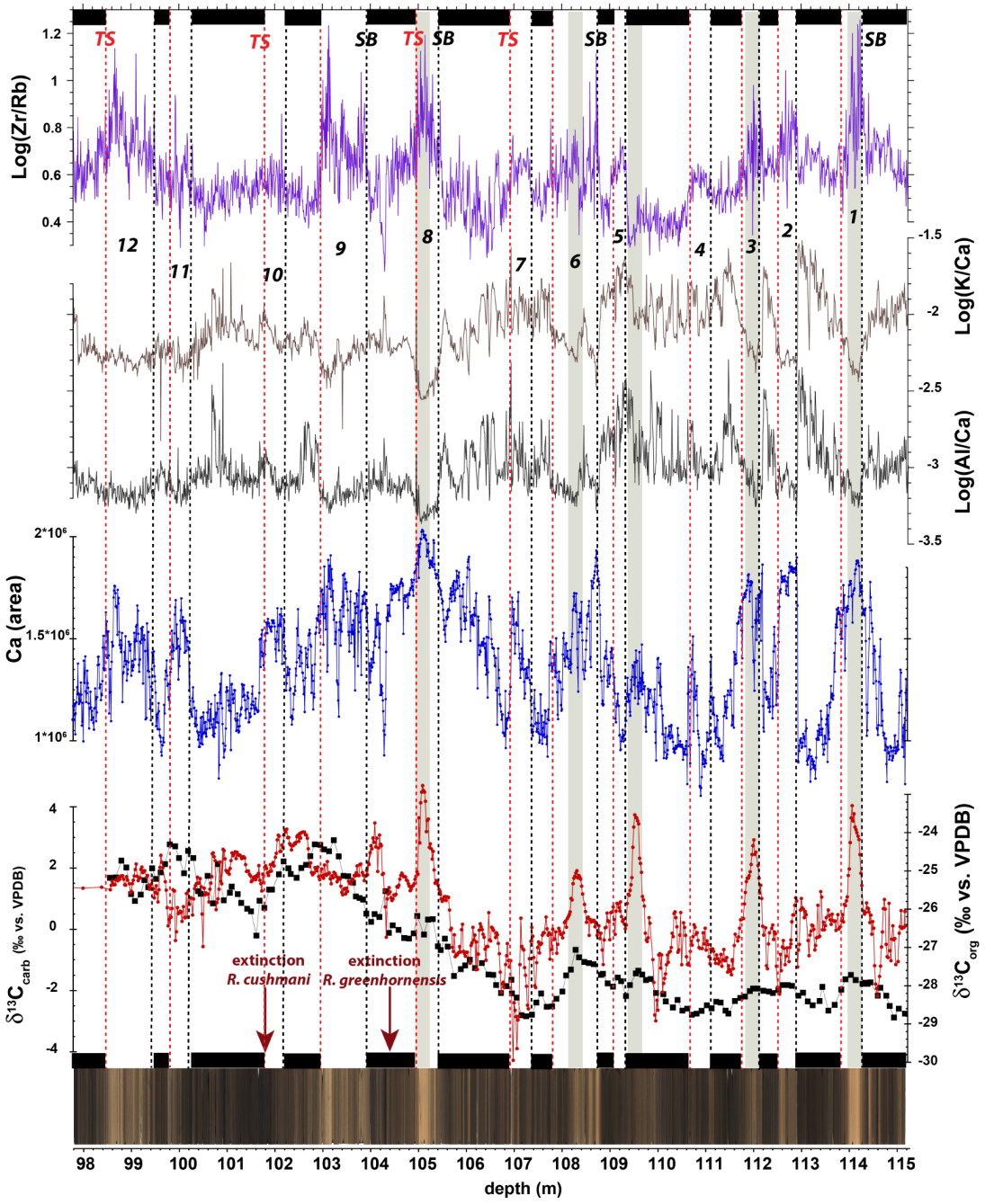

Figure 3.7: XRF-scanner derived variations in grain density/grains size from Log(Zr/Rb), fine grained terrigenous flux from Log(Al/Ca) and Log(K/Ca) and carbonate content from Ca area counts (cps) in Core SN°4. Gray shadings indicate $\delta^{13}C_{carbonate}$ maxima; red dashed lines mark changes from carbonate-rich sediments with high Log(Zr/Rb) to carbonate poor sediments with low Log(Zr/Rb), interpreted as transgressive surfaces (TS); black dashed lines indicate changes from organic-rich to carbonate rich sediments associated with increases in Log(Zr/Rb), interpreted as sequence boundaries (SB). Intervals dominated by black laminated organic rich

sediments (OMZ expansion and intensification) are marked with horizontal black bars; light, carbonate-rich intervals with elevated Log(Zr/Rb) are numbered from 1 to 12.

3.3.7 Foraminiferal extinction events

The last occurrence of *Rotalipora cushmani* was observed in section 40, segment 2, 34-37 cm (Fig. 3.8) (101.89-101.92 m), which is above the $\delta^{13}C_{carbonate}$ maximum at 102.0-102.4 m in Core SN°4 and close to the end of the second positive $\delta^{13}C$ shift in the global organic and carbonate $\delta^{13}C$ curves (Fig. 3.7). The extinction interval is bracketed by the sample with the common LO of *R. cushmani* and a sample above in section 40, segment 2, 22-25.5 cm (101.77-101.80 m) that yielded a well preserved foraminiferal assemblage consisting of small hedbergellids. The extinction, thus, occurred close to the peak of the "Plenus Cold Event", coincident with the onset of the dark, organic-rich, laminated part of cycle 0 indicating poor bottom water oxygenation (Fig. 3.6). The LO of *Rotalipora greenhornensis* occurs in section 41, segment 1, 41-43 cm (Fig. 3.8) (104.38-104.40 m) and is bracketed by a sample with common *R. cushmani* and *Whiteinella* spp. in section 41, segment 1, 31-32 cm (104.28-104.29 m), which does not contain *R. greenhornensis* (Fig. 3.8). The extinction interval is, thus, within the lower part of cycle 0 coincident with a distinct decrease in bottom water oxygenation, as shown by a change from light, homogeneous carbonate rich sediments to dark, laminated sediments (Fig. 3.8). The distance between the two extinction events is ~2.5 m or ~40 to 60 kyr considering sedimentation rates of 4-6 cm/kyr in this interval.

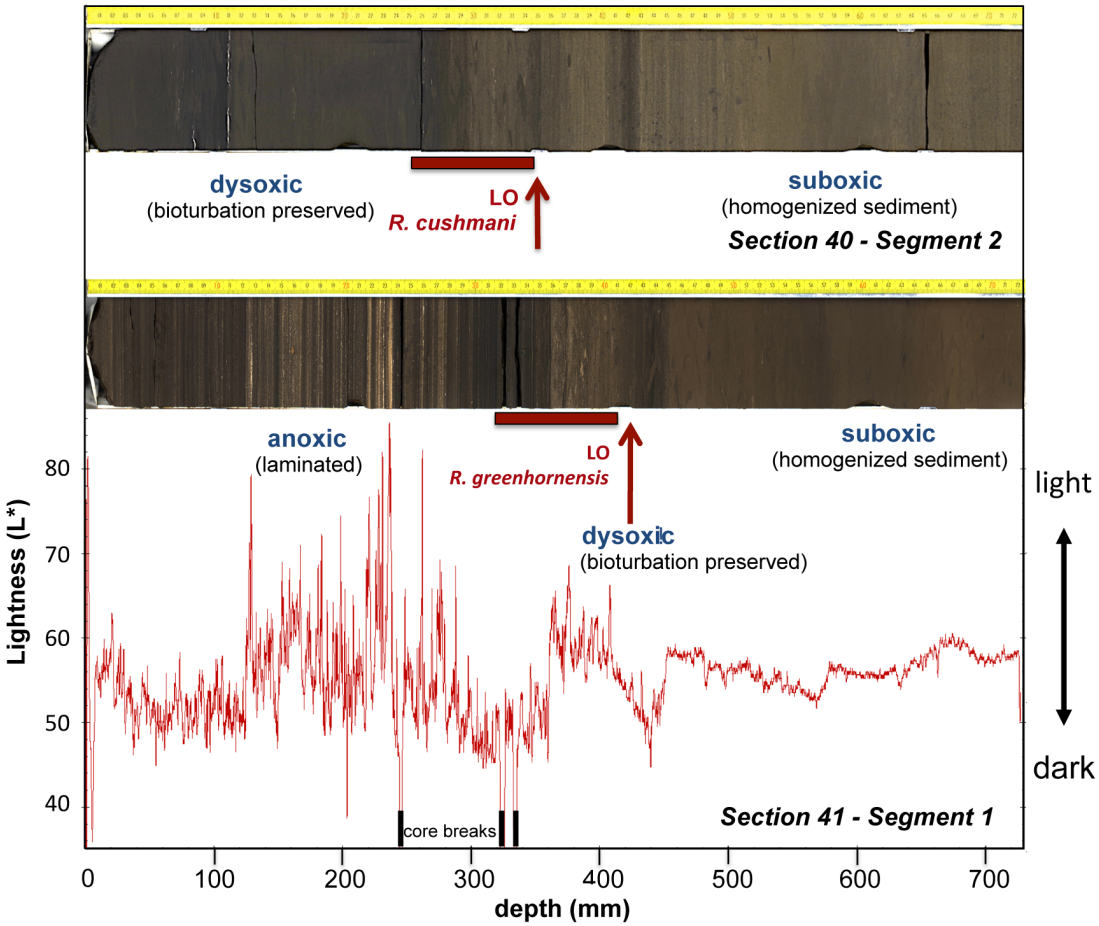

Figure 3.8: Position of main planktonic foraminiferal extinction events in Core SN°4. Extinction of *R. cushmani* occurs within bioturbated interval and change from light, carbonate-rich suboxic to dark dysoxic conditions. Extinction of *Rotalipora greenhornensis* coincides with onset of laminated sediments, which corresponds in modern upwelling-related OMZs to dissolved oxygen levels below 5 µmol kg-1 (Schönfeld et al., 2015). Red arrows indicate position of last sample with *R. cushmani* or *R. greenhornensis*, red bar marks interval of extinction, between the last sample with and the first sample without *R. cushmani* or *R. greenhornensis*.

3.4. Discussion

3.4.1 Fluctuations in bulk $\delta^{13}C_{carbonate}$: Influence of global carbon reservoir, carbonate composition, local water mass variability and early diagenesis

The bulk $\delta^{13}C_{carbonate}$ curve exhibits marked differences to published late Cenomanian bulk $\delta^{13}C_{carbonate}$ records (e.g., Jarvis et al., 2006; Wendler, 2013; Jarvis et al., 2015), which show overall higher $\delta^{13}C_{carbonate}$ values and lack the high-amplitude fluctuations, characterizing the late Cenomanian $\delta^{13}C_{carbonate}$ curve in Core SN°4. These high-amplitude fluctuations are reflected by lithological changes, and may be easily missing in low-intermediate resolution records as spikes of high $\delta^{13}C_{carbonate}$ generally occur within relatively thin organic carbon-depleted intervals. Peak $\delta^{13}C_{carbonate}$ values remain below 4‰, which is in the normal range of bulk carbonate values in chalk seas that are not affected by upwelling of nutrient-rich intermediate waters. In contrast, lower $\delta^{13}C_{carbonate}$ characterizes laminated organic-rich intervals, when nutrient-rich water-masses upwelled to the sea surface. A recent compilation of Late Cretaceous $\delta^{13}C_{carbonate}$ records (Wendler, 2013) points to substantial differences (1-2‰) in the amplitude of $\delta^{13}C$ events in the English Chalk reference section (Jarvis et al., 2006), the US Western Interior (Locklair and Sageman, 2008; Sageman et al., 2006; Tessin et al., 2015) and eastern Tethys sections in Tibet (Li et al., 2006), which nevertheless all preserve the major features of the global carbon isotope curve. We can exclude the possibility that the composition of bulk carbonate exhibits strong variability across OAE2 in Core SN°4 (Fig. 3.9). In particular, *Pithonella* tests, which occur commonly in more proximal Cenomanian-Turonian limestones in the Tarfaya Basin (i.e. Kuhnt et al., 1986,

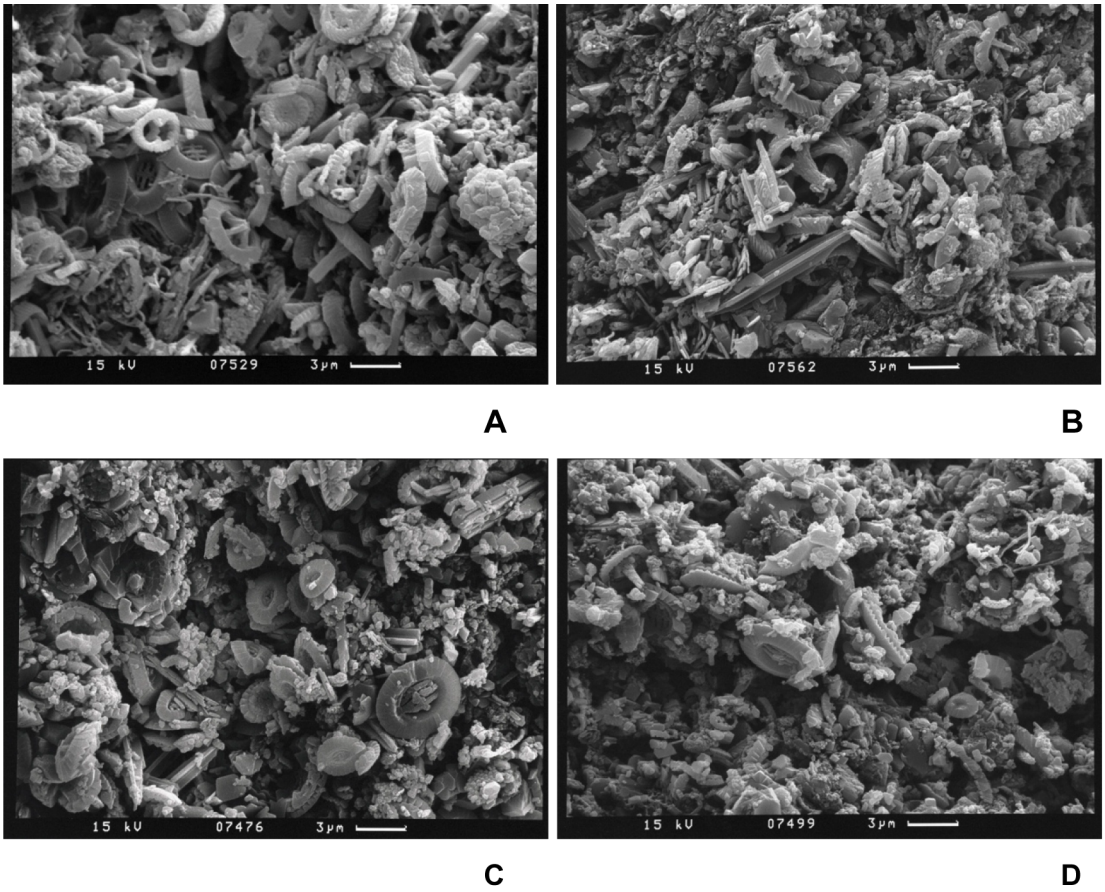

Figure 3.9: High magnification SEM images of sediment composition in organic-rich laminated and carbonate-rich homogenous intervals with low and high $\delta^{13}C_{carbonate}$ in Core SN°4. Carbonate fraction is mainly composed of pristine coccoliths with no evidence for major diagenetic cementation. ***A.*** Laminated interval: section 41, segment 1 0-1 cm, 103.80 m. ***B.*** Laminated interval: section 40, segment 4 0-1 cm, 102.90 m. ***C.*** Light homogenous interval: section 44, segment 2 40-41 cm, 114.06 m. ***D.*** Light homogenous interval: section 41, segment 2 43-44 cm, 104.95 m.

plate 10A) are very rare to absent in the OAE2 interval of Core SN°4. *Pithonella* tests exhibit unusually high carbon isotope values (Wendler et al., 2013), probably related to fractionation during photosynthesis. High proportions of *Pithonella* tests would, thus, explain unusually positive $\delta^{13}C_{carbonate}$ values in bulk carbonate. A possible influence of vital effects with changing coccolith assemblage composition is unlikely since Cretaceous coccoliths must have used

similar carbon acquisition strategies to Paleocene coccolithophorid algae with larger and/or more similar cell sizes and higher atmospheric carbon dioxide concentrations resulting in a smaller range of vital effects than today (Stoll, 2005).

Inter-basinal and latitudinal differences in the amplitude of Cretaceous $\delta^{13}C$ variations are likely related to locally differing upwelling regimes of nutrient-rich and $\delta^{13}C$-depleted water-masses and to the efficiency of the biological pump. Today, in a well-ventilated ocean, the dissolved inorganic carbon of nutrient-rich upwelling water masses can be depleted by >1‰ (Berger et al., 1978). This may have been substantially higher in the Late Cretaceous Atlantic Ocean, where intermediate water masses were strongly depleted in oxygen and enriched in nutrients and ^{12}C. For example, productivity- and pCO_2-dependent latitudinal differences in the amplitude of the OAE2 carbon isotope excursion (in the range of 1 to 4‰) were recorded in biomarkers for photosynthetic algae (van Bentum et al., 2012). We consider the generally lower values and high variability on orbital timescales of the $\delta^{13}C$ signal in carbonates from the Tarfaya Basin, which are mainly composed of coccoliths, to be largely a primary signal related to the upwelling of nutrient-enriched and $\delta^{13}C$ depleted intermediate water masses. Early diagenesis of organic-rich sediments and preferential formation of ^{12}C enriched authigenic carbonates in organic-rich pore waters may have additionally contributed to high frequency fluctuations in bulk $\delta^{13}C_{carbonate}$ in Core SN°4. In particular, the anomalously low $\delta^{13}C_{carbonate}$ at ~107, ~110, ~112.6 and ~104.5 m may be caused by locally precipitated carbonate cements derived from respired organic matter.

Changes in the global carbon cycle associated with OAE2, i.e. the effect of changing global organic carbon burial rates on the different carbon reservoirs and their isotopic composition, also influence bulk $\delta^{13}C_{carbonate}$. A 2.5% increase in $\delta^{13}C_{carbonate}$, as observed across the onset of OAE2 in Core SN°4, would require burial of ~4500 Gt of organic carbon, assuming that the size of the Cretaceous inorganic carbon pool was similar to today's and $\delta^{13}C_{organic}$ of -25‰ (Higgins and Schrag, 2006). This implies that a 0.1‰ increase in $\delta^{13}C_{carbonate}$ would require a burial of 180 Gt of organic carbon, which is in the range of the modern carbon flux reaching the sedimentary reservoir (100-200 Gt /kyr, Falkowski et al., 1998; Houghton, 2007). To maintain the elevated $\delta^{13}C_{carbonate}$ values during OAE2 over an estimated duration of 500 kyr, a total global excess organic carbon burial of 25 600 Gt would be necessary (Arthur et al., 1988). This value corresponds to an excess burial rate of 51.2 Gt/kyr or 25-50% of the present day global organic carbon flux into the sedimentary reservoir. Organic carbon fluxes in the Tarfaya Basin alone, with an extension of ~170 000 km^2 and a burial rate of 10 $g/(m^2*y)$ would amount to 1.7 Gt/kyr or ~1% of the excess burial necessary to produce the positive $\delta^{13}C$ shift at the onset of OAE2 and 3% of the excess burial to maintain the excursion over several 100 kyr. Highly productive subtropical shelf seas were widespread in the Western Tethys during the Cenomanian/Turonian (i.e. Tunisia-Northern Morocco, the huge Senegal Casamance Shelf, the La Luna Sea in Venezuela) and carbon burial in these seas may have been sufficient to cause and maintain the carbon isotope excursion. However, it remains unclear how the nutrient budgets in these high-productivity areas were balanced over several hundred thousand years.

3.4.2 Carbon isotope fractionation during CO_2 fixation in organic carbon

The $\delta^{13}C$ difference between marine carbonate and the contemporaneously produced organic matter ($\Delta\delta^{13}C_{carbonate\text{-}organic}$) is influenced by two main factors (Hayes et al., 1999): (1) a temperature dependent fractionation between dissolved inorganic carbon, organic carbon and carbonate carbon, (2) a fractionation during fixation of CO_2 in organic carbon, which is associated with different algal growth rates and morphologies and correlated to CO_2 concentrations at the sea surface. Likely explanations for the overall lower amplitude of the $\delta^{13}C_{carbonate}$ excursion at the onset of OAE2, thus, include an overall increase in temperature, especially in the early stage of the OAE, and/or an increase in $\delta^{13}C_{organic}$ fractionation in response to increased algal growth rates and a decrease in pCO_2, in particular during the final stage of the initial shift and ensuing $\delta^{13}C$ plateau.

The $\delta^{13}C_{organic}$ record of bulk organic matter in marine sediments is influenced by various factors, including contamination by terrestrial organic matter, differing rates of local CO_2 uptake in surface waters related to sea surface temperatures and the intensity of upwelling of nutrient-rich water masses and resulting local primary production. In-depth studies of the OM-composition of OAE2 sediments in the Tarfaya Basin showed that any terrestrial contribution, which could result in significant variability in $\delta^{13}C_{organic}$, was negligible (Kuhnt et al., 1990; Kuypers et al., 2002; Kolonic et al., 2005). However, variable rates of primary productivity may have caused significant spatial and temporal differences in the degree of carbon isotope fractionation, even in marine organic matter (Laws et al., 1995). Increases in upwelling/productivity promoting

phytoplankton growth rates would result in local positive $\delta^{13}C_{organic}$ anomalies and a decrease in $\Delta\delta^{13}C_{carbonate\text{-}organic}$. However, the decrease in $\Delta\delta^{13}C_{carbonate\text{-}organic}$ associated with the Plenus Cold Event appears to be a global phenomenon (Jarvis et al., 2011), probably related to a major drawdown of atmospheric pCO_2.

The variability of intermediate to high resolution marine organic carbon isotope records at subtropical latitudes is significant. Pre-OAE2 values range from -25‰ at the base of the Bonarelli level in central Italy (Tsikos et al., 2004) to -28‰ at Demerara Rise (Erbacher et al., 2005), while values from southern France and the Western Interior Basin (Jarvis et al., 2011; Du Vivier et al 2015) range between -26 and -27‰. The Pre-OAE2 values in Tarfaya SN°4 which vary between -28 and -29‰ are thus among the lightest marine late Cenomanian $\delta^{13}C_{org}$ values, only comparable to ODP Site 367 offshore the Casamance shelf, Senegal (Kuypers et al., 2002). This geographic pattern of extremely light $\delta^{13}C_{org}$ values along the tropical Cretaceous West African margin persists through the OAE2 carbon isotope excursion with peak $\delta^{13}C_{org}$ values around -24‰ in SN°4, in contrast to values around -22‰ at Demerara Rise and between -22 and -23‰ at Gubbio and the Western Interior. These geographic differences in $\delta^{13}C_{org}$ correlate to differences in local productivity (van Bentum et al., 2012) and may be related to intense late Cenomanian equatorial upwelling along the Northwest African continental margin.

An alternative explanation for the relatively light carbon isotopic compositions of organic matter in Tarfaya black shales before, during and after the positive $\delta^{13}C$ excursion associated with OAE2 would be intensified photic zone recycling of isotopically light organic carbon due to intensified surface

stratification (Küspert, 1982). Evidence of bacterial nitrogen fixation associated with photic zone anoxia common to OAE2 black shales and Mediterranean sapropels supports such a scenario of intensified surface stratification with enhanced organic carbon oxidation and re-utilization in the photic zone (Meyers, 2006). However, even potentially enhanced land-derived nutrient fluxes during times of a greenhouse-amplified hydrologic cycle (Van Helmond et al., 2013; Meyers, 2014) do not completely resolve the conundrum of nutrient supply for sustained high organic matter accumulation rates without vertical mixing (upwelling) of nutrient-enriched water masses.

3.4.3 Impact of anoxia on the stepwise extinction of Rotalipora greenhornensis and Rotalipora cushmani

The environmental context of the two main global extinction events of keeled planktonic foraminifers (*R. greenhornensis* and *R. cushmani*) in the Tarfaya Basin exhibits striking similarities. Both extinction events occurred during major changes towards poorly oxygenated bottom water conditions (Fig. 3.9) and probably were linked to transient cooling episodes within the "Plenus Cold Event" (Figs. 3.5-3.6). The *R. greenhornesis* extinction occurred during the first step of the three-stepped cooling of the "Plenus Cold Event" and the *R. cushmani* extinction occurred during the third and main cooling phase of this event.

The stratigraphic position of the two extinction events with respect to the carbon isotope stratigraphy is constrained on a global scale. In a recent study, stepwise marine extinctions across OAE2, including the *R. greenhornensis* and *R. cushmani* extinction events, were correlated to stable carbon isotope curves

along a depth transect at the northern Iberian margin (Kaiho et al., 2014). These authors found the same characteristic extinction pattern at all sections studied, independently of their bathymetric position: (1) the extinction of *R. greenhornensis* was encountered within the center of the main first positive $\delta^{13}C$ shift marking the onset of OAE2 and the extinction of *R. cushmani* in the trough between the first and second $\delta^{13}C$ maximum of OAE2, ~50 kyr later. A similar relationship between the extinction of the last two rotaliporids and the global $\delta^{13}C$ curve across OAE2 was previously reported from the Western Interior Basin US (Caron et al., 2006; Desmares et al., 2008), the Eastbourne section, UK (Paul et al., 1999; Tsikos et al., 2004) the Vocontian Basin in southern France (Grosheny et al., 2006; Desmares et al., 2008), Tunisia (Caron et al., 2006) and from outcrop and drill cores in the Tarfaya Basin (Luderer and Kuhnt, 1997; Tsikos et al., 2004; Kuhnt et al. 2005). Thus, we can exclude that the disappearance of *R. greenhornensis* and *R. cushmani* in the SN°4 record was driven by a local expansion of the OMZ and intensification of upwelling. These global extinctions suggest that the expansion of anoxia at 94.24 and 94.29 Ma occurred on a basin-wide scale including the entire Western Tethys and Atlantic/Western Interior Seaway.

Two environmental changes could have affected the habitat space of thermocline dwelling keeled rotaliporids: (1) extreme intensification and expansion of the oxygen minimum zone up to photic zone anoxia, which would have driven the entire habitat of *R. greenhornensis* and *R. cushmani* to become anoxic; (2) severe ocean acidification within the oxygen minimum zone, which would have affected wall thickness and calcification of these heavily keeled thermocline dwellers (De Moel et al., 2009). The second mechanism is supported

by the fact that both species develop thin walled morphotypes with strongly reduced keels or even completely lost imperforate keels just before their extinction (Longoria 1973; Luderer and Kuhnt 1997; Desmares et al., 2008). Ocean acidification as a driver of the extinction of rotaliporids during OAE2 is additionally supported by first intermediate resolution Ca-isotope records across the anoxic event from the European Eastbourne and Pont Issole secions and the Portland #1 Core in the US Western Interior basin (Du Vivier et al., 2015). Here, positive $\delta^{44/40}Ca_{sw}$ excursions, interpreted as changes to the calcium carbonate fractionation factor associated with brief ocean acidification events, precede the $\delta^{13}C$ maxima and thus closely match the *Rotalipora* extinction levels. These environmental deteriorations must have affected the global ocean in order to drive the extinction of these widely distributed tropical-subtropical species. The ~50 kyr offset between the two extinction events (approximating the duration of one obliquity cycle during the Cenomanian) and the almost identical evolution from suboxic to anoxic conditions suggest orbital control on both the spread of ocean anoxia/acidification and the extinction of thermocline dwelling planktonic foraminifers.

3.4.4 Transient cooling events and sea level fluctuations during the onset of OAE2

Decreasing Log(Al/Ca), Log(K/Ca) and Log(Terr/Ca) and non-dissolvable residue, as well as increasing carbonate content provide clear evidence that terrigenous input decreased in two steps between ~111 and ~105 m, prior to the onset and during the initial phase of OAE2 (Figs. 3.7 and 3.10). This decrease in terrigenous supply is most likely associated with a shoreward displacement of

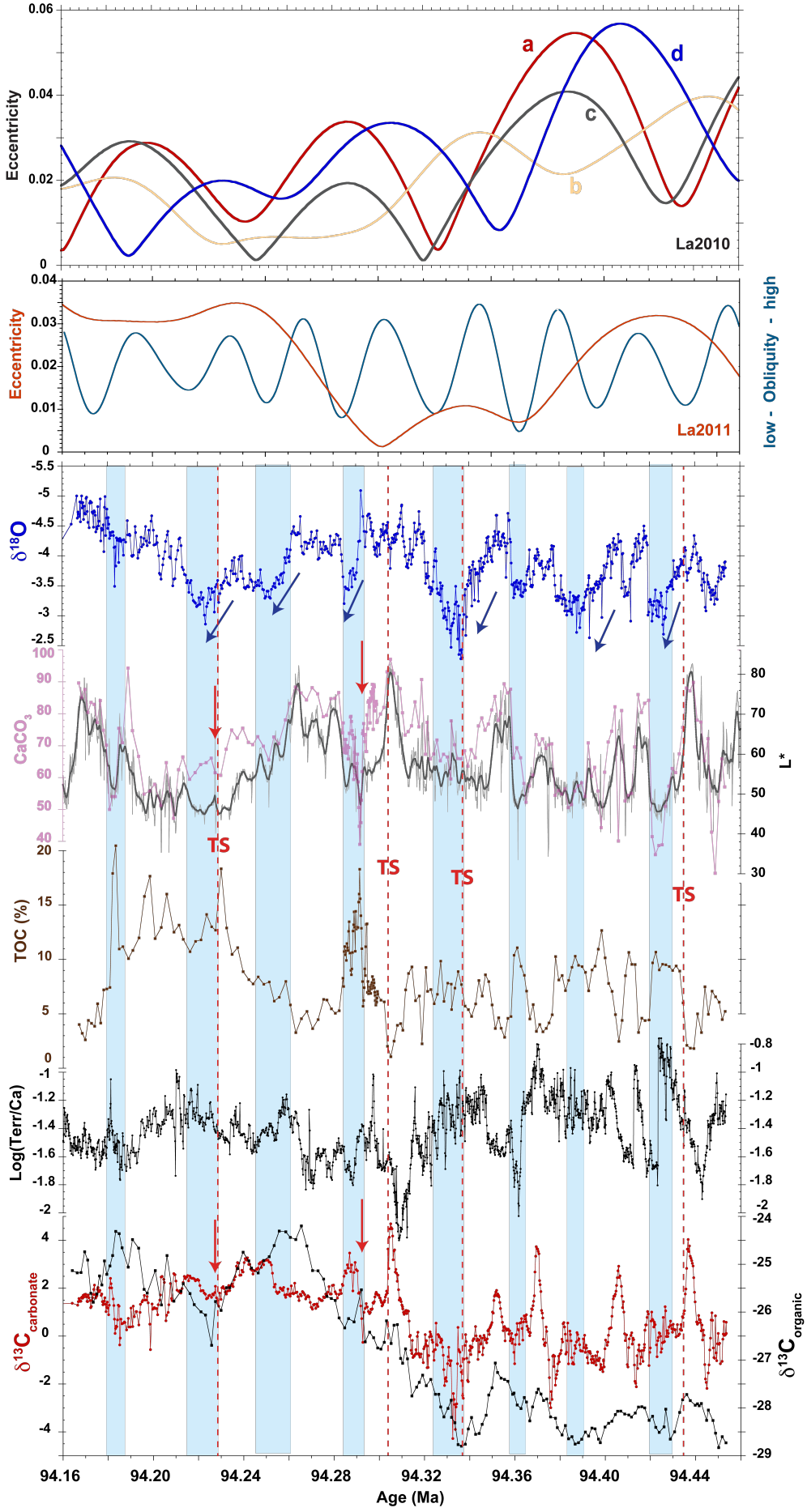
Eccentricity
a
d
c
b
La2010
Eccentricity
La2011
low - Obliquity - high
δ18O
CaCO3
L*
TS
TS
TS
TS
TOC (%)
Log(Terr/Ca)
δ13Ccarbonate
δ13Corganic
94.16
94.20
94.24
94.28
94.32
94.36
94.40
94.44
Age (Ma)

Figure 3.10: Upper panel: Alternative solutions for orbital eccentricity (La10a-d) from Laskar et al. (2011a) and for eccentricity and obliquity from Laskar et al. (2011b and 2004). Note that La10a and La10d indicate major decrease in 400 kyr eccentricity culminating in distinct (100 kyr and 400 kyr) eccentricity minimum coinciding with OAE2 onset. Lower panel: Core SN°4 proxy records in time domain. Light blue shaded areas indicate "cool" phases, characterized by heavy bulk $\delta^{18}O$, deposition of dark laminated black shales with elevated TOC and clay (Log(Terr/Ca)). Major TS (changes from light carbonate rich to dark organic carbon rich sedimentation marked with dashed red lines) coincide with $\delta^{18}O$ minima at obliquity maxima (highest temperature gradients between equator and high latitudes). Red arrows indicate extinction of *R. greenhornensis* and *R. cushmani* at onset of organic-rich laminated sedimentation following TS.

the shoreline, retraction of river deltas, creation of additional accommodation space on the shelf and overall reduction of sediment flux to the outer shelf location of Core SN°4 during a major transgressive phase. A first peak transgression (maximum flooding) is reached at ~106 m in the upper part of a thick interval of laminated organic-rich marlstones with minimum Log(Rb/Sr) at the base of the initial $\delta^{13}C_{org}$ increase of OAE2. This transgression has also been documented in the US Western Interior (e.g., Elder et al., 1994; Arthur and Sageman, 2004; Laurin and Sageman, 2007) and is in broad agreement with the interpretation of the Mexican platform-carbonate sea level record, where the onset of OAE2 is also related to a major transgressive event (Elrick et al., 2009).

A first regressive phase with a distinct sea level lowstand is associated with the very prominent limestone bed centered at 105 m (Fig. 3.7). This regressive phase again matches a similar trend in the Western Interior sea level record (Laurin and Sageman, 2007). We consider the limestone bed at 105 m as a lowstand deposit between a sequence boundary and a transgressive surface,

when the oxygen minimum zone did not impinge on the Tarfaya shelf and the location of Core SN°4 was still well oxygenated. The TS on top of the limestone bed represents the first significant flooding surface at the onset of a new transgressive sequence (sequence Ce5 in the global eustatic cycle scheme of Gale et al., 2002). This TS is typically characterized by a well cemented carbonate surface, which was intensely perforated by burrowing organisms. In shallower shelf areas of the Tarfaya Basin with low sediment supply, where falling sea level and/or lowstand facies are not usually preserved above the sequence boundary due to winnowing by intensified wave induced or tidal currents, hiatuses commonly develop during the sea level lowstands and the TS commonly falls together with the SB. However, in the more distal location of Core SN°4, we consider the relatively coarse grained carbonate beds to represent lowstand deposits, possibly a more distal equivalent of the lowstand skeletal limestones described from the Greenhorn Formation in the Western Interior (Sageman 1996). Sediments across and immediately overlying the TS are commonly carbonate rich, relatively coarse-grained, well-oxygenated and bioturbated. With progressing transgression they grade into organic-rich, laminated and more fine-grained, clay rich black shales, which are indicative of an impinging oxygen minimum zone on the outer to middle shelf. The interval above the TS (~105-104 m) represents such a typical sea level highstand deposit (Fig. 3.7), whereas a series of progressive stepwise regressions and subsequent transgressions is associated with the "Plenus Cold Event". This stepwise cooling culminated at 102-101 m with high $\delta^{18}O$ indicative of cool surface water conditions and organic rich sediments suggesting enhanced upwelling and intensification of the OMZ, which led to the extinction of *Rotalipora cushmani*.

To sum up, the Tarfaya sea level record reveals a longterm (>100 kyr) transgressive cycle before the onset of the main carbon isotope excursion, which reaches its maximum close to the onset of the main positive $\delta^{13}C$ excursion. The following sea level cycle is characterized by a lowstand midway during the positive carbon isotope shift and by a prominent TS at the base of the globally recognized eustatic sequence Ce5, which is correlative to a major hiatus in the more proximal Mohammed Plage Section (Mort et al., 2008; Kuhnt et al., 2009; Gertsch et al., 2010). The ensuing transgressive trend is punctuated by prominent stepwise regressions including the peak of the "Plenus Cold Event" coincident with the $\delta^{13}C$ trough between the two $\delta^{13}C$ maxima.

Recently, Wagreich et al. (2014), Sames et al. (2016) and Wendler and Wendler (2016) proposed that net transfer of water to the continent by the infill of dried-out groundwater reservoirs and large inland basins during transitions from arid to humid climate periods may have resulted in significant short-term sea level falls (aquifer eustasy). According to this scenario, rapid eustatic sea level falls (when aquifers and inland basins are filled) are associated with sudden increases in marine $\delta^{18}O$, which would mimic "glaciations" followed by longer periods of warm humid climate with decreasing marine $\delta^{18}O$ and rising sea level. Terrigenous proxies in Core SN°4 indicate a sudden regression during the carbonate maximum centered at 105 m, approximately midway within the initial OAE2 $\delta^{13}C_{org}$ increase and following a prominent decreasing (warming) phase in the longterm $\delta^{18}O$ record, which is in agreement with the aquifer-eustatic scenario. However, the main increase in $\delta^{18}O$ associated with enhanced terrigenous fluxes, indicating closest proximity to land and lowest sea level,

occurred gradually (stepwise) starting from 104.5 m to the peak of the "Plenus Cold Event" between 101 and 102 m. This gradual increase rather supports a glacio-eustatic scenario with slow buildup of ephemeral ice caps on Antarctica even under high atmospheric CO_2 conditions (Flögel et al., 2011) rather than rapid infill of continental aquifers.

3.4.5 Impact of orbital forcing on organic carbon burial and terrigenous supply

Correlation of the TOC, carbonate, lightness, terrigenous and stable isotope records in Core SN°4 to the latest orbital solutions encompassing this interval (Laskar et al., 2011) suggests an enhanced response to obliquity forcing during the onset of OAE2. In particular, the punctuation of the main $\delta^{13}C$ increase (approximate duration of 80 kyr) by a plateau in organic $\delta^{13}C_{org}$ and a distinct peak in bulk carbonate $\delta^{13}C_{carb}$ points to obliquity control on carbon isotope variations. Also time series analysis of the logging record from the nearby exploration well S13 (Meyers et al., 2012a) previously indicated a strong sedimentation response to obliquity in the Tarfaya Basin. In contrast, the response to the 100 kyr short eccentricity cycle, considered to be the dominant forcing during periods of greenhouse climate such as the Paleogene warm periods (Zachos et al., 2010; Kirtland Turner, 2014), appears muted over this interval (Figs. 3.10-3.11). The onset of OAE2 coincides with an extended interval of low eccentricity, during the low phase of a 400 kyr cycle coincident with dampened variability in short eccentricity and high amplitude variability in obliquity (Fig. 3.10-3.11). This relatively unusual orbital configuration likely accounts for the strong obliquity signal in the proxy records including carbonate

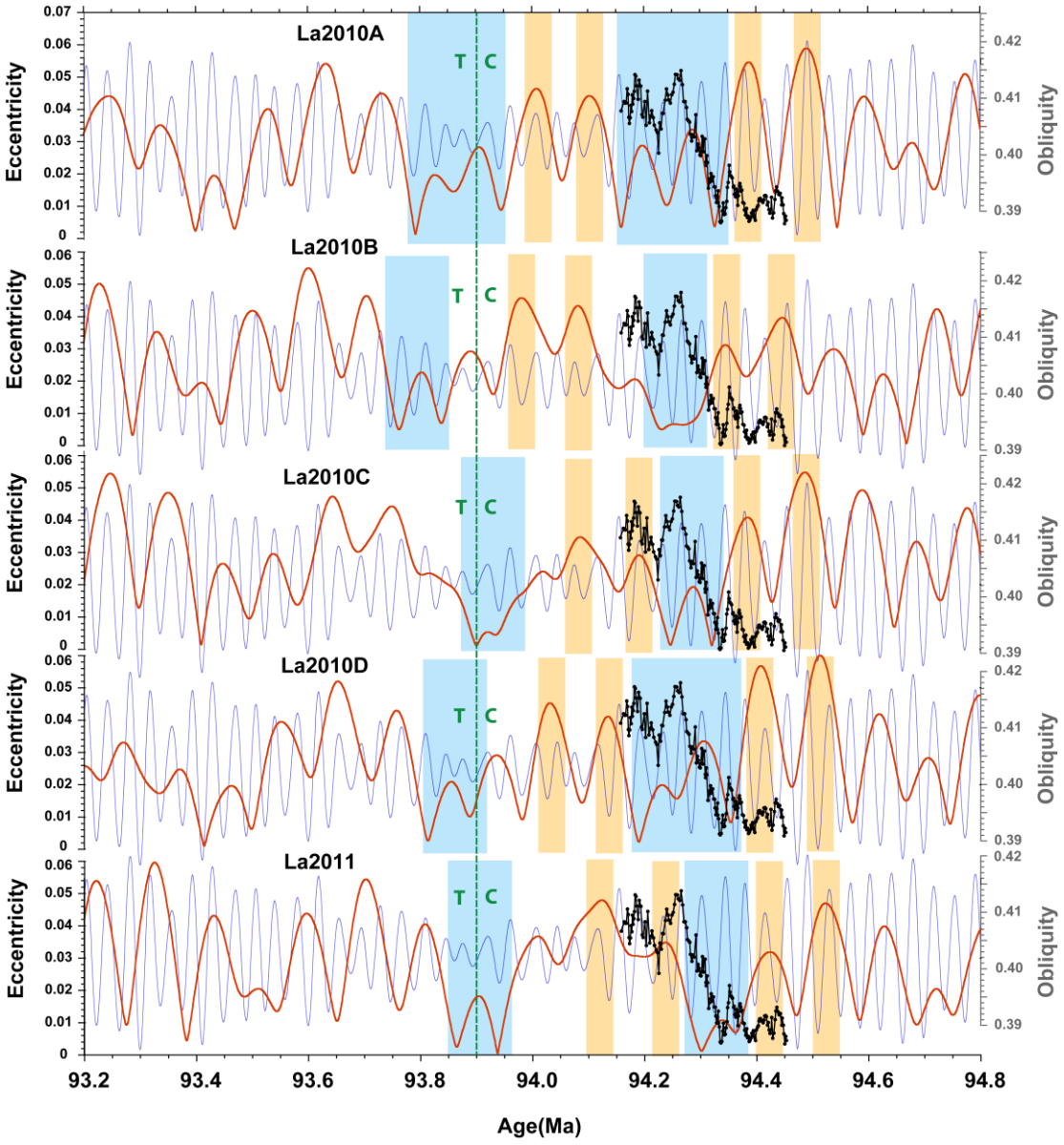

Figure 3.11: Orbital solutions across OAE2 onset. Orange bands indicate periods of "warm" orbits at 100 kyr eccentricity maxima, blue bands indicate extended periods of "cool" orbits at 400 kyr eccentricity minima. Even taking into account the relatively wide range of error from alternative orbital solutions, the onset of the positive carbon isotope excursion falls within an extended period of low eccentricity following a ~2 Myr interval of high amplitude 100 kyr eccentricity variability.

content, TOC, lightness, density and gamma ray data. The same periodicity is also evident in the bulk carbonate $\delta^{13}C$ and, at lower amplitude, in the organic carbon $\delta^{13}C$.

These results suggest that a change from low to high eccentricity at the 400 kyr band, which would result in increased precessional forcing, occurred during the main increase in $\delta^{13}C$ that characterizes the onset of OAE2. A sudden change in orbital cadence from low to high eccentricity could have triggered carbon cycle feedbacks fostering increases in atmospheric pCO_2 in several ways: (1) In analogy to Paleogene "hyperthermal events", rapid warming at high latitudes, related to the onset of precessional insolation maxima, would lead to fast release of greenhouse gases at high latitudes, when Antarctica was largely ice-free (DeConto et al., 2012; Kirtland Turner, 2014), (2) High amplitude variability in obliquity additionally result in strong fluctuations in the thermal pole-to-equator gradient, with repercussions on the meridional atmospheric heat and moisture transport and Antarctic climate variability.

On a first view, the strong response of the sedimentary and carbon isotope records to orbital obliquity at low latitudes is puzzling. A previous explanation for obliquity-driven productivity changes along the NW African margin invoked the transfer of high latitude climate dynamics via fluctuations in the intensity of coastal/equatorial upwelling in combination with changes in the hydrographic properties of the upwelling intermediate water masses (Kuhnt et al., 1997; Kolonic et al., 2005). However, this model does not explain the strong climate response to obliquity forcing in a greenhouse world on a supra-regional scale. Changes in oceanic circulation during OAE 2 represent another likely mechanism for the propagation of a high latitude signal through latitudinal

expansion of a new dense intermediate water mass of high latitude origin (Meyers et al., 2012a). A recent study, based on data from temperate northern hemisphere sections proposed that the unusually strong response of the Cretaceous greenhouse climate system to short-term and long-term obliquity forcing was introduced by a transient storage of organic matter or methane in quasi-stable reservoirs including wetlands, soils, marginal zones of marine euxinic strata, and potentially permafrost that responded nonlinearly to obliquity-driven changes in high latitude insolation and/or meridional insolation gradients (Laurin et al., 2015).

An alternative explanation is that orbital obliquity is the primary control on equatorial annual average insolation, which in the modern world has significant impact on West and East Pacific annual average SST and hydroclimate (Timmermann et al., 2007; Clement and Peterson, 2008). The annual mean insolation at the equator fluctuates at the obliquity band by ~3 W/m^2, which translates in numerical models (ECHO-G model, Timmermann et al., 2007) under modern boundary conditions into obliquity-driven SST changes in the tropical East and West Pacific Ocean that are in the range of 0.7°C. The impact of obliquity-controlled changes in tropical SST on convective and monsoonal precipitation was probably even stronger in the middle Cretaceous water world, which would have had substantial repercussion on tropical weathering and nutrient cycles.

3.5. Conclusions

The onset of OAE2, which corresponds to a two-stepped increase in $\delta^{13}C_{carbonate}$ and $\delta^{13}C_{org}$ spanning ~100 kyr, is preceded by negative carbon isotope excursions in both $\delta^{13}C_{carbonate}$ and $\delta^{13}C_{org}$ most likely resulting from massive injections of isotopically depleted carbon. During the main $\delta^{13}C$ increase and onset of intense oxygen-depleted conditions, bulk carbonate oxygen and carbon isotopes, terrigenous input, carbonate and organic matter exhibit a strong response to obliquity forcing. We interpret the top of the carbonate-rich interval, which is virtually devoid of any terrigenous input and characterized by a small plateau in the $\delta^{13}C_{org}$ curve and a distinct short-lived positive $\delta^{13}C_{carbonate}$ excursion, as the transgressive surface of the latest Cenomanian transgressive cycle.

A three-stepped transient climate cooling ("Plenus Cold Event") with intermittent brief warming/anoxia episodes occurred in the latest stage of the main $\delta^{13}C$ increase, reminiscent of the succession of events during OAE-1a (Kuhnt et al., 2011). We speculate that these cooling events reflect ephemeral Antarctic glaciations, triggered by biological drawdown of atmospheric CO_2 and changes in high latitude radiative forcing at periods of low orbital obliquity and eccentricity. Two major extinction events of thermocline dwelling keeled planktonic foraminifers, *Rotalipora greenhornensis* and *Rotalipora cushmani,* within the "Plenus Cold Event" appear to be closely linked to obliquity-paced periodic expansions and intensifications of the oxygen minimum zone. Both extinction events were probably associated with development of photic zone anoxia and ocean acidification affecting the habitat space of these species within the upper thermocline.

3.6. Acknowledgements

This research was funded by the German Research Council (DFG) in the framework of SFB 754, TP A7. RWE Dea AG in cooperation with the Office National des Hydrocarbures et des Mines, Morocco, enabled drilling SN°4 in the framework of the Atlantic Margin Integrated Basin Analysis Project. We thank Nils Andersen (Leibniz Laboratory for Radiometric Dating and Stable Isotope Research, Kiel) and Michael Joachimski (GeoZentrum Nordbayern, Friedrich-Alexander Universität Erlangen-Nürnberg) for stable isotope measurements, Dieter Garbe-Schönberg and Samuel Müller (Institute of Geosciences, Kiel) for advice with X-ray fluorescence scanning and Bettina Domeyer (GEOMAR) for technical help with the CHN Analyzer. We gratefully acknowledge constructive reviews from Phil Meyers and an anonymous referee. Data will be archived at PANGAEA, data publisher for Earth and Environmental Science, doi:10.1594/PANGAEA.

3.7. Supplementary Material

for

Unravelling the onset of Cretaceous Oceanic Anoxic Event 2 in an extended sediment archive from the Tarfaya-Laayoune Basin, Morocco

Wolfgang Kuhnt[1], Ann E. Holbourn[1], Sebastian Beil[1], Mohamed Aquit[1,2], Tim Krawczyk[1], Sascha Flögel[3], El Hassane Chellai[4] and Haddou Jabour[5]

[1]Institute of Geosciences, Christian-Albrechts-University, Ludewig-Meyn-Str.10-14, D-24118 Kiel, Germany
[2]OCP S.A., Direction de Recherche et Développement, Recherche Géologique, 46300 Youssoufia, Morocco
[3]GEOMAR Helmholtz-Zentrum für Ozeanforschung Kiel, Ozeanzirkulation und Klimadynamik, Paläo-Ozeanographie, Wischhofstr. 1-3, D-24148 Kiel, Germany
[4]Department of Geology, Faculty of Sciences Semlalia, Cadi Ayyad University, Marrakech, Morocco
[5]ONHYM, Office National des Hydrocarbures et des Mines, 5, Avenue Moulay Hassan, BP99 Rabat 10000, Morocco

Content of this file:

Supplementary Figures S1 – S3

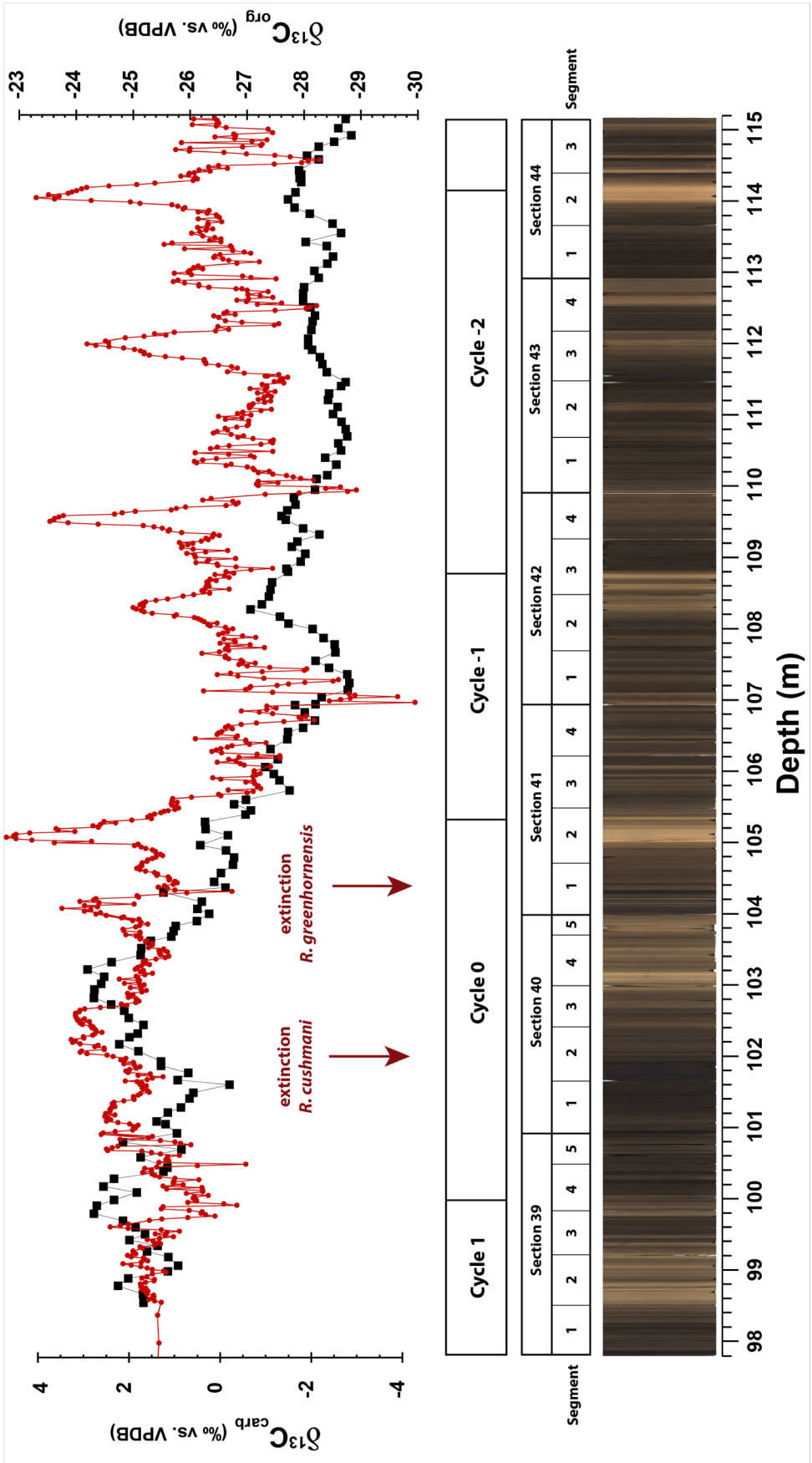

Supplementary Figure S3.1: Nomenclature of sections and segments across the onset of OAE2 in Core SN°4. Cycles -2, -1, 0 and +1 refer to the cycle scheme in Kuhnt et al. (1997, 2005).

Supplementary Figure S3.2A: Line scan images of section 39, segments 1-5 (97.80 – 100.92 m) in Core SN°4.

Supplementary Figure S3.2B: Line scan images of section 40, segments 1-5 (100.92 – 103.97 m) in Core SN°4.

Supplementary Figure S3.2C: Line scan images of section 41, segments 1-4 (103.97 m – 106.94 m) in Core SN°4.

Supplementary Figure S3.2D: Line scan images of section 42, segments 1-4 (106.94 – 109.90 m) in Core SN°4.

Supplementary Figure S3.2E: Line scan images of Section 43, segments 1-4 (109.90 m -112.92 m) in Core SN°4.

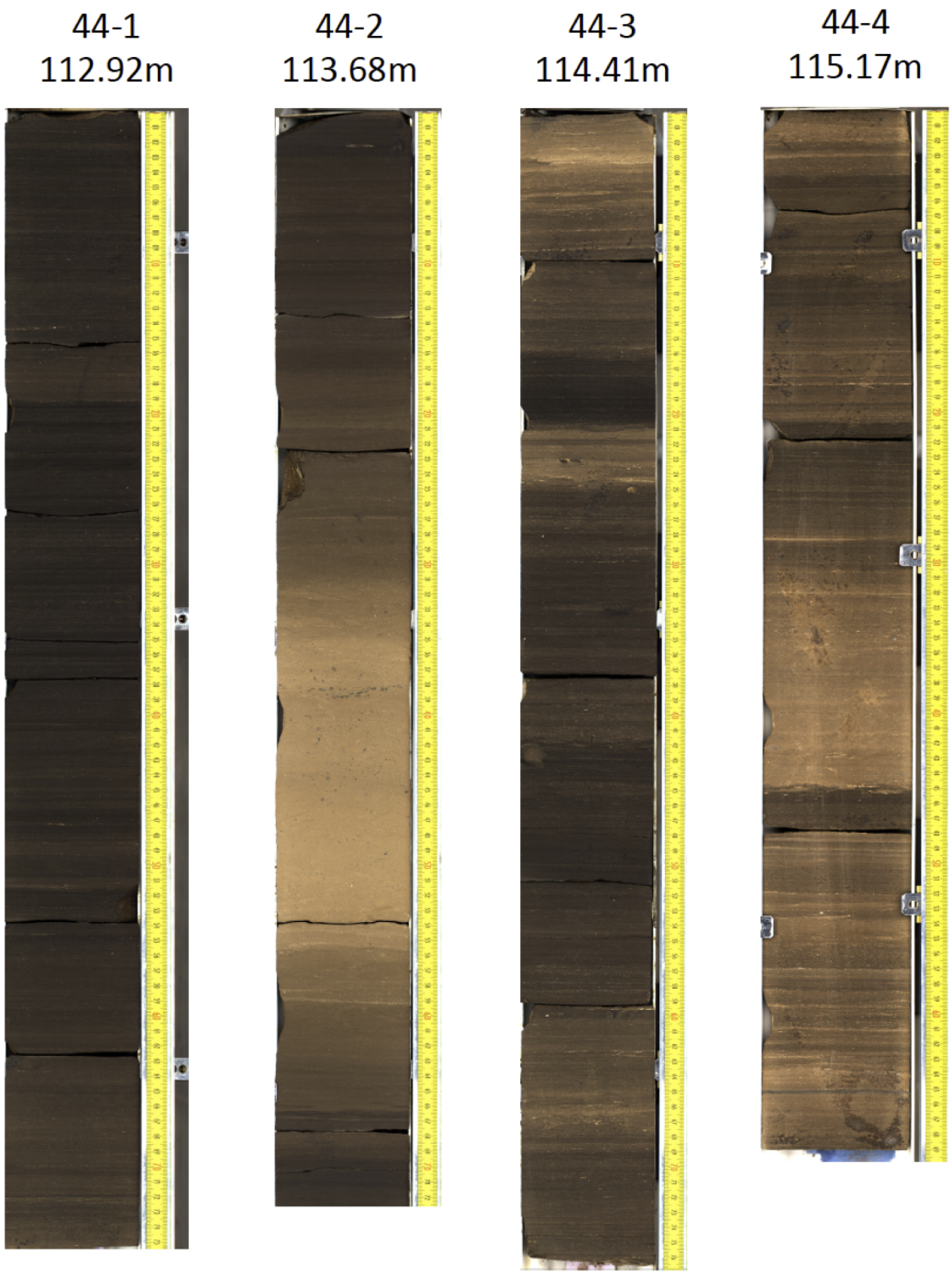

Supplementary Figure S3.2F: Line scan images of Section 44, segments 1-4 (112.92 – 115.90 m) in Core SN°4.

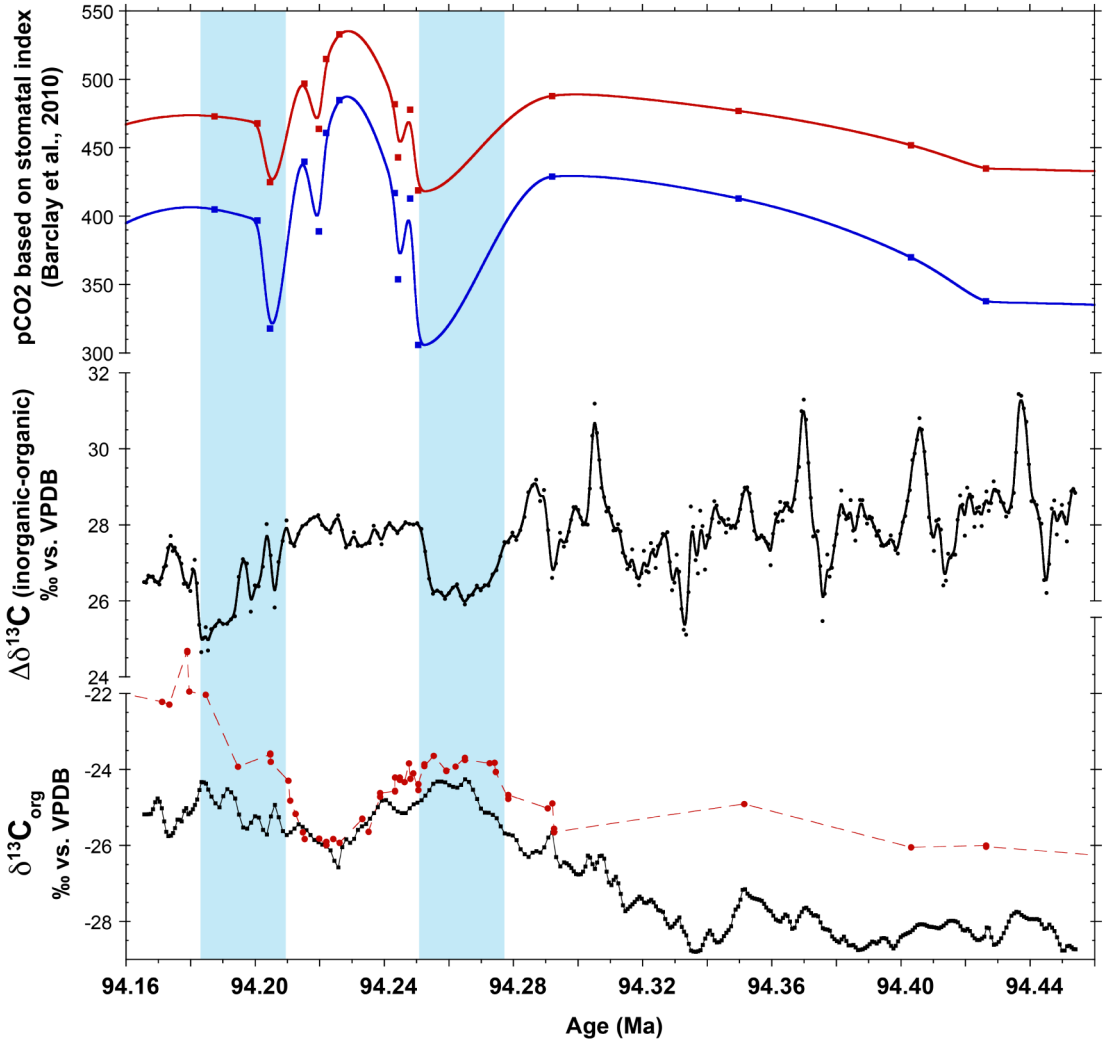

Supplementary Figure S3.3: Comparison of atmospheric pCO_2 reconstruction, based on transfer functions of stomatal indices to pCO_2 for *Hyphodapnis zenkeri* and *Laurus nobilis* from Barclay et al. (2010), to $\Delta\delta^{13}C_{org}$ in Core SN°4. Correlation of the two records is based on mapping the Western Interior $\delta^{13}C_{org}$ record in Barclay et al. (2010) to the $\delta^{13}C_{org}$ record in Core SN°4. The two pCO_2 drawdowns indicated by the stomatal index during the initial part of the OAE2 $\delta^{13}C_{org}$ excursion match the two extended drawdowns derived from $\Delta\delta^{13}C_{org}$ in Core SN°4, which are associated with thermocline dwelling planktonic foraminiferal extinctions (blue shading).

Chapter 4:

Phosphorus concentrations and speciations across the mid-Cenomanian Event and Oceanic Anoxic Event 2 in the Tarfaya Basin (SW Morocco)

Sebastian Beil, Wolfgang Kuhnt, Ann E. Holbourn, Julian Oxmann, Florian Scholz, Mohamed Aquit

Manuscript in preparation

Phosphorus concentrations and speciations across the mid-Cenomanian Event and Oceanic Anoxic Event 2 in the Tarfaya Basin (SW Morocco)

Sebastian Beil[1], Wolfgang Kuhnt[1], Ann E. Holbourn[1], Julian Oxmann[2], Florian Scholz[2], Mohamed Aquit[1,3]

[1]Institute of Geosciences, Christian-Albrechts-University, Ludewig-Meyn-Str.10-14, D-24118 Kiel, Germany

[2]GEOMAR Helmholtz-Zentrum für Ozeanforschung Kiel, Ozeanzirkulation und Klimadynamik, Paläo-Ozeanographie, Wischhofstr. 1-3, D-24148 Kiel, Germany

[3]OCP S.A., Direction de Recherche et Développement, Recherche Géologique, 46300 Youssoufia, Morocco

Abstract

Core SN°4 from the Tarfaya Basin (SW Morocco) exhibits maxima in concentrations of total phosphorus (P_{total}), calcium- (CaP) and aluminum-iron-bound (AlFeP) phosphorus and in the CaP/AlFeP ratio at the onsets of the mid-Cenomanian Event (MCE; 220 m downcore) and the Oceanic Anoxic Event 2 (OAE2; 104 m downcore). These maxima correspond to condensed intervals associated with sea level high stands at the beginning of these events. The ratios of C_{org}/P_{react} and N_{total}/P_{react} increase by a factor of 3 for the MCE and by a factor of 5 for OAE2, in parallel with the global positive carbon isotope excursions. These increases reflect changes in bottom waters towards permanent anoxic or euxinic conditions, which permitted the release of phosphorus from the sediments. C_{org}/P_{react} and N_{total}/P_{react} values below the Redfield ratio (C:N:P of 106:16:1) for the entire Cenomanian except the MCE and OAE2 imply P enrichment by release of the primary organic matter and iron-manganese oxyhydroxide bound phosphorus and resedimentation as authigenic calcium fluor apatite and in iron-manganese oxide surfaces during diagenesis (sink switching) and exclude phosphorus release from the sediments fertilizing primary productivity. Our results suggest that phosphorus was probably enhancing primary productivity during OAE2, as the most prominent maximum in C_{org}/P_{react} and N_{total}/P_{react}, indicative of phosphorus release from the sediments, occurs just before the peak phase of organic matter accumulation during OAE2.

4.1. Introduction

Primary production in the modern marine environment is limited primarily by the availability of iron and phosphorus. Phosphorus is considered to be the primary limiting nutrient on longer (e.g., geological) timescales (Holland, 1978; Broecker and Peng, 1982; Codispoti, 1989; Smith, 1984). The discussion about the impact of phosphorus limitation on global marine primary production and the global carbon cycle has largely focused on uncertainties of the residence time of dissolved phosphorus in the oceans (Ruttenberg, 2003). The wide range of residence time estimates between 10-17 (Ruttenberg, 2003) and 80 kyr (Broecker and Peng, 1982) is caused by uncertainties in burial rates and burial efficiency within the different phosphorus sinks. One of the sinks that moved into the focus of attention during the last decades (Ruttenberg, 2003) is the vast extent of continental margins and shallow seas.

Another open question remains to which extent and under which conditions phosphorus can be remobilized and act as a fertilizer to increase marine productivity during certain intervals. High productivity periods during the Mesozoic (oceanic anoxic events, defined by the global occurrence of organic carbon rich sediments and positive $\delta^{13}C$ shifts) remain, in particular, enigmatic. The largest of these global carbon isotope events is the Oceanic Anoxic Event 2 (OAE2) at the Cenomanian/Turonian boundary. Different explanations have been proposed to account for the enhanced preservation of organic matter in the sediments (e.g., Arthur et al., 1988; Jenkyns, 2010) and for the factors triggering and maintaining global anoxia and periods of enhanced primary productivity during OAEs. These include fertilization by nutrient input in the ocean system in association with the activity of large igneous provinces (LIPs) (e.g., Schlanger et

al., 1981; Larson, 1991; Trabucho Alexandre et al., 2010), sea level controlled remobilization of nutrients from flooded low altitude land areas associated with major marine transgressions (e.g., Mort et al., 2007, 2008), or release of phosphorus as a main limiting nutrient from deposited organic carbon into the water column under anoxic bottom water conditions (Ingall and Jahnke, 1994; Slomp and Van Cappellen, 2007).

There are conflicting views on the influence of expanding oxygen minimum zones or ocean anoxia on the phosphorus cycle and, in particular, whether anoxic sediments serve as a phosphorus source or sink. It has been argued that oxygen depleted bottom waters favour phosphorus release from the sediment to the water column (Ingall and Jahnke, 1994) and could stimulate primary production in surface waters (Wallmann, 2003). This in turn results in an increased organic carbon export flux, leading to higher oxygen demand, expansion and intensification of oxygen minima and a positive feedback with benthic phosphorus release (Slomp and Van Cappellen, 2007; Wallmann, 2010). In contrast, it has been suggested that intensified phosphorus burial occurs under anoxic conditions in shallow water environments, based on observations of calcium fluorapatite (CFA) precipitation in present-day shallow water oxygen-depleted upwelling areas (Schulz and Schulz, 2005; Arning et al., 2009a, b; Goldhammer et al., 2010; Ingall, 2010; Cosmidis et al., 2013). On a longterm global scale, the formation of CFA is approximately in balance with enhanced phosphorus release from anoxic sediments, implying that the dissolved oceanic phosphorus inventory is largely unaffected by regional changes of oxygen concentrations (Delaney, 1998; Anderson et al., 2001; Roth et al., 2014). However this equilibrium may be significantly disturbed during periods with

expanded and intensified oxygen minimum zones and development of intense deep-water anoxia, as in the Mediterranean Sea during intervals of sapropel formation (Slomp et al., 2004) and in the global ocean during Cretaceous OAEs.

Here, we focus on reconstructing phosphorus dynamics and changes of phosphorus speciation over the extended Cenomanian to lower Turonian interval, which encompasses the mid-Cenomanian carbon isotope event (MCE) and OAE2. The main question motivating this study is to resolve changes in phosphorus concentrations and speciations corresponding to periods of expanded and intensified oxygen minimum zones (OMZs) and high organic carbon burial in order to test the hypothesis of redox controlled phosphorus release as nutrient source initiating and/or enhancing carbon burial during OAEs. Combined evidence from modern OMZs points to a phosphorus release from the sediment into the water column and unusually high $C_{org}/P_{reactive}$ ratios in the center of OMZs, while the upper and lower margins of OMZs act as phosphorus sinks. During Cretaceous OAEs the central areas of OMZs dramatically expanded with respect to the marginal areas, in fact during the peak of OAE2 the lower margin of the OMZ virtually disappeared and the part of the OMZ, which acts as phosphorus source significantly increased (e.g., Schlanger et al., 1987; Erbacher and Thurow, 1997).

Core SN°4 situated in an outer shelf paleo-setting in the Tarfaya Basin (NW African Continental Margin, SW Morocco) permited the reconstruction of regional background conditions preceding these events and to distinguish between short-term fluctuations and longterm trends of the variability of different phosphorus species. The paleogeographic position of Core SN°4 in the

distal part of a shelf basin permits the reconstruction of phosphorus dynamics in a continental margin setting, which is typically the locus of high phosphorus burial (Ruttenberg, 1993).

4.2. Geochemical background

Shallow marine environments are considered as the focus of phosphorus burial (Ruttenberg, 1993). Most sedimentary rocks and sea floor sediments are characterized by low concentrations of phosphorus of less than 0.13% (Riggs, 1979). Different species of phosphorus (P_{detr}, P_{auth}, P_{Fe}, P_{org}) can be discriminated in sediments of shallow marine systems. Detrital phosphorus (P_{detr}) is passively transported as fluviatile sediment load and is regarded as not bio-available due to its inert nature. Phosphorus adhesively bound to iron- or aluminum crusts (AlFeP) constitutes another possible sink for phosphorus in marine sediments. Early diagenetic conversion of FeP via biochemical process can convert this pool to authigenic phosphorus (CaP) (Jarvis et al., 1994). Authigenic phosphorus (P_{auth}) mainly consists of authigenic apatite (CFA) precipitated during early diagenesis and is typically enriched in organic rich sediments of coastal upwelling systems (Ruttenberg, 1993). The two main sources for CFA are microbial remineralization of organic material or direct or indirect (e.g., by changes of the redox environment) remobilization of phosphorus bound to iron-oxyhydroxides (Jarvis et al., 1994) during sink switching (Ruttenberg and Berner, 1993; Ruttenberg, 1993; Slomp et al., 1996a, b). CFA constitutes the main component extracted as CaP with the SEDEX method (Ruttenberg, 1992). In contrast to organic phosphorus or phosphorus bound to Al-/Fe-oxyhydroxides, CFA is a permanent sink for reactive phosphorus (Ruttenberg, 2003).

4.3. Material and Methods

4.3.1 Core Tarfaya SN°4

For this study, sample material covering the Cenomanian and early Turonian from Core SN°4 (N 27° 59' 46.4'', W 12° 32' 40.6'') drilled in the Tarfaya Basin (Fig. 4.1) was used. A detailed description (e.g., lithology, biostratigraphy, isotope sampling) was provided in Beil et al. (2018). Stable isotope records, carbonate, organic carbon and nitrogen data are from Kuhnt et al. (2017) and Beil et al. (2018). The distribution of major and trace elements and the phosphorus speciation were determined on new samples taken close to the published organic stable isotope samples. Samples cover the interval between 42.11 m (Section 18, Segment 3, 23-24 cm) and 305.77 m (Section 111, Segment 2, 29-31 cm). The core was sampled every ~2.4 m with increased resolution of ~1.2 m over the global isotope excursions OAE2 and MCE. The sampled material was surface cleaned with a metal free porcelain knife and ground down with a rotary mill with agate balls to prevent metallic contaminations. The powdered material was subdivided into aliquots for major and trace elements analysis and material for determination of phosphorus speciation. A further aliquot was used for carbonate and organic carbon measurements for samples not close to the already published organic isotope samples. Additional samples from high carbonate content intervals were prepared and measured to study the influence of low clay and organic content.

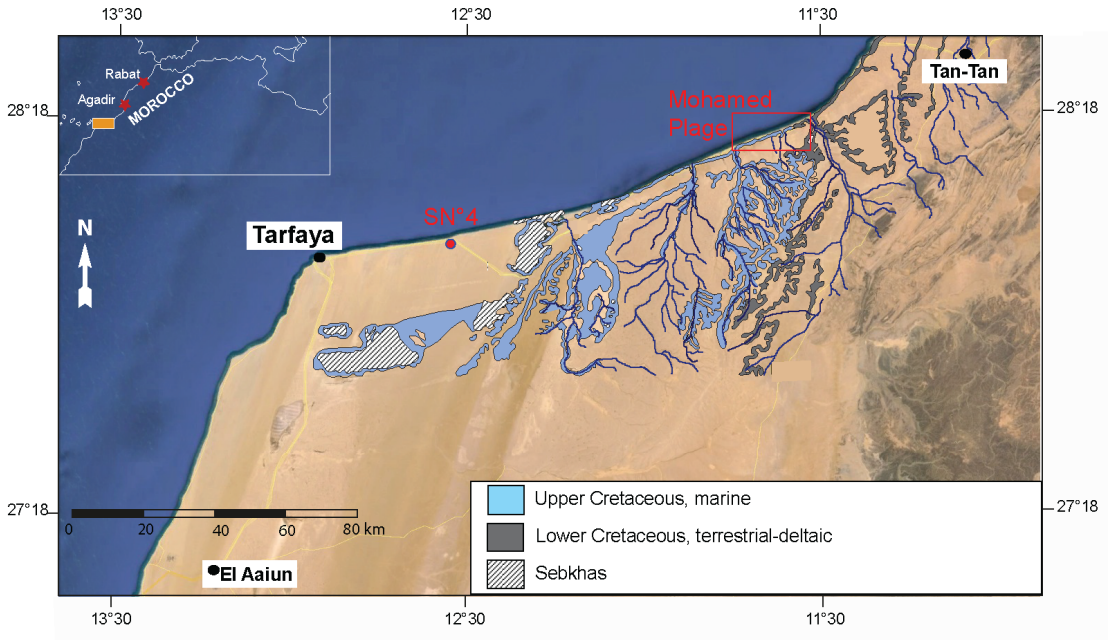

Figure 4.1: Modern location of drilling site SN°4 (modified from Aquit et al., 2016). Indicated in red are location of Core SN°4 and outcrop section Mohamed Plage.

4.3.2 Sampling for major and trace element analysis

Aliquots of 100 mg were weighed with a high precision scale into PTBE vessels. Each sample was treated with 2 cm^3 HF, 2 cm^3 HNO_3 and 3 cm^3 $HCLO_4$, sealed and heated for 8 hours at 185°C. The acid was subsequently smoked off at 190°C. The almost dry residue was dissolved again in 1 cm^3 HNO_3, smoked off and dissolved again in 5 cm^3 ultrapure water and 1 cm^3 HNO_3 to be heated again for 2 hours in sealed vessels. The solution was finally transferred to and diluted with 10 ml HNO_3 in volumetric flasks. The solutions were measured with a VARIAN 720-ES ICP-OES for major elements and an Agilent Technologies 7500 Series ICP-MS for trace elements at GEOMAR Helmholtz-Zentrum für Ozeanforschung, Kiel

4.3.3 Samples for determination of phosphorus speciation

Phosphorus speciation was determined on aliquots of samples for the measurements of major and trace elements. A modified SEDEX extraction method (Ruttenberg, 1992; Supplementary Material S4.1) was used to extract Ca-bound and Al/Fe-oxyhydroxide bound phosphorus. A high precision scale was used to weigh in 250 mg of sample material that was first washed three times with 3.75 ml KCl/EtOH. Al/Fe-bound phosphorus was extracted from the centrifuged residue with the addition of first 3.75 ml NaOH/Na_2SO_4 (incubated for 1h at 25°C), then 3.75 ml NaOH/Na_2SO_4 (incubated for 2h at 99°C) and finally 7 ml Na_2SO_4. Solutions were centrifuged and decanted after each of the three treatment steps and stored for measurement. The centrifuged residue was decarbonated for 8h with 3.75 ml H_2SO_4. The Ca-bound phosphorus fraction was extracted by adding further 3.75 ml H_2SO_4 (incubated for 2h at 99°C) and twice Na_2SO_4 (3.75 and 7 ml). Each of the three steps was followed by centrifugation and decanting of the solution. Supernatants of each step were again mixed and stored for measurements. A detailed schematic of the preparation is provided in Supplementary Material S4.1.

For the measurement of Ca-bound phosphorus an aliquot of 0.1 ml was diluted with 4.9 ml MilliQ. Concentrations of Fe-/Al-bound phosphorus were measured on 4.5 ml of sample solution equilibrated with the addition of 0.5 ml of sol7 (Supplementary Material S4.2) to pH of ~1. Concentration measurements of Al/Fe- and Ca-bound phosphorus were calibrated with the PO_4-Merck Standard (1000 mg PO_4 / l) diluted to specific concentrations. The ammonium molybdate solution (0.1 ml; Supplementary Material S4.3) was added 30 min before

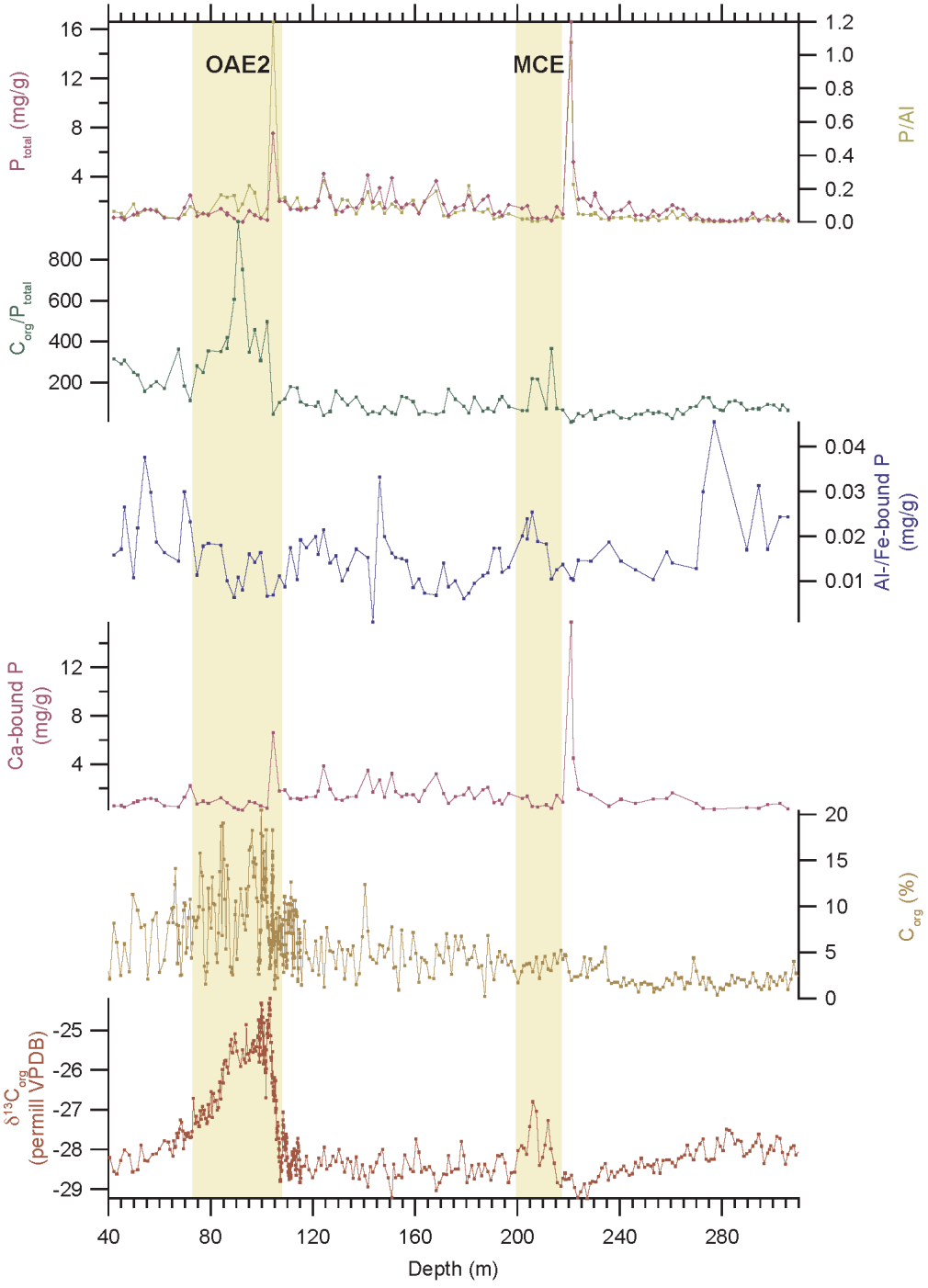

Figure 4.2: Phosphorus content and speciation in Core SN°4. **A.** Total phosphorus content in mg/g and P_{total}/Al. **B.** C_{org}/P_{total}. **C.** Phosphorus bound to Al-/Fe-oxyhydroxides in mg/g. **D.** Calcium bound phosphorus in mg/g. **E.** Organic matter content in %. **F.** $\delta^{13}C_{org}$ in permill VPDB.

measurements. For samples close to the photometric saturation level a new aliquot was diluted to lower concentration within the measurement range.

A detailed list with used chemicals and respective concentrations is available as Supplementary Material S4.2.

4.4. Results

4.4.1 Trends in major elements

Total phosphorus (P_{total}) concentrations (Fig. 4.2) are overall below 5 mg/g except during two periods of enrichment peaking at 220.19 m with 16.61 mg/g and at 104.4 m with 7.53 mg/g. Corresponding peaks in P_{total}/Al (Fig. 4.2) give a weight ratio of 1.07 at 220.19 m and 1.20 at 104.4 m. Concentrations and variability of P_{total} are low in the lowermost (305 – 267 m) and uppermost (67.51 – 42,11 m) parts of the studied interval with means of 0.54 mg/g (StDev = 0.19 mg/g) and 0.86 mg/g (StDev = 0.3 mg/g), respectively.

The molar C_{org}/P_{total} ratio (Fig. 4.2) shows low values (mean = 62.2) and low variability (StDev = 27.6) between 305.77 and 215.39 m. Low values (mean = 99.7) with increased variability (StDev = 58.4) characterize the adjacent interval between 215.39 and 104.4 m. A minor enrichment is recorded during the MCE between 213.36 and 205.75 m (median = 218.1). Higher average values (mean = 416) and an increased variability (StDev = 222.1) are recorded over OAE2 (104.4 – 72.09 m). Average values remain high (mean = 245,7) but variability is reduced (StDev = 66.8) for the uppermost interval until 42.11 m.

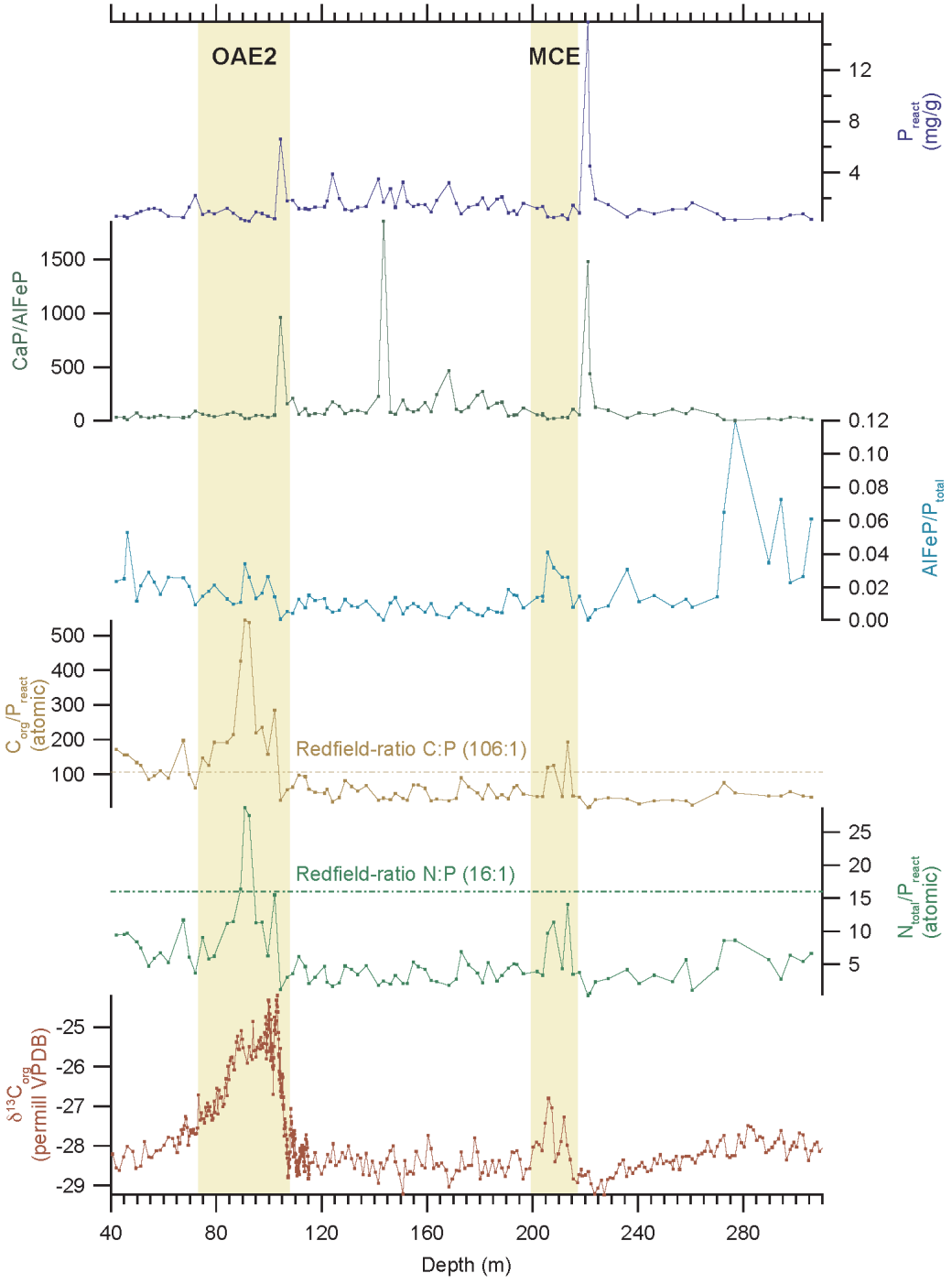

Figure 4.3: Ratios of extracted phosphorus species in Core SN°4. A. Al-/Fe- and Ca-bound phosphorus in mg/g. B. Ratio of Ca- and Al-/Fe-bound phosphorus. C. Ratio of Al-Fe-bound phosphorus and total phosphorus content. D. Atomic ratio of organic matter content C_{org} and Al-/Fe- and Ca-bound phosphorus with corresponding Redfield-ratio of 106 (Redfield, 1958;

Redfield et al., 1963) indicated by dashed line. E. Atomic ratio of total nitrogen N_{total} and Al-/Fe- and Ca-bound phosphorus with corresponding Redfield-ratio of 106 (Redfield, 1958; Redfield et al., 1963) indicated by dashed line. F. $\delta^{13}C_{org}$.

4.4.2 Phosphorus speciation

Phosphorus concentrations calculated by summing up Al/Fe- and Ca-bound phosphorus (P_{react}; Fig. 4.3) are always lower than total phosphor (P_{total}; Fig. 4.2) measured with ICP-OES, confirming the reliability of the fraction extraction method. Differences are caused by not extractable phosphorus bound in insoluble minerals or adhesively bound phosphorus extracted and discarded during the first step with KCl/EtOH (Supplementary Material S4.1).

Concentrations of phosphorus bound to aluminum- or iron-oxyhydroxides (AlFe P; Fig. 4.3) are low (median = 0.015 mg/g). Increased concentrations (mean = 0.027 mg/g) are determined for the lowermost interval between 305 and 272.58 m, followed by an interval with lower average concentration (mean = 0.014 mg/g) and lower variability (StDev = 0.005 mg/g) until 72.09 m. The uppermost interval is again characterized by increased variability (StDev = 0.008 mg/g).

Calcium-bound phosphorus (CaP; Fig. 4.2) is the dominant species in the studied interval of Core SN°4. Concentrations are below 4 mg/g except for two periods of enrichment peaking at 220.19 and 104.4 m with 15.76 and 6.62 mg/g, respectively. Both maxima coincide with maximum enrichment of total phosphorus.

The ratio of Ca- to Al/Fe-bound phosphorus (CaP/AlFeP; Fig. 4.3) is dominated by large concentration differences between both species in the order

of magnitudes. Three prominent maxima are determined peaking at 220.19, 143.51 and 104.4 m. The lowermost (305 – 228.68 m) and uppermost (102.16 m – 42.11 m) intervals show a decreased variability of 37.5 and 19.4. All these characteristics are reflected in the sum of Ca- and Al/Fe-bound phosphorus with the exception of the peak at 143.51 m that is caused in case of the CaP/AlFeP-ratio by a drop in Ca-bound phosphorus.

The atomic ratio of organic carbon to $P_{reactive}$ (defined as the sum of loosely sorbed, organic, authigenic and iron bound phosphorus) was interpreted by Anderson et al. (2001) as a proxy for marine paleoproductivity. Due to sink switching (redox- or biochemical-mediated transfer between different phosphorus pools) between the different phosphorus species especially during early diagenesis the authors assumed that most phosphorus in the different pools is originally derived from the remineralization of organic material and could therefore be seen equivalent to P_{org}. Here, P_{react} is calculated by summing up the two SEDEX-derived P-pools CaP (seen as equivalent to P_{auth}) and AlFeP. Both loosely absorbed and organic P were not measured. It is assumed that the concept of Andersen et al. (2001) is applicable, as both extracted P-pools (CaP and AlFeP) contain the majority of P_{total} (mean = 89%; Supplementary Figure S4.4).

The atomic ratios of C_{org} and N_{total} against P_{react} were calculated (Fig. 4.3). Both ratios show very similar trends except for the lower part between 305 and 258.35 m that is characterized in N/P_{react} by increased values (5.7) and in C_{org}/P_{react} by low values and low variability (median = 37.6, StDev = 16.9), albeit in an interval with low resolution. Afterwards both ratios show similar characteristics of low values (median of C_{org}/P_{react} 37.6 and of N/P_{react} 3.4) and

low variability (StDev of C_{org}/P_{react} 20.9 and of N/P_{react} 1.7) until 104.4 m punctuated by short-lived maxima during the MCE (median of C_{org}/P_{react} 122.6 and of N_{total}/P_{react} 10.5). OAE2 is again characterized by markedly increased ratios (maxima of C_{org}/P_{react} 544.8 and of N_{total}/P_{react} 28.7). The uppermost part is again characterized by increased values (median of C_{org}/P_{react} 117.6 and of N_{total}/P_{react} 7.1).

The ratio of SEDEX-extracted AlFeP to P_{total} (Fig. 4.3) shows increased values (mean = 0.058) in the lower part between 305 and 272.58 m followed by low ratios (mean = 0.014) until the top of the sampled interval of Core SN°4.

4.4.3 Temporal concentration changes of different P-species in relation to anoxia

Two maxima in P_{total} are recorded in the sediments of Core SN°4 during the Cenomanian, coinciding with two maxima in the P_{total}/Al-ratio (Fig. 4.2). The more prominent of these phosphorus enrichments peaking at 220.19 m precedes the onset of the MCE by ca. 3.04 m or 82 kyr with the sedimentation rate of 3.7 cm/kyr reconstructed by Beil et al. (2018). The second maximum falls within the increase towards the first $\delta^{13}C_{org}$ maximum of OAE2. The depth difference of 1.18 m to the onset of and 2.84 m to the first $\delta^{13}C_{org}$ maximum of OAE2 results in a delay of 15.5 kyr to the onset and a lead of 36 kyr to the first peak using the reconstructed sedimentation rate of 7.7 cm/kyr for this time interval from Beil et al. (2018).

The ratio of Ca-bound to Al/Fe-bound phosphorus (Fig. 4.3) is characterized by three prominent peaks at 220.19, 143.51 and 104.40 m. Two of these peaks at 220.19 and 104.40 m are also characterized by high P_{total}

concentrations and maxima in the P_{total}/Al ratio (Fig. 4.2). The first peak at 220.19 m precedes the onset of the MCE, and the second peak at 104.4 m corresponds to the initial onset of the $\delta^{13}C_{org}$ excursion of OAE2. Both peaks of CaP/AlFeP and P_{total} coincide with minima in the C_{org}/P_{total}-ratio, suggesting an inorganic source of the deposited phosphorus or enhanced recycling of organic carbon and reprecipitation of the organic-bound phosphorus as Ca-bound phosphorus.

The increase in the atomic C_{org}/P_{total}-ratio (Fig. 4.2) during OAE2 postdates the increase in the atomic C_{org}/N_{total}-ratio interpreted by Beil et al. (2018) as enhanced cycling of nitrogen rich organic matter within a dysoxic or anoxic water column. The increase in C_{org}/P_{total} starts immediately above the prominent peak in Ca-/AlFe-bound and total phosphorus and coincides with the first $\delta^{13}C_{org}$ maximum of OAE2. The highest C_{org}/P_{total} ratio is determined at 90.78 m within the plateau phase of OAE2. This peak coincides with minima in P_{total} and P_{total}/Al (Fig. 4.2) implying secondary remobilization either synsedimentary due to preferred cycling of phosphorus in the water column and/or at the sediment surface or postsedimentary due to cycling within the sediments. This decrease in P_{total}-content is paralleled by a decrease in C_{org} (Fig. 4.2), suggesting enhanced cycling of phosphorus as well as organic matter.

The atomic ratios of C_{org}/P_{react} and N_{total}/P_{react} are shown in Fig. 4.3 and compared to the respective Redfield ratio (Redfield, 1958; Redfield et al., 1963) representative of the mean composition of marine phytoplankton assumed to represent the main source of organic matter. Both ratios are always lower then predicted by the Redfield ratio (C:N:P of 106:16:1), except for two intervals. The first falls within the MCE when C_{org}/P_{react} is equal to or higher then 106:1 and

N_{total}/P_{react} is close to the predicted ratio of 16:1. The second interval starts during OAE2 above the prominent peak in P_{total}, synchronous with the TS of Ce5. Both ratios surpass predicted values at the first maximum in $\delta^{13}C_{org}$, decrease slightly during the interval influenced by the Plenus Cold Event (Kuhnt et al., 2017) and show a large increase during the Plateau Phase (Kuhnt et al., 2005) following the second peak of OAE2. The remaining part of the sampled interval is characterized by increased values above the background level that is characteristic for the lower part of Core SN°4 until the onset of OAE2.

4.5. Discussion

The overall low and nearly constant concentrations of Al/Fe-bound phosphorus (Fig. 2) imply either constant anoxic or euxinic conditions causing desorption of phosphorus bound to aluminum- and iron-oxyhydroxides or early diagenetic conversion of Al/Fe-bound phosphorus into authigenic phosphorus-carbonates. Beil et al. (2018) suggested an onset of episodic dysoxic to anoxic conditions above 273 m in Core SN°4, and consistently oxygen depleted to anoxic environmental conditions above 185 m, based on the XRF-core scanner derived ratio Log(Mn/S) (their Fig. 5A). Increased concentrations of Al/Fe-bound phosphorus and a decreased $AlFeP/P_{total}$ ratio (Fig. 4.3) below 270 m are in line with these sedimentological observations. However, low variability in Al/Fe-bound phosphorus and $AlFeP/P_{total}$ ratio between 273 and 185 m, albeit in an interval of low sampling resolution, do not support the episodic spread of anoxia in the transition interval between 273 and 185 m described by Beil et al. (2018). Concentrations of Ca-bound phosphorus (Fig. 4.2) decrease slightly above 84 m.

However, low concentrations of Al/Fe-bound phosphorus and a stable ratio of Ca- to Al/Fe-bound phosphorus rather suggest a secondary, syn- or postdepositional conversion of Al/Fe-bound phosphorus into Ca-bound phosphorus.

It was suggested, that flooding of low altitude land areas and shallow seas associated with the late Cenomanian sea level rise (Haq, 2014) would result in high phosphorus concentrations and fertilize adjacent seas directly and/or by redox-controlled release of nutrients by impinging of the OMZ onto large areas of shallow shelf seas (Mort et al., 2007).

Rising sea level culminating in transgressive surfaces (TS) and condensed section would offer an explanation for the enrichment in P_{total} and CaP (Fig. 4.2). The P_{total} enrichment at the onset of OAE2 is within sampling resolution identical to the TS of Ce5 at 205 m (Beil et al., 2018). The onset of maximum P_{total} preservation preceding the MCE at 220.19 m falls within sampling resolution within the TS of Ce2.1 between 222 and 223 m. As both enrichments are connected to sea level high stands, the most likely interpretation is condensed horizons deposited during periods of very low sediment supply. The absence of P_{total} enrichment at the TSs of Ce4 between 139 and 140 m and Ce3 at 207.3 m in SN°4 of Beil et al. (2018) requires alternative explanations. One possibility is limitations by the sampling resolution for phosphorus analysis. Alternatively the extent of sediment starvation during these sea level high stands or the supply of phosphorus-rich (e.g., organic) material was not sufficient to produce phosphorus anomalies in the sedimentary record. The sequence boundary of Ce3 during the MCE is globally significant, recording a large eustatic sea level drop

during the mid-Cenomanian (Stoll and Schrag, 2000; Miller et al., 2003, 2005; Gale et al. 2002, 2007; Haq, 2014). The regional expression in the Tarfaya Basin of this sea level cycle is of lesser significance in comparison to Ce2.1 (Gebhardt et al., 2004; Kuhnt et al., 2009; Beil et al., 2018).

Overall low background values (below the Redfield ratio) of C_{org}/P_{react} (Fig. 4.3) suggest intensive organic carbon cycling in combination with sink switching and phosphorus shuttling in the sediments during early diagenesis, which enriched phosphorus in comparison to organic carbon. Prominent exceptions are the MCE and OAE2, when C_{org}/P_{react} increased markedly. C_{org}/P_{react} and N_{total}/P_{react} close to or above the Redfield ratio are only measured during the MCE and OAE2, suggesting preservation of the initial atomic ratio of organic material produced by primary production enhanced by a possible shift in the phytoplankton community (Geider and La Roche, 2002) or even significant depletion in P_{react}. As C_{org} concentrations are not dramatically increased during periods with enhanced P_{react} ratios a secondary enrichment of organic carbon can be excluded. We favour as a likely explanation regional changes of redox-conditions in the lower water column towards anoxic or euxinic conditions that would inhibit fixation of remobilized phosphorus in authigenic CaP, permitting the leakage of phosphorus into the water column and therefore preserving the initial or even increasing C:P and N:P ratios. Strongest intensification of anoxia / euxinia during the plateau phase of OAE2 is assumed to cause strong increases of C_{org}/P_{react} and N_{total}/P_{react} by reducing diagenetical phosphorus cycling and permitting phosphorus leakage from the sediment column that was controlling phosphorus dynamics especially between 273 m and approx. 107 m. This trend

to more euxinic conditions was also found by Kolonic et al. (2005) based on high accumulation rates of redox-sensitive elements during their carbon isotope stage B and C (corresponding to the plateau and recovery phase of OAE2 of Kuhnt et al., 2005).

The pattern of phosphorus variability reconstructed by Mort et al. (2008) for the proximal Mohamed Plage section differs in timing and amplitude. Caused by the hiatus in Mohamed Plage during the onset phase of OAE2 their record of C_{org}/P_{total} (Fig. 4.3) is characterized by a synchronous increase with $\delta^{13}C_{org}$. The record of SN°4 in contrast shows a time lag between the onset of OAE2 and phosphorus depletion of the sediments. Lowest phosphorus retention is recorded in both records during the plateau phase, albeit with larger amplitude in SN°4. This may reflect the direct effect of the impinging core zone of the OMZ in connection with the deeper paleo-environment of SN°4. The predominance of Ca-bound phosphorus causing very similar characteristics of the Ca-bound P and P_{total} (Fig. 4.2) records underlines the importance of sink switching for phosphorus burial in shelfal areas. Following an initial fertilization by submarine volcanic activity (e.g., Schlanger et al., 1981; Trabucho Alexandre et al., 2010) and / or remobilization and leeching of nutrients from flooded low altitude land areas (e.g., Mort et al., 2007, 2008) the reduction of the shelfal phosphorus sink by widespread anoxic conditions was important for maintaining high rates of organic carbon burial during the later phase of OAE2. Therefore, phosphorus remobilization from the sediments under anoxic conditions may have supported high organic carbon burial rates during the peak of both anoxic events, and may have acted as a positive feedback process enhancing carbon burial and removal

of light carbon isotopes from the marine DIC reservoir resulting in the positive carbon isotope excursions.

4.6. Conclusions

We generated a new record of phosphorus concentration and speciation covering the Cenomanian and early Turonian for Core SN°4 from the Tarfaya Basin, southern Morocco. Phosphorus speciation shows a predominance of Ca-bound phosphorus surpassing concentrations of Al/Fe-bound P by one to two orders of magnitude. Phosphorus bound to Al- and Fe-oxyhydroxides is increased during the early Cenomanian (between 305 and 273 m in Core SN°4), reflecting sedimentation in a shallower environment or less intensive redox-induced, early diagenetic cycling of iron oxyhydroxides, and during the early Turonian (74 - 42 m). Two of three increases in Ca-bound phosphorus / Al-bound phosphorus during the middle (222 – 218 m) and latest Cenomanian (104.4 m), also characterized by increased P_{total} concentrations, are synchronous within sampling resolution with Transgressive Surfaces of Ce2.1 and Ce5. Both enrichments are therefore interpreted as condensed horizons caused by sediment starvation during sea level high stand. Besides these maxima, P_{total} concentrations are characterized by slightly increased variability between the early Cenomanian and earliest Turonian (267 - 68 m in Core SN°4). The slight increase in P_{total} variability in combination with a decreased AlFeP/CaP ratio could have been caused by the emplacement of an increasingly stable OMZ above 273 m of Beil et al. (2018).

Only the ratios C_{org}/P_{react} and N_{total}/P_{react} produce a signal indicative for paleoceanographic changes during the global carbon isotope events MCE and OAE2. In contrast to the original interpretation of Anderson et al. (2001) they are interpreted to represent a change in the water column to constant anoxic or euxinic conditions. Oxygen-free bottom water permitted the leakage of dissolved phosphorus from the sedimentary column and increased therefore the ratios of C_{org} and N_{total} to P_{react} within the sediments. This change is within sampling resolution synchronous to enhanced organic carbon burial in the Tarfaya basin. Highest values during the plateau phase of OAE2 are in agreement with the study of Kolonic et al. (2005). The delayed increase of C_{org}/P_{react} and N_{total}/P_{react} in comparison to $\delta^{13}C_{org}$ argues against a direct initiation of Cenomanian OAEs by shelfal phosphorus remobilization. The coincidence of maximum organic carbon burial and highest C_{org}/P_{react} and N_{total}/P_{react} in contrast underlines the significance of phosphorus leakage from sediments in maintaining high organic carbon burial rates for extended periods of time.

4.7. Supplementary Material

for

Phosphorus concentrations and speciations across the mid-Cenomanian Event and Oceanic Anoxic Event 2 in the Tarfaya Basin (SW Morocco)

Sebastian Beil[1], Wolfgang Kuhnt[1], Ann E. Holbourn[1], Julian Oxmann[2], Florian Scholz[2], Mohamed Aquit[1,3]

[1]Institute of Geosciences, Christian-Albrechts-University, Ludewig-Meyn-Str.10-14, D-24118 Kiel, Germany
[2]GEOMAR Helmholtz-Zentrum für Ozeanforschung Kiel, Ozeanzirkulation und Klimadynamik, Paläo-Ozeanographie, Wischhofstr. 1-3, D-24148 Kiel, Germany
[3]OCP S.A., Direction de Recherche et Développement, Recherche Géologique, 46300 Youssoufia, Morocco

Contents of this file:

Supplementary Material Figures S4.1 and S4.4
Supplementary Material Tables S4.2 to S4.3

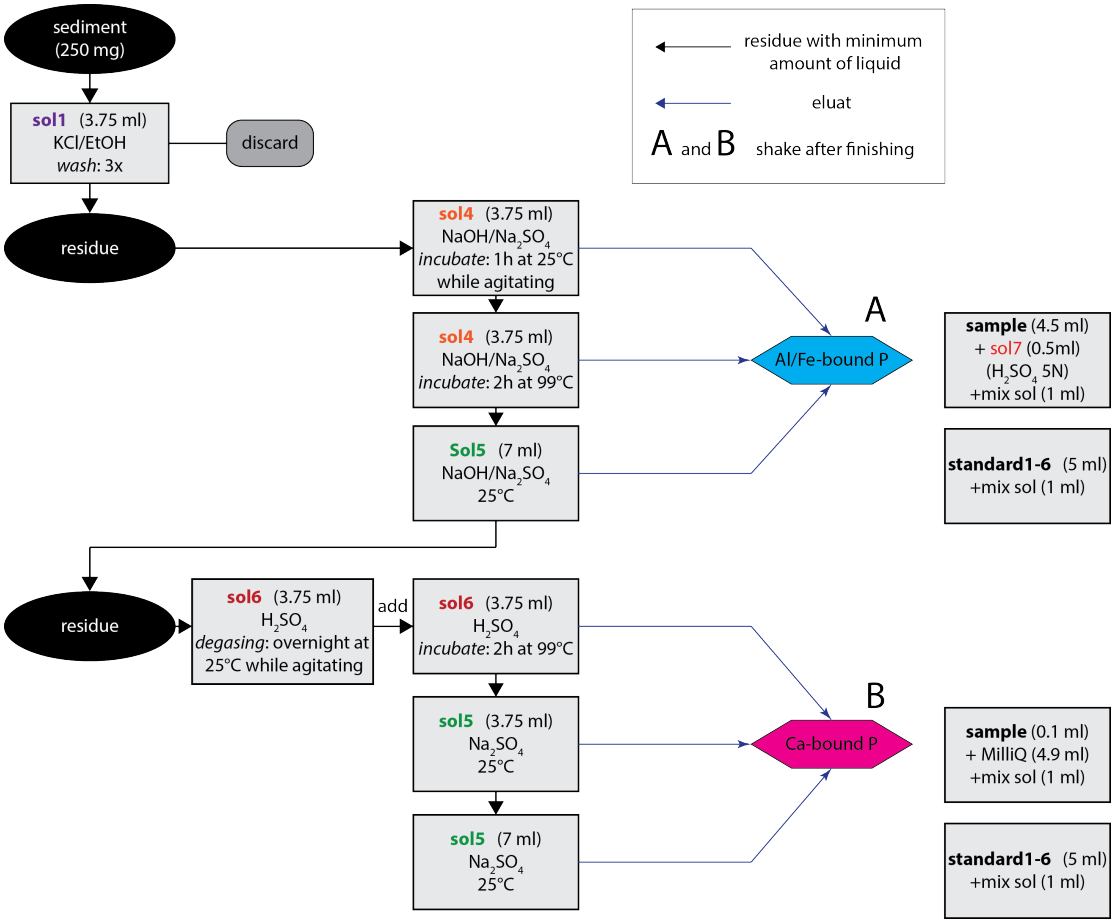

Supplementary Figure S4.1: Steps of SEDEX-extraction protocol. Compositions of mentioned solutions are presented in Supplementary Material Table S4.2.

Supplementary Material Table S4.2: Composition of solutions used for SEDEX-protocol (Supplementary Material Figure S4.1)

Solution 1 – KCl 1N

Dry KCl at 110°C for 2h

Dissolve dry KCl	in H_2O (MilliQ)	add etilic alcohol
14.912 g	200 ml	300 ml
29.824 g	400 ml	600 ml
37.28 g	500 ml	750 ml

Mix well

Solution 2 – NaOH 2N

Dissolve NaOH	in H_2O (MilliQ)
8 g	100 ml
40 g	0.5 l
80 g	1 l

Mix well

Solutions 3 – Na_2SO_4 2N

Dissolve Na_2SO_4	in H_2O (MilliQ)
14.2 g	100 ml
71 g	0.5 l
142 g	1 l

Mix well

Solution 4 – (Sol2 + Sol3)

NaOH (Sol2)	and	Na_2SO_4 (Sol3)
50%	+	50%

Mix well

Solution 5 – Na_2SO_4 4%

Dissolve Na_2SO_4	in H_2O (MilliQ)
40 g	1 l
80 g	2 l

Mix well

Solutions 6 – H_2SO_4 1N

Dilute H_2SO_4	in H_2O (MilliQ)
27 ml	1 l

Mix well

Solution 7 – H_2SO_4 5N

Dilute H_2SO_4	in H_2O (MilliQ)
135 ml	1 l

Mix well

Supplementary Material Table S4.3: Mix-solution and standards for photometric measurement of phosphorus extracts from SEDEX.

Mix-solution

1. 4.9N Sulphuric acid
   (1) Ca. 500 ml MilliQ into 1l-flask
   (2) Add 136 ml conc. H_2SO_4 (95-97%) (corrosive!)
   (3) Fill up to 1000 ml MilliQ
2. Ammonium molybdate solution
   (use plastic spatula!)
   (1) Dissolve 10 g ammonium heptamolybdate tetrahydrate (harmful!)
   (2) Fill up to 250 ml with MilliQ
   Solution is stable for 2 weeks.
   Discard if a blue colour occurs.
3. Ascorbic acid solutions
   (1) Dissolve 4.5 g L-ascorbin-acid in MilliQ in 250 ml flask
   (2) Fill up to 250 ml with MilliQ
   Solution is stable for 1 week.
   Store cool and in darkness.
4. Potassium antimony tartrate solution
   (1) Dissolve 1.25 g Potassium antimony-(III)-oxitartrate hemihydrate (toxic) in MilliQ in 500 ml flask with magnetic stirrer on heating plate
   (2) Fill up to 500 ml with MilliQ
   Solution is stable for 1 month.

Mixed reagent: For	20 ml	40 ml	50 ml	100 ml	120 ml
4.9N H_2SO_4	10 ml	20 ml	25 ml	50 ml	60 ml
Ammonium molybdate solution	3 ml	6 ml	7.5 ml	15 ml	18 ml
Ascorbic acid solution	6 ml	12 ml	15 ml	30 ml	36 ml
Potassium antimony tartrate solution	1 ml	2 ml	2.5 ml	5 ml	6 ml

Solution is stable for only 12 hours!

Standards

Standard-solution

1. 5 ml Merck standard (1000 mg PO_4/l) into 1l flask
2. Fill up with MilliQ → 5 mg PO_4/l

Standards

Std#	concentration	Standard-solution	MilliQ	Total Volume
1	0	0 µl	5000 µl	5 ml
2	1%	50 µl	4950 µl	5 ml
3	5%	250 µl	4750 µl	5 ml
4	10%	500 µl	4500 µl	5 ml
5	50%	2500 µl	2500 µl	5 ml
6	75%	3750 µl	1250 µl	5 ml

Add 1 ml mix solution to 5 ml standards or 5 ml samples

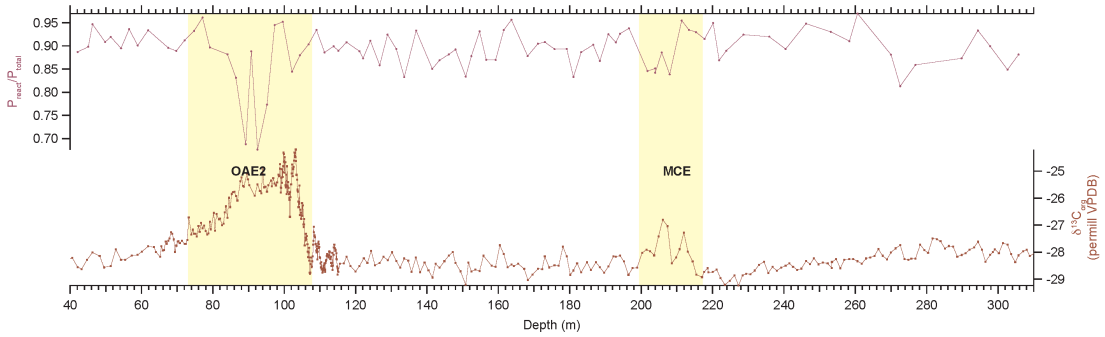

Supplementary Material Figure S4.4: P_{react}/P_{total}

Chapter 5:

Conclusions and outlook for future research

5. Conclusions and outlook for future research

For this study, samples and data from Core SN°4 recovered from the Tarfaya Basin (SW Morocco) on the Northwest African Atlantic Margin were used to reconstruct environmental variability over the time interval from the late Albian to early Turonian. The paleogeographic position and sedimentary characteristics (e.g. high burial rates of organic carbon) at this key location allowed detailed reconstruction of the onset and development of one of the most intense global anoxic events OAE2 as well as comparison with preceding lower amplitude global carbon isotope excursions in the middle Cenomanian and at the Albian-Cenomanian boundary. The continuous and extended records from Core SN°4 further allowed to derive estimates of the duration of the Cenomanian stage – a topic still under intense debate.

The Cretaceous interval of 325 m in Core SN°4 covering the time interval between the latest Albian and early Turonian, is the focus of ***Chapter 2***. Taking advantage of the continuous record available at this site, orbitally driven sedimentation cycles and the pacing of climatic and environmental change during the Albian-Cenomanian boundary event (ACB), the mid-Cenomanian Event (MCE) and the Oceanic Anoxic Event 2 (OAE2) were reconstructed. The overall duration of the Cenomanian Stage is estimated to be 4.8 +/- 0.2 Myr, based on frequency analysis of the Natural-Gamma-Ray- and XRF-scanning derived Log(Zr/Rb)-records. Sedimentation rates are generally high reaching 4.5-6 cm/kyr from the late Albian to middle Cenomanian and 8-9 cm/kyr for the late Cenomanian to early Turonian. The onset of upwelling in the Tarfaya Basin causing increased productivity and enhancing organic carbon burial occurred in

the latest Albian and intensified in two steps following the MCE and at the onset of OAE2. The global carbon isotope excursions during OAE2 and the MCE show strikingly similar characteristics and durations of their onset and main phases, suggestive of common driving mechanisms and climate-carbon cycle feedbacks. They are also both characterized by eustatic sea level falls that resulted in prominent sequence boundaries in the Tarfaya Basin. Elevated primary productivity triggering intense oxygen depletion during the carbon isotope excursions are indicated by low XRF-scanning derived Log(Mn/S) and elevated C_{org}/N_{total} and organic matter content.

Chapter 3 focuses on the onset and peak phase of the global anoxic event OAE2. High-resolution proxy records (stable isotopes, organic matter content, carbonate content, XRF-scanner derived elemental log-ratios, linescan data) at centimeter to sub-millimeter intervals provide a centennial to annual time scale resolution that retraces the highly dynamic behavior of the ocean-climate system during the onset of OAE2. The main carbon isotope increase, likely coinciding with an extended minimum in eccentricity, occurs in two steps and spans a period of ca. 100 kyr. Terrigenous sedimentation and accumulation of organic matter and carbonate additionally appear strongly modulated by obliquity over this interval. Two minima preceding the main increase in $\delta^{13}C_{org}$ were probably caused by the injection of isotopic depleted carbon into the atmosphere. The transient plateau in $\delta^{13}C_{org}$ during the main increase towards the first peak of OAE2, concomitant with a peak in $\delta^{13}C_{carbonate}$ and the top of a carbonate-rich interval, is interpreted as the transgressive surface of the globally recognized eustatic sea level cycle Ce5. Maximum organic carbon sequestration in the

Tarfaya Basin occurred during the latest phase of the main carbon isotope excursion close to the first $\delta^{13}C_{org}$ maximum of OAE2. Three stepwise increases in $\delta^{18}O_{carbonate}$ during the onset and main phase of the $\delta^{13}C_{org}$ excursion are interpreted as three cooling events within the globally identified Plenus Cold Event. These events were probably triggered by periodic reductions of atmospheric pCO_2 caused by drastically enhanced burial of organic carbon during periods of low obliquity and eccentricity, resulting in decreased insolation at high-latitudes. The first and third $\delta^{18}O_{carbonate}$ increases of the Plenus Cold Event are also marked by the extinction of the upper thermocline dwelling foraminiferal species *Rotalipora greenhornensis* and *Rotalipora cushmani*. These extinctions were potentially caused by periodic, obliquity-paced intensification and expansion of the oxygen minimum zone, leading to deterioration of their habitat due to increasingly anoxic conditions in the photic zone and ocean acidification.

Chapter 4 focuses on the reconstruction of phosphorus dynamics in Core SN°4 from the Tarfaya Basin during the Cenomanian and early Turonian encompassing the globally recognized carbon isotope excursions MCE and OAE2. Maximum concentration in total phosphorus (P_{total}), aluminum-iron- (AlFeP) and calcium-bound (CaP) phosphorus and in CaP/AlFeP at 221 m and 104 m (during the onset of the MCE and OAE2, respectively) are attributed to condensed intervals caused by the sea level high stands of Ce2.1 and Ce5, respectively. Otherwise low concentrations of AlFeP and high CaP/AlFeP-ratios imply intense redox-induced, early diagenetic cycling of phosphorus between the different P-pools. Strong increases of C_{org}/P_{react} and N_{total}/P_{react} occurred during MCE and

OAE2. The increases parallel the positive carbon isotope excursions, albeit with larger relative amplitude change in C_{org}/P_{react} and N_{total}/P_{react} for OAE2 in comparison to the MCE. Both phosphorus excursions are interpreted as changes in bottom water redox state towards permanent anoxic or euxinic, promoting leakage of phosphorus from the sediments. Otherwise low ratios, significantly below the Redfield ratio C:N:P of 106:16:1, imply secondary phosphorus enrichment in the sediments by sink switching between the different phosphorus pools. Water column fertilization by phosphorus leakage from the sediments under permanent anoxic/euxinic conditions is only identified during OAE2. The first maximum in C_{org}/P_{react} an N_{total}/P_{react} immediately precedes the peak phase in organic matter accumulation implying P-fertilization enhanced primary production during that interval.

These results provide new insights into the processes and mechanisms driving changes in climate, the biosphere and the carbon cycle under high pCO_2 conditions of a greenhouse world and open up new questions for future research. In particular, concentrations and isotopic composition of osmium and other volcanogenic elements should be measured prior to and during the onset phases to better understand the triggering mechanism of OAE2 and the MCE. These results could be combined with modeling to better constrain the timing and driving mechanisms and the volume of injected volcanogenic CO_2. The comparison of molybdenum concentrations and isotopes with other redox-sensitive elements would additionally help to constrain variations in the level of oxygen depletion.

The new results for the MCE and OAE2 highlight the importance of orbital forcing for long- and short-term changes in the ocean-climate system. This study underlines the highly dynamic behavior of climate-carbon cycle interactions in a greenhouse world characterized by high pCO_2-conditions. However, a better understanding of feedback processes and thresholds in the response of the ocean-climate system to radiative forcing remains elusive. Comparison with more geologically recent Cenozoic records would allow to disentangle the influence of different orbital periodicities on the evolution of the climate system as well as the role of paleogeography (e.g., continental configuration, opening and closing of marine gateways) and the varying sensitivity to changing boundary conditions within the long-term climate trend from warm to cold greenhouse and finally to icehouse conditions. This would ultimately contribute to better constrain projections of future climate dynamics in relation to anthropogenic climate warming.

References

References

Anderson, L. D., Delaney, M. L., Faul, K. L., 2001. Carbon to phosphorus ratios in sediments: Implications for nutrient cycling. *Global Biogeochemical Cycles*, 15(1), 65-79. http://dx.doi.org/ 10.1029/2000GB001270.

Ando, A., Huber, B. T., MacLeod, K. G., Ohta, T., Boo-Keun Khim, B.-K., 2009. Blake Nose stable isotopic evidence against the mid-Cenomanian glaciation hypothesis. *Geology*, 37, 451-454. http://dx.doi.org/10.1130/G25580A.1.

Aquit, M., Kuhnt, W., Holbourn, A., Chellai, E. H., Stattegger, K., Kluth, O., Jabour, H., 2013. Late Cretaceous paleoenvironmental evolution of the Tarfaya Atlantic coastal basin, SW Morocco. *Cretaceous Research*, 45, 288-305. http://dx.doi.org/10.1016/j.cretres.2013.05.004.

Aquit, M., Kuhnt, W., Holbourn, A. E., Chellai, E. H., Lees, J. A., Kluth, O., Jabour, H., 2016. Complete archive of middle Turonian to early Campanian sedimentary deposition in newly drilled cores from the Tarfaya Basin, SW Morocco. *Geological Society of America Bulletin*, B31523.1. http://dx.doi.org/10.1130/B31523.1.

Arning, E. T., Birgel, D., Brunner, B., Peckmann, J., 2009. Bacterial formation of phosphatic laminites off Peru. *Geobiology*, 7(3), 295-307. http://dx.doi.org/10.1111/j.1472-4669.2009.00197.x.

Arning, E. T., Lückge, A., Breuer, C., Gussone, N., Birgel, D., Peckmann, J., 2009. Genesis of phosphorite crusts off Peru. *Marine Geology*, 262(1), 68-81. http://dx.doi.org/10.1016/j.margeo.2009.03.006.

Arthur, M. A., Dean, W. E., and Pratt, L. M., 1988. Geochemical and climatic effects of increased marine organic carbon burial at the Cenomanian/Turonian boundary. *Nature*, 335, 714–717. http://dx.doi.org/10.1038/335714a0.

Arthur, M. A. and Sageman, B. B., 2004. Sea-level control on source-rock development: Perspectives from the Holocene Black Sea, the mid-Cretaceous Western Interior Basin of North America and the Late Devonian Appalachian Basin. In SEPM (*Society for Sedimentary Geology*) Special Publication 82 (The Deposition of Organic-Carbon-Rich Sediments: Models, Mechanisms, and Consequences), 35–59. http://dx.doi.org/10.2110/pec.05.82.0035.

Barclay, R. S., McElwain, J. C., Sageman, B. B., 2010. Carbon sequestration activated by a volcanic CO2 pulse during Ocean Anoxic Event 2. *Nature Geoscience*, 3(3), 205-208. http://dx.doi.org/10.1038/ngeo757.

Barker, I. R., Moser, D. E., Kamo, S. L., Plint, A. G., 2011. High-precision U–Pb zircon ID–TIMS dating of two regionally extensive bentonites: Cenomanian Stage, Western Canada Foreland Basin. *Canadian Journal of Earth Sciences*, 48(2), 543-556. http://dx.doi.org/10.1139/E10-042.

Batenburg, S. J., Vleeschouwer, D., Sprovieri, M., Hilgen, F. J., Gale, A. S., Singer, B. S., Koeberl, C., Coccioni, R., Claeys, P., and Montanari. A., 2016. Orbital control on the timing of oceanic anoxia in the Late Cretaceous. *Climate of the Past*, 12, 1995–2009. http://dx.doi.org/10.5194/cp-12-1995-2016.

Beil, S., Kuhnt, W., Holbourn, A. E., Aquit, M., Flögel, S., Chellai, E. H., Jabour, H., 2018. New insights into Cenomanian paleoceanography and climate evolution from the Tarfaya Basin, southern Morocco. *Cretaceous Research*, 84, 451–473. http://dx.doi.org/10.1016/j.cretres.2017.11.006.

Berger, A. L., Loutre, M. F., Laskar, J., 1992. Stability of the astronomical frequencies over the Earth's history for paleoclimate studies. *Science*, 255(5044), 560. http://dx.doi.org/10.1126/science.255.5044.560.

Berger, W. H., Diester-Haass, L. Killingley, J.S., 1978. Upwelling off Northwest Africa: the Holocene decrease as seen in carbon isotopes and sedimentological indicators. *Oceanologica Acta*, 1, 3-7.

Bouloubassi, I., Rullkötter, J., Meyers, P. A., 1999. Origin and transformation of organic matter in Pliocene–Pleistocene Mediterranean sapropels: organic geochemical evidence reviewed. *Marine Geology*, 15*3*(1), 177-197. http://dx.doi.org/10.1016/S0025-3227(98)00082-6.

Boulila, S., Galbrun, B., Miller, K. G., Pekar, S. F., Browning, J. V., Laskar, J., Wright, J. D., 2011. On the origin of Cenozoic and Mesozoic “third-order” eustatic

sequences. *Earth-Science Reviews*, 109(3), 94-112. http://dx.doi.org/10.1016/j.earscirev.2011.09.003.

Bowman, A. R., Bralower, T. J., 2005. Paleoceanographic significance of high-resolution carbon isotope records across the Cenomanian–Turonian boundary in the Western Interior and New Jersey coastal plain, USA. *Marine Geology*, 217(3-4), 305-321. http://dx.doi.org/10.1016/j.margeo.2005.02.010.

Broecker, W. S., Peng T.-H., 1982. Tracers in the Sea. *Eldigio Press, Columbia University, Palisades, New York*, 690 pp.

Bruland, K. W., 1983. Trace Elements in Sea-water. In: "Chemical Oceanography, Vol. 8" (Eds JP Riley and R. Chester), pp. 157–220. *Elsevier*. https://doi.org/10.1016/B978-0-12-588608-6.50009-2

Brumsack, H. J., 2006. The trace metal content of recent organic carbon-rich sediments: implications for Cretaceous black shale formation. *Palaeogeography, Palaeoclimatology, Palaeoecology*, 232(2), 344-361. http://dx.doi.org/10.1016/j.palaeo.2005.05.011.

Calvert, S. E., Pedersen, T. F., 2007. Chapter fourteen elemental proxies for palaeoclimatic and palaeoceanographic variability in marine sediments: interpretation and application. *Developments in Marine Geology*, 1, 567-644. http://dx.doi.org/10.1016/S1572-5480(07)01019-6.

Caron, M., Dall'Agnolo, S., Accarie, H., Barrera, E., Kauffman, E. G., Francis Amédro, F., Robaszynski, F., 2006. High-resolution stratigraphy of the Cenomanian–Turonian boundary interval at Pueblo (USA) and Wadi Bahloul (Tunisia): stable isotope and bio-events correlation. *Geobios*, 39, 171–200. http://dx.doi.org/10.1016/j.geobios.2004.11.004.

Choubert, G., Faure Muret, A., Hottinger, L., 1966. Aperçu géologique du Bassin côtier de Tarfaya (Stratigraphie), in Choubert, G., Faure Muret, A., Hottinger, L., Viotti, C. Lecointre, G., eds., Le bassin côtier de Tarfaya (Maroc Méridional): *Notes et Mémoire Service Géologique du Maroc*, 175, 7–106.

Clarke, L. J., Jenkyns, H. C., 1999. New oxygen isotope evidence for long-term Cretaceous climatic change in the Southern Hemisphere. *Geology*, 27(8), 699–702. http://dx.doi.org/10.1130/0091-7613(1999)027<0699:NOIEFL>2.3.CO;2.

Clement, A. C., Peterson, L. C., 2008. Mechanisms of abrupt climate change of the last glacial period. *Reviews of Geophysics*. 46, RG4002, http://dx.doi.org/10.1029/2006RG000204.

Coccioni, R., Galeotti, S., 2003. The mid-Cenomanian Event: prelude to OAE 2. *Palaeogeography, Palaeoclimatology, Palaeoecology*, 190, 427-440. http://dx.doi.org/10.1016/S0031-0182(02)00617-X.

Codispoti L. A., 1989. Phosphorus vs. nitrogen limitation of new and export production. In Productivity of the Ocean: Present and Past (Eds. W. H. Berger, V. S. Smetacek, and G. Wefer). *Wiley, New York*, 377–394.

Cosmidis, J., Benzerara, K., Menguy, N., Arning, E., 2013. Microscopy evidence of bacterial microfossils in phosphorite crusts of the Peruvian shelf: Implications for phosphogenesis mechanisms. *Chemical Geology*, 359, 10-22. http://dx.doi.org/10.1016/j.chemgeo.2013.09.009.

De Moel, H., Ganssen, G. M., Peeters, F. J. C., Jung, S. J. A., Kroon, D., Brummer, G. J.A ., Zeebe, R. E., 2009. Planktic foraminiferal shell thinning in the Arabian Sea due to anthropogenic ocean acidification?. *Biogeosciences*, 6, 1917–1925, 2009, www.biogeosciences.net/6/1917/2009/.

Dean, W. E., Arthur, M. A., Claypool, G. E., 1986. Depletion of ^{13}C in Cretaceous marine organic matter: Source, diagenetic, or environmental signal?. *Marine Geology*, 70(1-2), 119-157. http://dx.doi.org/10.1016/0025-3227(86)90092-7.

DeConto, R. M., Galeotti, S., Pagani, M., Tracy, D., Schaefer, K., Zhang, T., Pollard, D., Beerling, D. J., 2012. Past extreme warming events linked to massive carbon release from thawing permafrost. *Nature*, 484, 87-91. http://dx.doi.org/10.1038/nature10929.

Delaney M. L., 1998. Phosphorus accumulation in marine sediments and the oceanic phosphorus cycle. Gl*obal Biogeochemical Cycles*, 12, 563–672. http://dx.doi.org/10.1029/98GB02263.

Desmares, D., Grosheny, D., Beaudoin, B., 2008. Ontogeny and phylogeny of Upper Cenomanian rotaliporids (Foraminifera). *Marine Micropaleontology*, 69, 91–105. http://dx.doiorg/10.1016/j.marmicro.2008.07.003.

Dickson, A. J., Saker-Clark, M., Jenkyns, H. C., Bottini, C., Erba, E., Russo, F., Gorbanenko, O., Naafs, B. D. A., Pancost, R. D., Robinson, S. A., van den Boorn, S. H. J. M., Idiz, E., 2017. A Southern Hemisphere record of global trace-metal drawdown and orbital modulation of organic-matter burial across the Cenomanian–Turonian boundary (Ocean Drilling Program Site 1138, Kerguelen Plateau). *Sedimentology*, 64(1), 186-203. http://dx.doi.org/10.1111/sed.12303.

Du Vivier, D. S., Sageman, B. B., Jarvis, I., Gröcke, D. R., Voigt, S., 2014. Marine 187Os/188Os isotope stratigraphy reveals the interaction of volcanism and ocean circulation during Oceanic Anoxic Event 2. *Earth and Planetary Science Letters*, 389, 23-33. http://dx.doi.org/10.1016/j.epsl.2013.12.024.

Du Vivier, A. D. C., Jacobson, A. D., Lehn, G. O., Selby, D., Hurtgen, M. T., Sageman, B. B., 2015. Ca isotope stratigraphy across the Cenomanian–Turonian OAE 2: Links between volcanism, seawater geochemistry, and the carbonate fractionation factor. *Earth and Planetary Science Letters*, 416, 121–131. http://dx.doi.org/10.1016/j.epsl.2015.02.001.

Eiler, J. M., 2007. “Clumped-isotope” geochemistry—The study of naturally-occurring, multiply-substituted isotopologues. *Earth and Planetary Science Letters*, 262(3-4), 309-327. http://dx.doi.org/10.1016/j.epsl.2007.08.020.

Eiler, J. M., Bonifacie, M., & Daëron, M., 2009. “Clumped isotope”thermometry for high-temperature problems. *Geochimica et Cosmochimica Acta*, 73(13), A322-A322. http://dx.doi.org/10.1016/j.gca.2009.05.004.

Elbatal, Y., Aadjour, M., Saber, N., Elabibi, R., Nahim, M., 2010. Étude sismo-structurale du basin de Tarfaya-Boujdour Onshore. *Afrique Science*, 06(2), 49-59.

Elder, W. P., Gustason, E. R., and Sageman, B. B., 1994. Correlation of basinal carbonate cycles to nearshore parasequences in the Late Cretaceous Greenhorn Seaway, Western Interior, U.S.. *GSA Bulletin*, 106, 892–902.

El Khatib, J., Ruellan, E., El Foughali, A., & El Morabet, A. M., 1995. Evolution de la marge atlantique sud marocaine: bassin de Tarfaya-Laayoune (Evolution of the southern Morocco Atlantic margin: Tarfaya-Laayoune Basin). *Oceanographic Literature Review*, 9(42), 747.

El Khatib, J., El Foughali, A., Ruellan, E., El Morabet, A., 1996. Évolution post-rift des secteurs NE et SW du bassin Tarfaya-Laâyoune. *Mines. Géologie et Energie.*, 55, 57–72.

Elrick, M., Garza, Roberto, Duncan, R., Snow, L., 2009. C-isotope stratigraphy and paleoenvironmental changes recorded in Cenomanian-Turonian (mid-Cretaceous) platform carbonates of southern Mexico. *Earth and Planetary Science Letters*, 277, 295-306. http://dx.doi.org/10.1016/j.epsl.2008.10.020.

Erbacher, J., Thurow, J., 1997. Influence of oceanic anoxic events on the evolution of mid-Cretaceous radiolaria in the North Atlantic and western Tethys. *Marine Micropaleontology*, 30(1), 139–158. http://dx.doi.org /10.1016/S0377-8398(96)00023-0.

Erbacher, J., Friedrich, O., Wilson, P. A., Birch, H., and Mutterlose, J., 2005. Stable organic carbon isotope stratigraphy across Oceanic Anoxic Event 2 of Demerara Rise, western tropical Atlantic. *Geochemistry, Geophysics, Geosystems*, 6, Q06010. http://dx.doi.org/10.1029/2004GC000850.

Erdem, Z., Schönfeld, J., Glock, N., Dengler, M., Mosch, T., Sommer, S., Elger, J. Eisenhauer, A., 2016. Peruvian sediments as recorders of an evolving hiatus for the last 22 thousand years. *Quaternary Science Reviews*, 137, 1-14. http://dx.doi.org/10.1016/j.quascirev.2016.01.029.

Falkowski P. G., Barber R. T., Smetacek V. V., 1998. Biogeochemical Controls and Feedbacks on Ocean Primary Production. *Science*, 281(5374), 200-207.

Flögel, S., Wallmann, K., Poulsen, C. J., Zhou, J., Oschlies, A., Voigt, S., Kuhnt, W., 2011. Simulating the biogeochemical effects of volcanic CO2 degassing on the

oxygen-state of the deep ocean during the Cenomanian/Turonian Anoxic Event (OAE2). *Earth and Planetary Science Letters*, 305(3–4), 371-384. http://dx.doi.org/10.1016/j.epsl.2011.03.018.

Forster, A., Schouten, S., Baas, M., Damsté, J. S. S., 2007. Mid-Cretaceous (Albian–Santonian) sea surface temperature record of the tropical Atlantic Ocean. *Geology*, 35(10), 919-922. http://dx.doi.org/10.1130/G23874A.1.

Friedrich, O., Erbacher, J., Mutterlose, J., 2006. Paleoenvironmental changes across the Cenomanian/Turonian boundary event (oceanic anoxic event 2) as indicated by benthic foraminifera from the Demerara Rise (ODP Leg 207). *Revue de micropaleontology*, 49(3), 121-139. http://dx.doi.org/10.1016/j.revmic.2006.04.003.

Gale, A. S., Jenkyns, H. C., Kennedy, W. J., Corfield, R. M., 1993. Chemostratigraphy versus biostratigraphy: data from around the Cenomanian–Turonian boundary. *Journal of the Geological Society*, 150(1), 29-32. http://dx.doi.org/10.1144/gsjgs.150.1.0029.

Gale, A. S., Christensen, W. K., 1996. Occurrence of the belemnite Actinocamax plenus in the Cenomanian of SE France and its significance, *Bulletin of Geological Society. Denmark*, 43, 68–77.

Gale, A. S., Young, J. R., Shackleton, N. J., Crowhurst, S. J., Wray, D. S., 1999. Orbital tuning of Cenomanian marly chalk successions: towards a Milankovitch time-

scale for the Late Cretaceous. *Philosophical Transactions of the Royal Society of London A: Mathematical, Physical and Engineering Sciences*, 357(1757), 1815-1829. http://dx.doi.org/10.1098/rsta.1999.0402.

Gale, A. S., Hardenbol, J., Hathway, B., Kennedy, W. J., Young, J. R., Phansalkar, V., 2002. Global correlation of Cenomanian (Upper Cretaceous) sequences: Evidence for Milankovitch control on sea level. *Geology*, 30(4), 291-294. http://dx.doi.org/10.1130/0091-7613(2002)030%3C0291:GCOCUC%3E2.0.CO;2.

Gale, A. S., 2007. A Milankovitch scale for the Cenomanian. Terra Nova 1, 420-425.

Gale, A. S., Voigt, S., Sageman, B. B., Kennedy, W. J., 2008. Eustatic sea-level record for the Cenomanian (Late Cretaceous) - extension to the Western Interior Basin, USA. *Geology*, 36(11), 859-862. http://dx.doi.org/10.1130/G24838A.1.

Gale, A. S., Bown, P., Caron, M., Crampton, J., Crowhurst, S. J., Kennedy, W. J., Petrizzo, M. R., Wray, D. S., 2011. The uppermost Middle and Upper Albian succession at the Col de Palluel, Hautes-Alpes, France: An integrated study (ammonites, inoceramid bivalves, planktonic foraminifera, nannofossils, geochemistry, stable oxygen and carbon isotopes, cyclostratigraphy). *Cretaceous Research*, 32(2), 59-130. http://dx.doi.org/10.1016/j.cretres.2010.10.004.

Gebhardt, H., Kuhnt, W., Holbourn, A., 2004. Foraminiferal response to sea level change, organic flux and oxygen deficiency in the Cenomanian of the Tarfaya Basin, southern Morocco. *Marine Micropaleontology*, 53(1), 133-157. http://dx.doi.org/10.1016/j.marmicro.2004.05.007.

Geider, R., La Roche, J., 2002. Redfield revisited: variability of C:N:P in marine microalgae and its biochemical basis. *European Journal of Phycology*, 37(1), 1-17. http://dx.doi.org/10.1017/S0967026201003456.

Gertsch, B., Adatte, T., Keller, G., Tantawy, A. A. M., Berner, Z., Mort, H. P., Fleitmann, D., 2010. Middle and late Cenomanian oceanic anoxic events in shallow and deeper shelf environments of western Morocco. *Sedimentology*, 57, 1430–1462. http://dx.doi.org/10.1111/j.1365-3091.2010.01151.x.

Ghosh, P., Adkins, J., Affek, H., Balta, B., Guo, W., Schauble, E. A., Schrag, D., Eiler, J. M., 2006. 13C–18O bonds in carbonate minerals: a new kind of paleothermometer. *Geochimica et Cosmochimica Acta*, 70(6), 1439-1456. http://dx.doi.org/10.1016/j.gca.2005.11.014.

Giraud, F., Reboulet, S., Deconinck, J. F., Martinez, M., Carpentier, A. Bréziat, C., 2013. The Mid-Cenomanian Event in southeastern France: Evidence from palaeontological and clay mineralogical data. *Cretaceous Research*, 46, 43-58. http://dx.doi.org/10.1016/j.cretres.2013.09.004.

Goldhammer, T., Brüchert, V., Ferdelman, T. G., Zabel, M., 2010. Microbial sequestration of phosphorus in anoxic upwelling sediments. *Nature Geoscience*, 3(8), 557-561. http://dx.doi.org/10.1038/ngeo913.

Govin, A., Holzwarth, U., Heslop, D., Ford Keeling, L., Zabel, M., Mulitza, S., Collins, J. A., Chiessi, C. M., 2012. Distribution of major elements in Atlantic surface sediments (36 N–49 S): Imprint of terrigenous input and continental weathering. *Geochemistry, Geophysics, Geosystems*, 1*3*(1), Q01013. http://dx.doi.org/10.1029/2011GC003785.

Gradstein, F. M., Ogg, J. G., Schmitz, M., Ogg, G. (Eds.), 2012. The geologic time scale 2012. *Elsevier*. http://dx.doi.org/10.1016/c2011-1-08249-8.

Grippo, A., Fischer, A.G., Hinnov, L.A., Herbert, T.M., Premoli Silva, I., 2004. Cyclostratigraphy and chronology of the Aptian (Piobbico Core, Italy). In: D'Argenio, B., Fischer, A.G., Premoli Silva, I., Weissert, H., Ferreri, V. (Eds.), Cyclostratigraphy: Approaches and Case Histories. *SEPM Special Publications*,. 81, 57–82. Tulsa, OK. http://dx,doi.org/10.2110/pec.04.81.0057.

Grosheny, D., Beaudoin, B., Morel, L., Desmares, D., 2006. High-resolution biostratigraphy and chemostratigraphy of the Cenomanian/Turonian boundary event in the Vocontian Basin, Southern France. *Cretaceous Research*, 27, 629–640. http://dx.doi.org/10.1016/j.cretres.2006.03.005.

Haq, B. U., Hardenbol, J., Vail, P. R., 1987. Chronology of fluctuating sea levels since the Triassic. *Science*, 235(4793), 1156-1167. http://dx.doi.org/10.1126/science.235.4793.1156

Haq, B. U., Hardenbol, J., Vail, P. R., 1988. Mesozoic and Cenozoic chronostratigraphy and cycles of sea-level change. *SEPM Special Publication*, 42, 71-108. http://dx.doi.org/10.2110/pec.88.01.0071

Haq, B. U., 2014. Cretaceous eustasy revisited. *Global and Planetary Change*, 113, 44-58. http://dx.doi.org/10.1016/j.gloplacha.2013.12.007.

Hardas, P., Mutterlose, J., Friedrich, O., Erbacher, J., 2012. The Middle Cenomanian Event in the equatorial Atlantic: The calcareous nannofossil and benthic foraminiferal response. *Marine Micropaleontology*, 96–97, 66–74. http://dx.doi.org/10.1016/j.marmicro.2012.08.003.

Haug, G.H. Hughen, K.A; Sigman, D.M., Peterson, L.S., Röhl, U., 2001. Southward migration of the Intertropical Convergence Zone through the Holocene. *Science*, 293(5533), 1304-1308. http://dx.doi.org/10.1126/science.1059725.

Hay, W. W., Floegel, S., 2012. New thoughts about the Cretaceous climate and oceans. *Earth-Science Reviews*, 115(4), 262-272. http://dx.doi.org/10.1016/j.earscirev.2012.09.008,

Hay, W. W., Leslie, M. A., 1990. Could possible changes in global groundwater reservoir cause eustatic sea-level fluctuations?. In: Sea- Level Change. National *Academy Press, Washington D.C.*, pp. 161–170.

Hayes, J.M., Strauss, H., Kaufman, A.J., 1999. The abundance of 13C in marine organic matter and isotopic fractionation in the global biogeochemical cycle of carbon during the past 800 Ma. *Chemical Geology*, 161, 103-125.

Higgins, J.A., Schrag, D.P., 2006. Beyond methane: Towards a theory for the Paleocene–Eocene Thermal Maximum. *Earth and Planetary Science Letters*, 245, 523–537, http://dx.doi.org/10.1016/j.epsl.2006.03.009.

Holbourn, A., Kuhnt, W., El Albani, A., Pletsch, T., Luderer, F., Wagner, T., 1999. Upper Cretaceous palaeoenvironments and benthonic foraminiferal assemblages of potential source rocks from the western African margin, Central Atlantic. *Geological Society, London, Special Publications*, 153(1), 195-222. http://dx.doi.org/10.1144/GSL.SP.1999.153.01.13.

Holbourn, A.E., W. Kuhnt, K. G. D. Kochhann, N. Andersen, S. Meier, 2015. Global perturbation of the carbon cycle at the onset of the Miocene Climatic Optimum. *Geology*, 43, 123–126. http://dx.doi.org/10.1130/G36317.1.

Holland H. D., 1978. The Chemistry of the Atmosphere and Oceans. *Wiley, New York*, 351pp.

Hopmans, E. C., Weijers, J. W., Schefuß, E., Herfort, L., Damsté, J. S. S., Schouten, S., 2004. A novel proxy for terrestrial organic matter in sediments based on branched and isoprenoid tetraether lipids. *Earth and Planetary Science Letters*, 224(1-2), 107-116. http://dx.doi.org/10.1016/j.epsl.2004.05.012.

Houghton, R.A., 2007. Balancing the Global Carbon Budget. *Annual Review of Earth and Planetary Sciences*, 35, 313-347. http://dx.doi.org/10.1146/annurev.earth.35.031306.140057.

Huang, C., Hinnov, L., Fischer, A. G., Grippo, A., Herbert, T., 2010. Astronomical tuning of the Aptian Stage from Italian reference sections. *Geology*, 38(10), 899-902. http://dx.doi.org/10.1130/G31177.1.

Husson, D., Galbrun, B., Laskar, J., Hinnov, L. A., Thibault, N., Gardin, S., & Locklair, R. E. (2011). Astronomical calibration of the Maastrichtian (late Cretaceous). *Earth and Planetary Science Letters*, 305(3-4), 328-340. http://dx.doi.org/10.1016/j.epsl.2011.03.008.

Ingall, E., Jahnke, R., 1994. Evidence for enhanced phosphorus regeneration from marine sediments overlain by oxygen depleted waters. *Geochimica et Cosmochimica Acta*, 58(11), 2571-2575. http://dx.doi.org/10.1016/0016-7037(94)90033-7.

Ingall, E. D., 2010. Biogeochemistry: phosphorus burial. *Nature Geoscience*, 3(8), 521-522. http://dx.doi.org/10.1038/ngeo926.

Jarvis, I., Burnett, W. C., Nathan, Y., Almbaydin, F. S. M., Attia, A. K. M., Castro, L. N., Flicoteaux, R., Ezzeldim Hilmy, M., Husain, V., Qutawnah, A. A., Serjani, A., Zanin, Y. N., 1994. Phosphorite geochemistry: state-of-the-art and environmental concerns. *Eclogae Geologicae Helvetiae*, 87(3), 643-700.

Jarvis, I., Murphy, A. M., Gale, A. S., 2001. Geochemistry of pelagic and hemipelagic carbonates: criteria for identifying systems tracts and sea-level change. *Journal of the Geological Society*, London 158, 685-696. http://dx.doi.org/10.1144/jgs.158.4.685.

Jarvis, I. A. N., Gale, A. S., Jenkyns, H. C., Pearce, M. A., 2006. Secular variation in Late Cretaceous carbon isotopes: a new δ 13 C carbonate reference curve for the Cenomanian–Campanian (99.6–70.6 Ma). *Geological Magazine*, 143(05), 561-608. http://dx.doi.org/10.1017/S0016756806002421.

Jarvis, I., Lignum, J. S., Gröcke, D. R., Jenkyns, H. C., Pearce, M. A., 2011. Black shale deposition, atmospheric C02 drawdown, and cooling during the Cenomanian-Turonian Oceanic Anoxic Event. *Paleoceanography*, 26, PA3201. http://dx.doi.org/10.1029/2010pa002081, 2011.

Jarvis, I., Trabucho-Alexandre, J., Gröcke, D. R., Ulicny, D., Lurin, J., 2015. Intercontinental correlation of organic carbon and carbonate stable isotope records: evidence of climate and sea-level change during the Turonian

(Cretaceous). *The Depositional Record*, 1(2), 53-90. http://dx.doi.org/10.1002/dep2.6.

Jenkyns, H. C., 1980. Cretaceous anoxic events: from continents to oceans. *Journal of Geological Society*, 137(2), 171-188. http://dx.doi.org/10.1144/gsjgs.137.2.0171.

Jenkyns, H. C., 2010. Geochemistry of oceanic anoxic events. *Geochemistry, Geophysics, Geosystems*, 11(3). http://dx.doi.org/10.1029/2009GC002788.

Jenkyns, H. C., Dickson, A. J., Ruhl, M., Can den Boorn, S. H. J. M., 2017. Basalt-seawater interaction, the Plenus Cold Event, enhanced weathering and geochemical change: Deconstructing OAE 2 (Cenomanian-Turonian, Late Cretaceous). *Sedimentology*, 64, 16–43. http://dx.doi.org/10.1111/sed.12305.

Kaiho, K., Katabuchi, M., Oba, M., Lamolda, M., 2014. Repeated anoxia–extinction episodes progressing from slope to shelf during the latest Cenomanian. *Gondwana Research*, 25, 1357–1368. http://dx.doi.org/10.1016/j.gr.2012.12.008.

Kemp, A. E. S., 1996. Laminated sediments as palaeo-indicators, in Kemp A.E.S. (ed) Palaeoclimatology and Palaeoceanography from Laminated Sediments, *Geological Society Special Publication*, 116, vii-xii. http://dx.doi.org/10.1144/GSL.SP.1996.116.01.01.

Kidder, D. L., Worsley, T. R., 2010. Phanerozoic large igneous provinces (LIPs), HEATT (haline euxinic acidic thermal transgression) episodes, and mass extinctions. *Palaeogeography, Palaeoclimatology, Palaeoecology*, 295(1), 162-191. http://dx.doi.org/10.1016/j.palaeo.2010.05.036.

Kidder, D. L., Worsley, T. R., 2012. A human-induced hothouse climate. *GSA Today*, 22(2), 4-11. http://dx.doi.org/10.1130/G131A.1.

Kirtland Turner, S., 2014. Pliocene switch in orbital-scale carbon cycle/climate dynamics. *Paleoceanography*, 29, 1256-1266 (2014).

Kolonic, S., Sinninghe Damsté, J. S., Böttcher, M. E., Kuypers, M. M. M., Kuhnt, W., Beckmann, B., Scheeder, G., Wagner, T., 2002. Geochemical characterization of Cenomanian/Turonian black shales from the Tarfaya Basin (SW Morocco). *Journal of Petroleum Geology*, 25, 325–350. http://dx.doi.org/10.1111/j.1747-5457.2002.tb00012.x.

Kolonic, S., Wagner, T., Forster, A., Sinninghe Damsté, J. S., Walsworth-Bell, B., Erba, E., Turgeon, S., Brumsack, H. J., Chellai, E. H., Tsikos, H., Kuhnt, W., Kuypers, M.M.M., 2005. Black shale deposition on the northwest African Shelf during the Cenomanian/Turonian oceanic anoxic event: Climate coupling and global organic carbon burial: *Paleoceanography*, 20, 1–18. http://doi.org/10.1029/2003PA000950.

Küspert, W., 1982. Environmental change during oil shale deposition as deduced from stable isotope ratios, In: Cyclic and Event Stratification (Eds. Einsele, S., and Seilacher, A.), *Springer*, N.Y., 482–501.

Kuhnt, W., Thurow, J., Wiedmann, J., Herbin, J. P., 1986. Oceanic anoxic conditions around the Cenomanian/Turonian Boundary and the response of the biota. In: Biogeochemistry of Black Shales (Eds. Degens, E. T., Meyers, P .A., and Brassell, S. C.). *Mitteilungen aus dem Geologischen Institut der Universität Hamburg*, 60, 205-246.

Kuhnt, W., Herbin, J. P., Thurow, J., Wiedmann, J., 1990. Distribution of Cenomanian-Turonian organic facies in the western Mediterranean and along the adjacent Atlantic margin. In: Deposition of organic facies (Vol. 30) (Ed. Huc, A. Y.). *AAPG, Tulsa*, 133-160.

Kuhnt, W., Nederbragt, A., Leine, L., 1997. Cyclicity of Cenomanian-Turonian organic-carbon-rich sediments in the Tarfaya Atlantic coastal basin (Morocco). *Cretaceous Research*, 18(4), 587-601. https://doi.org/10.1006/cres.1997.0076.

Kuhnt, W., Chellai, E. H., Holbourn, A., Luderer, F., Thurow, J., Wagner, T., El Albani, A., Beckmann, B., Herbin, J.-P., Kawamura, H., Kolonic, S., 2001. Morocco Basin's sedimentary record may provide correlations for Cretaceous paleoceanographic events worldwide. *Eos*, Transactions American Geophysical Union, 82(33), 361-364. http://dx.doi.org/10.1029/01EO00223.

Kuhnt, W., Luderer, F., Nederbragt, S., Thurow, J., Wagner, T., 2005. Orbital-scale record of the late Cenomanian–Turonian oceanic anoxic event (OAE-2) in the Tarfaya Basin (Morocco). *International Journal of Earth Sciences*, 94(1), 147-159. http://dx.doi.org/10.1007/s00531-004-0440-5.

Kuhnt, W., Holbourn, A., Gale, A., Chellai, E. H., Kennedy, W. J., 2009. Cenomanian sequence stratigraphy and sea-level fluctuations in the Tarfaya Basin (SW Morocco). *Geological Society of America Bulletin*, 121(11-12), 1695-1710. http://dx.doi.org/10.1130/B26418.1.

Kuhnt, W., Holbourn, A., Moullade, M., 2011. Transient global cooling at onset of early Aptian Anoxic Event (OAE1a). *Geology*, 39(4), 323-326. http://dx.doi.org/10.1130/G31554.1.

Kuhnt, W., Holbourn, A. E., Beil, S., Aquit, M., Krawczyk, T., Flögel, S., Chellai, E. H., Jabour, H., 2017. Unraveling the onset of Cretaceous Oceanic Anoxic Event 2 in an extended sediment archive from the Tarfaya-Laayoune Basin, Morocco. *Paleoceanography*, 32, 923–946. http://dx.doi.org/10.1002/2017PA003146.

Kump, L. R. Arthur, M. A., 1999. Interpreting carbon-isotope excursions: carbonates and organic matter. *Chemical Geology*, 161, 181-198.

Kuroda, J., Ohkouchi, N., Ishii, T., Tokuyama, H., Taira A., 2005. Lamina-scale analysis of sedimentary components in Cretaceous black shales by chemical

compositional mapping: Implications for paleoenvironmental changes during the Oceanic Anoxic Events. *Geochimica et Cosmochimica Acta*, 69(6), 1479-1494.

Kuypers, M. M. M., Pancost, R. D., Nijenhuis, I. A., Sinninghe Damsté, J. S., 2002. Enhanced productivity led to increased organic carbon burial in the euxinic North Atlantic basin during the late Cenomanian oceanic anoxic event. *Paleoceanography*, 17, 4, 1051. http://dx.doi.org/10.1029/2000PA000569.

Landing, W. M., Bruland, K. W., 1980. Manganese in the north Pacific. *Earth and Planetary Science Letters*, 49(1), 45-56. http://dx.doi.org/10.1016/0012-821X(80)90149-1.

Larson, R. L., 1991, Latest pulse of Earth: Evidence for a mid‐Cretaceous Superplume, *Geology*, 19, 547–550. http://dx.doi.org/10.1130/0091-7613(1991)019<0547:LPOEEF>2.3.CO;2.

Larson, R. L. Erba, E., 1999. Onset of the mid-Cretaceous greenhouse in the Barremian -Aptian: igneous events and the biological, sedimentary, and geochemical responses. *Paleoceanography*, 14, 663–678.

Laskar, J., Robutel, P., Joutel, F., Gastineau, M., Correia, A. C. M., Levrard, B., 2004. A long-term numerical solution for the insolation quantities of the Earth. *Astronomy & Astrophysics*, 428(1), 261-285. http://dx.doi.org/10.1051/0004-6361:20041335.

Laskar, J., Fienga, A., Gastineau, M., Manche, H., 2011a. La2010: a new orbital solution for the long-term motion of the Earth. *Astronomy & Astrophysics*, 532, A89. http://dx.doi.org/10.1051/0004-6361/201116836.

Laskar, J., Gastineau, M., Delisle, J. B., Farrés, A., Fienga, A., 2011b. Strong chaos induced by close encounters with Ceres and Vesta. *Astronomy & Astrophysics*, 532, L4. http://dx.doi.org/10.1051/0004-6361/201117504.

Laurin, J., Sageman, B. B., 2007. Cenomanian-Turonian coastal record in SW Utah, U.S.A.: Orbital-scale transgressive-regressive events during Oceanic Anoxic Event II. *Journal of Sedimentary Research*, 77, 731-756. http://dx.doi.org/10.2110/jsr.2007.076.

Laurin, J., Meyers, S. R., Uličný, D., Jarvis, I., Sageman, B. B., 2015. Axial obliquity control on the greenhouse carbon budget through middle- to high-latitude reservoirs. *Paleoceanography*, 30, 133–149. http://dx.doi.org/10.1002/2014PA002736.

Laws, E. A., Popp, B. N., Bidigare, R. R., Kennicutt, M. C. and Macko, S. A., 1995. Dependence of phytoplankton carbon isotope composition on growth rate and (CO_2)aq: theoretical considerations and experimental results. *Geochimica Cosmochimca Acta*, 59, 1131–1138.

Leine, L. 1986. Geology of the Tarfaya oil shale deposit, Morocco. *Geologic en Mijnbouw*, 65, 57-74.

Lhomme, N., Clarke, G. K. C., Ritz, C., 2005. Global budget of water isotopes inferred from polar ice sheets. *Geophysical Research Letters*, 32, L20502, http://dx.doi.org/10.1029/2005GL023774.

Li, X., Jenkyns, H. C., Wang, C., Hu, X., Xi, C., Wei, Y., Huang, Y., Jie, C., 2006. Upper Cretaceous carbon- and oxygen-isotope stratigraphy of hemipelagic carbonate facies from southern Tibet, China. *Journal of the Geological Society*, London, 163, 375–382.

Locklair, R. E., Sageman, B. B., 2008. Cyclostratigraphy of the Upper Cretaceous Niobrara Formation, Western Interior, U.S.A.: a Coniacian–Santonian orbital timescale. *Earth and Planetary Science Letters*, 269, 539–552. http://dx.doi.org/10.1016/j.epsl.2008.03.021.

Longoria, J.F., 1973. *Pseudoticinella*, a new genus of planktonic foraminifera from the early Turonian of Texas. *Revista Española de Micropaleontologia*, 5, 417–423.

Lorenzen, J., Kuhnt, W., Holbourn, A., Flögel, S., Moullade, M., Tronchetti, G., 2013. A new sediment core from the Bedoulian (Lower Aptian) stratotype at Roquefort-La Bédoule, SE France. *Cretaceous Research*, 39, 6-16. http://dx.doi.org/10.1016/j.cretres.2012.03.019.

Luderer, F. Kuhnt, W., 1997. A high resolution record of the *Rotalipora* extinction in laminated organic-carbon rich limestones of the Tarfaya Atlantic coastal basin (Morocco). *Annaöes Societe Géologique du Nord* (2eme série), 5, 199-205.

Ma, C., Meyers, S., Sageman, B., Singer, B., Jicha, B., 2014. Testing the Astronomical Time Scale for Oceanic Anoxic Event 2, and its Extension into Cenomanian Strata of the Western Interior Basin. *GSA Bulletin*, 126, 974-989.

Mackenzie, A. S., Patience, R. L., Maxwell, J. R., Vandenbroucke, M., & Durand, B. (1980). Molecular parameters of maturation in the Toarcian shales, Paris Basin, France-I. Changes in the configurations of acyclic isoprenoid alkanes, steranes and triterpanes. *Geochimica et Cosmochimica Acta*, 44(11), 1709-1721. http://dx.doi.org/10.1016/0016-7037(80)90222-7.

Mann, M. E., Lees, J. M., 1996. Robust estimation of background noise and signal detection in climatic time series. *Climatic Change*, 33(3), 409-445. http://dx.doi.org/10.1007/BF00142586.

Meissner, K. J., McNeil, B. I., Eby, M., Wiebe, E. C., 2012. The importance of the terrestrial weathering feedback for multimillennial coral reef habitat recovery. *Global Biogeochemical Cycles*, 26, GB3017. http://dx.doi.org/10.1029/2011GB004098.

Meyers, P. A., 1989. Sources and deposition of organic matter in Cretaceous passive margin deep-sea sediments: a synthesis of organic geochemical studies from Deep Sea Drilling Project Site 603, outer Hatteras Rise. *Marine and petroleum geology*, 6(2), 182-189. http://dx.doi.org/10.1016/0264-8172(89)90021-4.

Meyers, P. A., 2006. Paleoceanographic and paleoclimatic similarities between Mediterranean sapropels and Cretaceous black shales. *Palaeogeography, Palaeoclimatology, Palaeoecology*, 235(1), 305-320. http://dx.doi.org/10.1016/j.palaeo.2005.10.025.

Meyers, P. A., Bernasconi, S. M., Forster, A., 2006. Origins and accumulation of organic matter in expanded Albian to Santonian black shale sequences on the Demerara Rise, South American margin. *Organic Geochemistry*, 37(12), 1816-1830. http://dx.doi.org/10.1016/j.orggeochem.2006.08.009.

Meyers, P. A., 2014. Why are the $\delta^{13}C_{org}$ values in Phanerozoic black shales more negative than in modern marine organic matter?. *Geochemistry, Geophysics, Geosystems*, 15, 3085–3106. http://dx.doi.org/10.1002/2014GC005305.

Meyers, S. R., Sageman, B. B., 2007. Quantification of deep-time orbital forcing by average spectral misfit. *American Journal of Science*, 307(5), 773-792. http://dx.doi.org/10.2475/05.2007.01.

Meyers, S. R., Siewert, S. E., Singer, B. S., Sageman, B. B., Condon, D. J., Obradovich, J. D., Jicha, B. R., Sawyer, D. A., 2010. Reducing Error Bars through the Intercalibration of Radioisotopic and Astrochronologic Time Scales for the Cenomanian/Turonian Boundary Interval, Western Interior Basin, USA. In *American Geophysical Union, Fall Meeting 2010*. abstract id:V31A-2302.

Meyers, S. R., Sageman, B. B., Arthur, M. A., 2012a. Obliquity forcing of organic matter accumulation during Oceanic Anoxic Event 2. *Paleoceanography*, 27, 1–19. http://dx.doi.org/10.1029/2012PA002286.

Meyers, S. R., Siewert, S. E., Singer, B. S., Sageman, B. B., Condon, D. J., Obradovich, J. D., Jicha, B. R., Sawyer, D.A., 2012b. Intercalibration of radioisotopic and astrochonologic time scales for the Cenomanian- Turonian boundary interval, Western Interior Basin, USA. *Geology*, 40, 7–10. http://dx.doi.org/10.1130/G32261.1.

Miller, K. G., Sugarman, P. J., Browning, J. V., Kominz, M. A., Hernández, J. C., Olsson, R. K., Wright, J. D., Feigenson, M. D., Van Sickel, W., 2003. Late Cretaceous chronology of large, rapid sea-level changes: Glacioeustasy during the greenhouse world. *Geology*, 31, 585–588. http://dx.doi.org/10.1130/0091-7613(2003)031%3C0585:LCCOLR%3E2.0.CO;2.

Miller, K. G., Wright, J. D., Browning, J. V. 2005. Visions of ice sheets in a greenhouse world. *Marine Geology*, 217, 215–231. http://dx.doi.org/10.1016/j.margeo.2005.02.007.

Mitchell, S. F., Paul, C. R. C., Gale A. S., 1996. Carbon isotopes and sequence Stratigraphy. In:.High Resolution Sequence Stratigraphy: Innovations and Applications (Eds. Howell, J. A., Aitken, J. F). *Geological Society, London, Special Publications*, 104, 11-24. http://dx.doi.org/10.1144/GSL.SP.1996.104.01.02.

Mitchell, S. F., Carr, I. T., 1998. Foraminifera response to mid-Cenomanian (Upper Cretaceous) palaeoceanographic events in the Anglo-Paris Basin (Northwest Europe). *Palaeogeography, Palaeoceanography, Palaeoecology*, 137, 103-125. http://dx.doi.org/10.1016/S0031-0182(97)00087-4.

Moriya, K., Wilson, P. A., Friedrich, O., Erbacher, J., Kawahata, H., 2007. Testing for ice sheets during the mid-Cretaceous greenhouse using glassy foraminiferal calcite from the mid-Cenomanian tropics on Demerara Rise. *Geology*, 35, 615–618. http://dx.doi.org/10.1130/G23589A.1.

Mort, H. P., Adatte, T., Föllmi, K. B., Keller, G., Steinmann, P., Matera, V., Berner, Z., Stüben, D., 2007. Phosphorus and the roles of productivity and nutrient recycling during oceanic anoxic event 2. *Geology*, 35(6), 483–486. https://dx.doi.org/10.1130/G23475A.1.

Mort, H. P., Adatte, T., Keller, G., Bartels, D., Föllmi, K. B., Steinmann, P., Berner, Z., Chellai, E. H., 2008. Organic carbon deposition and phosphorus accumulation during Oceanic Anoxic Event 2 in Tarfaya, Morocco. *Cretaceous Research*, 29(5–6), 1008-1023. https://dx.doi.org/10.1016/j.cretres.2008.05.026.

Mosch, T., Sommer, S., Dengler, M., Noffke, A., Bohlen, L., Pfannkuche, O., Liebetrau, V., Wallmann, K., 2012. Factors influencing the distribution of epibenthic megafauna across the Peruvian oxygen minimum zone. *Deep-Sea Research*, 168, 123–135. http://dx.doi.org/10.1016/j.dsr.2012.04.014.

Mulitza, S., Prange, M., Stuut, J. B., Zabel, M., von Dobeneck, T., Itambi, A. C., Nizou, J., Schulz, M., Wefer, G., 2008. Sahel megadroughts triggered by glacial slowdowns of Atlantic meridional overturning. *Paleoceanography*, 23(4), PA4206. http://dx.doi.org/10.1029/2008PA001637.

Müller, P. J., 1977. CN ratios in Pacific deep-sea sediments: Effect of inorganic ammonium and organic nitrogen compounds sorbed by clays. *Geochimica et Cosmochimica Acta*, 41(6), 765-776. http://dx.doi.org/10.1016/0016-7037(77)90047-3.

Nederbragt, A., Fiorentino, A., 1999. Stratigraphy and palaeoceanography of the Cenomanian–Turonian boundary event in Oued Mellegue, north-western Tunisia. *Cretaceous Research*, 20, 47–62.

Nelson, C. S., Smith, A. M., 1996. Stable oxygen and carbon isotope compositional fields for skeletal and diagenetic components in New Zealand Cenozoic nontropical carbonate sediments and limestones: A synthesis and review. New Zealand Journal of Geology and Geophysics, 39(1), 93–107. http://dx.doi.org/10.1080/00288306.1996.9514697.

Niebuhr, B., 2005. Geochemistry and time-series analyses of orbitally forced Upper Cretaceous marl–limestone rhythmites (Lehrte West Syncline, northern Germany). *Geological Magazine*, 142(01), 31-55. http://dx.doi.org/10.1017/S0016756804009999.

O'Brien, C. L., Robinson, S. A., Pancost, R. D., Damsté, J. S. S., Schouten, S., Lunt, D. J., Alsenz, H., Bornemann, A., Bottini, C., Brassell, S. C., Farnsworth, A., Forster, A., Huber, B. T., Inglis, G. N., Jenkyns, H. C., Linnert, C., Littler, K., Markwick, P., McAnena, A., Mutterlose, J., Naafs, B. D. A., Püttmann, W., Sluijs, A., van Helmond, N. A. G. M., Vellekoop, J., Wagner, T., Wrobel, Neil E., 2017. Cretaceous sea-surface temperature evolution: Constraints from TEX86 and planktonic foraminiferal oxygen isotopes. *Earth-Science Reviews*, 172, 224-247. http://dx.doi.org/10.1016/j.earscirev.2017.07.012.

Obradovitch, J. D., 1993. A Cretaceous time scale. In: (Evolution of the Western Interior basin (Eds. Caldwell, W. G. E., Kauffman, E. G.,), *Geological Association of Canada Special Paper*, 39, 379–396.

Ogg, J. G., Ogg, G., Gradstein, F. M., 2016. A concise geologic time scale: 2016. *Elsevier*.

Patriat, M., Labails, C., 2006. Linking the Canary and Cape-Verde Hot-Spots, Northwest Africa. *Marine Geophysical Researches*, 27(3), 201-215. http://dx.doi.org/10.1007/s11001-006-9000-7.

Patterson, M. O., McKay, R., Naish, T., Escutia, C., Jimenez-Espejo, F. J., Raymo, M. E., Meyers, S. R., Tauxe, L., Brinkhuis, H., IODP Expedition 318 Scientists, 2014. Orbital forcing of the East Antarctic ice sheet during the Pliocene and Early Pleistocene. *Nature Geoscience*, 7(11), 841-847. http://dx.doi.org/10.1038/ngeo2273.

Paul, C. R. C., Mitchell, S. F., Marshall, J. D., Leary, P. N., Gale, A. S., Duane, A. M, Ditchfield, P. W., 1994. Palaeoceanographic events in the middle Cenomanian of Northwest Europe. *Cretaceous Research* 15, 707-738. http://dx.doi.org/10.1006/cres.1994.1039.

Paul, C. R. C., Lamolda, M. A., Mitchell, S. F., Vaziri, M. R., Gorostidi, A., Marshall, J. D., 1999. The Cenomanian–Turonian boundary at Eastbourne (Sussex, UK): a proposed European reference section. *Palaeogeography, Palaeoclimatology, Palaeoecology*, 150, 83–121.

Pearce, M. A., Jarvis, I., Tocher, B. A., 2009. The Cenomanian–Turonian boundary event, OAE2 and palaeoenvironmental change in epicontinental seas: New insights from the dinocyst and geochemical records. *Palaeogeography, Palaeoclimatology, Palaeoecology*, 280(1), 207-234. http://dx.doi.org/10.1016/j.palaeo.2009.06.012.

Peterson, L. C., Haug, G. H., Hughen, K. A., Röhl, U., 2000. Rapid changes in the hydrologic cycle of the tropical Atlantic during the last

glacial. *Science*, 290(5498), 1947-1951. http://dx.doi.org/10.1126/science.290.5498.1947.

Petrizzo, M., Caron, M., Premoli Silva, I., 2015. Remarks on the identification of the Albian/Cenomanian boundary and taxonomic clarification of the planktonic foraminifera index species globotruncanoides, brotzeni and tehamaensis. *Geological Magazine*, 152(3), 521-536. http://dx.doi.org/10.1017/S0016756814000478.

Poulton, S. W., Henkel, S., März, C., Urquhart, H., Flögel, S., Kasten, S., Sinninghe Damsté, J. S., Wagner, T., 2015. A continental-weathering control on orbitally driven redox-nutrient cycling during Cretaceous Oceanic Anoxic Event 2. *Geology*, 43(11), 963-966. http://dx.doi.org/10.1130/G36837.1.

R Core Team, 2017. R: A language and environment for statistical computing. R Foundation for Statistical Computing, Vienna, Austria. URL https://www.R-project.org/.

Rachold, V., Brumsack, H. J., 2001. Inorganic geochemistry of Albian sediments from the Lower Saxony Basin NW Germany: palaeoenvironmental constraints and orbital cycles. *Palaeogeography, Palaeoclimatology, Palaeoecology*, 174(1), 121-143. http://dx.doi.org/10.1016/S0031-0182(01)00290-5.

Ranke, U., von Rad, U., Wissmann, G., 1982. Stratigraphy, Facies and Tectonic Development of the On- and Offshore Aaiun-Tarfaya Basin - A Review. In:

Geology of the Northwest African Continental Margin (Eds. : von Rad, U., K. Hinz, Sarnthein, M., Seibold, E.). *Springer*, Berlin, Heidelberg, 86–105. http://dx.doi.org/10.1007/978-3-642-68409-8_6.

Ratschiller L.K., 1970. Lithostratigraphy of the northern Spanish Sahara. *Memorie Museo Tridentino di Science naturali*, Trento 18 (1), 1-80.

Redfield, A. C., 1942. The processes determining the concentration of oxygen, phosphate and other organic derivatives within the depths of the Atlantic Ocean. *Massachusetts Institute of Technology and Woods Hole Oceanographic Institution*. http://dx.doi.org/10.1575/1912/1053.

Redfield A. C., 1958. The biological control of chemical factors in the environment. *American scientist*, 46, 205–222.

Redfield A. C., Ketchum B. H., Richards F. A., 1963. The influence of organisms on the composition of sea water. In: The Sea (Ed. M. N. Hill). *Interscience*, New York, 2, 26–77.

Riggs S. R., 1979. Phosphorite sedimentation in Florida - a model phosphogenic system. *Economic Geology*, 74, 285–314. http://dx.doi.org/10.2113/gsecongeo.74.2.285.

Robaszynski, F., Caron, M., 1995. Foraminifères planctoniques du Crétacé; commentaire de la zonation Europe-Méditerranée. *Bulletin de la Société géologique de France*, 166(6), 681-692.

Roth, R., Ritz, S. P., Joos, F., 2014. Burial-nutrient feedbacks amplify the sensitivity of carbon dioxide to changes in organic matter remineralisation. *Earth System Dynamics Discussions*, 5(1), 473-528. http://dx.doi.org/10.5194/esd-5-321-2014.

Rothwell, R.G. Croudace, I.W., 2015. Twenty Years of XRF Core Scanning Marine Sediments: What do Geochemical Proxies tell us? In: Micro-XRF Studies of Sediment Cores (Eds. Croudace, I.W. and Rothwell, R.G.), *Developments in Paleoenvironmental Research*, 17, 25-102. http://dx.doi.org/10.1007/978-94-017-9849-5_2.

Ruttenberg, K. C., 1992. Development of a sequential extraction method for different forms of phosphorus in marine sediments. *Limnology and oceanography*, 37(7), 1460-1482. http://dx.doi.org/ 10.4319/lo.1992.37.7.1460.

Ruttenberg K. C., 1993. Reassessment of the oceanic residence time of phosphorus. *Chemical Geology*, 107, 405–409. http://dx.doi.org/10.1016/0009-2541(93)90220-D.

Ruttenberg K. C., Berner R. A., 1993. Authigenic apatite formation and burial in sediments from non-upwelling continental margins. *Geochimica et Cosmochimica Acta*, 57, 991–1007. http://dx.doi.org/10.1016/0016-7037(93)90035-U.

Ruttenberg, K. C., 2003. The Global Phosphorus Cycle. In: Treatise on Geochemistry, vol. 8 (Eds. Turekian, K. K., Holland, H. D.). *Elsevier*, 585–643. http://dx.doi.org/10.1016/B0-08-043751-6/08153-6.

Ryan, W. B. F., Carbotte, S. M., Coplan, J. O., O'Hara, S., Melkonian, A., Arko, R., Weissel, R. A., Ferrini, V., Goodwillie, A., Nitsche, F., Bonczkowski, J., Zemsky, R., 2009. Global multi-resolution topography synthesis. *Geochemistry, Geophysics, Geosystems*, 10(3), Q03014. http://dx.doi.org/10.1029/2008GC002332.

Sageman, B. B., 1996. Lowstand tempestites: Depositional model for Cretaceous skeletal limestones, Western Interior basin. *Geology*, 24/10, 888-892.

Sames, B., Wagreich, M., Wendler, J. E., Haq, B. U., Conrad, C. P., Melinte-Dobrinescu, M. C., Hu, X., Wendler, I., Wolfgring, E., Yilmaz, I.Ö., Zorina, S. O., 2016. Short-term sea-level changes in a greenhouse world - A view from the Cretaceous. *Palaeogeography, Palaeoclimatology, Palaeoecology*, 441, 393-411. http://dx.doi.org/10.1016/j.palaeo.2015.10.045.

Schlanger, S. O., Jenkyns, H. C., 1976. Cretaceous oceanic anoxic events: Causes and consequences. *Geologie en Minjnbouw*, 55, 179–184.

Schlanger, S. O., Jenkyns, H. C.,, Premoli-Silva, I., 1981. Volcanism and vertical tectonics in the Pacific Basin related to global Cretaceous transgressions. *Earth and Planetary Science Letters*, 52(2), 435-449. http://dx.doi.org/10.1016/0012-821X(81)90196-5.

Schlanger, S. O., Arthur, M. A., Jenkyns, H. C., Scholle, P. A., 1987. The Cenomanian-Turonian Oceanic Anoxic Event, I. Stratigraphy and distribution of organic carbon-rich beds and the marine δ13C excursion. *Geological Society, London, Special Publications*, 26(1), 371-399.

Schönfeld, J., Kuhnt, W., Erdem, Z., Flögel, S., Glock, N., Aquit, M., Frank, M. Holbourn, A., 2015, Records of past mid-depth ventilation: Cretaceous ocean anoxic event 2 vs. Recent oxygen minimum zones. *Biogeosciences* (BG), 12 (4), 1169-1189. http://dx.doi.org/10.5194/bg-12-1169-2015.

Schouten, S., Hopmans, E.C., Schefuß, E., Sinninghe Damsté, J.S., 2002, Distributional variations in marine crenarchaeotal membrane lipids: A new tool for reconstructing ancient sea water temperatures?. *Earth and Planetary Science Letters*, 204, 265–274. http://dx.doi.org/10.1016/S0012-821X(02)00979-2.

Schouten, S., Hopmans, E.C., Forster, A., van Breugel, Y., Kuypers, M.M.M., Sinninghe Damsté, J.S., 2003, Extremely high sea-surface temperatures at low latitudes during the middle Cretaceous as revealed by archaeal membrane lipids. *Geology*, 31, 1069–1072. http://dx.doi.org/10.1130/G19876.1.

Schulz H. N., Schulz H. D., 2005. Large sulfur bacteria and the formation of phosphorite. *Science*, 307, 416–418. http://dx.doi.org/10.1126/science.1103096.

Scott, R. W., Oboh-Ikuenobe, F. E., Benson Jr, D. G., Holbrook, J. M., 2009. Numerical age calibration of the Albian/Cenomanian boundary. *Stratigraphy*, 6(1), 17-32.

Scott, R. W., 2014. A Cretaceous chronostratigraphic database: construction and applications. *Carnets de Geologie-Notebooks on Geology*, 14(2), 15-37. http://dx.doi.org/10.4267/2042/53522.

Seifert, W.K., Moldowan, J.M., 1986. Use of biological markers in petroleum exploration. In: (Methods in Geochemistry and Geophysics, Vol 24, (Ed. Johns, R.B.). *Elsevier*, Amsterdam, 261-290.

Slomp C. P., Epping E. H. G., Helder W., Van Raaphorst W., 1996a. A key role for iron-bound phosphorus in authigenic apatite formation in North Atlantic continental platform sediments. *Journal of Marine Research*, 54, 1179–1205. http://dx.doi.org/10.1357/0022240963213745.

Slomp C. P., Van der Gaast S. J., Van Raaphorst W., 1996b. Phosphorus binding by poorly crystalline iron oxides in North Sea sediments. *Marine Chemistry*, 52, 55–73. http://dx.doi.org/10.1016/0304-4203(95)00078-X.

Slomp C. P., Thomson J., de Lange G. J., 2004. Controls on phosphorus regeneration and burial during formation of eastern Mediterranean sapropels. *Marine Geology*, 203, 141–159. http://dx.doi.org/10.1016/S0025-3227(03)00335-9.

Slomp C. P., Van Cappellen P., 2007. The global marine phosphorus cycle: sensitivity to oceanic circulation. *Biogeosciences*, 4, 155–171. http://dx.doi.org/10.5194/bg-4-155-2007.

Smith S. V., 1984. Phosphorus versus nitrogen limitation in the marine environment. *Limnology and Oceanography*, 29, 1149–1160. http://dx.doi.org/10.4319/lo.1984.29.6.1149.

Stoll, H. M., Schrag, D. P., 2000. High-resolution stable isotope records from the Upper Cretaceous rocks of Italy and Spain: Glacial episodes in a greenhouse planet?. *Geological Society of America Bulletin*, 112, 308–319. http://dx.doi.org/10.1130/0016-7606(2000)112%3C308:HSIRFT%3E2.0.CO;2.

Stoll, H. M., 2005. Limited range of interspecific vital effects in coccolith stable isotopic records during the Paleocene-Eocene thermal maximum. *Paleoceanography*, 20, PA1007. http://dx.doi.org/10.1029/2004PA001046.

Storey, M., Duncan, R. A., Swisher, C. C., 2007. Paleocene-Eocene thermal maximum and the opening of the northeast Atlantic. *Science*, 316 (5824), 587-589. http://dx.doi.org/10.1126/science.1135274.

Tessin, A., I. Hendy, N. Sheldon, Sageman, B. B., 2015. Redox-controlled preservation of organic matter during “OAE 3” within the Western Interior Seaway. *Paleoceanography*, 30(6), 702-717. http://dx.doi.org/10.1002/2014PA002729.

Timmermann, A., Lorenz, S. J., An, S.-I., Clement, A., Xie, S.-P., 2007. The Effect of Orbital Forcing on the Mean Climate and Variability of the Tropical Pacific. *Journal of Climate*, 20, 4147-4159. http://dx.doiorg/10.1175/JCLI4240.1.

Tisserand, A., Malaizé, B., Jullien, E., Zaragosi, S., Charlier, K., Grousset, F., 2009. African monsoon enhancement during the penultimate glacial period (MIS 6.5~170 ka) and its atmospheric impact. *Paleoceanography*, 24(2), PA2220. http://dx.doi.org/10.1029/2008PA001630.

Torrence, C., Compo, G. P., 1998. A practical guide to wavelet analysis. *Bulletin of the American Meteorological Society*. 79, 61-78. http://dx.doi.org/10.1175/1520-0477(1998)079%3C0061:APGTWA%3E2.0.CO;2.

Trabucho Alexandre, J., Tuenter, E., Henstra, G. A., van der Zwan, K. J., van de Wal, R. S., Dijkstra, H. A., de Boer, P. L., 2010. The mid‐Cretaceous North Atlantic nutrient trap: Black shales and OAEs. *Paleoceanography*, 25(4), PA4201. http://dx.doi.org/10.1029/2010PA001925.

Tsikos, H., Jenkyns, H. C., Walsworth-Bell, B., Petrizzo, M. R., Forster, A., Kolonic, S., Erba, E., Primoli Silva, I., Baas, M., Wagner, T., Sinninghe Damsté, J. S., 2004. Carbon-isotope stratigraphy recorded by the Cenomanian–Turonian Oceanic Anoxic Event: correlation and implications based on three key localities. *Journal of the Geological Society*, 161(4), 711-719. http://dx.doi.org/10.1144/0016-764903-077.

Turgeon, S. C., Ceaser, R. A., 2008. Cretaceous oceanic anoxic event 2 triggered by a massive magmatic episode. *Nature*, 454, 323–326. http://dx.doi.org/10.1038/nature07076.

Twichell, S. C., Meyers, P. A., Diester-Haass, L., 2002. Significance of high C/N ratios in organic-carbon-rich Neogene sediments under the Benguela Current upwelling system. *Organic Geochemistry*, *33*(7), 715-722. http://dx.doi.org/10.1016/S0146-6380(02)00042-6.

van Bentum, E. C., Reichart, G. J., Forster, A., Sinninghe Damsté, J. S., 2012. Latitudinal differences in the amplitude of the OAE-2 carbon isotopic excursion: pCO_2 and paleoproductivity. *Biogeosciences*, 9, 717–731. http://dx.doi.org/10.5194/bg-9-717-2012.

Van Mooy, B. A., Keil, R. G., Devol, A. H., 2002. Impact of suboxia on sinking particulate organic carbon: Enhanced carbon flux and preferential degradation of amino acids via denitrification. *Geochimica et Cosmochimica Acta*, 66(3), 457-465. http://dx.doi.org/10.1016/S0016-7037(01)00787-6.

Voigt, S., Hilbrecht, H., 1997. Late Cretaceous carbon isotope stratigraphy in Europe: Correlation and relations with sea level and sediment stability. *Palaeogeography, Palaeoclimatology, Palaeoecology*, 134(1–4), 39-59. http://dx.doi.org/10.1016/S0031-0182(96)00156-3.

Voigt, S., Gale, A. S., Flögel, S., 2004. Midlatitude shelf seas in the Cenomanian-Turonian greenhouse world: Temperature evolution and North Atlantic circulation. *Paleoceanography*, 19, PA4020, http://dx.doi.org/10.1029/2004PA001015.

Voigt, S., Erbacher, J., Mutterlose, J., Weiss, W., Westerhold, T., Wiese, F., Wilmsen, M., Wonik, T., 2008. The Cenomanian–Turonian of the Wunstorf section (north Germany): Global stratigraphic reference section and new orbital time scale for oceanic anoxic event 2. *Newsletter on Stratigraphy*, 43, 65–89. http://dx.doi.org/10.1127/0078-0421/2008/0043-0065.

Wagreich, M., Lein, R., Sames, B., 2014. Eustasy, its controlling factors, and the limnoeustatic hypothesis - concepts inspired by Eduard Suess. *Austrian Journal of Earth Sciences*, 107, 115–131.

Wallmann, K., 2003. Feedbacks between oceanic redox states and marine productivity: A model perspective focused on benthic phosphorus cycling. *Global biogeochemical cycles*, 17(3). http://dx.doi.org/10.1029/2002GB001968.

Wallmann, K., 2010. Phosphorus imbalance in the global ocean?. *Global Biogeochemical Cycles*, 24(4). http://dx.doi.org/10.1029/2009GB003643.

Waples, D. W., & Sloan, J. R., 1980. Carbon and nitrogen diagenesis in deep sea sediments. *Geochimica et Cosmochimica Acta*, 44(10), 1463-1470. http://dx.doi.org/10.1016/0016-7037(80)90111-8.

Weaver, C. E., 1967. Potassium, illite and the ocean. *Geochimica et Cosmochimica Acta*, *31*(11), 2181-2196. http://dx.doi.org/10.1016/0016-7037(67)90060-9.

Weaver, C. E., 1989. Clays, muds, and shales (Vol. 44). *Elsevier*.

Weaver, A. J., Eby, M., Wiebe, E. C., Bitz, C. M., Duffy, P. B., Ewen, T. L., Fanning, A. F., Holland, M. M., MacFadyen, A., Matthews, H. D., Meissner, K. J., Saenko, O., Schmittner, A., Wang, H., Yoshimori, M., 2001 The UVic earth system climate model: Model description, climatology, and applications to past, present and future climates. *Atmosphere-Ocean*, 39, 4. http://dx.doi.org/10.1080/07055900.2001.9649686.

Weltje, G. J., Tjallingii, R., 2008. Calibration of XRF core scanners for quantitative geochemical logging of sediment cores: theory and application. *Earth and Planetary Science Letters*, 274(3), 423-438. http://dx.doi.org/10.1016/j.epsl.2008.07.054.

Wendler, I., 2013. A critical evaluation of carbon isotope stratigraphy and biostratigraphic implications for Late Cretaceous global correlation. *Earth-Science Reviews*, 126, 116–146.

Wendler, I., Wendler, J. E., Clarke, L. J., 2016. Sea-level reconstruction for Turonian sediments from Tanzania based on integration of sedimentology, microfacies, geochemistry and micropaleontology. *Palaeogeography, Palaeoclimatology, Palaeoecology*, 441, 528-564. http://dx.doi.org/10.1016/j.palaeo.2015.08.013.

Wendler, J. E., Wendler, I., Huber, B. T., 2013. Revision and Evaluation of the Systematic Affinity of the Calcitarch Genus *Pithonella* Based on Exquisitely Preserved Turonian Material from Tanzania. *Journal of Paleontology*, 87(6), 1077-1106. http://dx.doi.org/10.1666/12-121.

Wendler, J. E., Meyers, S. R., Wendler, I., Kuss, J., 2014. A million-year-scale astronomical control on Late Cretaceous sea-level. *Newsletters on Stratigraphy*, 47(1), 1-19. http://dx.doi.org/10.1127/0078-0421/2014/0038.

Wendler, J. E., Wendler, I., 2016. What drove sea-level fluctuations during the mid-Cretaceous greenhouse climate?. *Palaeogeography, Palaeoclimatology, Palaeoecology*, 441, 412-419. http://dx.doi.org/10.1016/j.palaeo.2015.08.029.

Wiedmann, J., Butt, A., Einsele, G., 1978. Vergleich von marokkanischen Kreide-Küstenaufschlüssen und Tiefseebohrungen (DSDP): Stratigraphie,

Paläoenvironment und Subsidenz an einem passiven Kontinentalrand. *Geologische Rundschau*, 67, 454–508, http://dx.doi.org/10.1007/BF01802800.

Wiedmann, J., Butt, A., Einsele, G., 1982. Cretaceous Stratigraphy, Environment, and Subsidence History at the Moroccan Continental Margin. In: (Eds.), Geology of the Northwest African Continental Margin (Eds von Rad, U., Hinz, K., Sarnthein, M., Seibold, E.), pp. 366–395. *Springer*, Berlin Heidelberg.

Wilson, P. A., Norris, R. D., Cooper, M. J., 2002. Testing the Cretaceous greenhouse hypothesis using glassy foraminiferal calcite from the core of the Turonian tropics on Demerara Rise. *Geology*, 30(7), 607–610. http://dx.doi.org/10.1130/0091-7613(2002)030<0607:TTCGHU>2.0.CO;2.

Zachos, J. C., McCarren, H., Murphy, B., Röhl, U., Westerhold, T., 2010. Tempo and scale of late Paleocene and early Eocene carbon isotope cycles: Implications for the origin of hyperthermals. *Earth and Planetary Science Letters*, 299(1-2), 242-249. http://dx.doi.org/10.1016/j.epsl.2010.09.004.

Appendix A:

XRF-data

XRF-data

Plotted in the following diagrams are the raw-XRF-data available for Log-ratio calculation. The labels 10kV, 30kV and 50kV refer to the different tube-settings. Further information are presented in Supplementary Material Table S2.2.

10kV-setting:

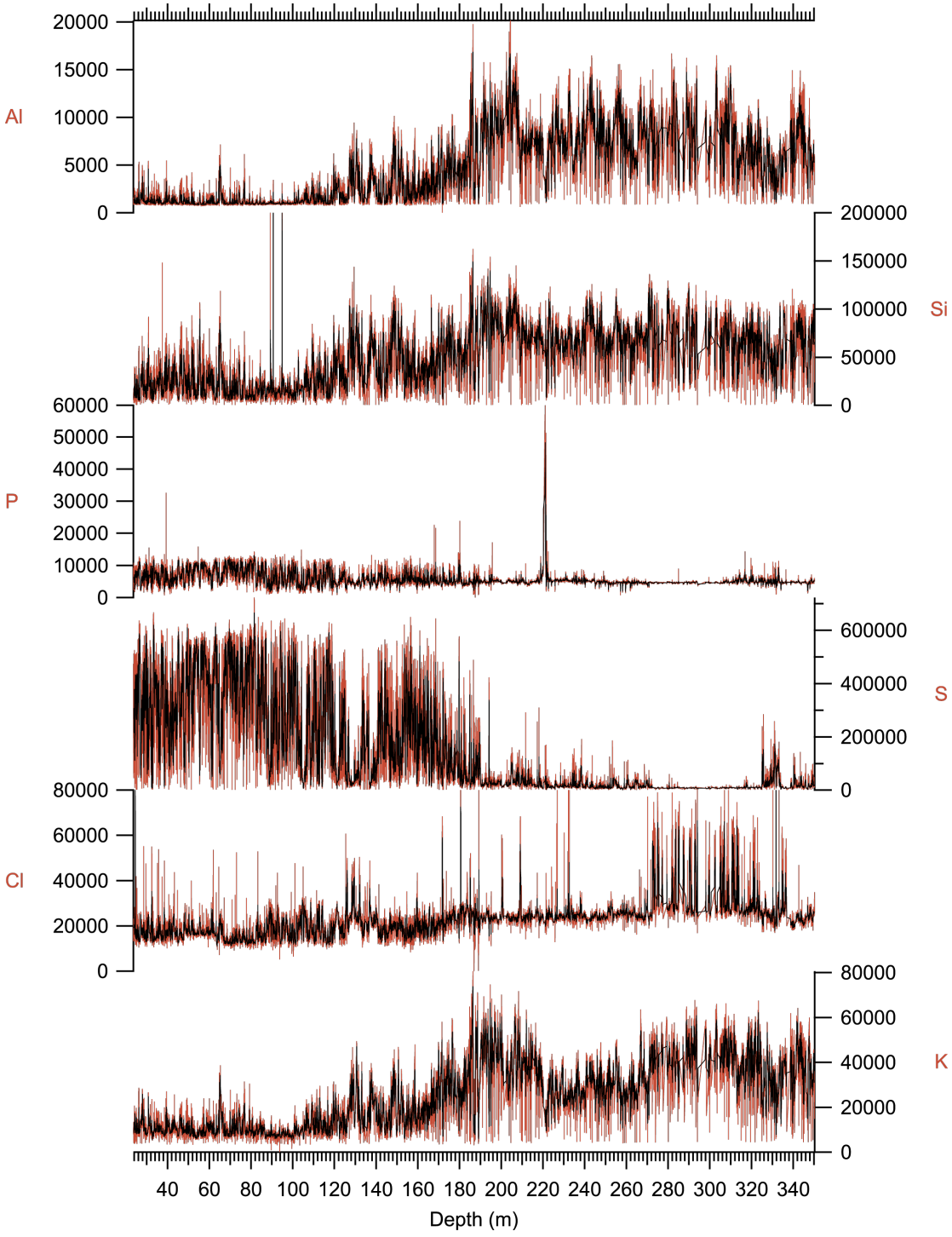

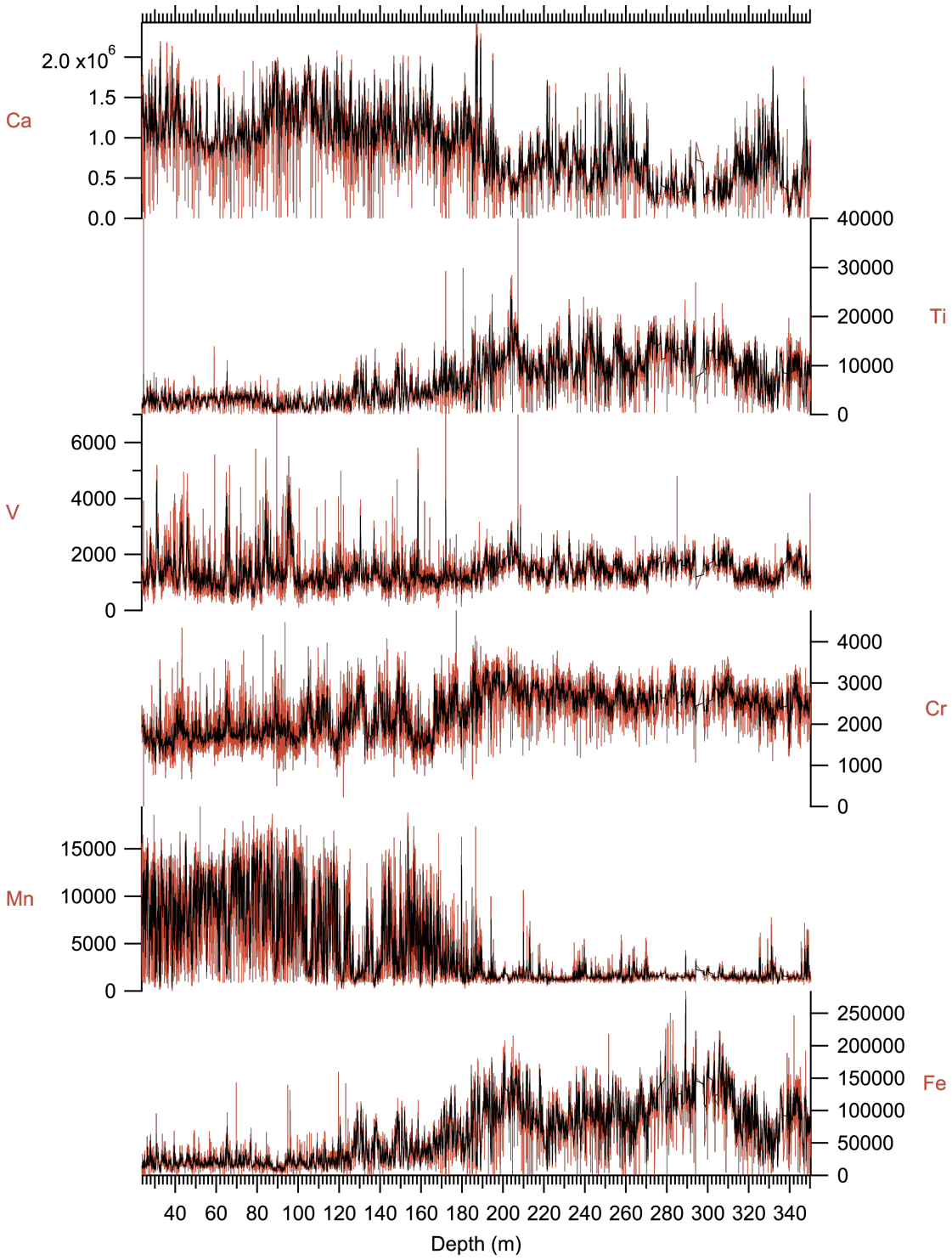
Ca
2.0 x10^6
1.5
1.0
0.5
0.0
Ti
40000
30000
20000
10000
0
V
6000
4000
2000
0
Cr
4000
3000
2000
1000
0
Mn
15000
10000
5000
0
Fe
250000
200000
150000
100000
50000
0
40 60 80 100 120 140 160 180 200 220 240 260 280 300 320 340
Depth (m)

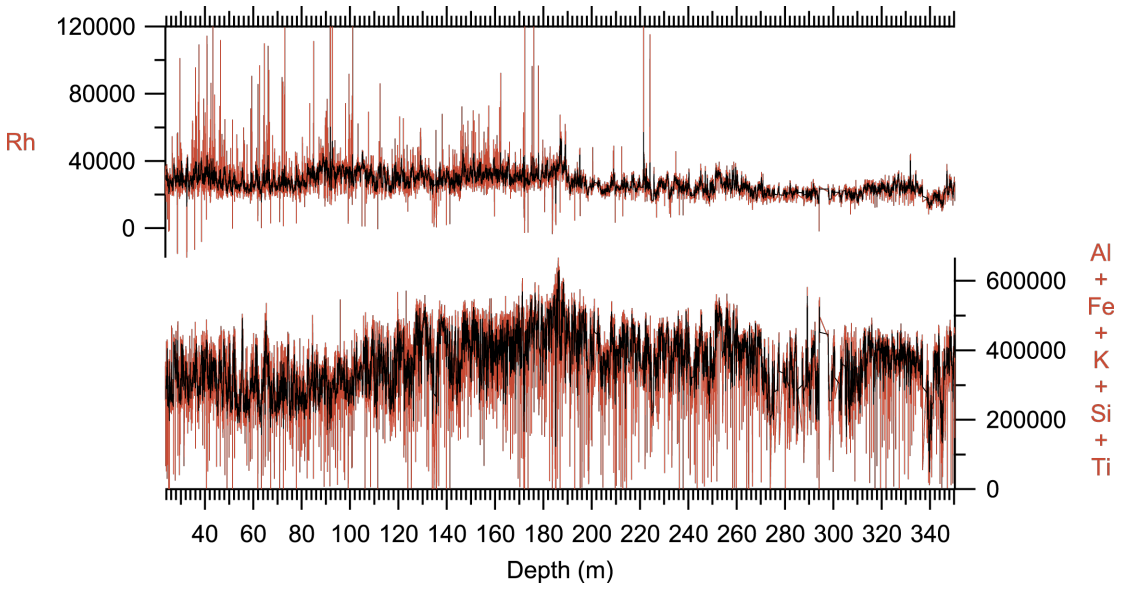

30kV-setting:

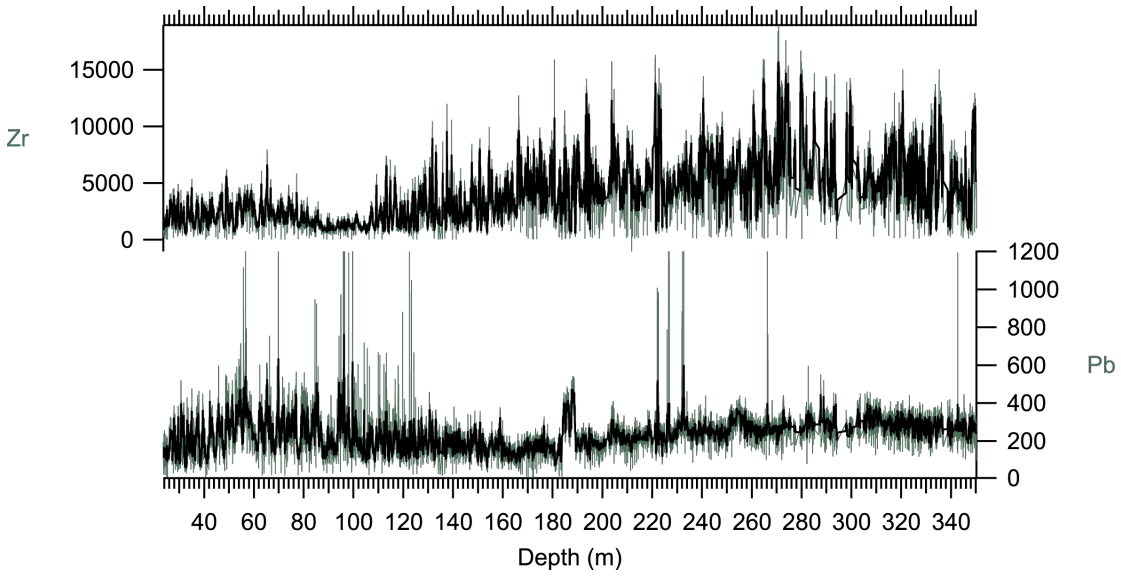

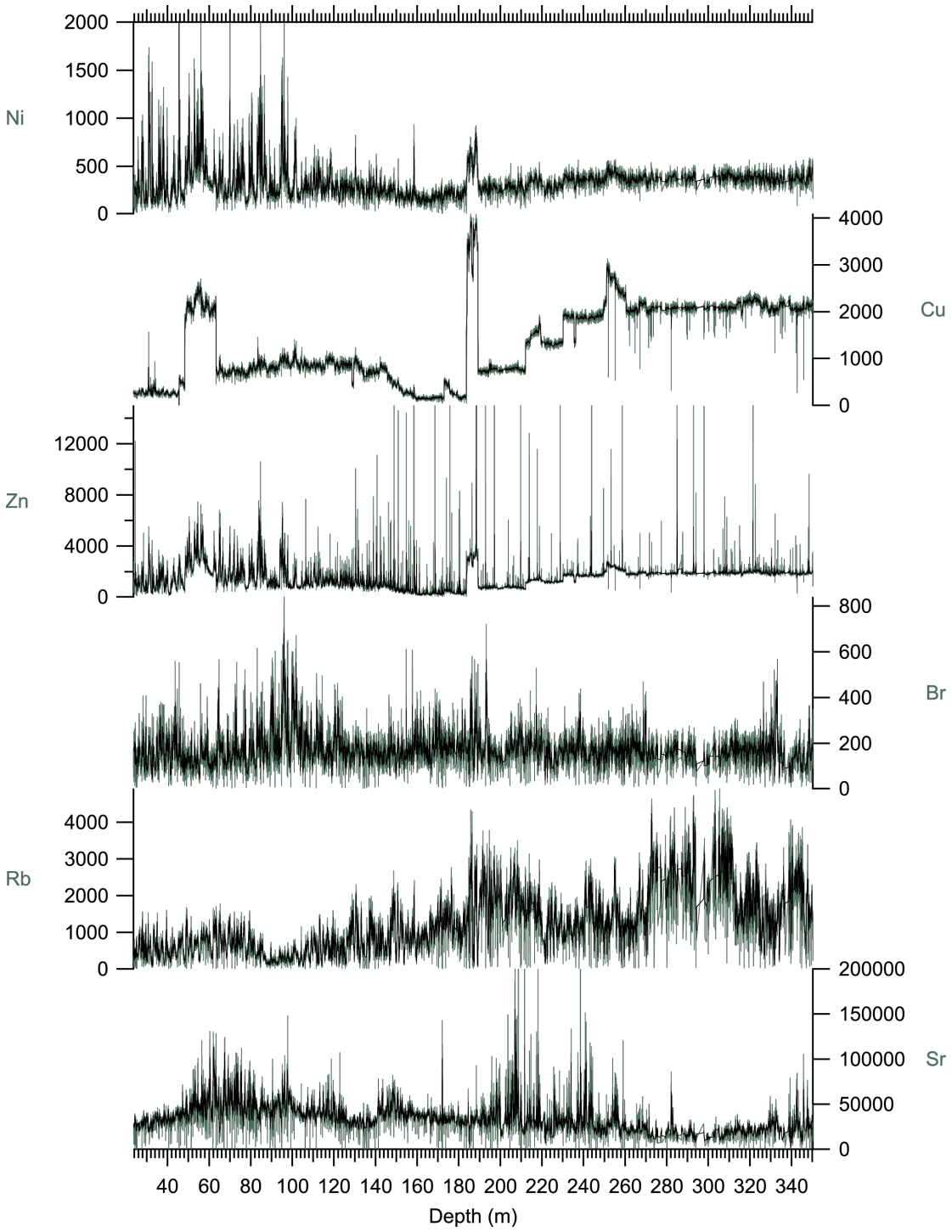
Ni
2000
1500
1000
500
0
Cu
4000
3000
2000
1000
0
Zn
12000
8000
4000
0
Br
800
600
400
200
0
Rb
4000
3000
2000
1000
0
Sr
200000
150000
100000
50000
0
40 60 80 100 120 140 160 180 200 220 240 260 280 300 320 340
Depth (m)

50kV-setting:

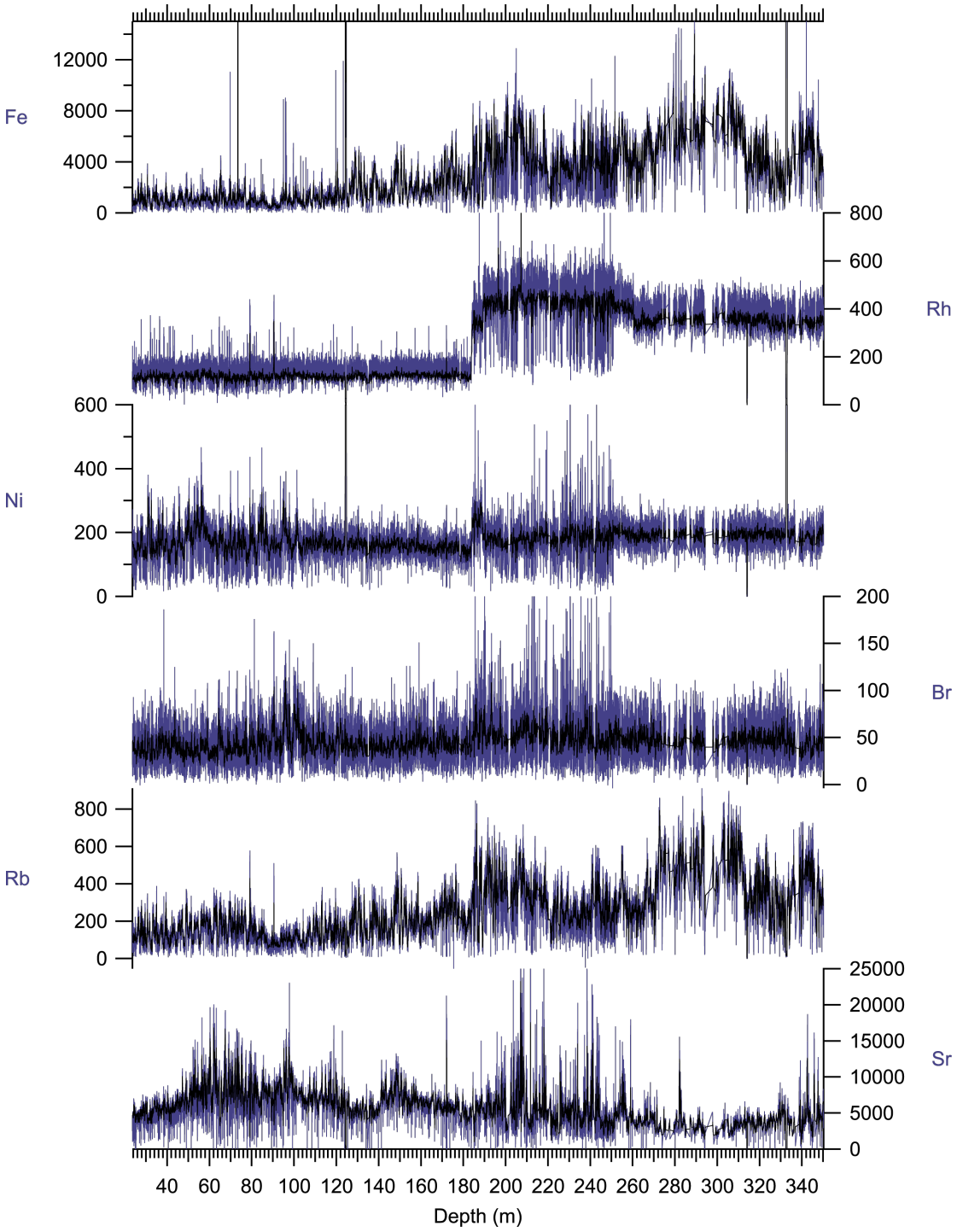

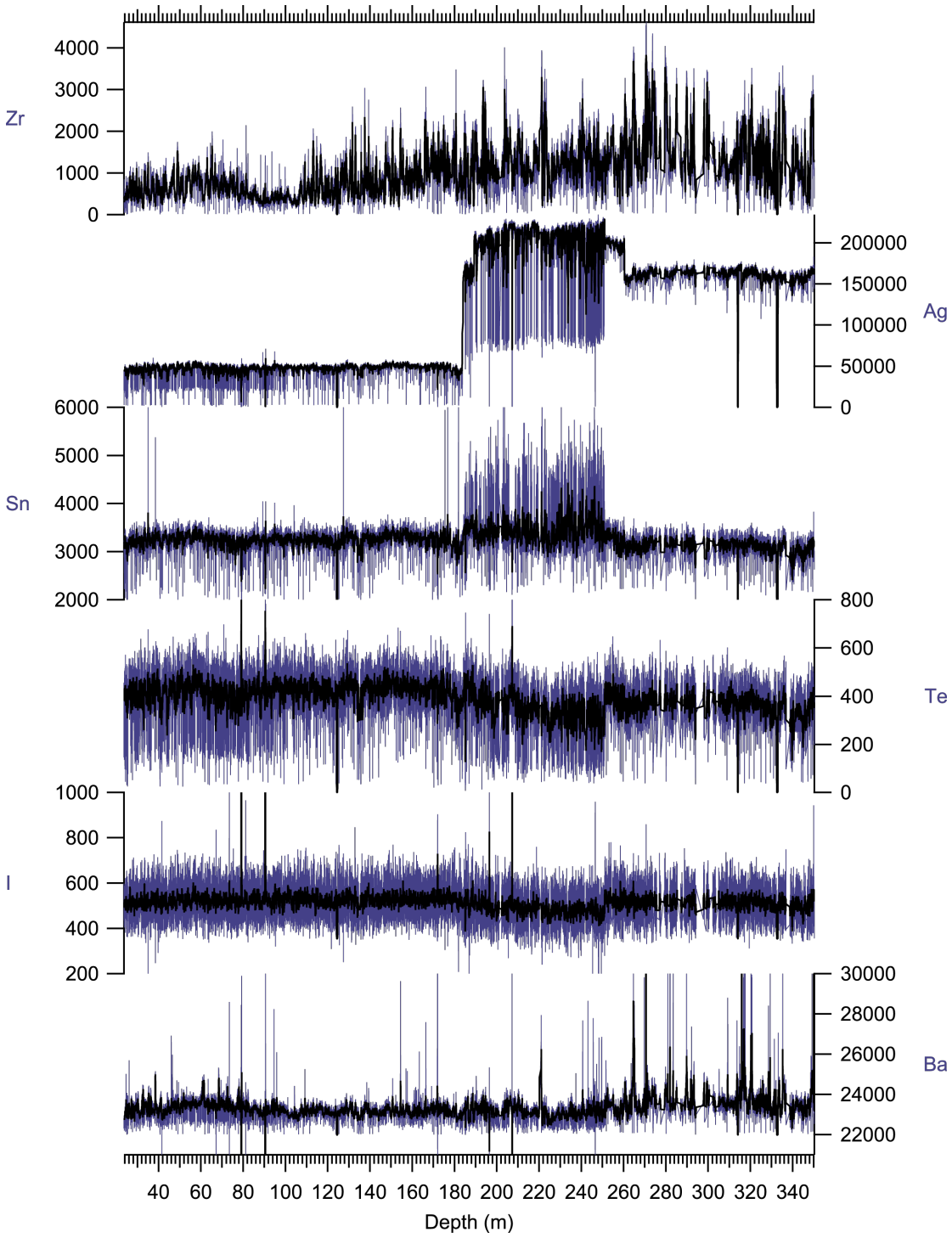
Zr
4000
3000
2000
1000
0
Ag
200000
150000
100000
50000
0
Sn
6000
5000
4000
3000
2000
Te
800
600
400
200
0
I
1000
800
600
400
200
Ba
30000
28000
26000
24000
22000
40 60 80 100 120 140 160 180 200 220 240 260 280 300 320 340
Depth (m)

Appendix B:

Linescan Core Images

Assembled Core Images

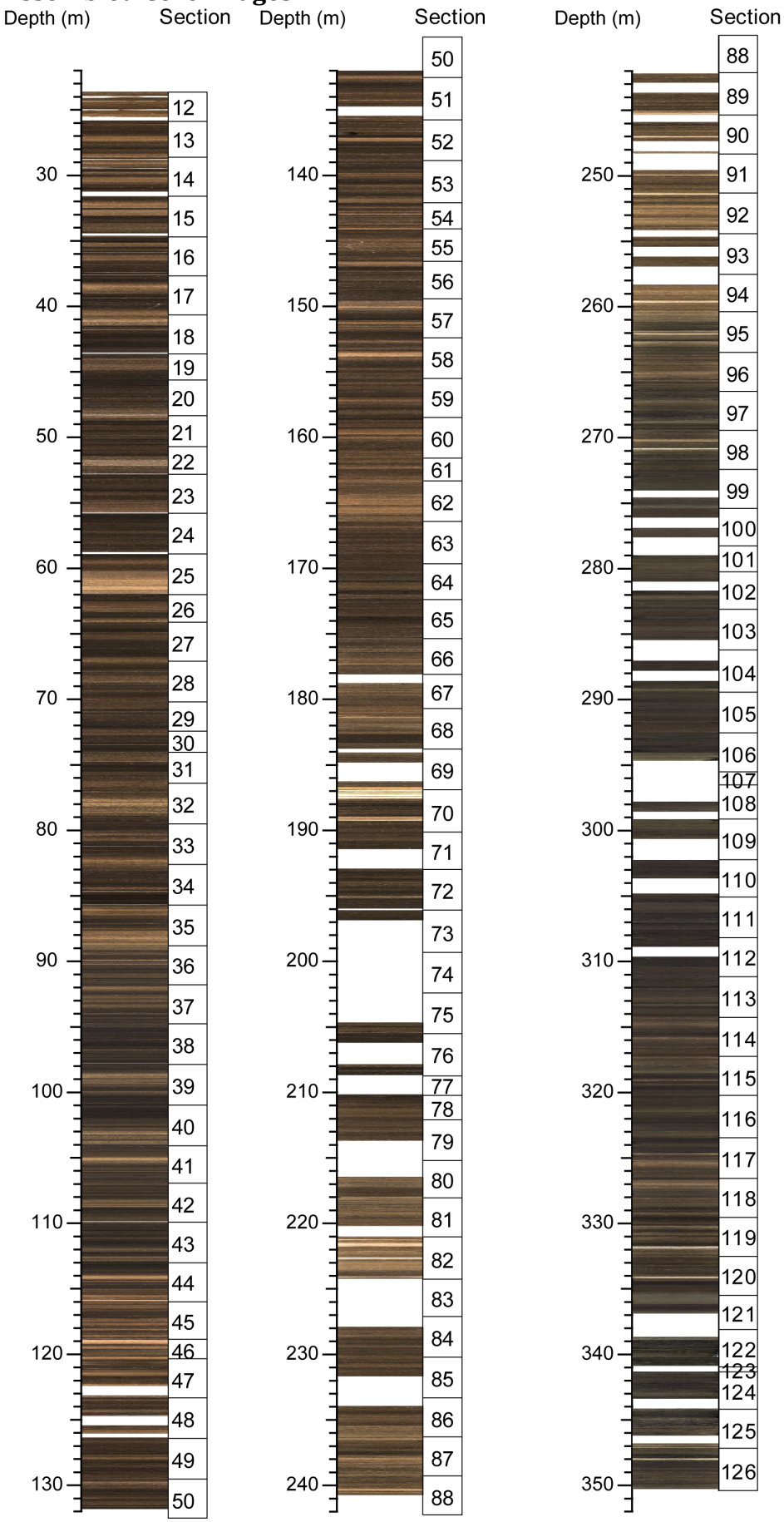

Detailed Linescan Images of individual Segments

Numbers on the right side of the core is the depth in cm within the Segment. Numbers at the bottom of the image identify Section / Segment. Numbers on the top left side of the core is the depth of the top of the segment in drillers depth (grey) and composite depth scale (black) used for plotting and analysis in m. Segments too fragile for linescanning are represented by white spaces. The length of these Segments is presented in Supplementary Material Table S2.1 of chapter 2.

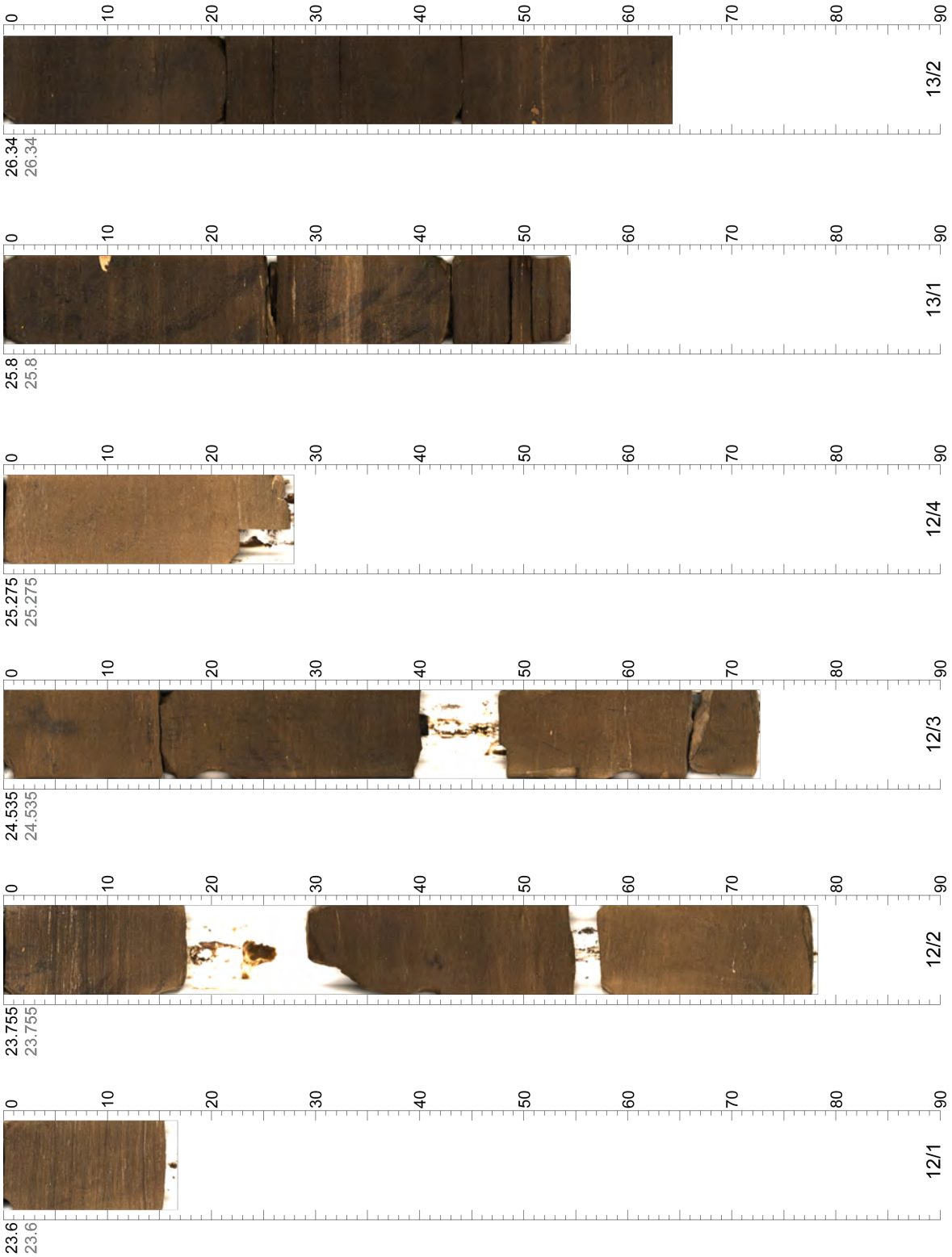
13/2
26.34
26.34
13/1
25.8
25.8
12/4
25.275
25.275
12/3
24.535
24.535
12/2
23.755
23.755
12/1
23.6
23.6

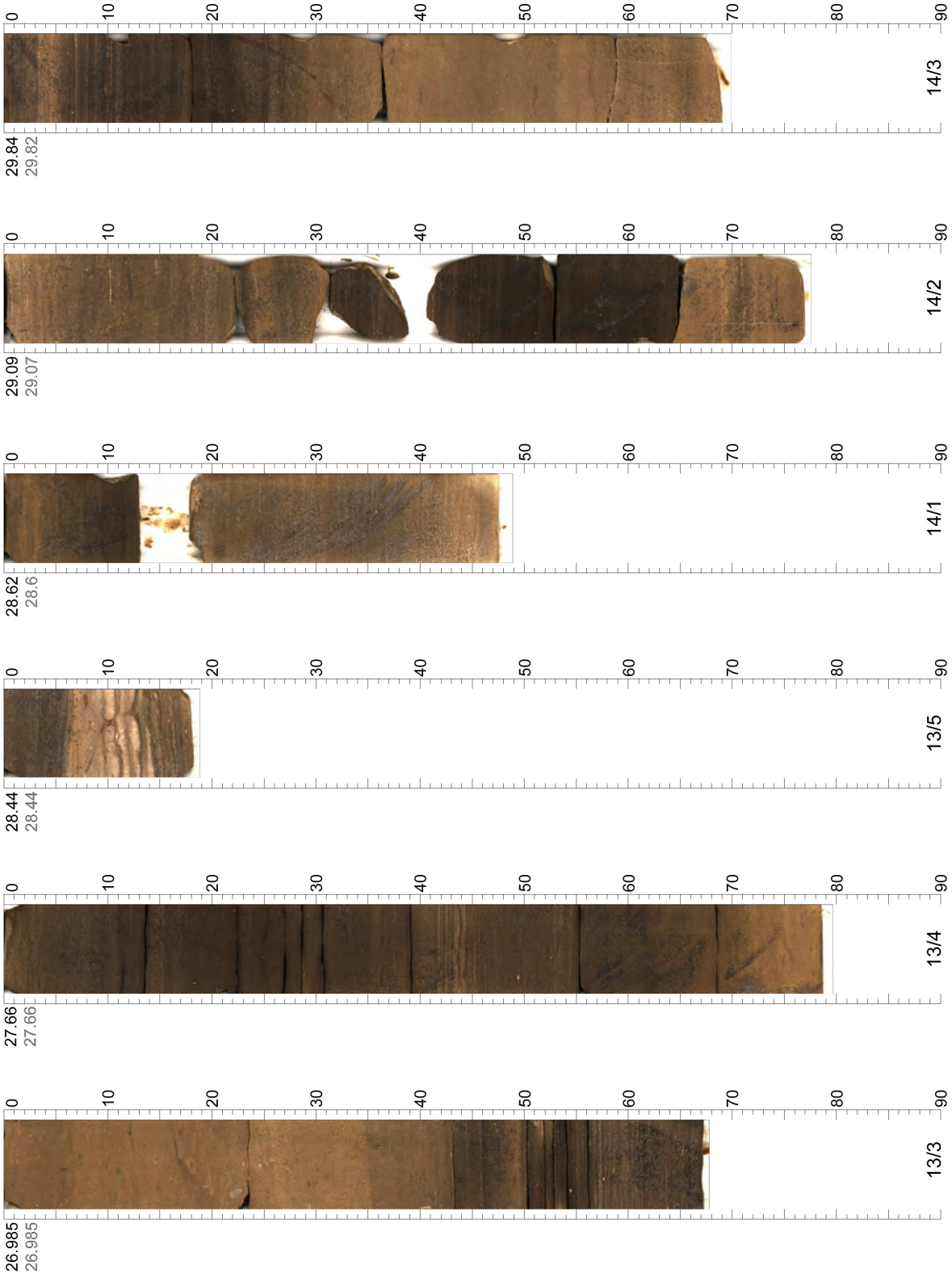
14/3
29.84
29.82
14/2
29.09
29.07
14/1
28.62
28.6
13/5
28.44
28.44
13/4
27.66
27.66
13/3
26.985
26.985

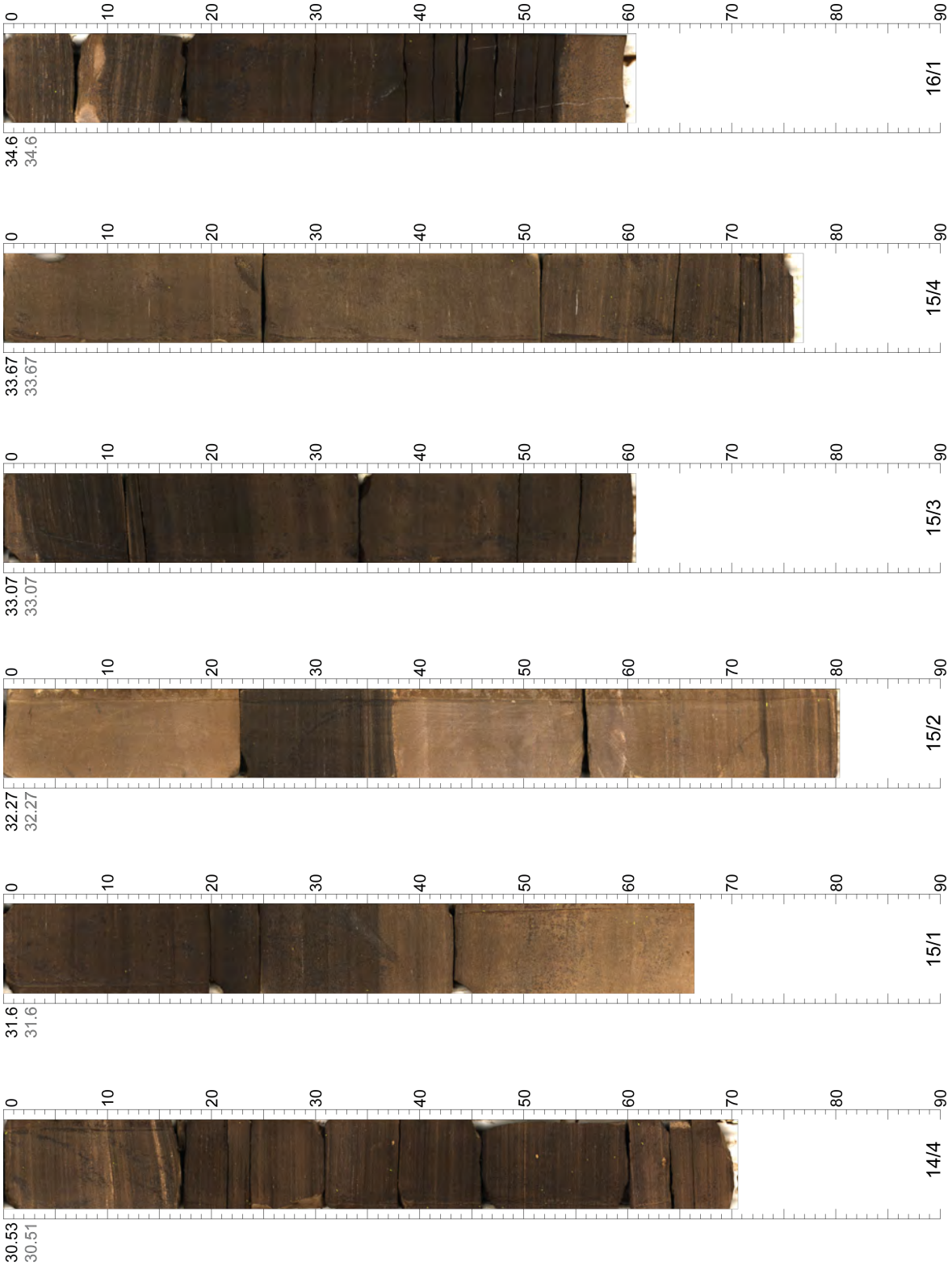
0
10
20
30
40
50
60
70
80
90
16/1
34.6
34.6
15/4
33.67
33.67
15/3
33.07
33.07
15/2
32.27
32.27
15/1
31.6
31.6
14/4
30.53
30.51

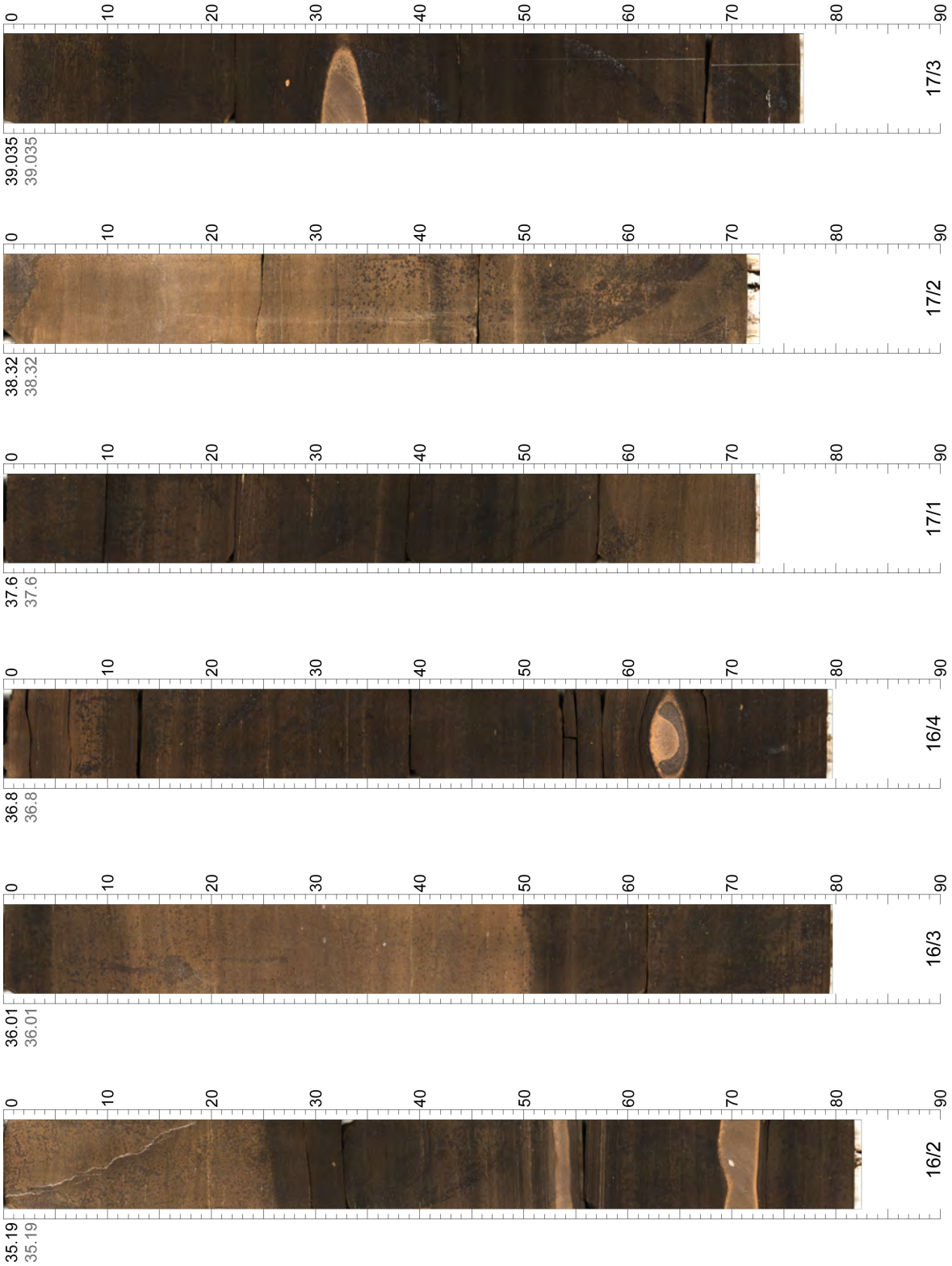
0
10
20
30
40
50
60
70
80
90
17/3
39.035
39.035
17/2
38.32
38.32
17/1
37.6
37.6
16/4
36.8
36.8
16/3
36.01
36.01
16/2
35.19
35.19

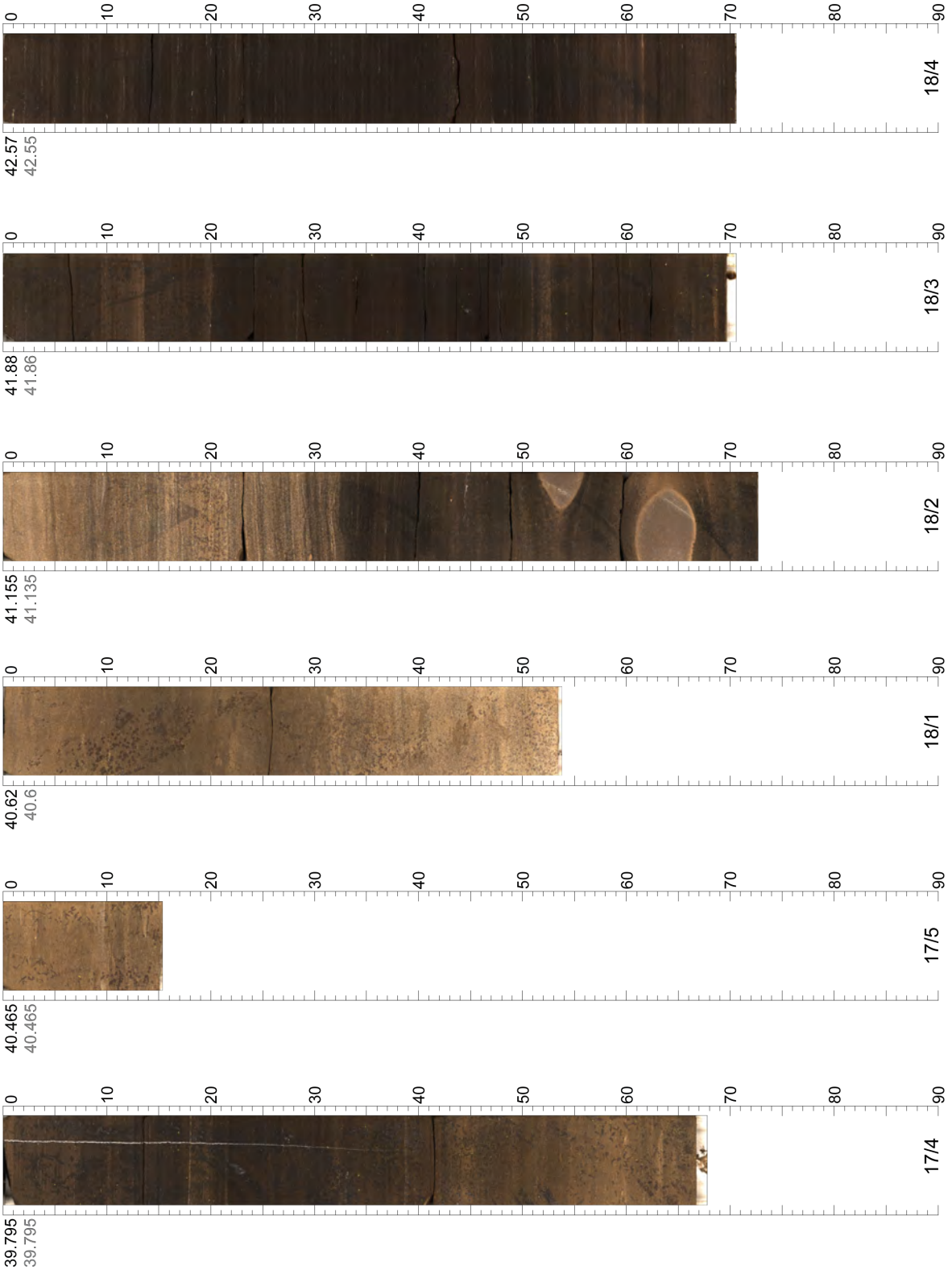
0
10
20
30
40
50
60
70
80
90
18/4
42.57
42.55
18/3
41.88
41.86
18/2
41.155
41.135
18/1
40.62
40.6
17/5
40.465
40.465
17/4
39.795
39.795

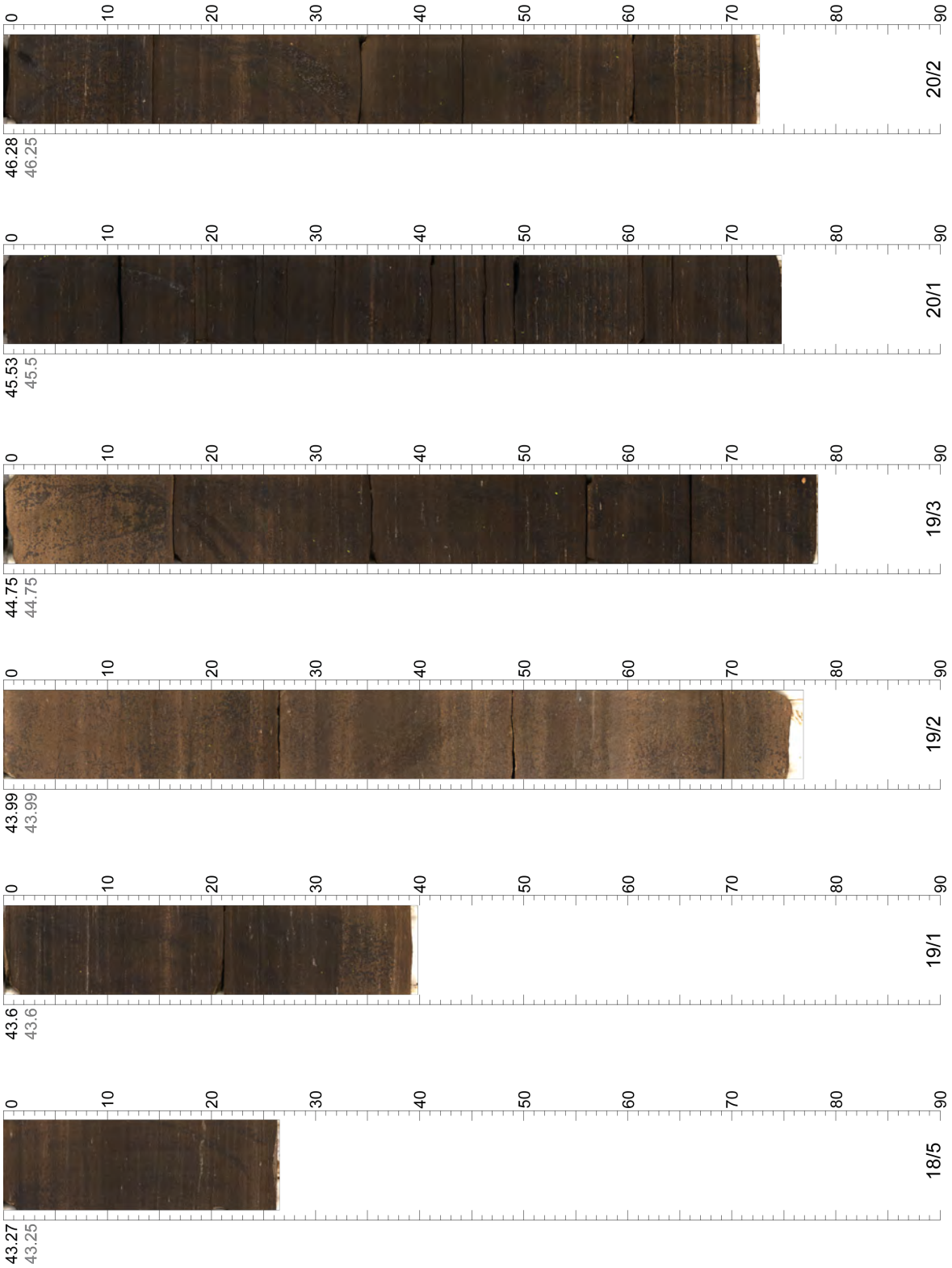
0
10
20
30
40
50
60
70
80
90
20/2
46.28
46.25
20/1
45.53
45.5
19/3
44.75
44.75
19/2
43.99
43.99
19/1
43.6
43.6
18/5
43.27
43.25

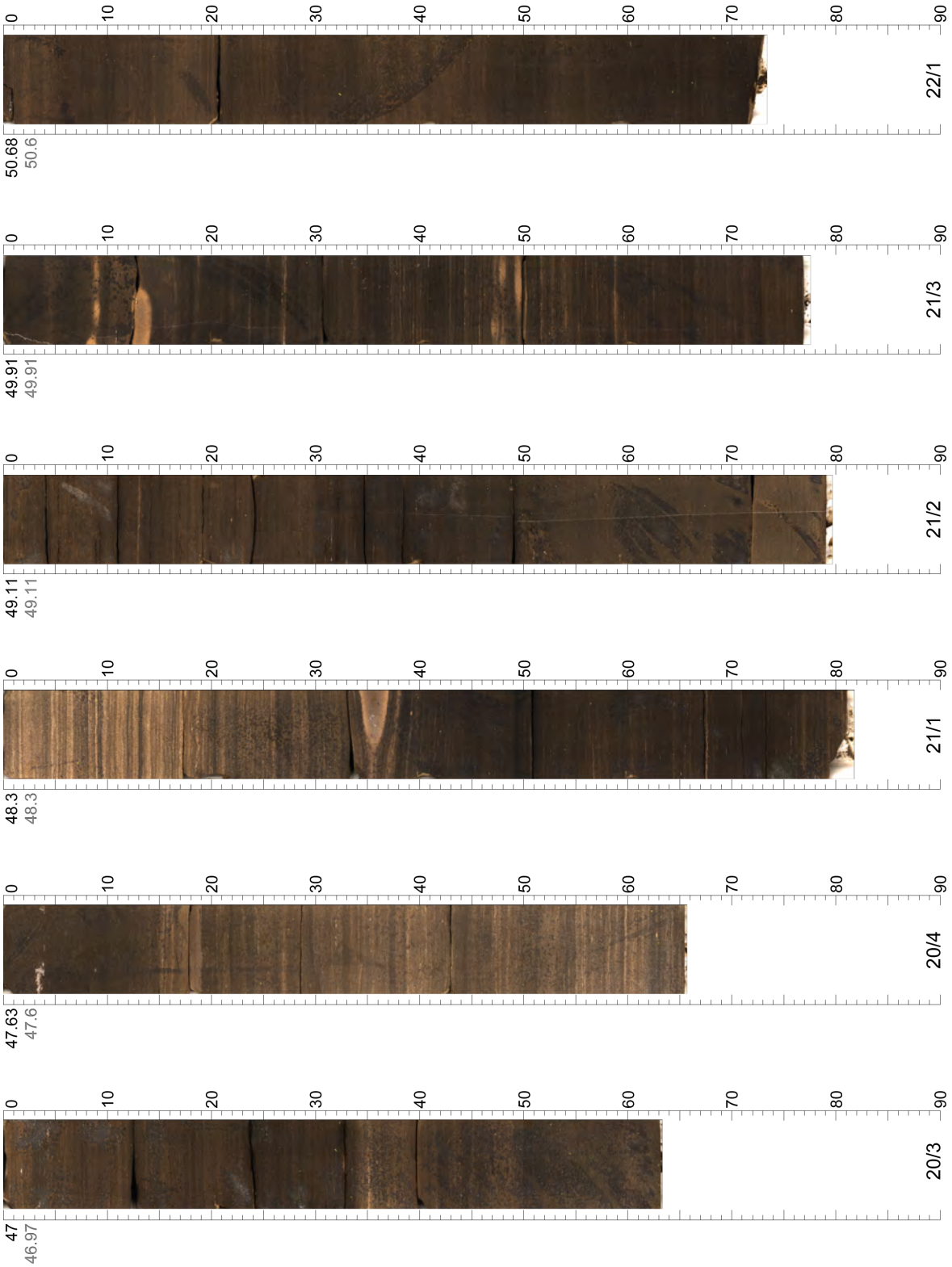
0
10
20
30
40
50
60
70
80
90
22/1
50.68
50.6
21/3
49.91
49.91
21/2
49.11
49.11
21/1
48.3
48.3
20/4
47.63
47.6
20/3
47
46.97

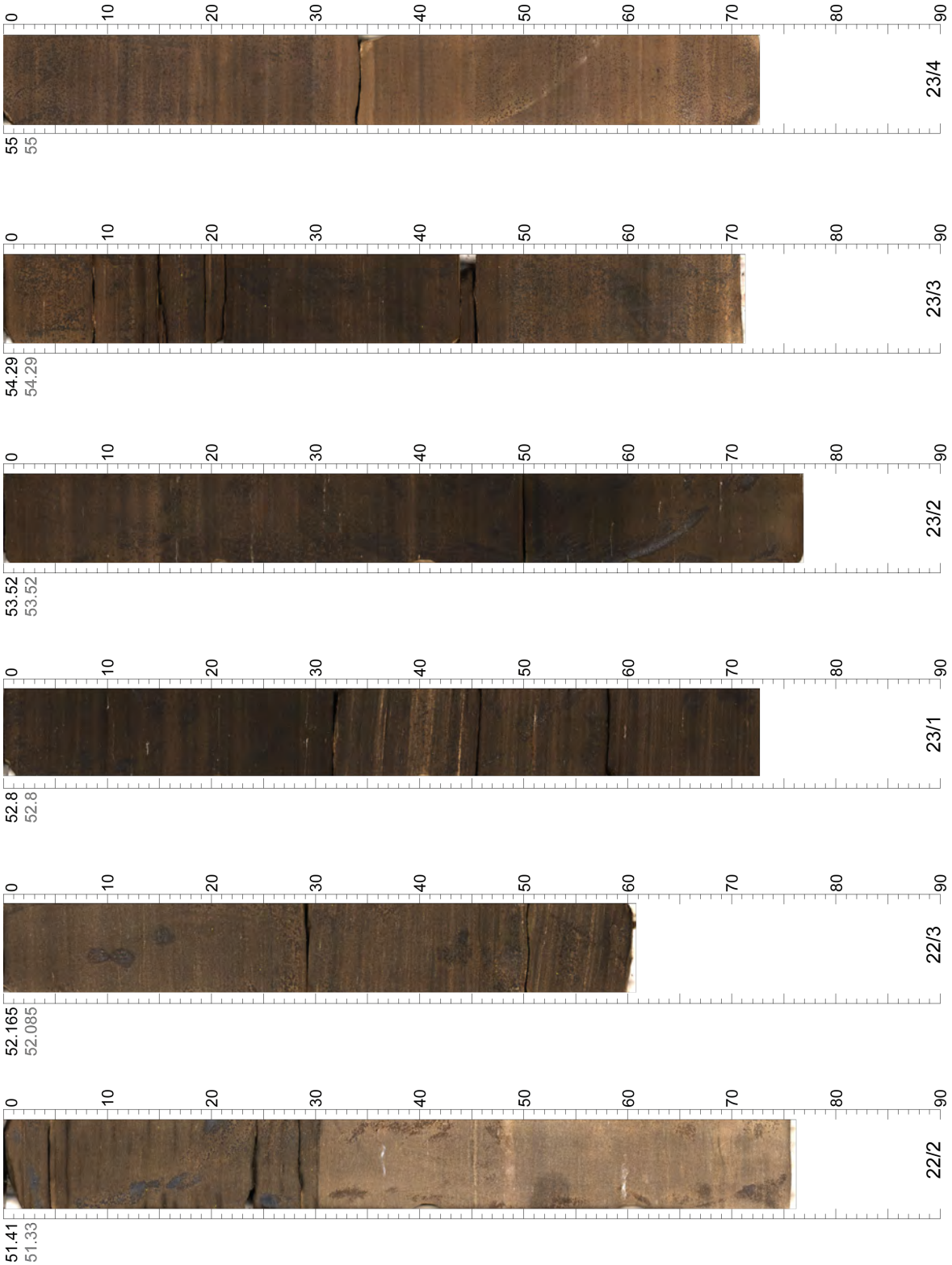
0
10
20
30
40
50
60
70
80
90
23/4
55
55
23/3
54.29
54.29
23/2
53.52
53.52
23/1
52.8
52.8
22/3
52.165
52.085
22/2
51.41
51.33

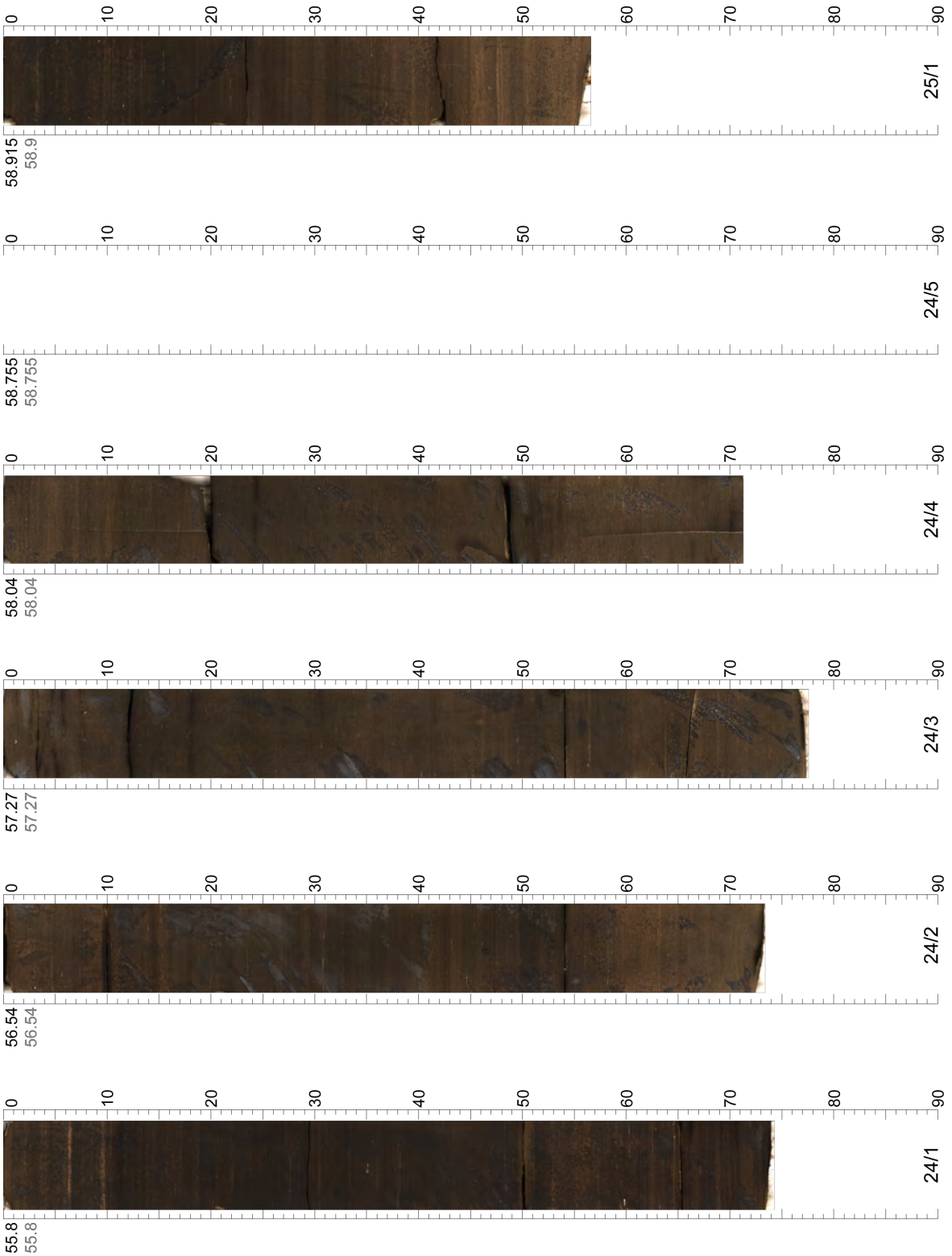
25/1
58.915
58.9
24/5
58.755
58.755
24/4
58.04
58.04
24/3
57.27
57.27
24/2
56.54
56.54
24/1
55.8
55.8

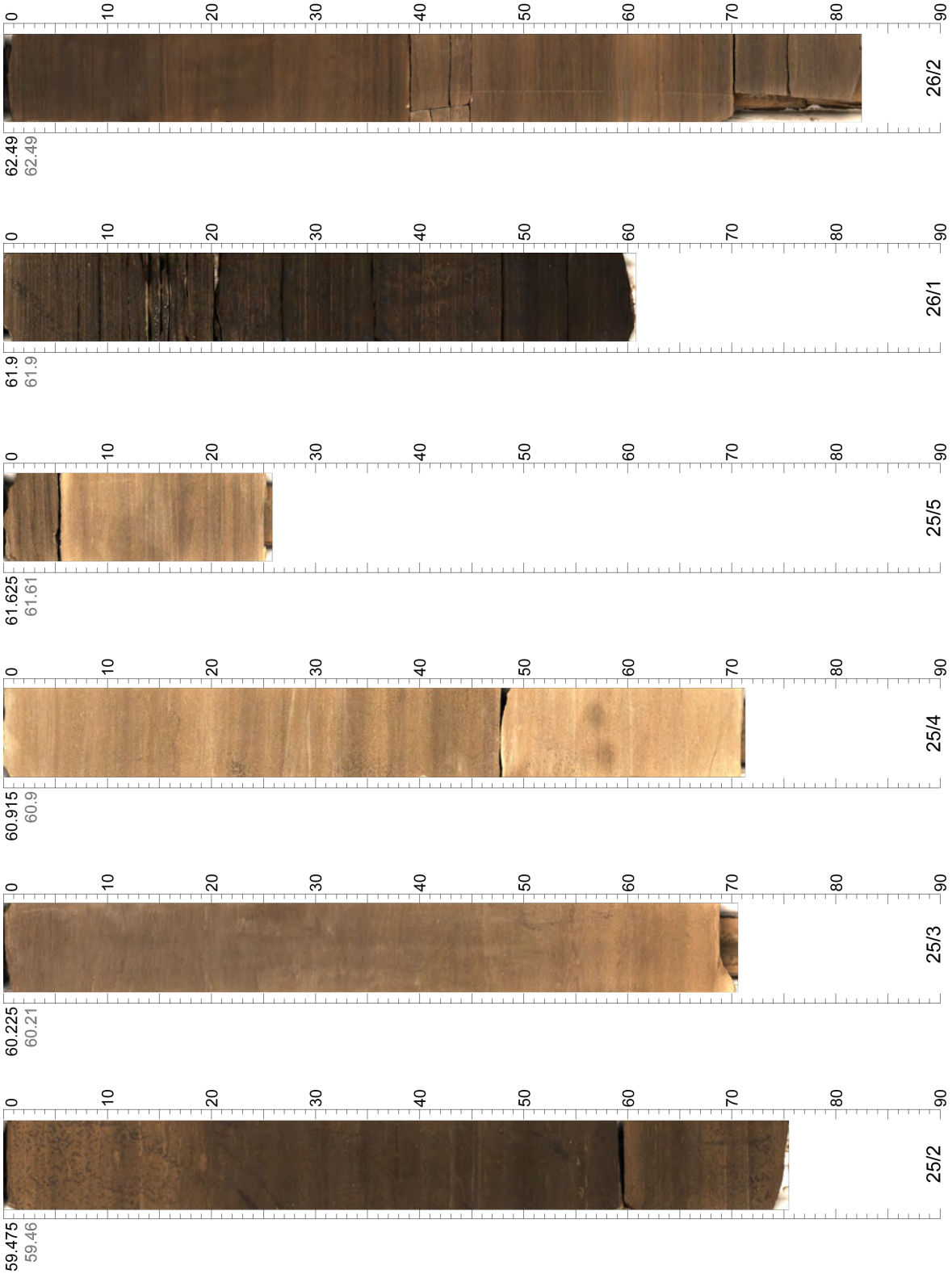
0
10
20
30
40
50
60
70
80
90
26/2
62.49
62.49
26/1
61.9
61.9
25/5
61.625
61.61
25/4
60.915
60.9
25/3
60.225
60.21
25/2
59.475
59.46

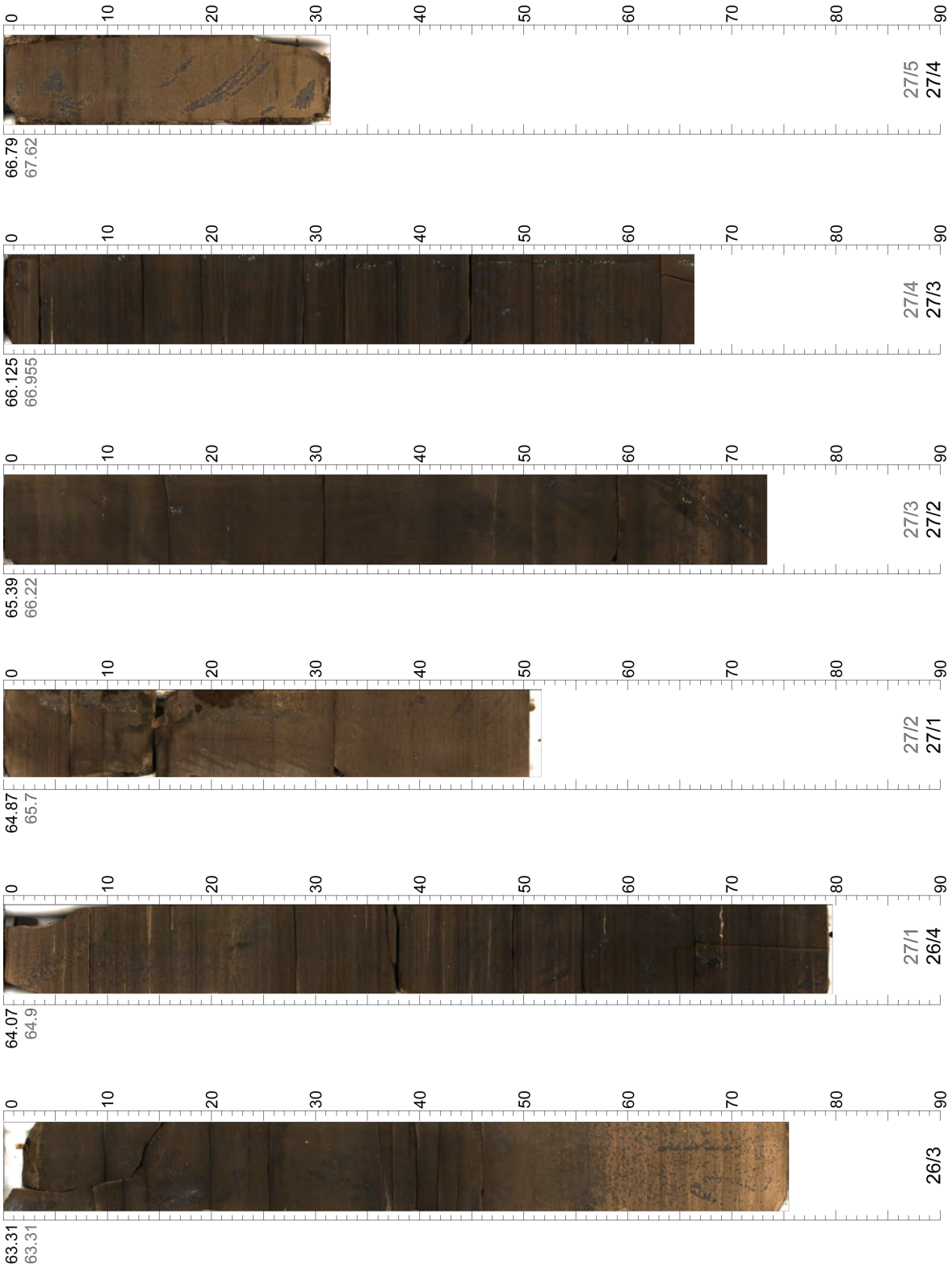
0
10
20
30
40
50
60
70
80
90
27/5
27/4
66.79
67.62
27/4
27/3
66.125
66.955
27/3
27/2
65.39
66.22
27/2
27/1
64.87
65.7
27/1
26/4
64.07
64.9
26/3
63.31
63.31

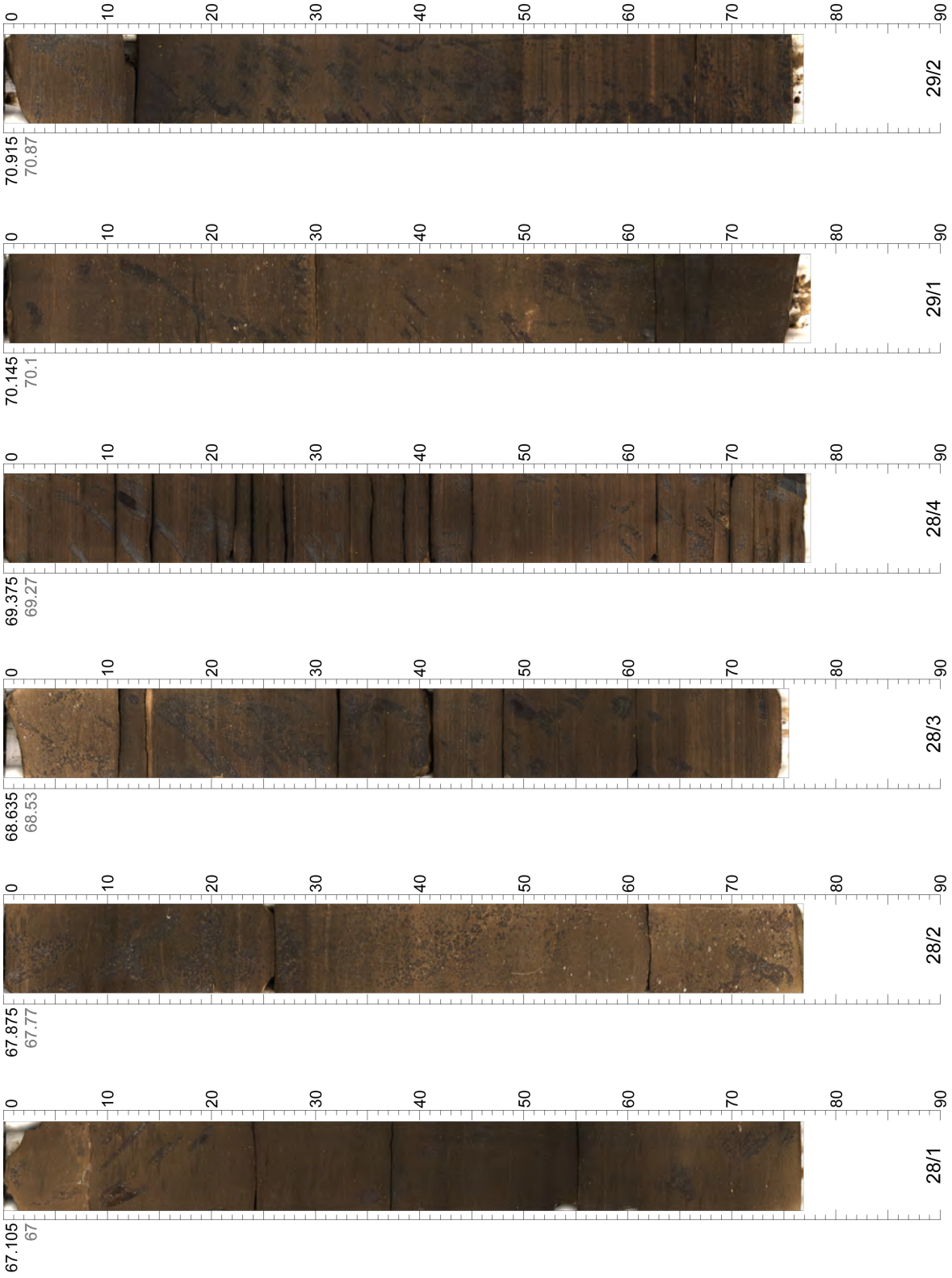
0
10
20
30
40
50
60
70
80
90
29/2
70.915
70.87
29/1
70.145
70.1
28/4
69.375
69.27
28/3
68.635
68.53
28/2
67.875
67.77
28/1
67.105
67

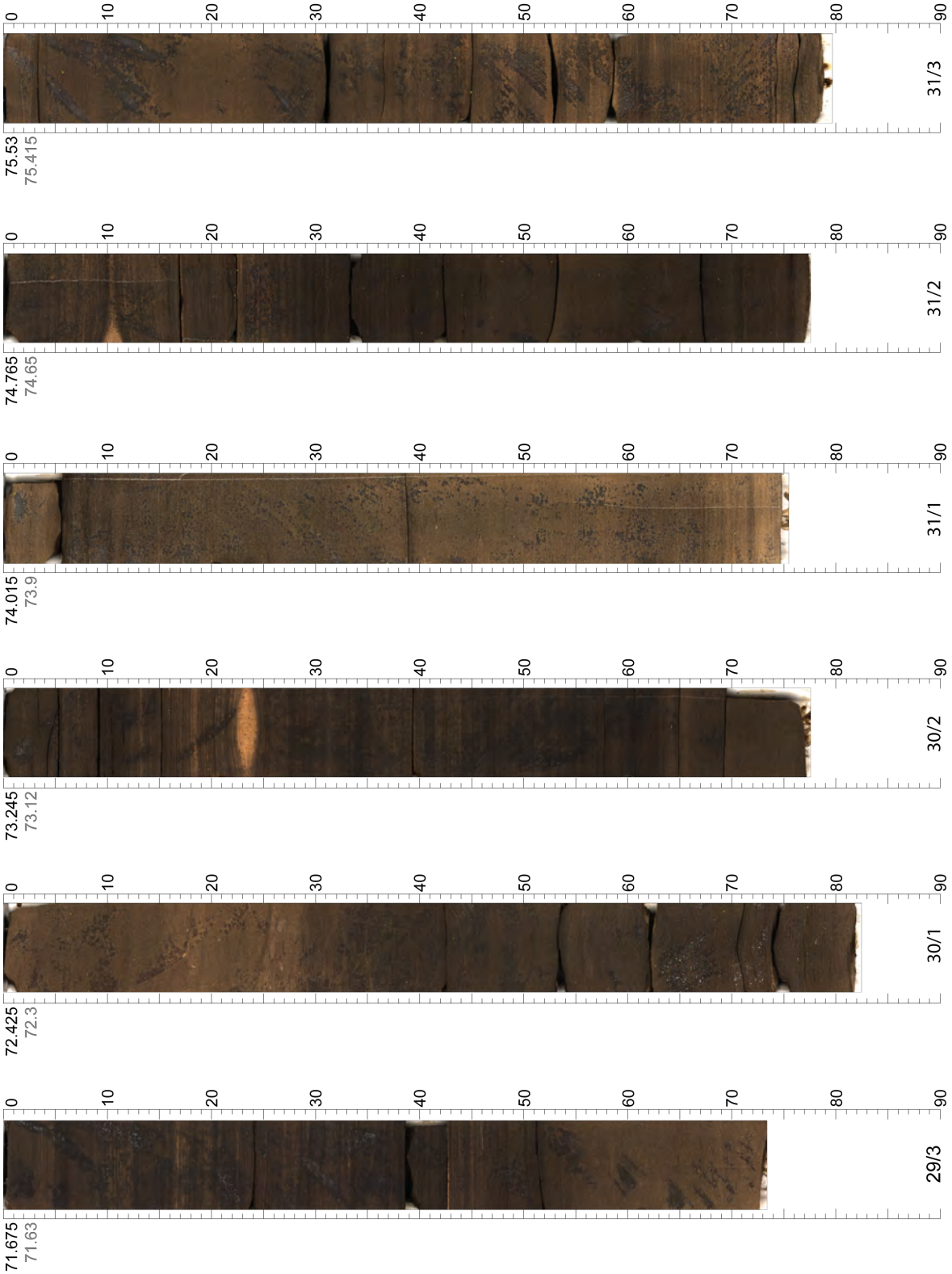
0
10
20
30
40
50
60
70
80
90
31/3
75.53
75.415
31/2
74.765
74.65
31/1
74.015
73.9
30/2
73.245
73.12
30/1
72.425
72.3
29/3
71.675
71.63

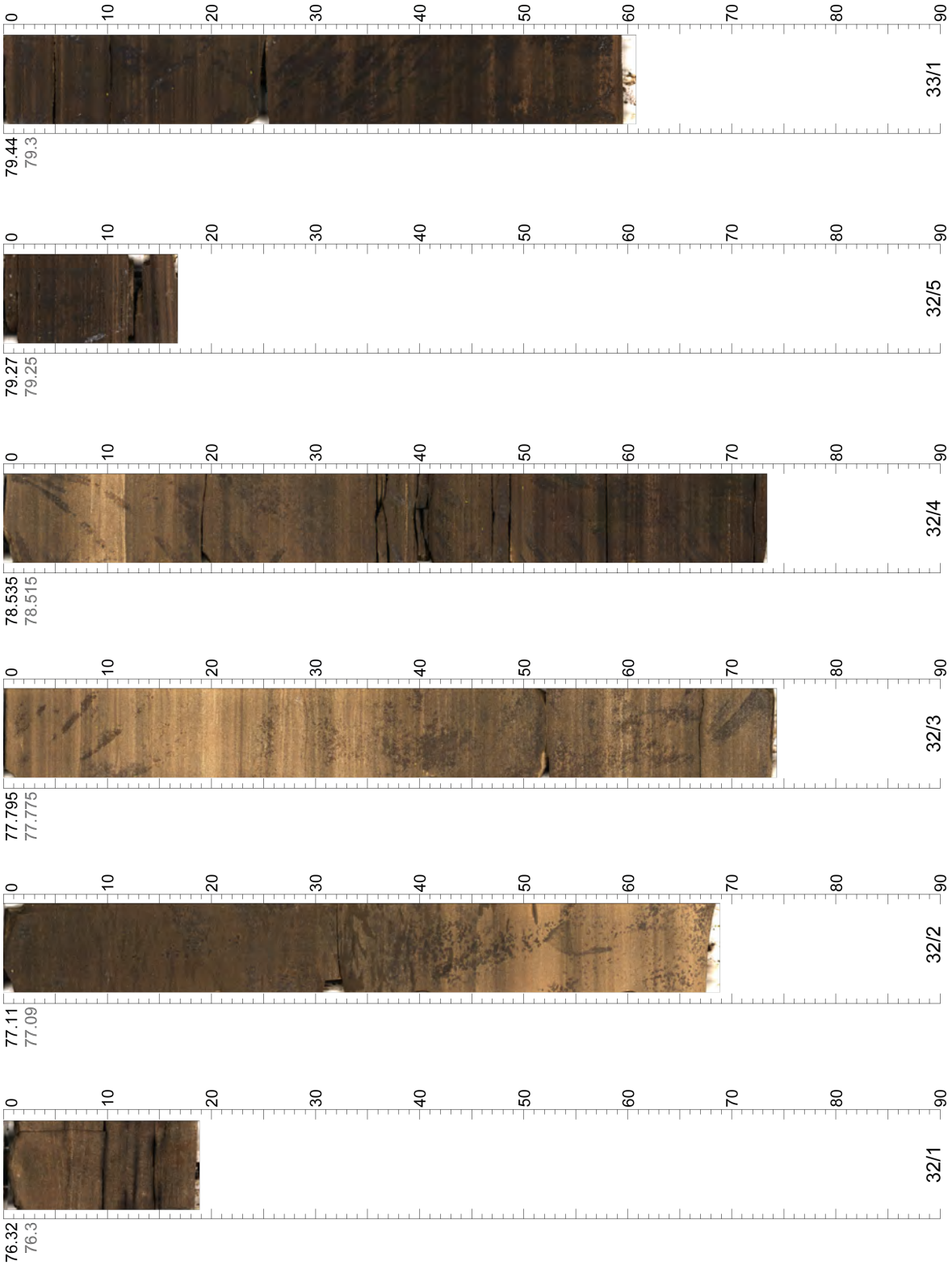
0
10
20
30
40
50
60
70
80
90
33/1
79.44
79.3
32/5
79.27
79.25
32/4
78.535
78.515
32/3
77.795
77.775
32/2
77.11
77.09
32/1
76.32
76.3

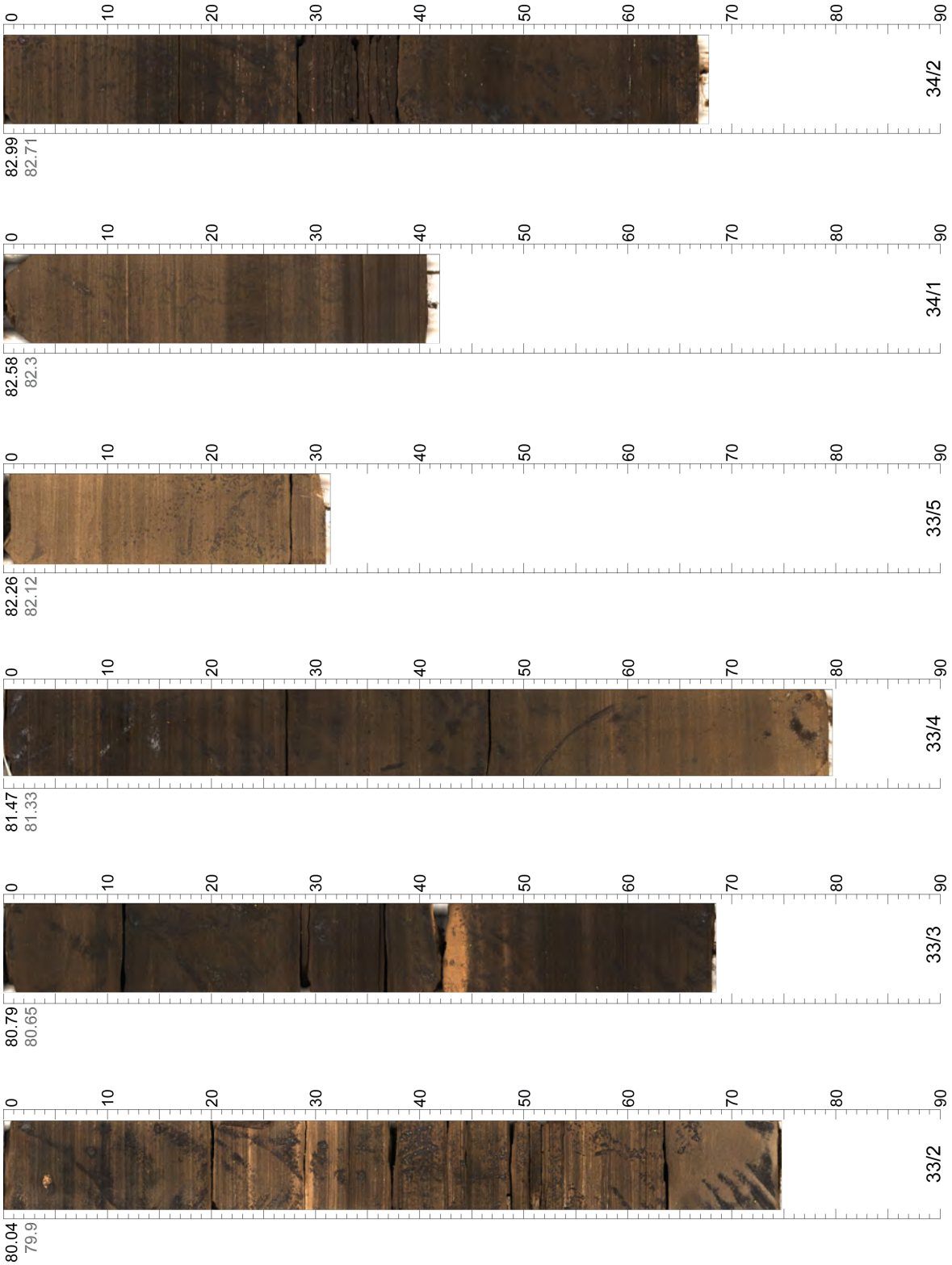
0
10
20
30
40
50
60
70
80
90
34/2
82.99
82.71
34/1
82.58
82.3
33/5
82.26
82.12
33/4
81.47
81.33
33/3
80.79
80.65
33/2
80.04
79.9

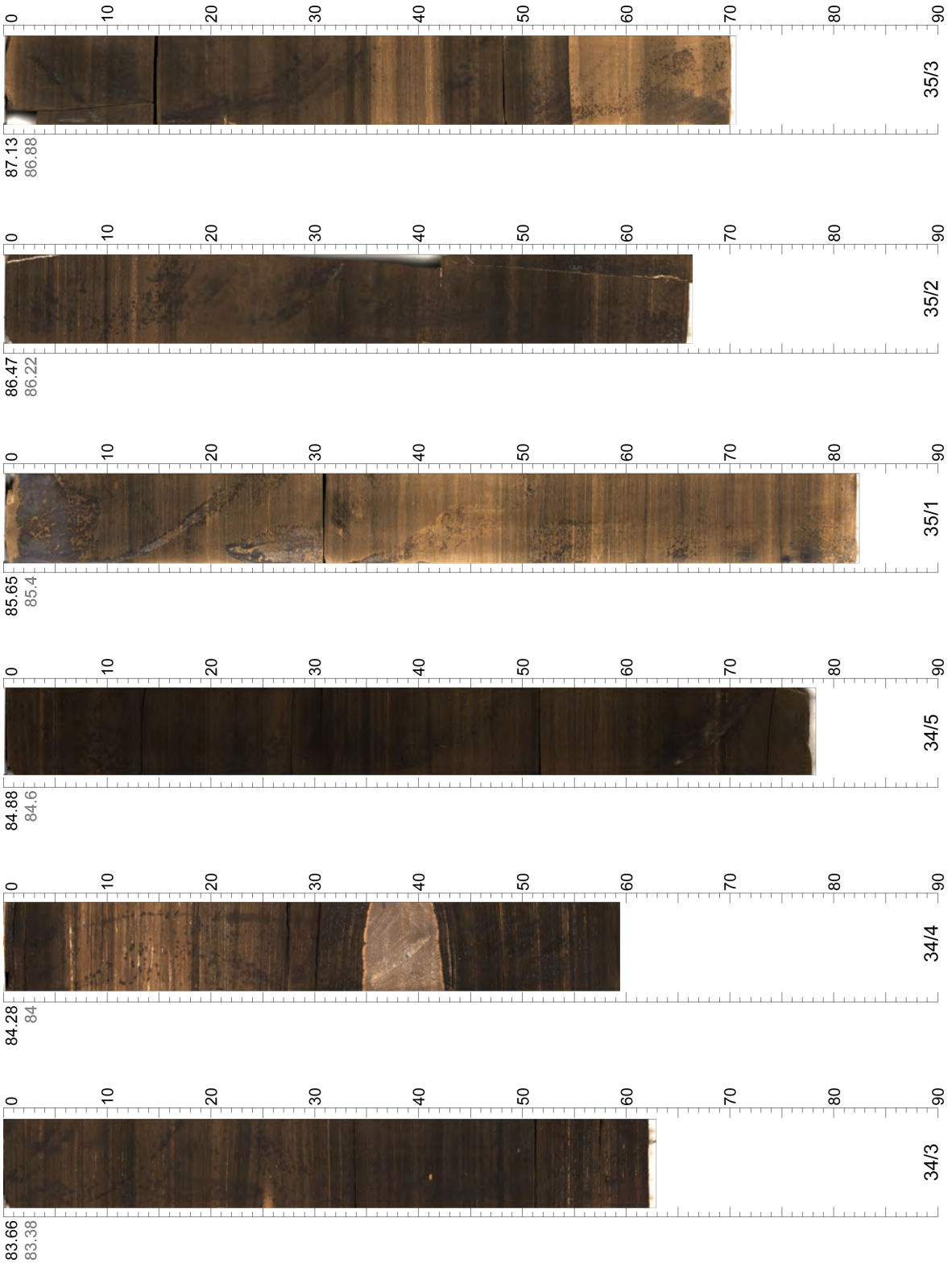
0
10
20
30
40
50
60
70
80
90
35/3
87.13
86.88
35/2
86.47
86.22
35/1
85.65
85.4
34/5
84.88
84.6
34/4
84.28
84
34/3
83.66
83.38

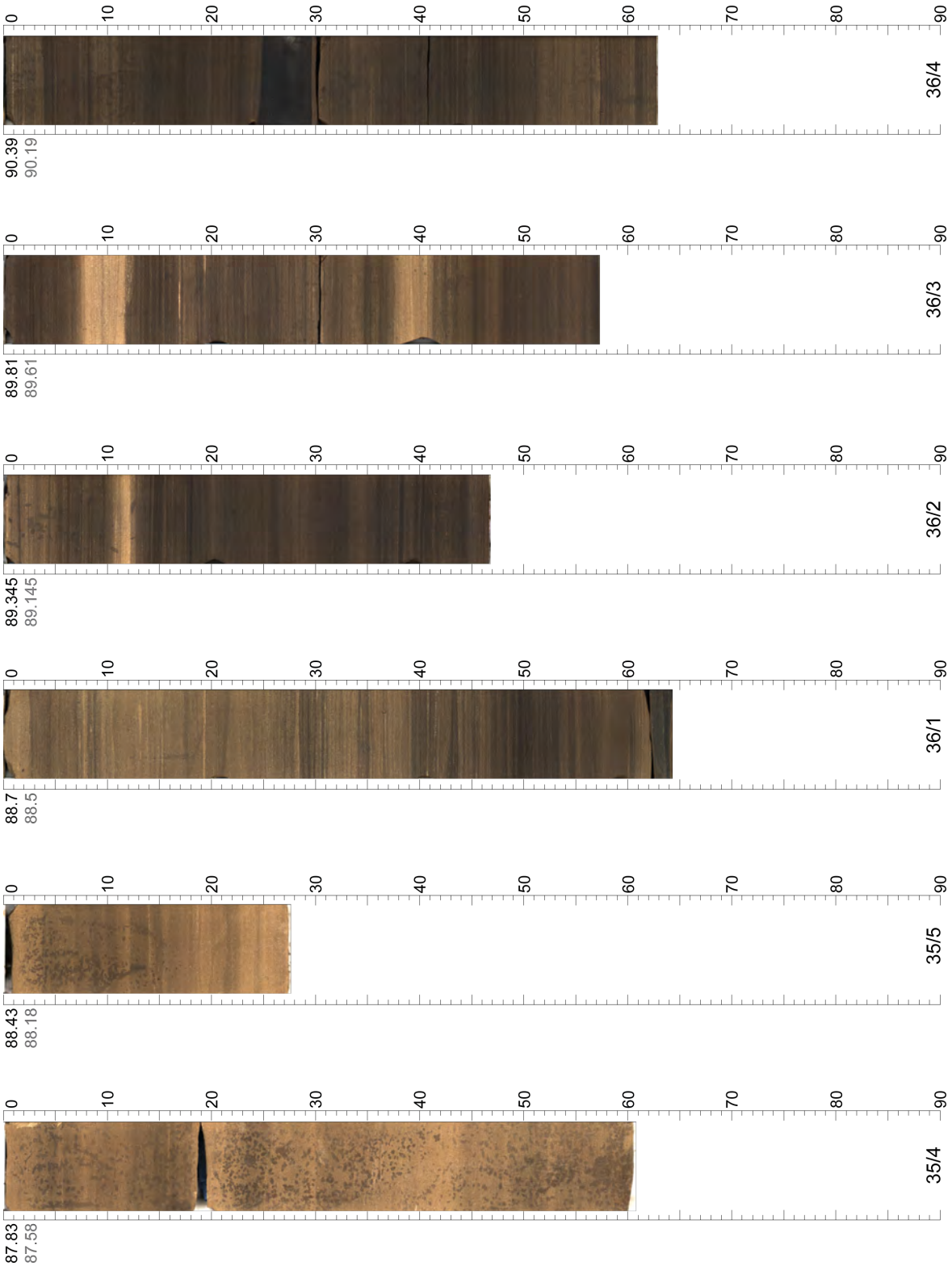
0
10
20
30
40
50
60
70
80
90
36/4
90.39
90.19
36/3
89.81
89.61
36/2
89.345
89.145
36/1
88.7
88.5
35/5
88.43
88.18
35/4
87.83
87.58

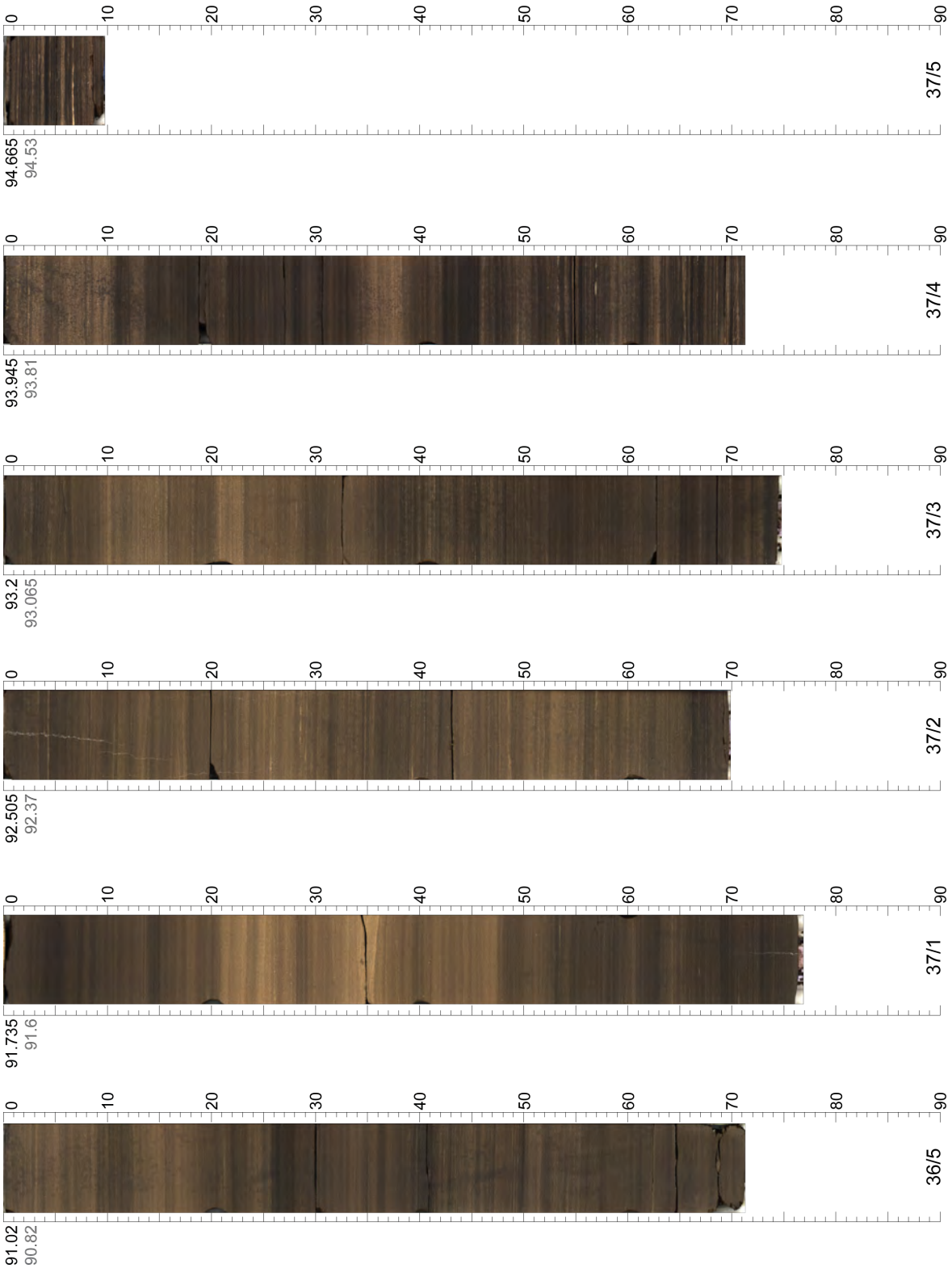
0
10
20
30
40
50
60
70
80
90
37/5
94.665
94.53
37/4
93.945
93.81
37/3
93.2
93.065
37/2
92.505
92.37
37/1
91.735
91.6
36/5
91.02
90.82

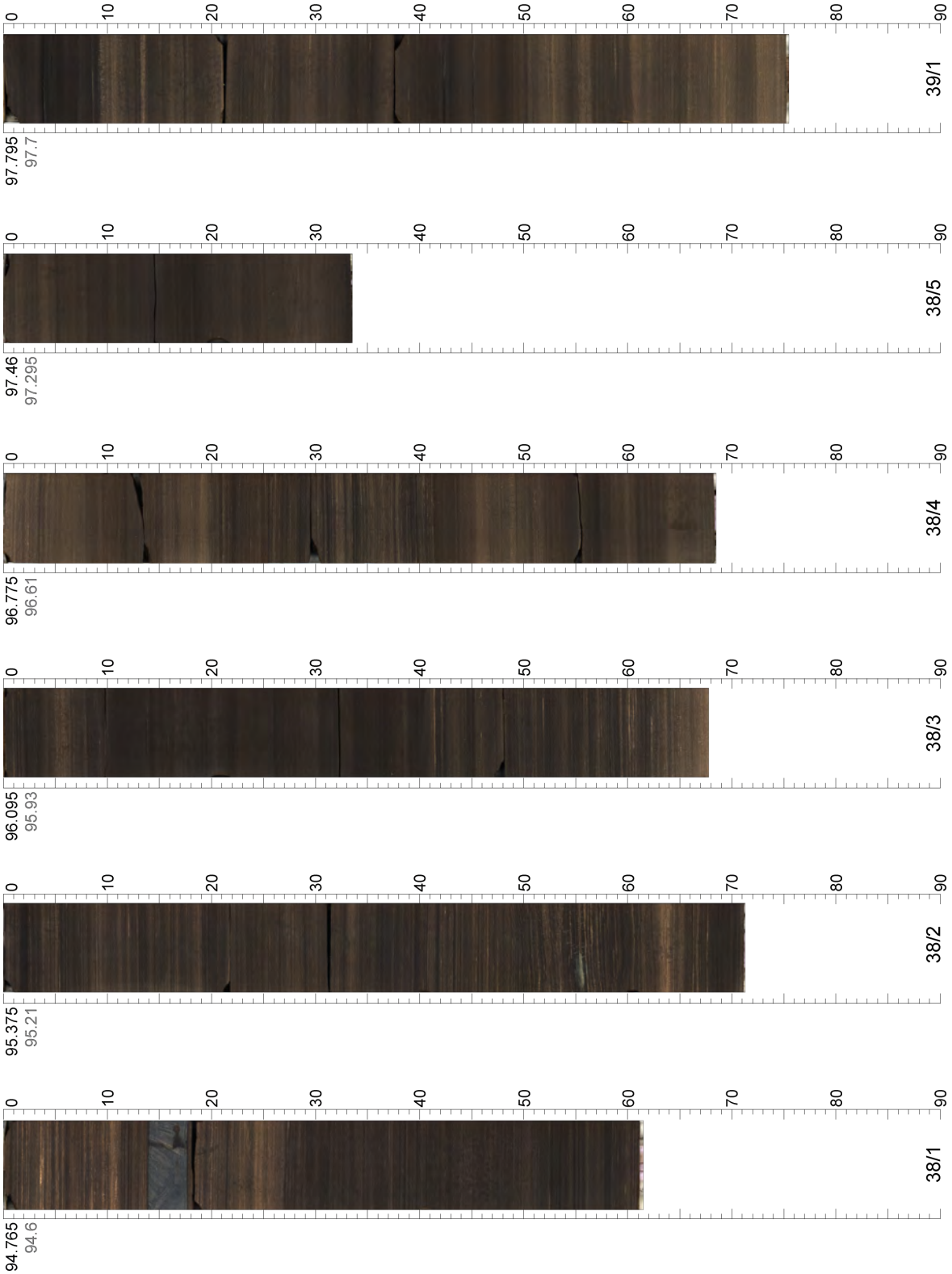
0
10
20
30
40
50
60
70
80
90
39/1
97.795
97.7
38/5
97.46
97.295
38/4
96.775
96.61
38/3
96.095
95.93
38/2
95.375
95.21
38/1
94.765
94.6

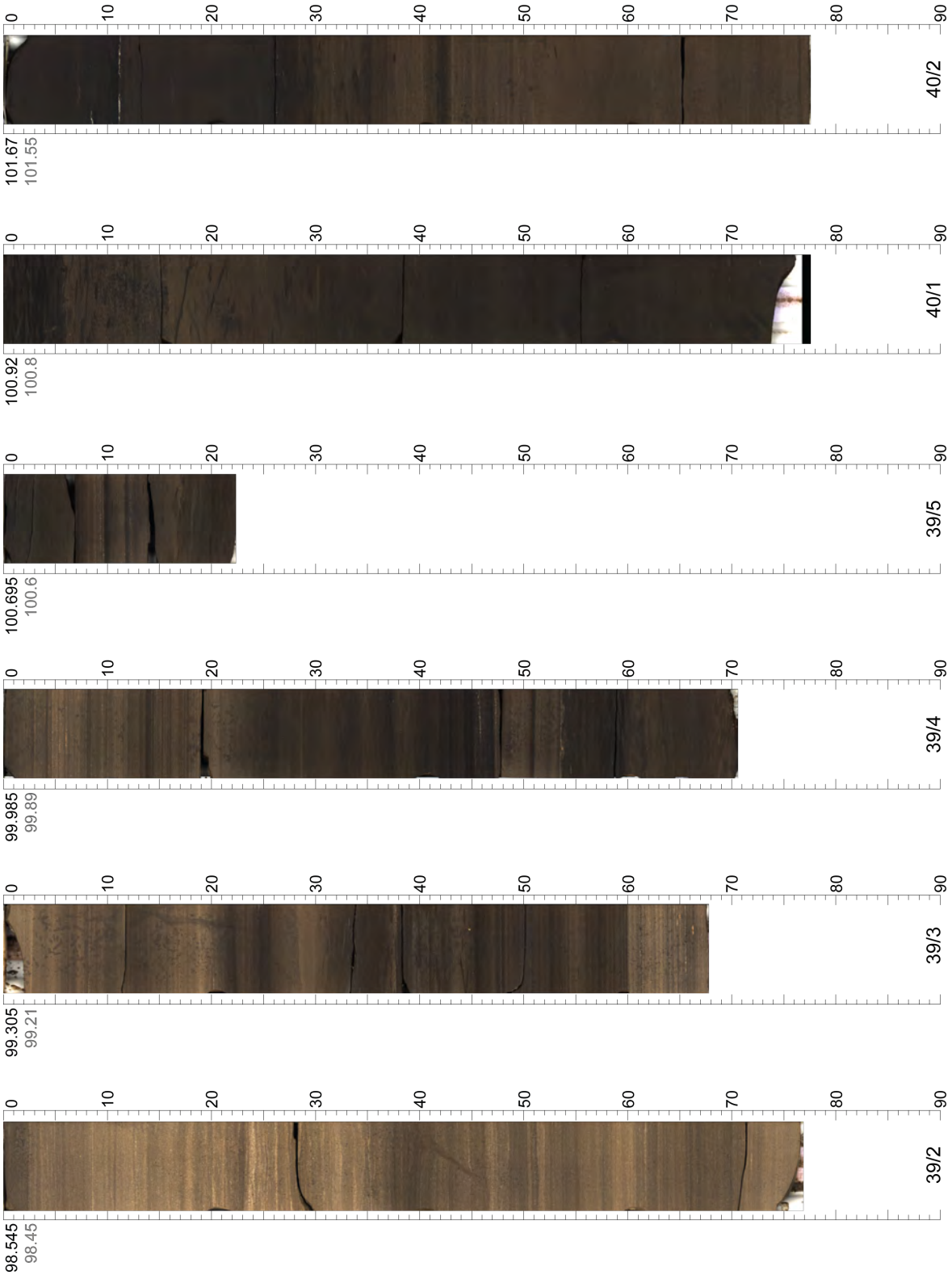
0
10
20
30
40
50
60
70
80
90
40/2
101.67
101.55
40/1
100.92
100.8
39/5
100.695
100.6
39/4
99.985
99.89
39/3
99.305
99.21
39/2
98.545
98.45

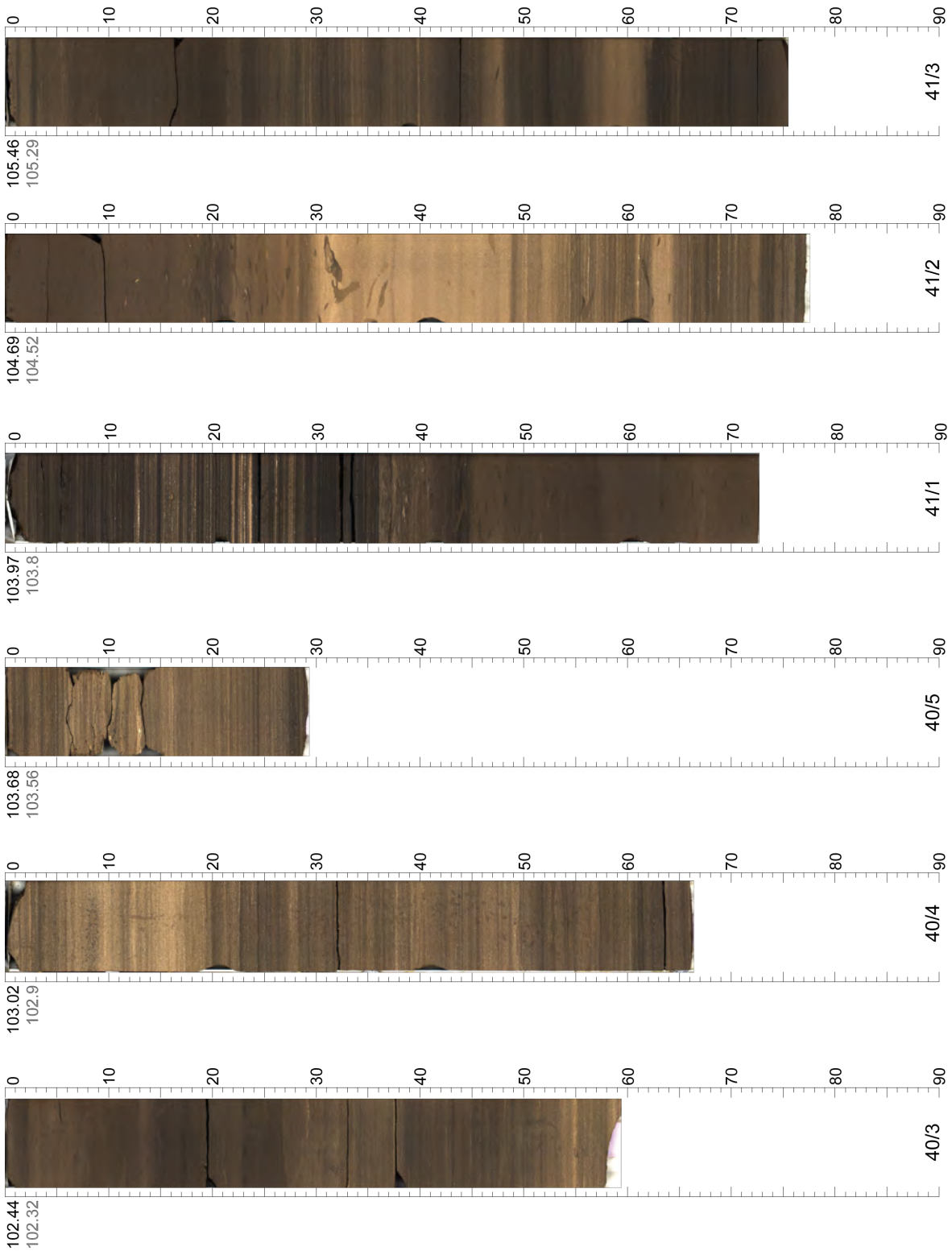
0 10 20 30 40 50 60 70 80 90
41/3
105.46
105.29
0 10 20 30 40 50 60 70 80 90
41/2
104.69
104.52
0 10 20 30 40 50 60 70 80 90
41/1
103.97
103.8
0 10 20 30 40 50 60 70 80 90
40/5
103.68
103.56
0 10 20 30 40 50 60 70 80 90
40/4
103.02
102.9
0 10 20 30 40 50 60 70 80 90
40/3
102.44
102.32

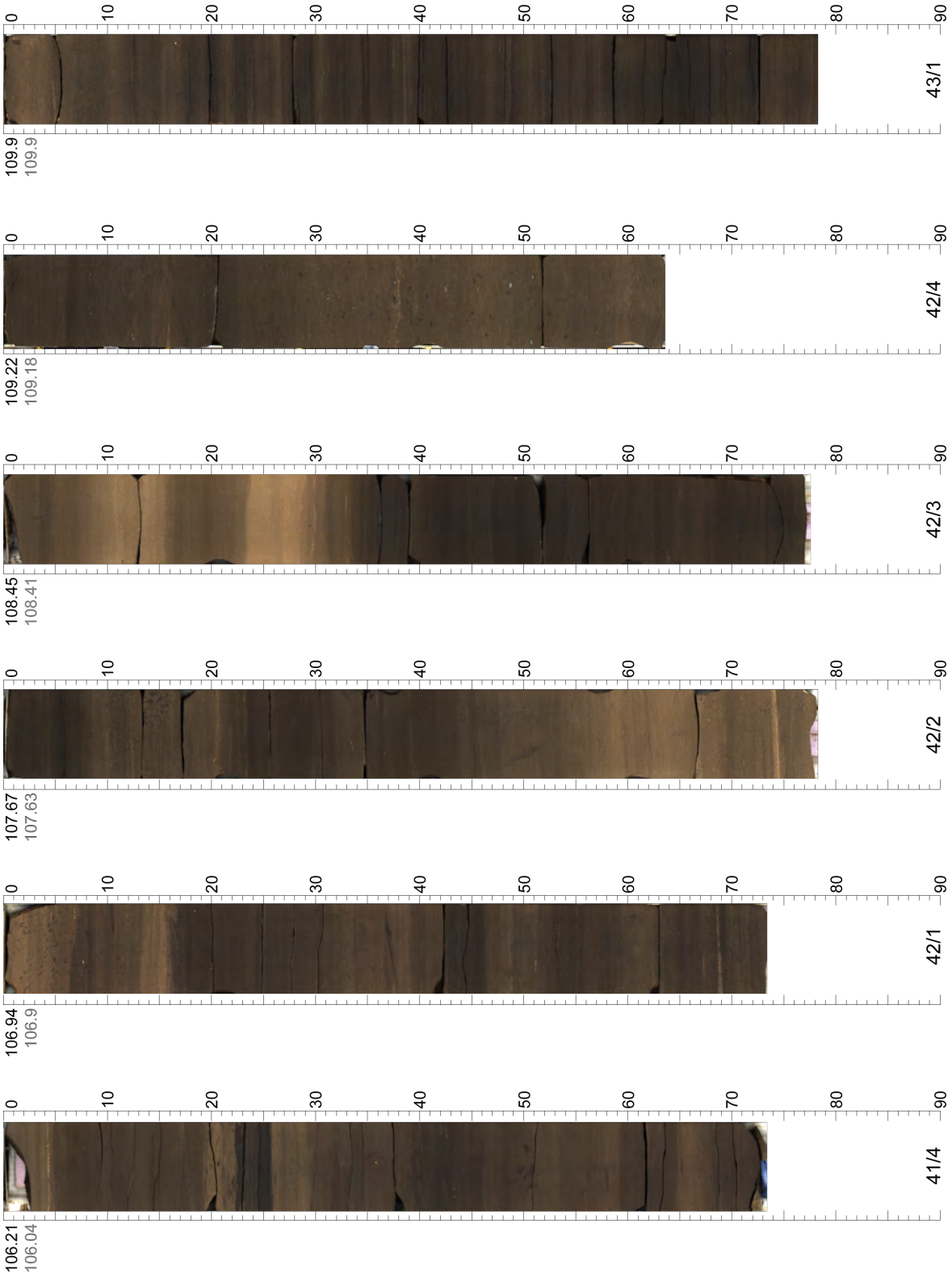
0
10
20
30
40
50
60
70
80
90
43/1
109.9
109.9
42/4
109.22
109.18
42/3
108.45
108.41
42/2
107.67
107.63
42/1
106.94
106.9
41/4
106.21
106.04

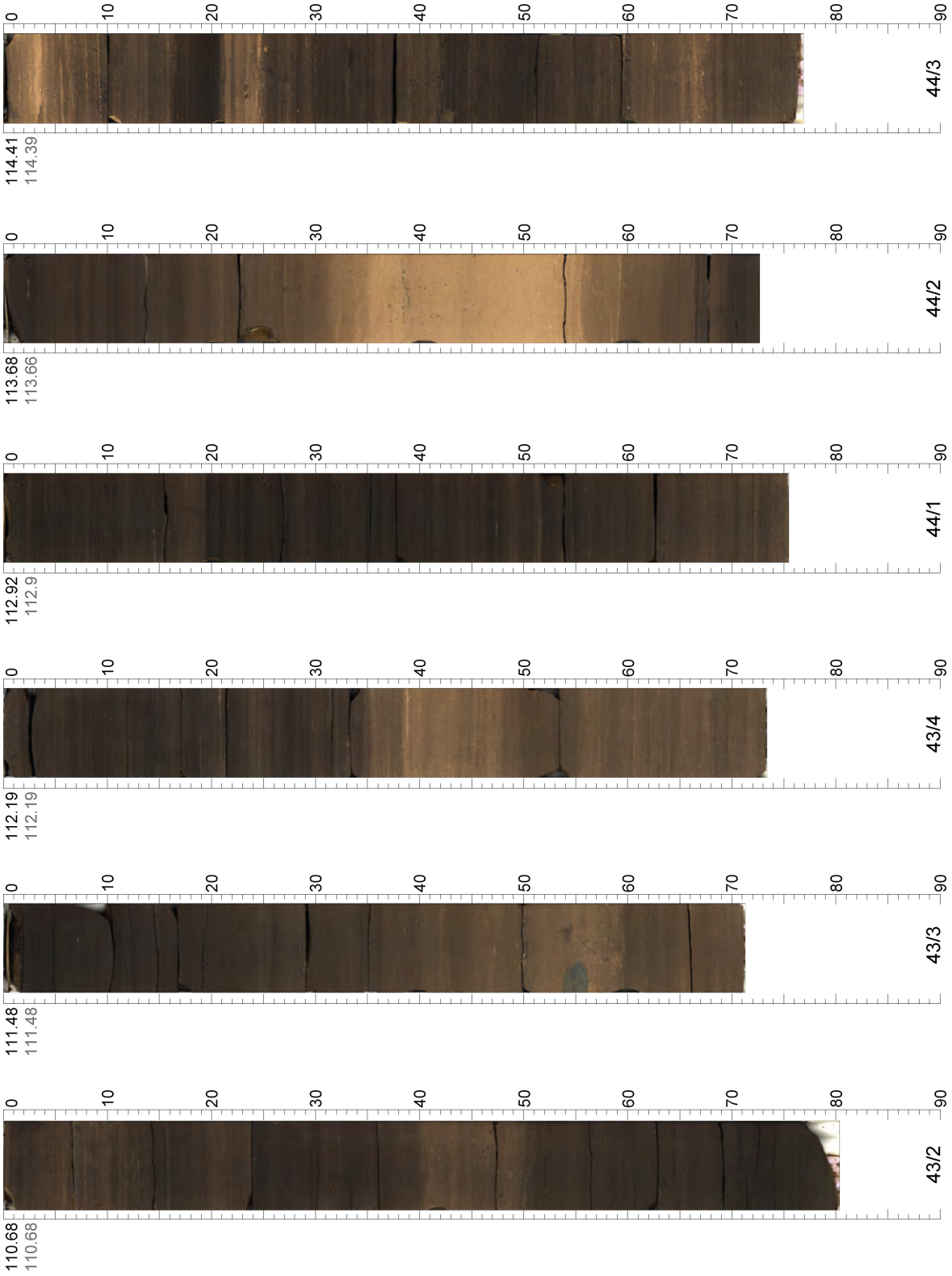
0
10
20
30
40
50
60
70
80
90
44/3
114.41
114.39
44/2
113.68
113.66
44/1
112.92
112.9
43/4
112.19
112.19
43/3
111.48
111.48
43/2
110.68
110.68

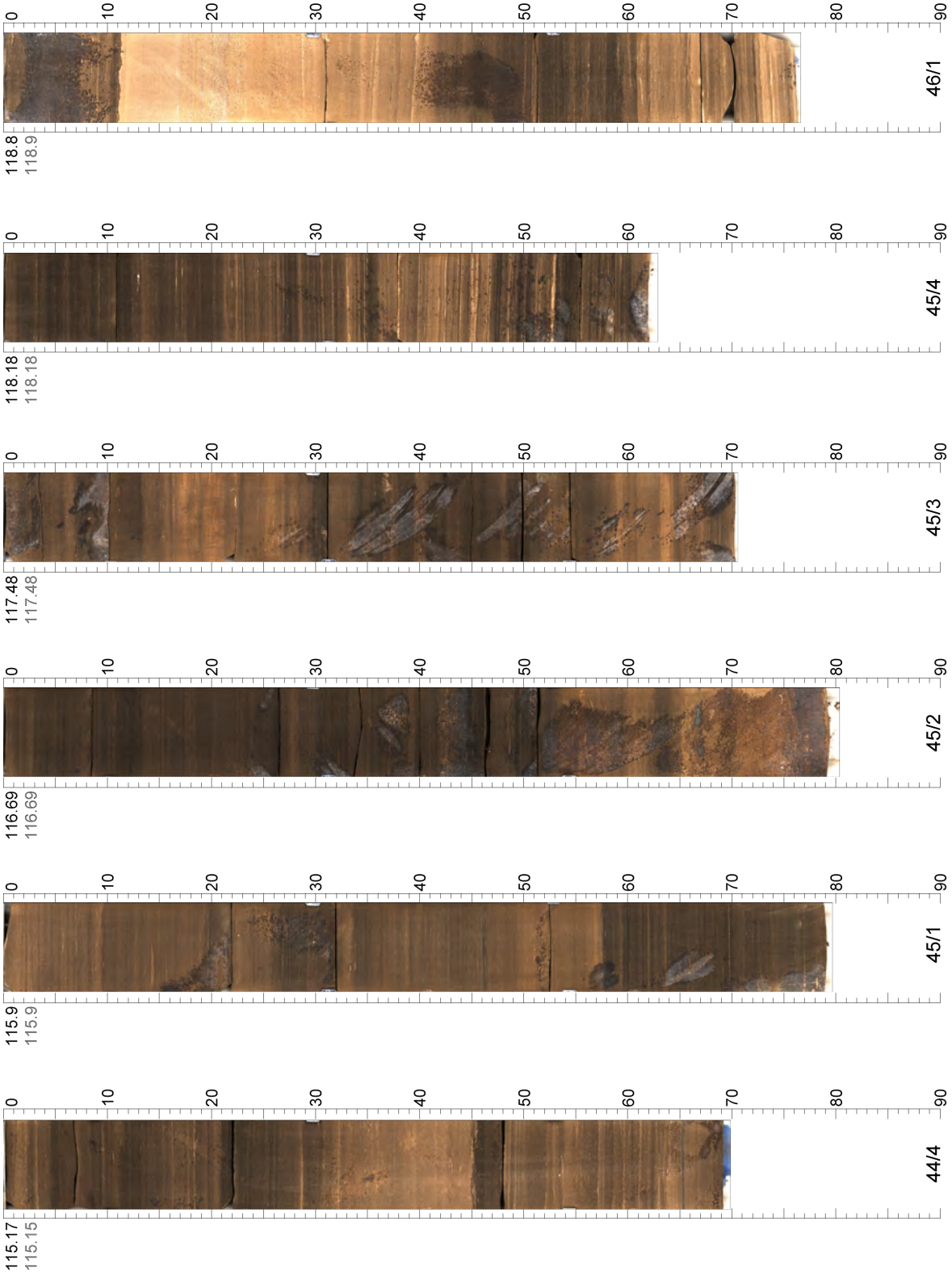
0
10
20
30
40
50
60
70
80
90
46/1
118.8
118.9
45/4
118.18
118.18
45/3
117.48
117.48
45/2
116.69
116.69
45/1
115.9
115.9
44/4
115.17
115.15

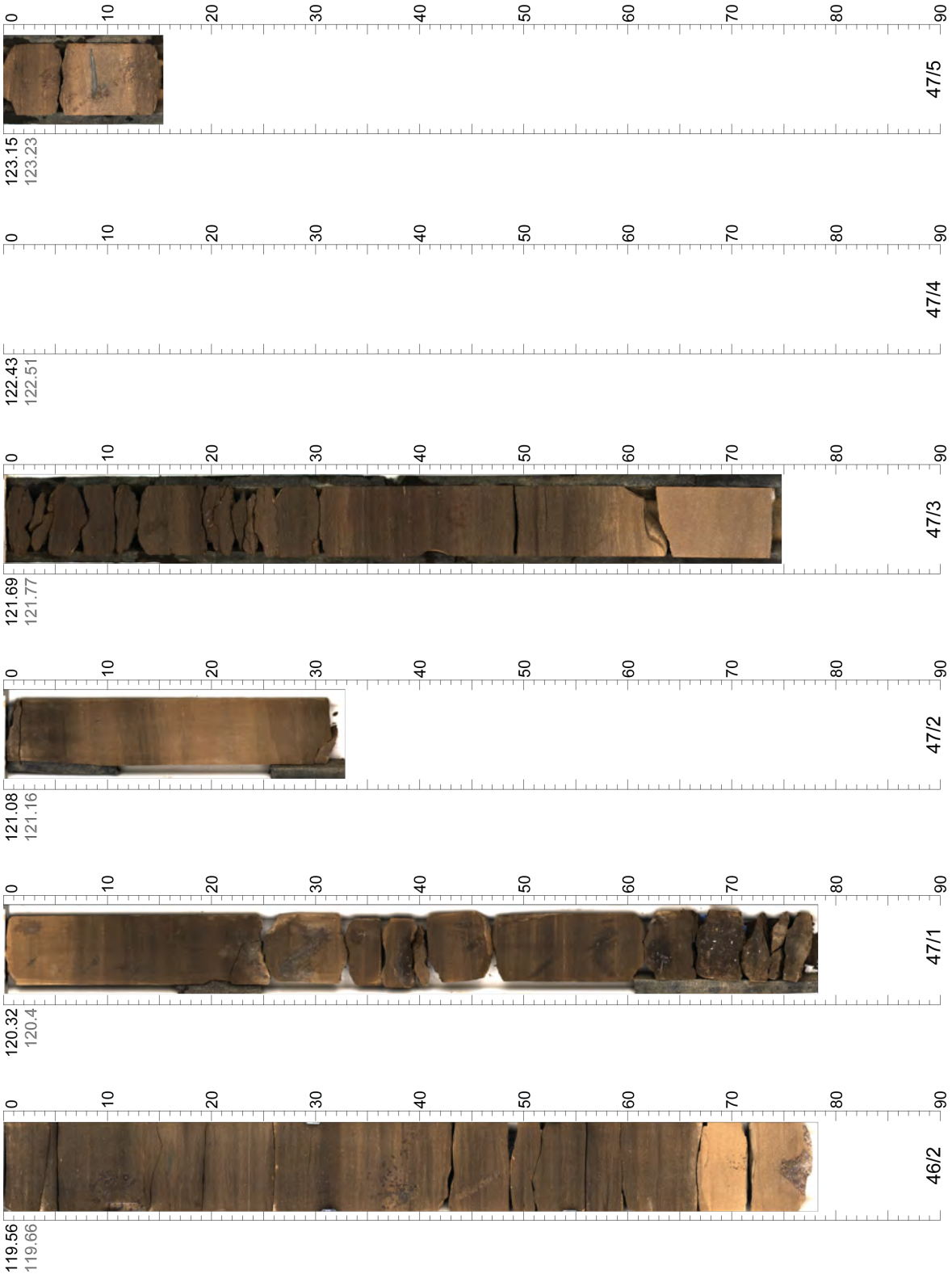
0
10
20
30
40
50
60
70
80
90
47/5
123.15
123.23
47/4
122.43
122.51
47/3
121.69
121.77
47/2
121.08
121.16
47/1
120.32
120.4
46/2
119.56
119.66

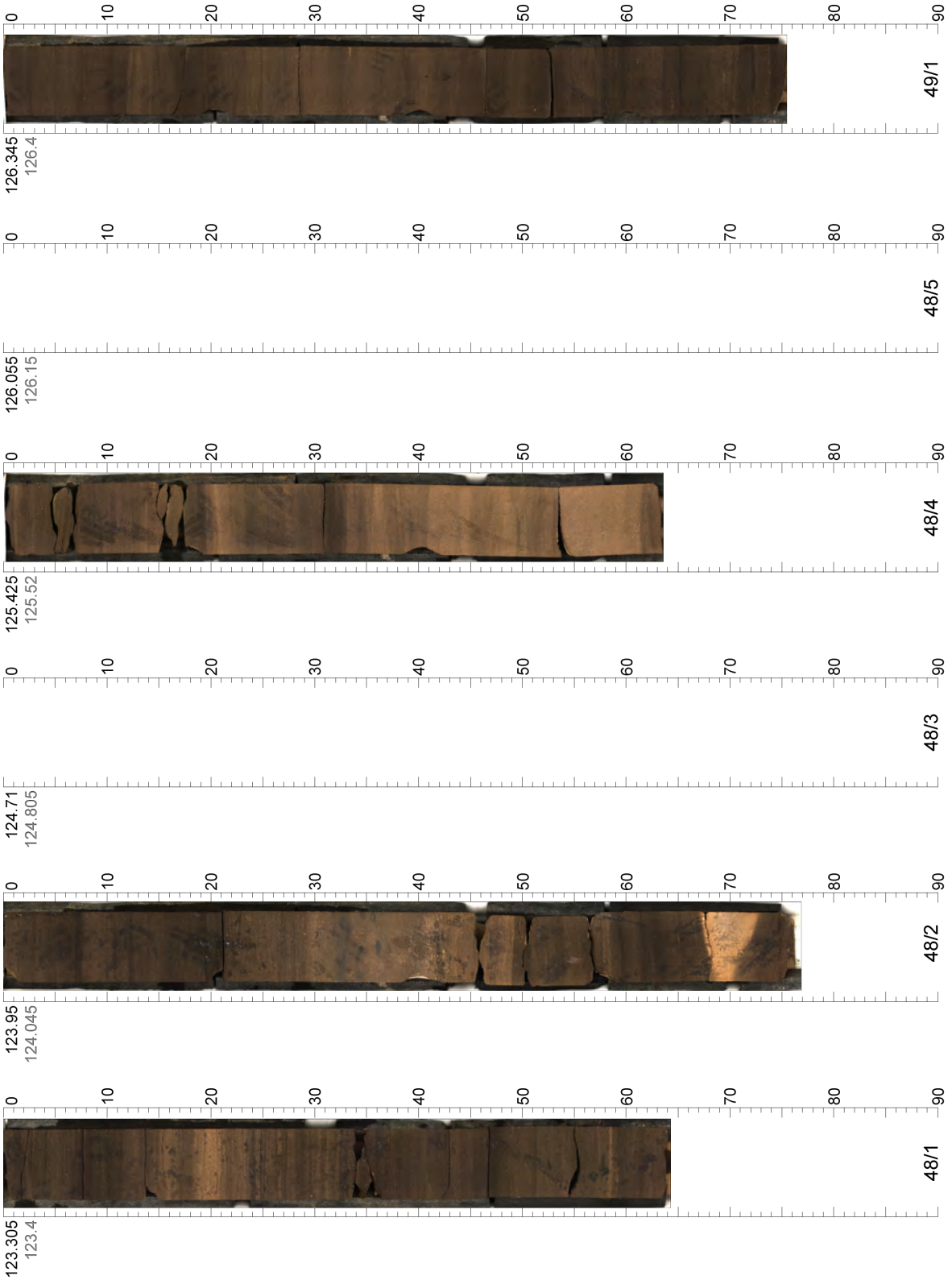
0
10
20
30
40
50
60
70
80
90
49/1
126.345
126.4
48/5
126.055
126.15
48/4
125.425
125.52
48/3
124.71
124.805
48/2
123.95
124.045
48/1
123.305
123.4

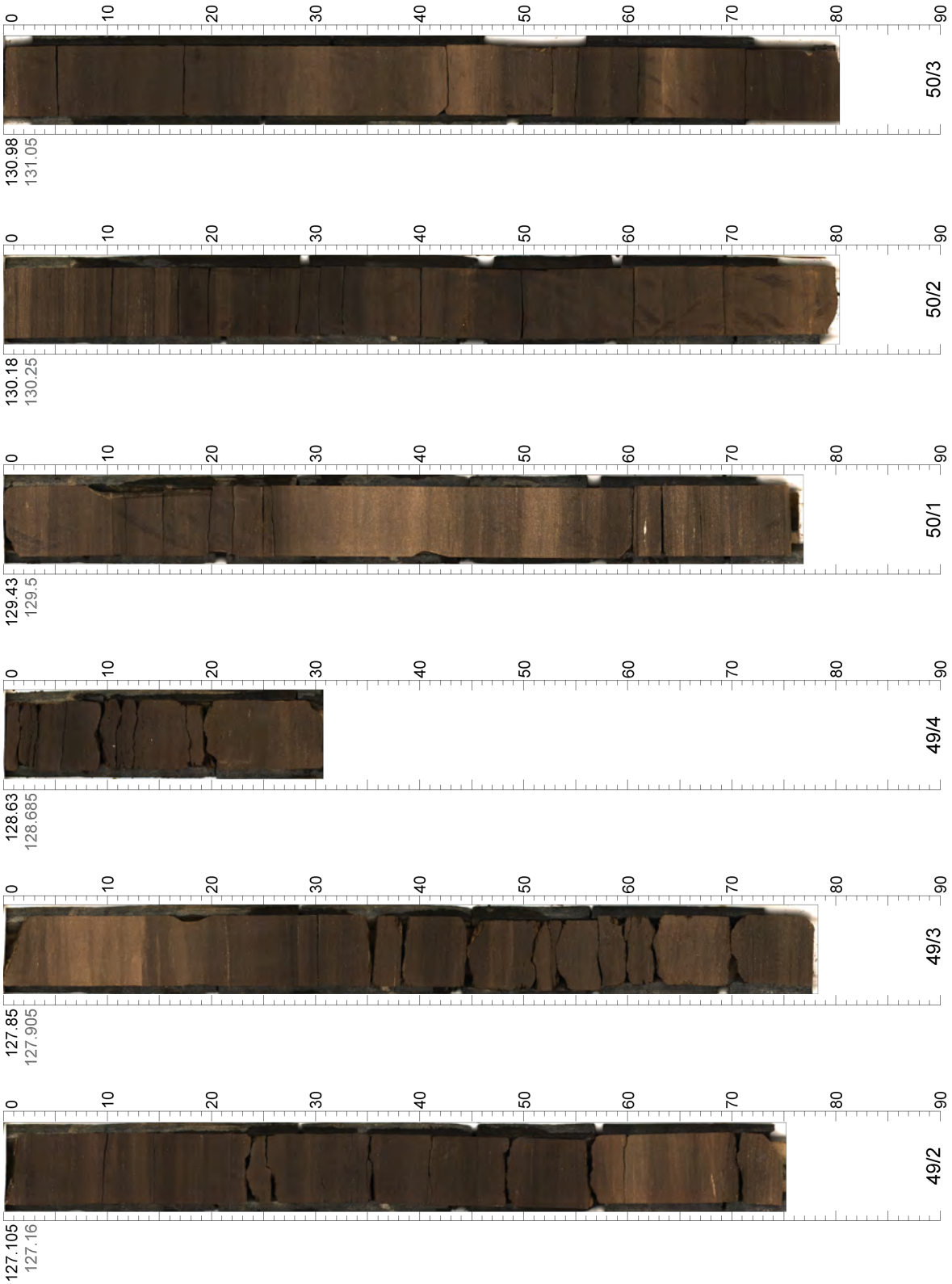
0 10 20 30 40 50 60 70 80 90
50/3
130.98
131.05
0 10 20 30 40 50 60 70 80 90
50/2
130.18
130.25
0 10 20 30 40 50 60 70 80 90
50/1
129.43
129.5
0 10 20 30 40 50 60 70 80 90
49/4
128.63
128.685
0 10 20 30 40 50 60 70 80 90
49/3
127.85
127.905
0 10 20 30 40 50 60 70 80 90
49/2
127.105
127.16

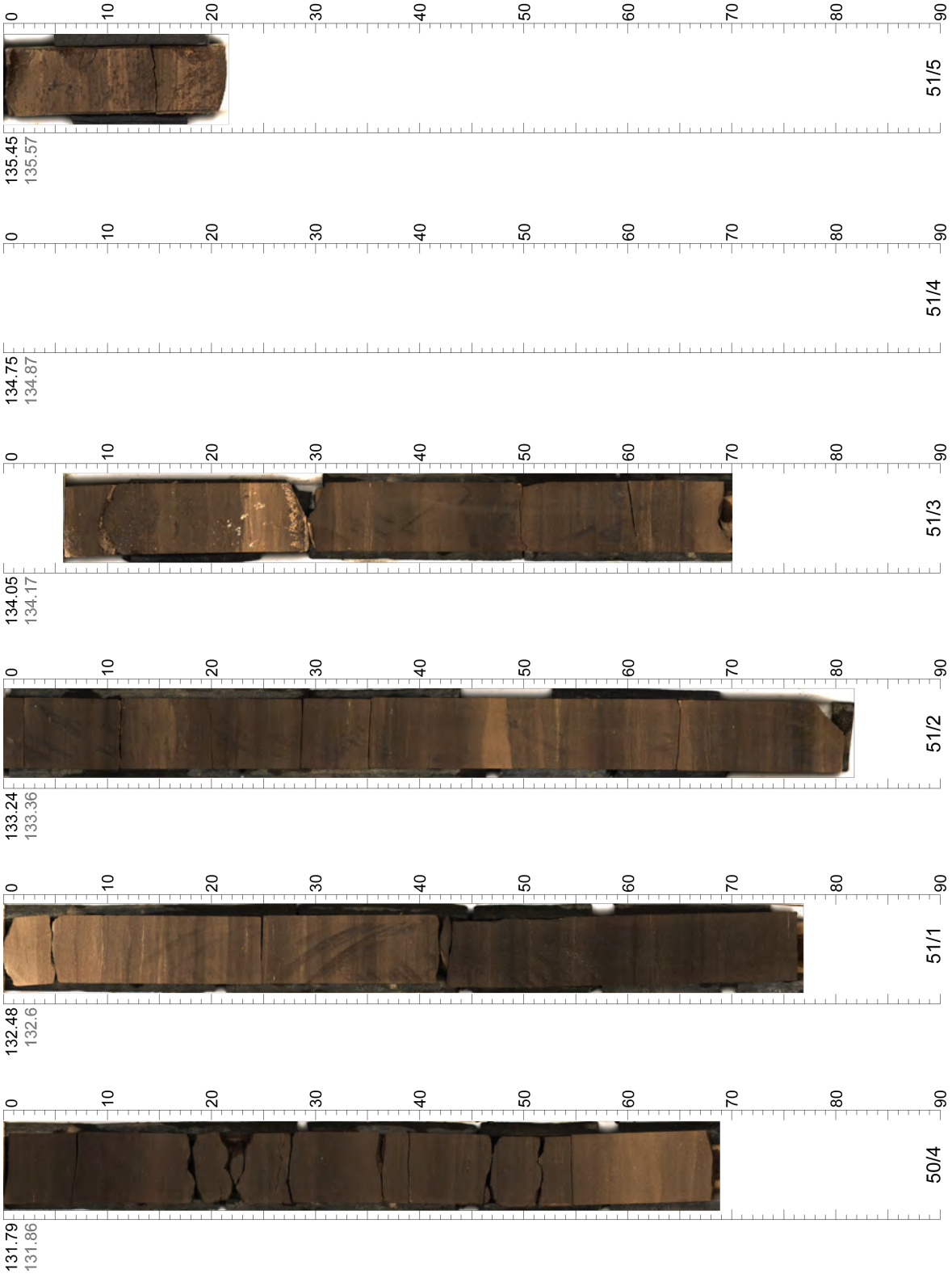
0
10
20
30
40
50
60
70
80
90
51/5
135.45
135.57
51/4
134.75
134.87
51/3
134.05
134.17
51/2
133.24
133.36
51/1
132.48
132.6
50/4
131.79
131.86

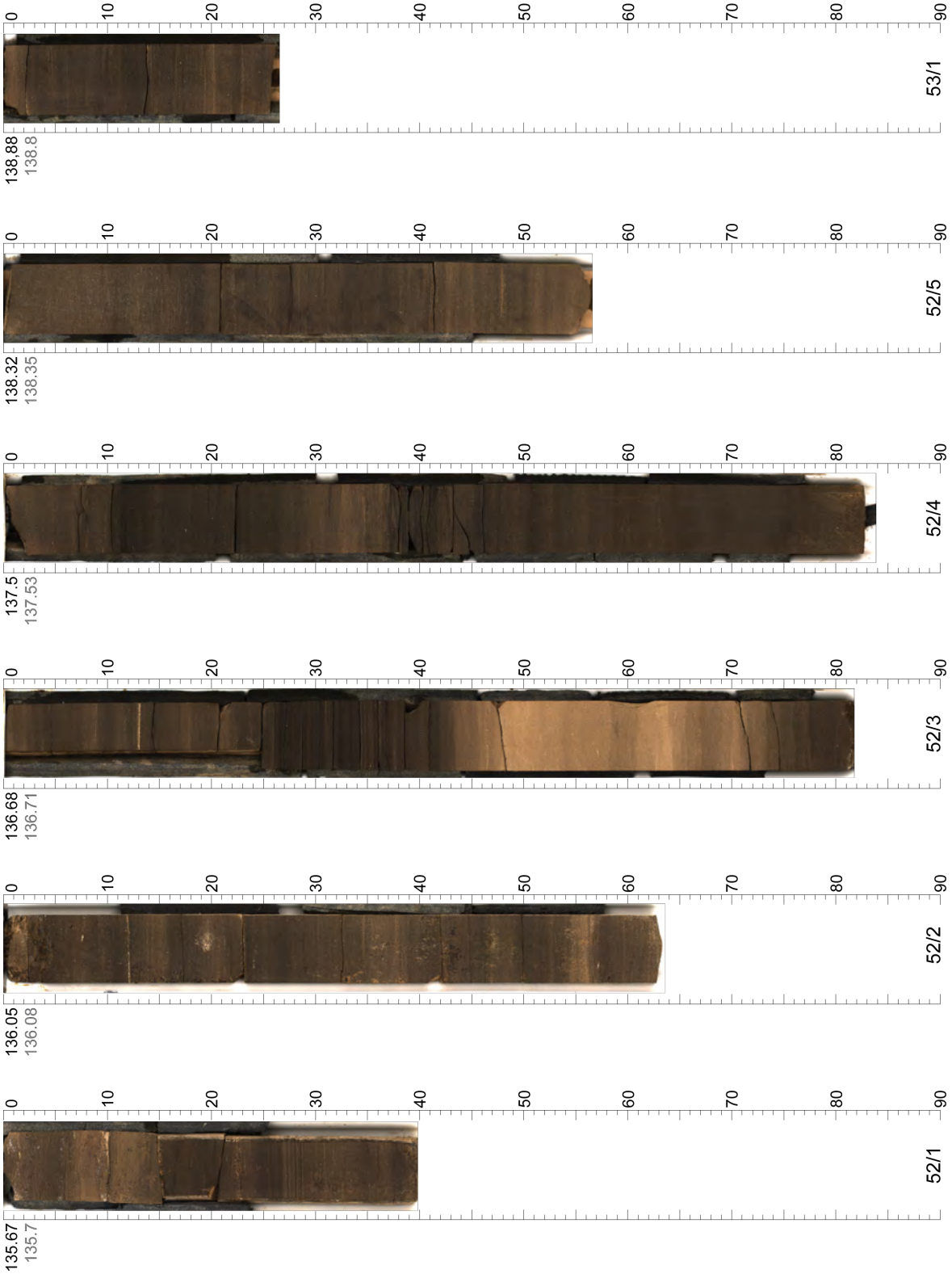
53/1
138.88
138.8
52/5
138.32
138.35
52/4
137.5
137.53
52/3
136.68
136.71
52/2
136.05
136.08
52/1
135.67
135.7

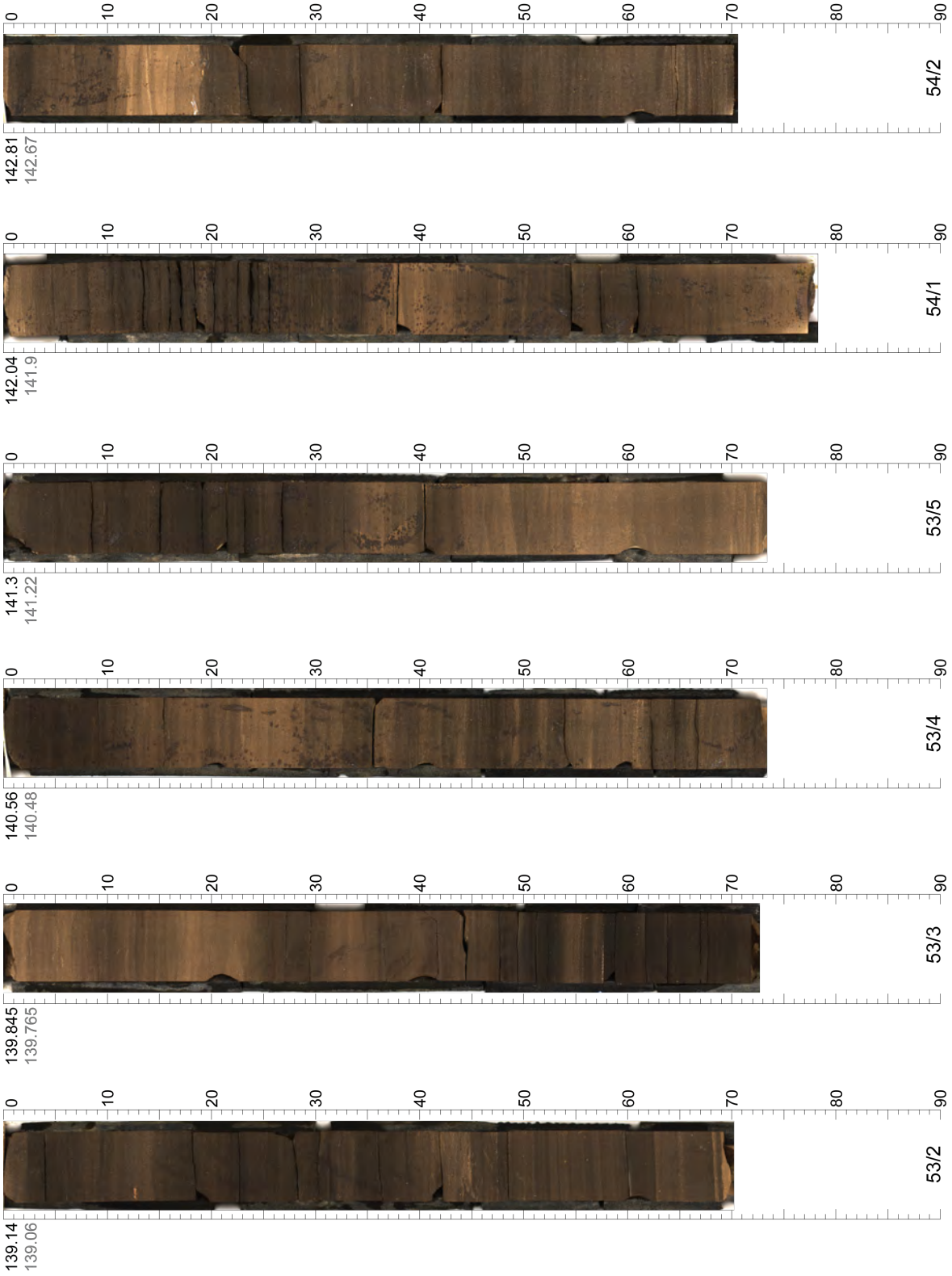
0
10
20
30
40
50
60
70
80
90
54/2
142.81
142.67
54/1
142.04
141.9
53/5
141.3
141.22
53/4
140.56
140.48
53/3
139.845
139.765
53/2
139.14
139.06

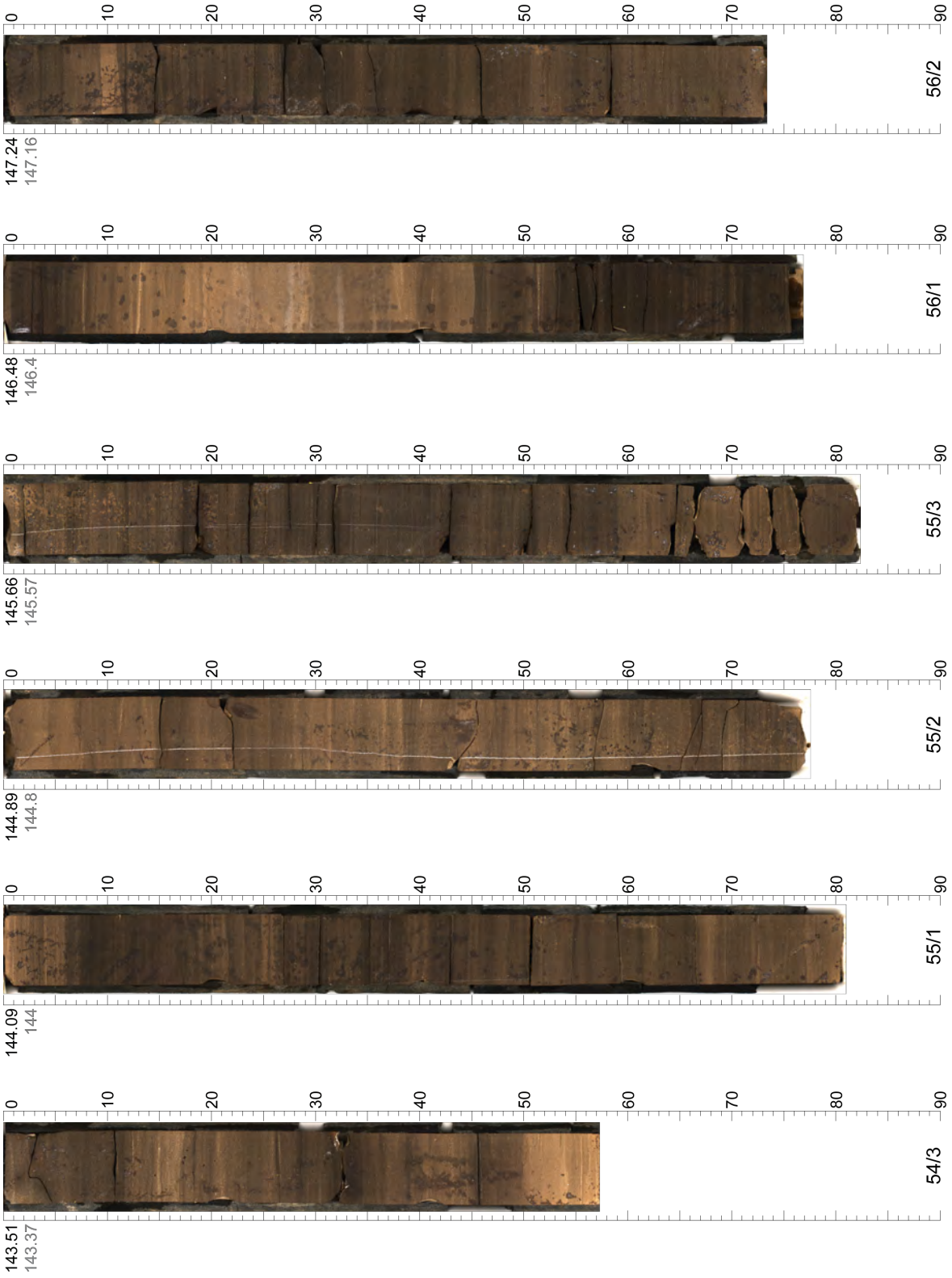
0
10
20
30
40
50
60
70
80
90
56/2
147.24
147.16
56/1
146.48
146.4
55/3
145.66
145.57
55/2
144.89
144.8
55/1
144.09
144
54/3
143.51
143.37

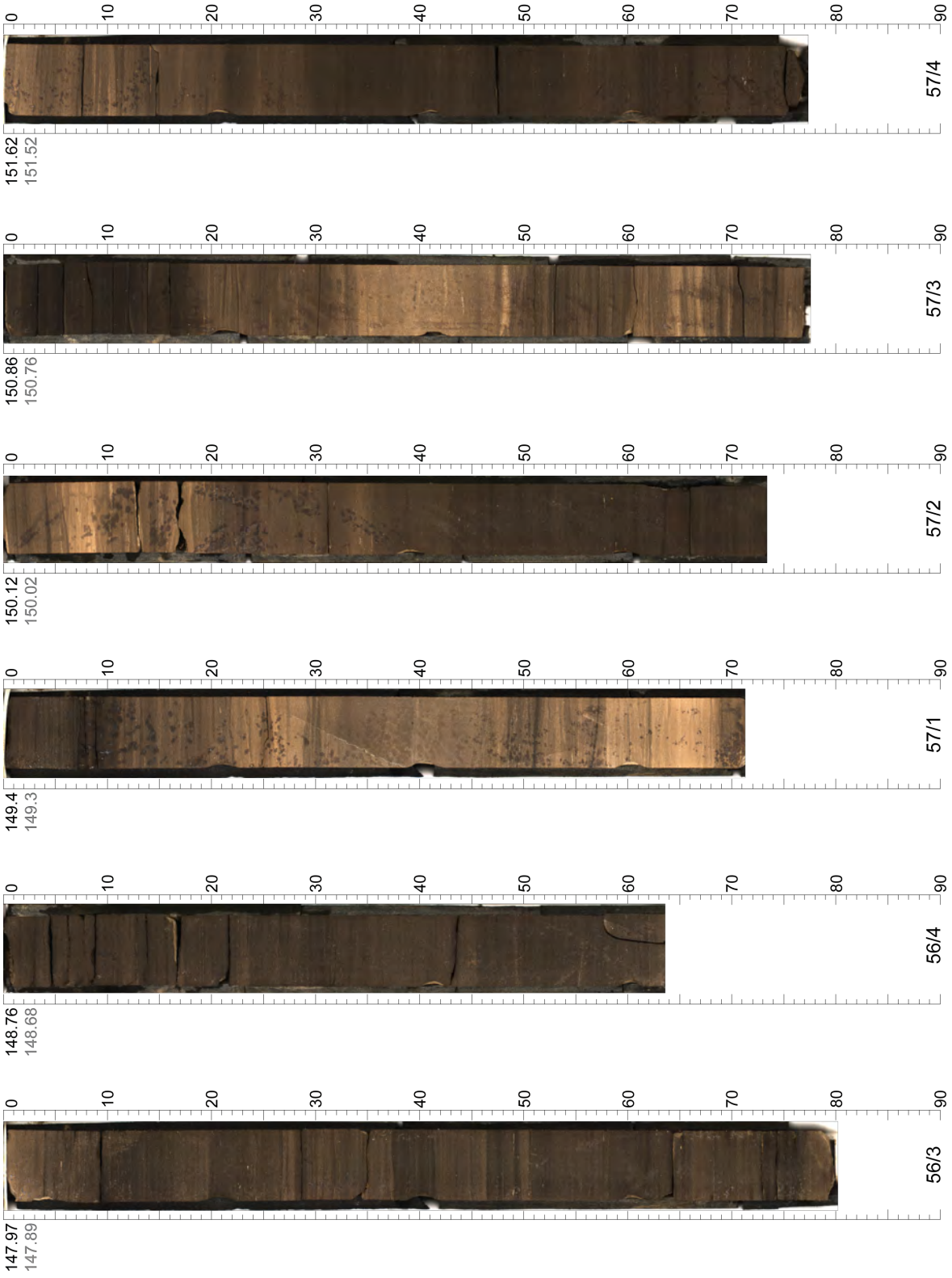
0
10
20
30
40
50
60
70
80
90
57/4
151.62
151.52
57/3
150.86
150.76
57/2
150.12
150.02
57/1
149.4
149.3
56/4
148.76
148.68
56/3
147.97
147.89

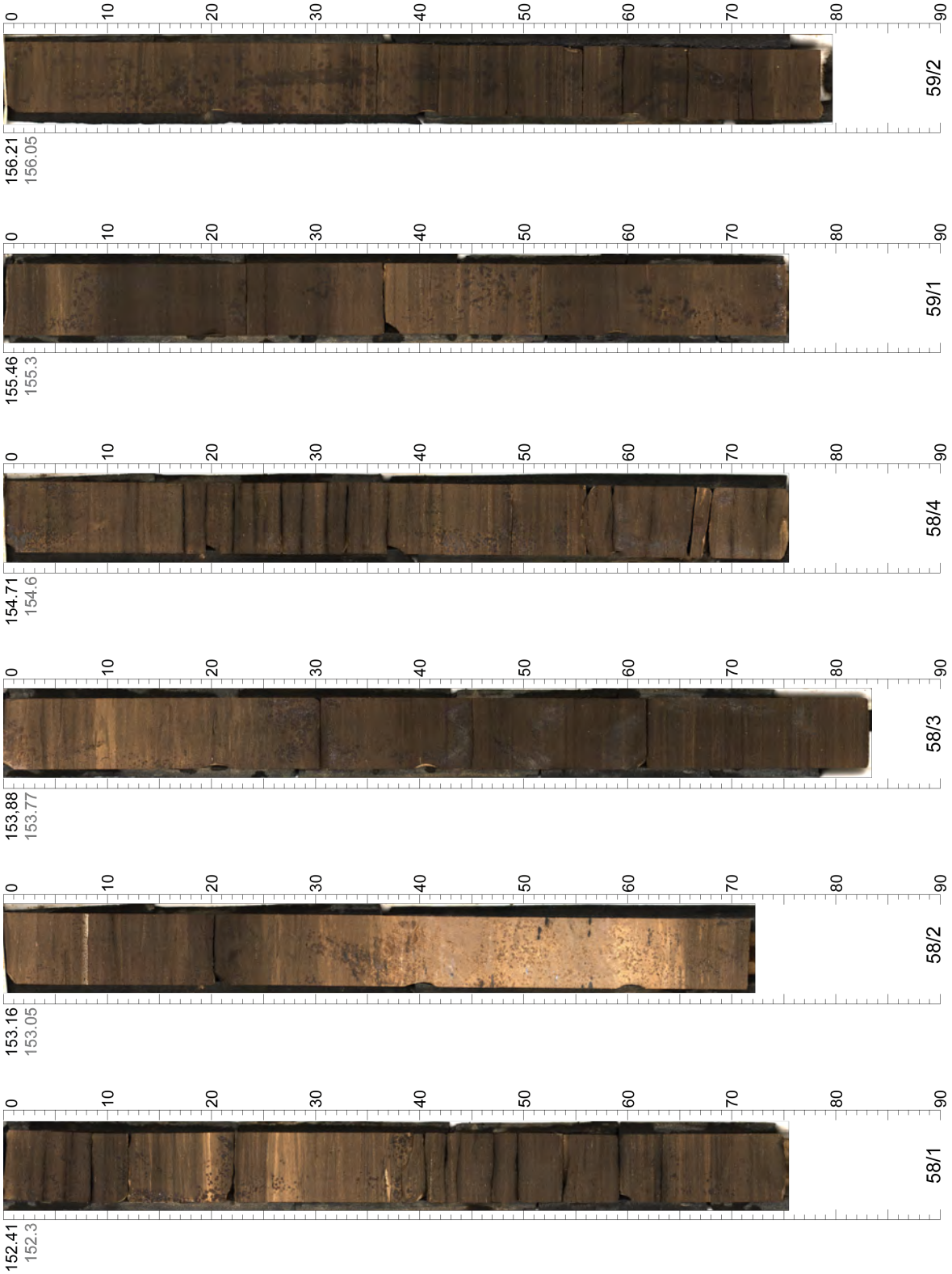
0
10
20
30
40
50
60
70
80
90
59/2
156.21
156.05
59/1
155.46
155.3
58/4
154.71
154.6
58/3
153.88
153.77
58/2
153.16
153.05
58/1
152.41
152.3

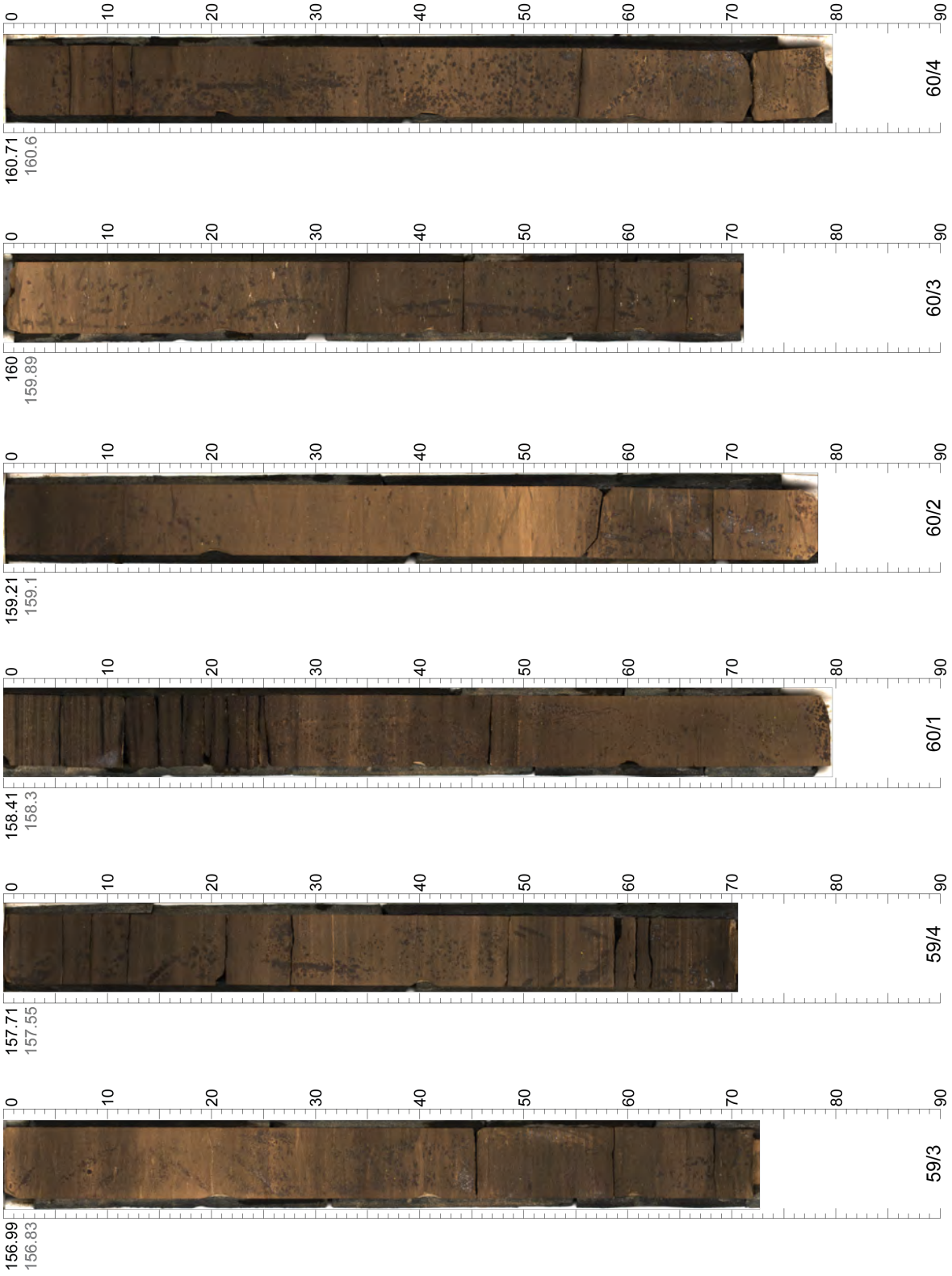
0
10
20
30
40
50
60
70
80
90
60/4
160.71
160.6
60/3
160
159.89
60/2
159.21
159.1
60/1
158.41
158.3
59/4
157.71
157.55
59/3
156.99
156.83

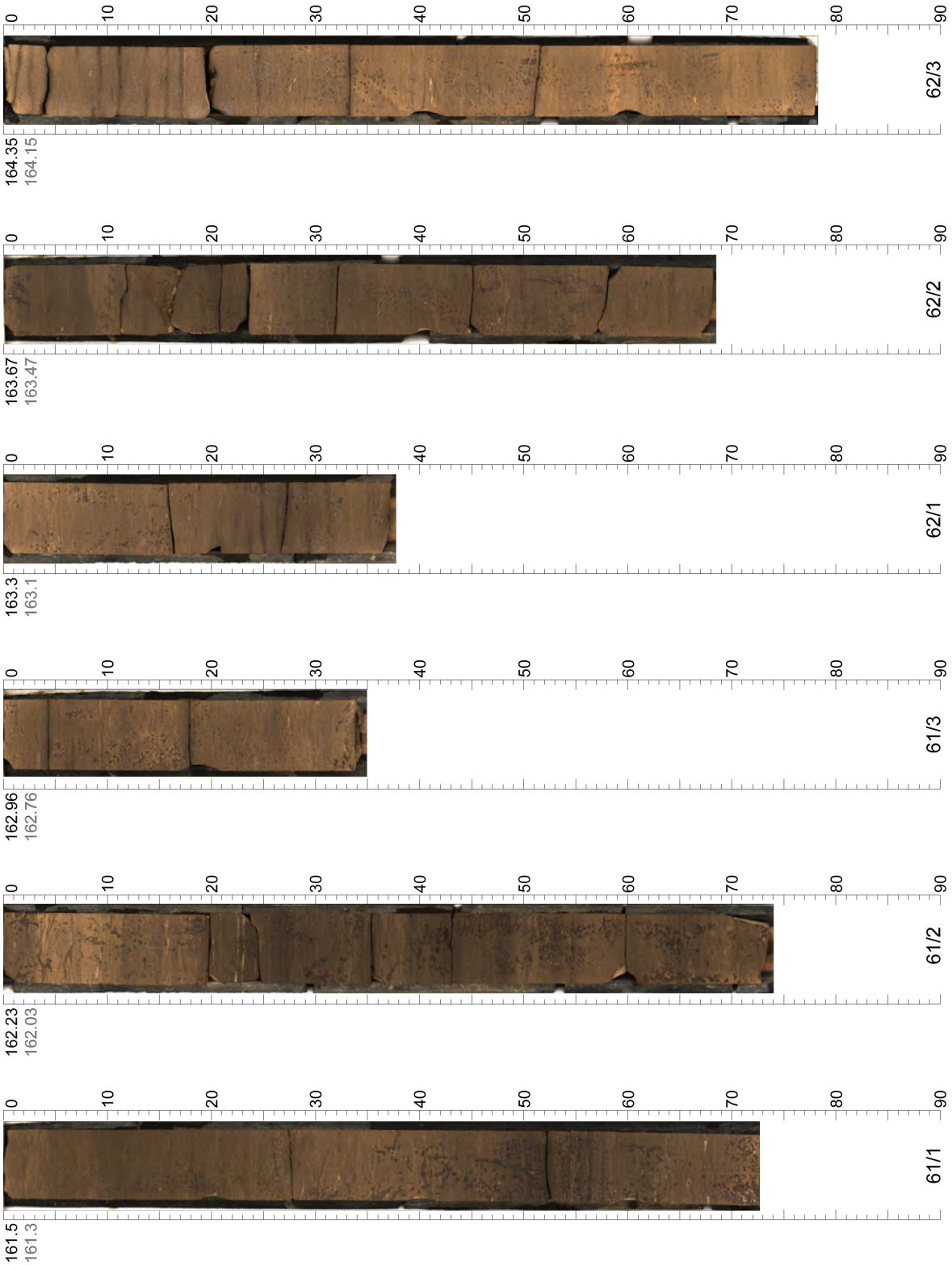
0 10 20 30 40 50 60 70 80 90
62/3
164.35
164.15
0 10 20 30 40 50 60 70 80 90
62/2
163.67
163.47
0 10 20 30 40 50 60 70 80 90
62/1
163.3
163.1
0 10 20 30 40 50 60 70 80 90
61/3
162.96
162.76
0 10 20 30 40 50 60 70 80 90
61/2
162.23
162.03
0 10 20 30 40 50 60 70 80 90
61/1
161.5
161.3

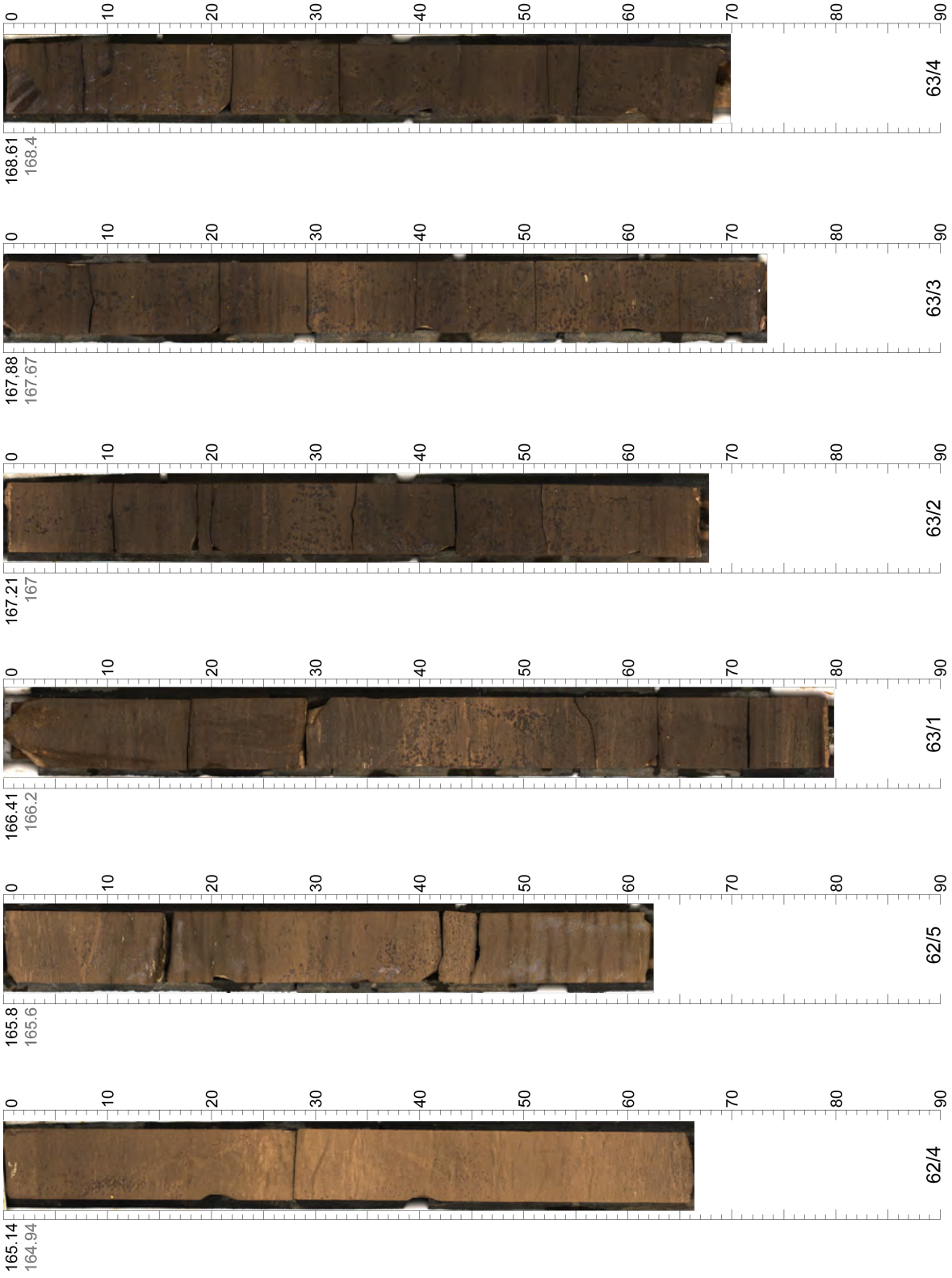
0
10
20
30
40
50
60
70
80
90
63/4
168.61
168.4
63/3
167.88
167.67
63/2
167.21
167
63/1
166.41
166.2
62/5
165.8
165.6
62/4
165.14
164.94

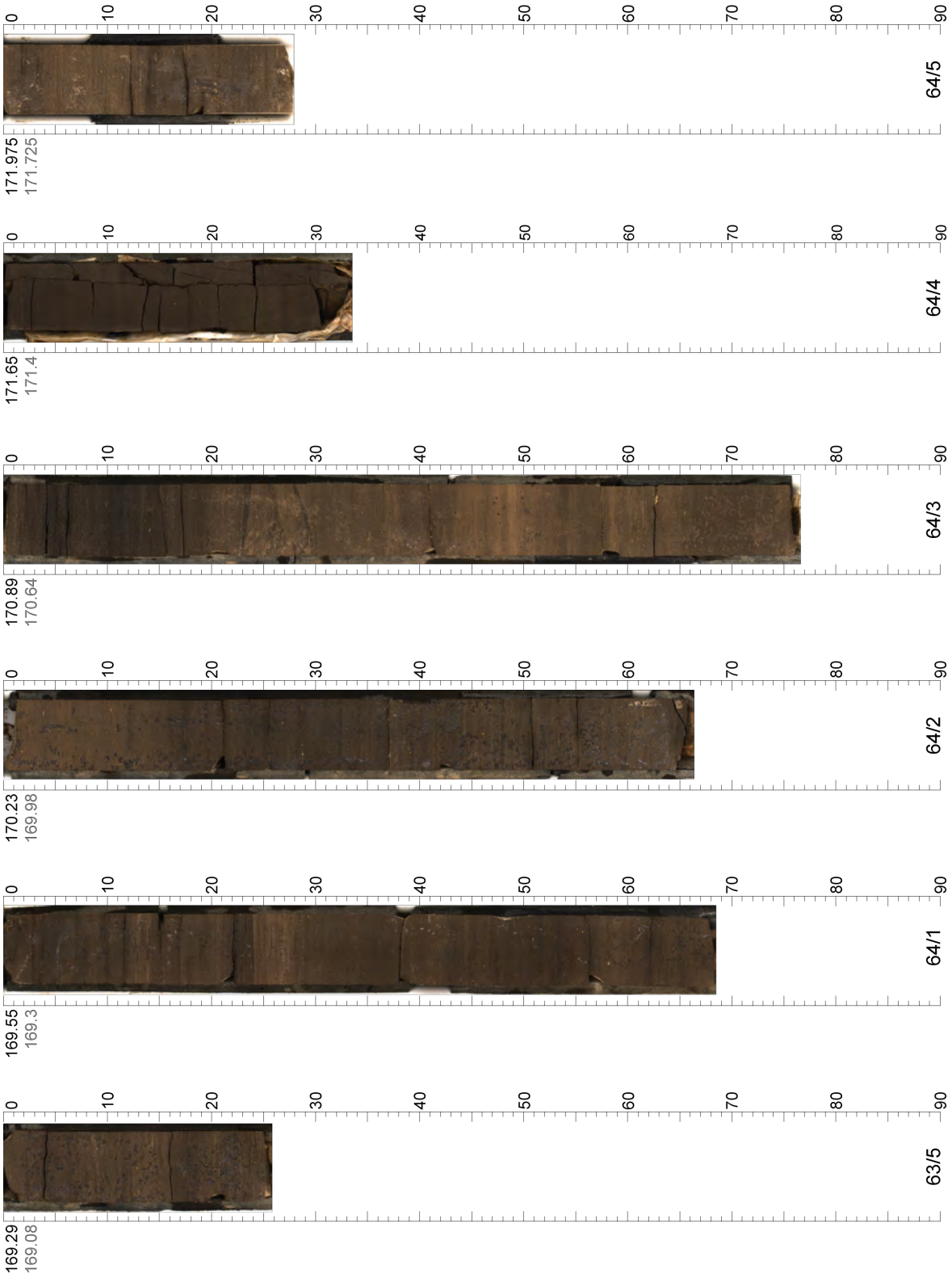
64/5
171.975
171.725
64/4
171.65
171.4
64/3
170.89
170.64
64/2
170.23
169.98
64/1
169.55
169.3
63/5
169.29
169.08

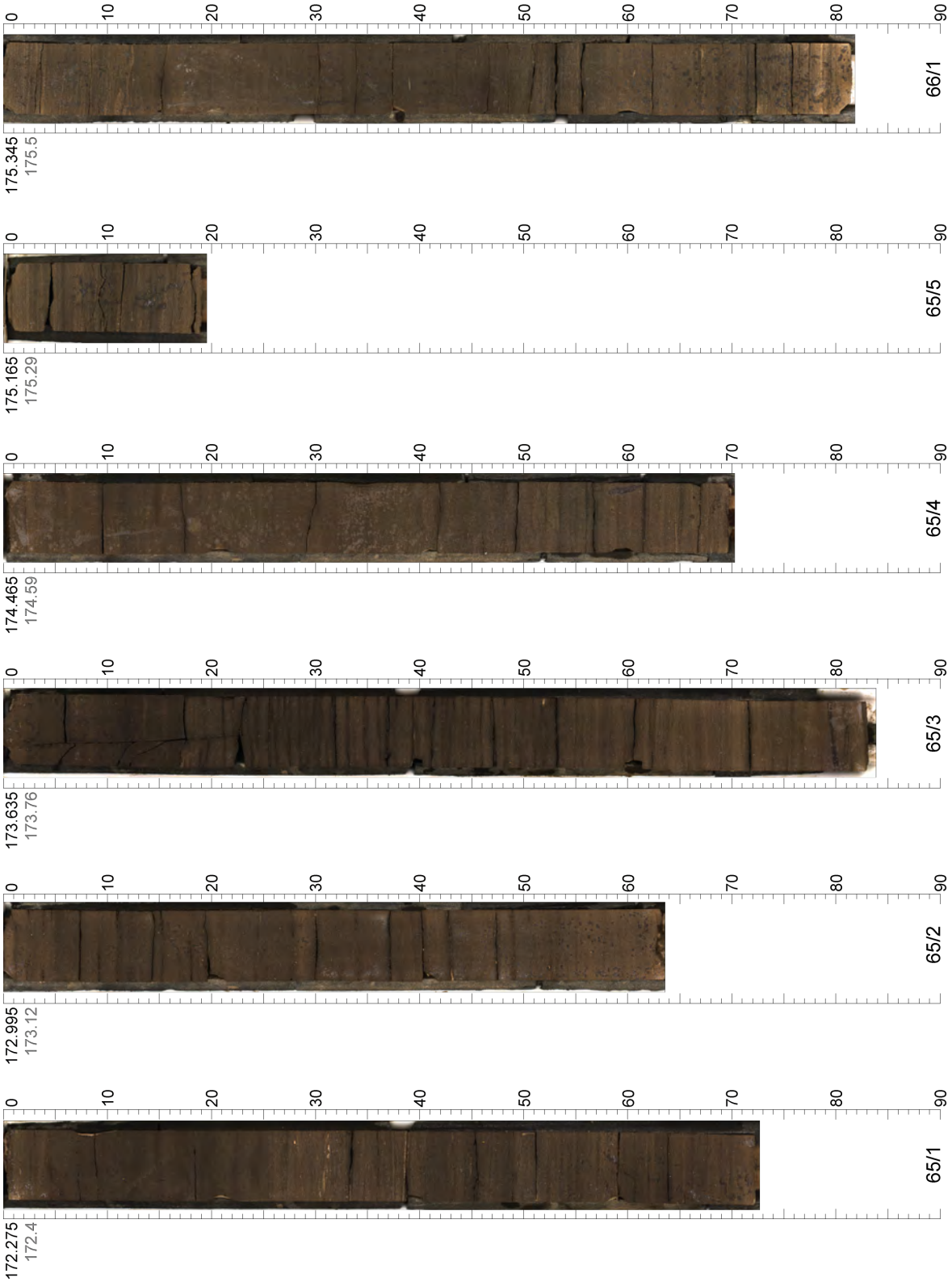
66/1
175.345
175.5
65/5
175.165
175.29
65/4
174.465
174.59
65/3
173.635
173.76
65/2
172.995
173.12
65/1
172.275
172.4

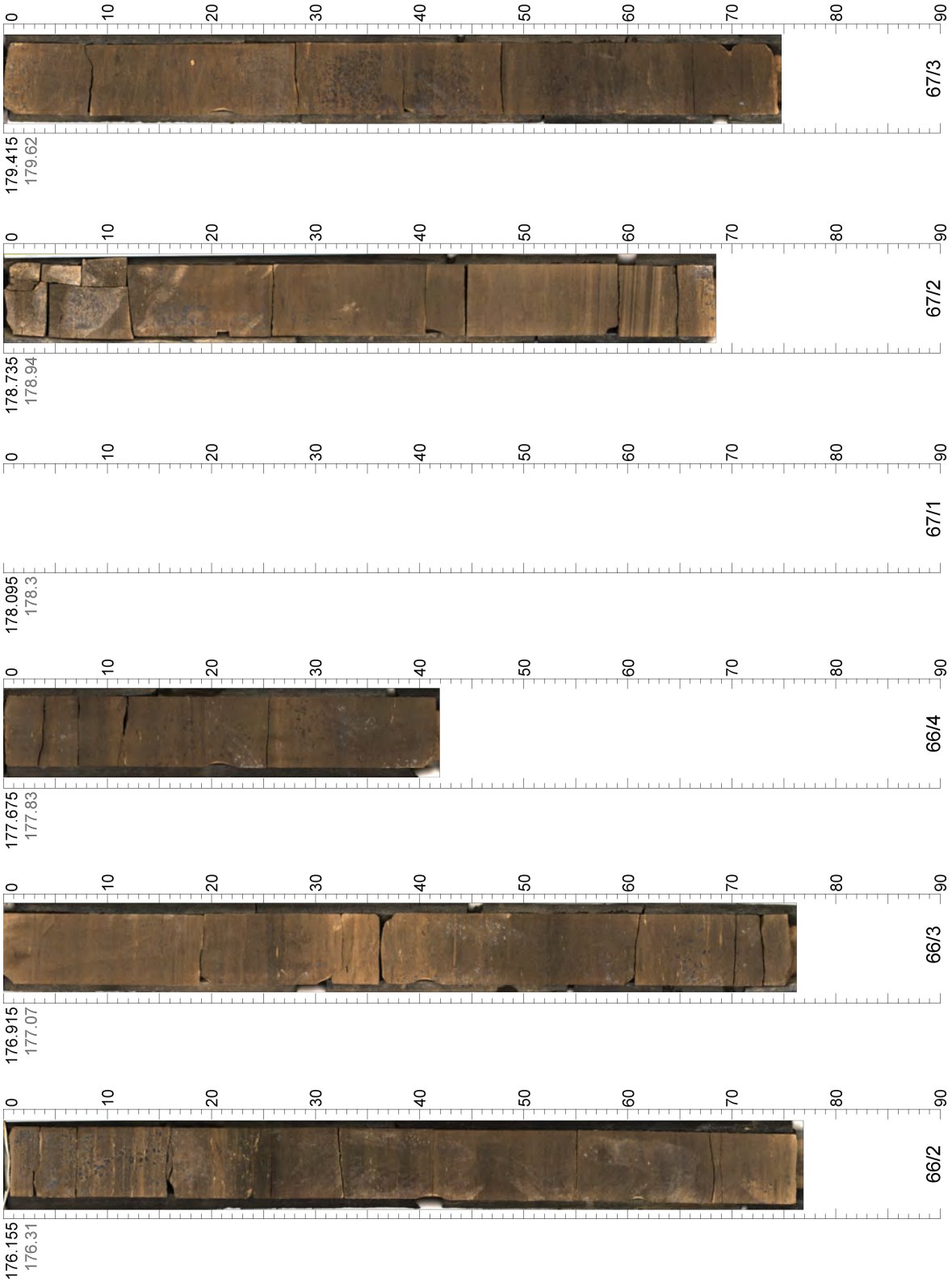
0
10
20
30
40
50
60
70
80
90
67/3
179.415
179.62
67/2
178.735
178.94
67/1
178.095
178.3
66/4
177.675
177.83
66/3
176.915
177.07
66/2
176.155
176.31

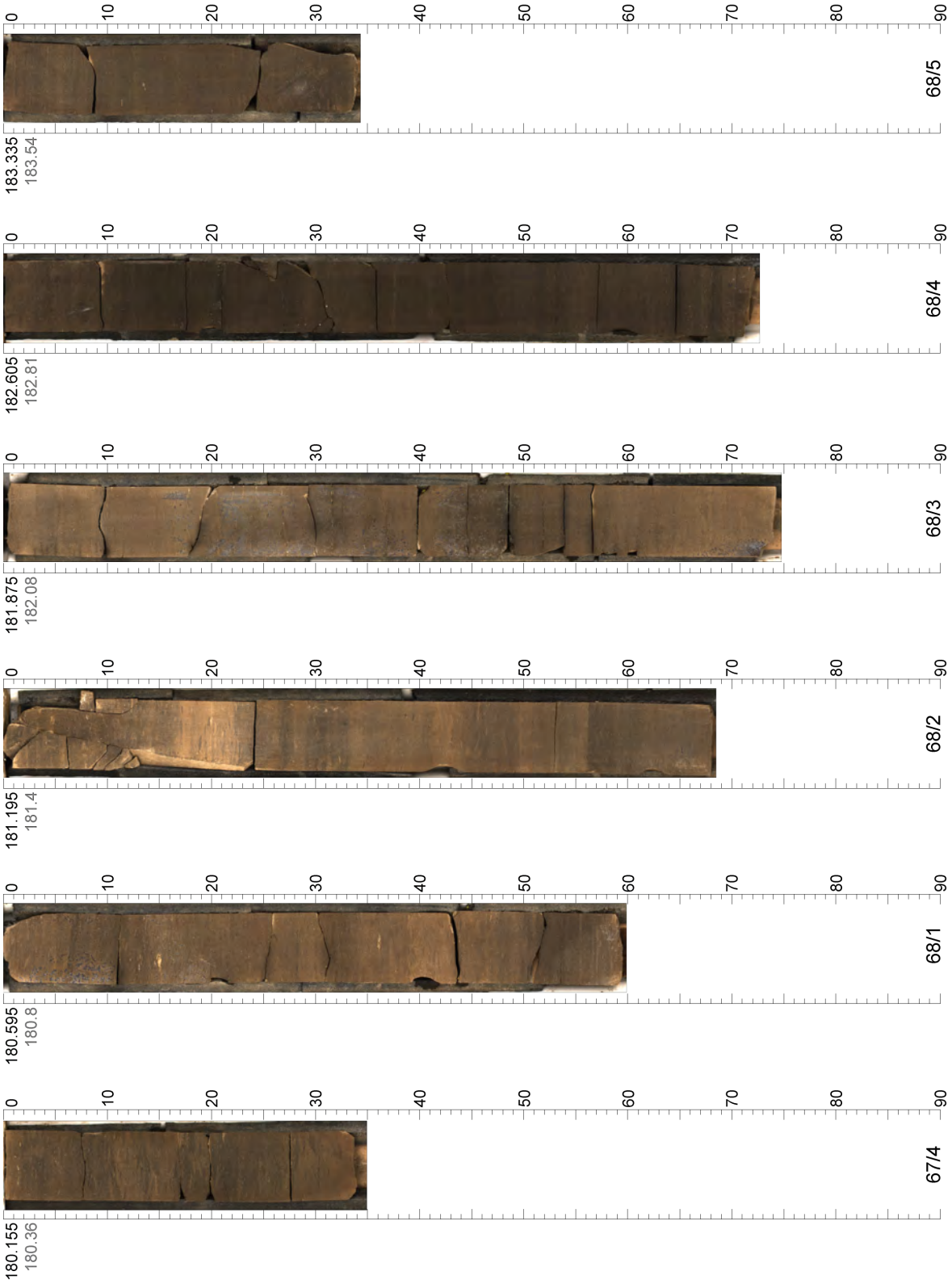
0
10
20
30
40
50
60
70
80
90
68/5
183.335
183.54
68/4
182.605
182.81
68/3
181.875
182.08
68/2
181.195
181.4
68/1
180.595
180.8
67/4
180.155
180.36

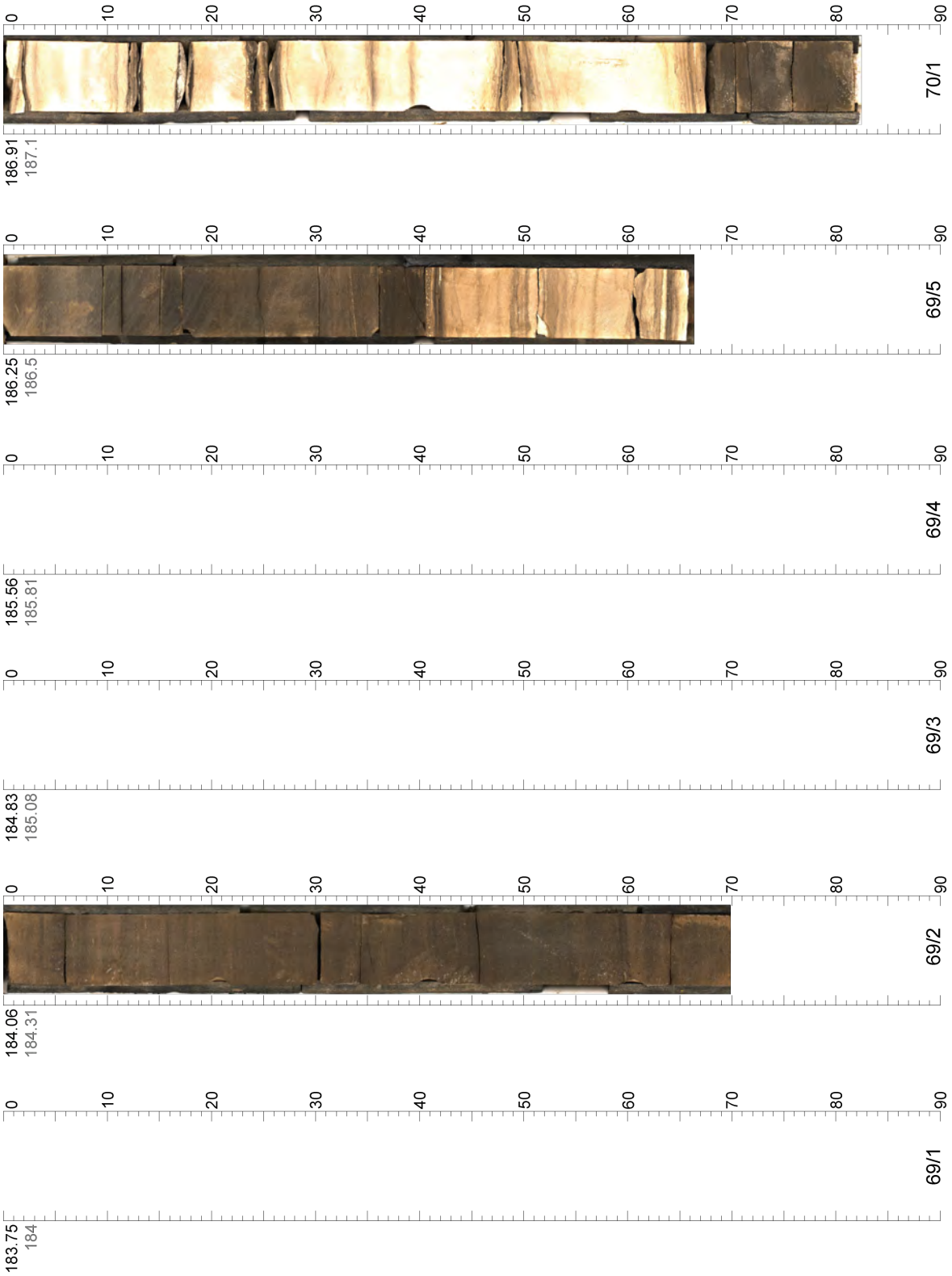
0
10
20
30
40
50
60
70
80
90
70/1
186.91
187.1
69/5
186.25
186.5
69/4
185.56
185.81
69/3
184.83
185.08
69/2
184.06
184.31
69/1
183.75
184

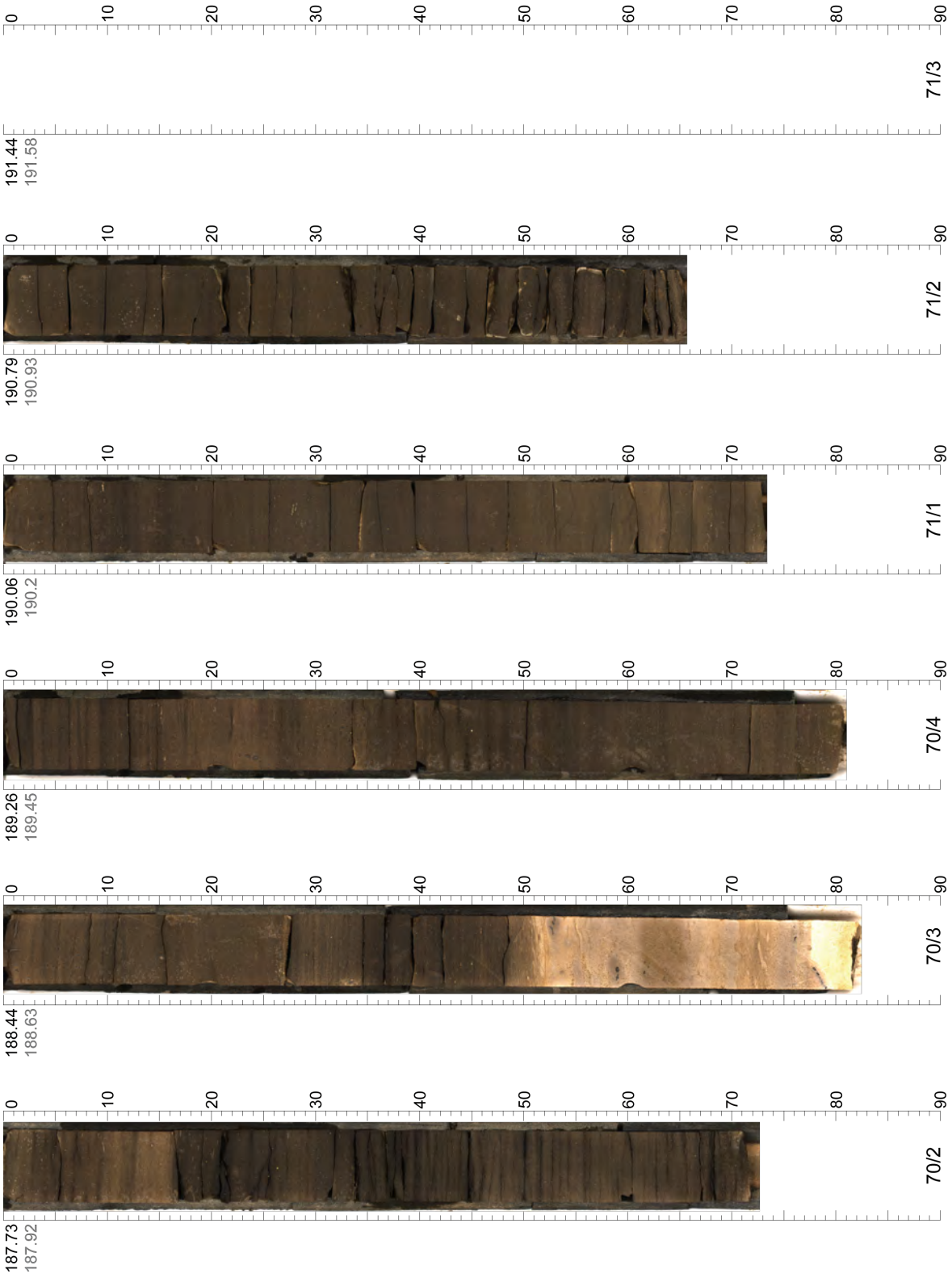
0 10 20 30 40 50 60 70 80 90
71/3
191.44
191.58
0 10 20 30 40 50 60 70 80 90
71/2
190.79
190.93
0 10 20 30 40 50 60 70 80 90
71/1
190.06
190.2
0 10 20 30 40 50 60 70 80 90
70/4
189.26
189.45
0 10 20 30 40 50 60 70 80 90
70/3
188.44
188.63
0 10 20 30 40 50 60 70 80 90
70/2
187.73
187.92

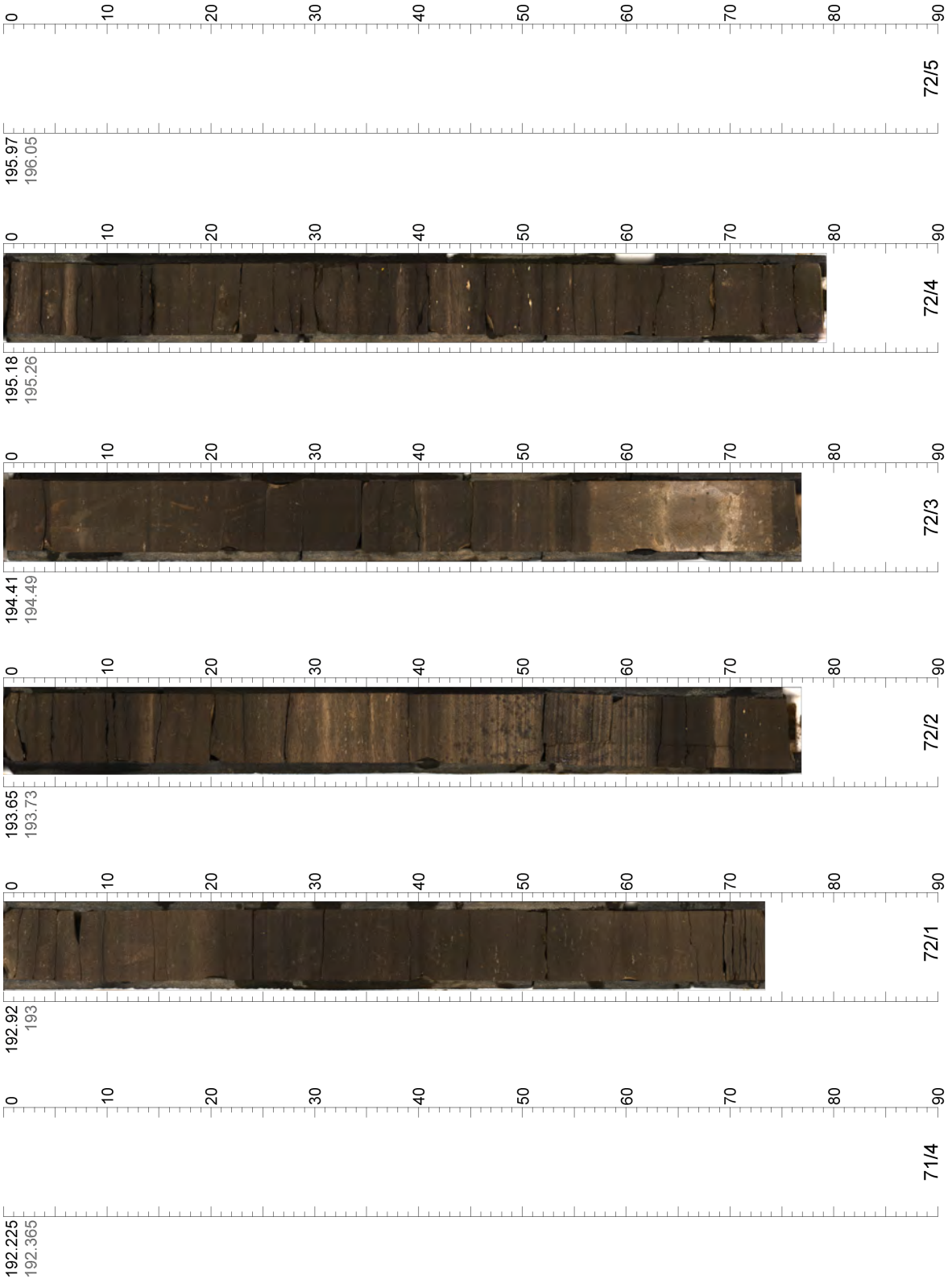
0
10
20
30
40
50
60
70
80
90
72/5
195.97
196.05
72/4
195.18
195.26
72/3
194.41
194.49
72/2
193.65
193.73
72/1
192.92
193
71/4
192.225
192.365

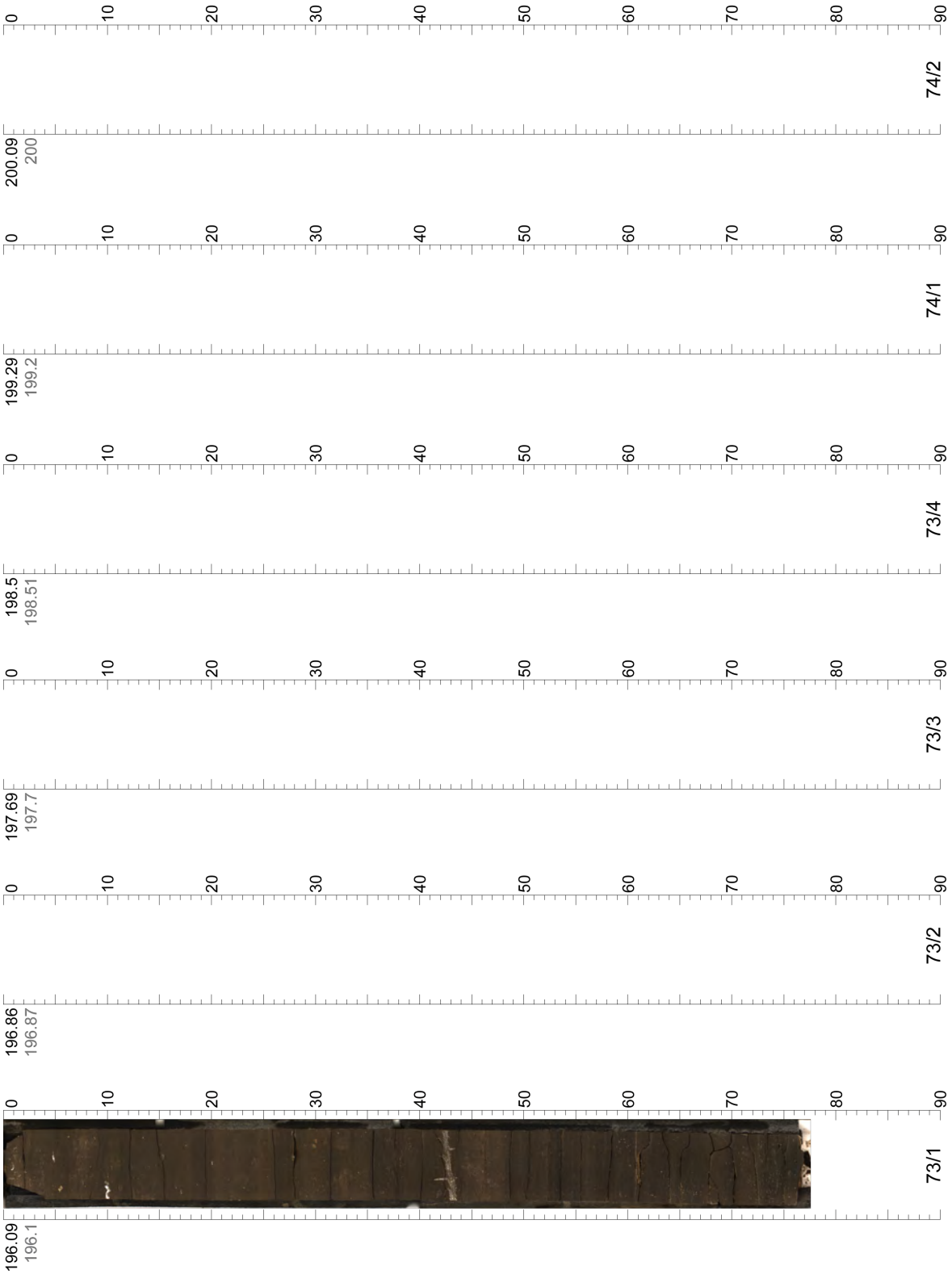
196.09
196.1
73/1
196.86
196.87
73/2
197.69
197.7
73/3
198.5
198.51
73/4
199.29
199.2
74/1
200.09
200
74/2
0
10
20
30
40
50
60
70
80
90

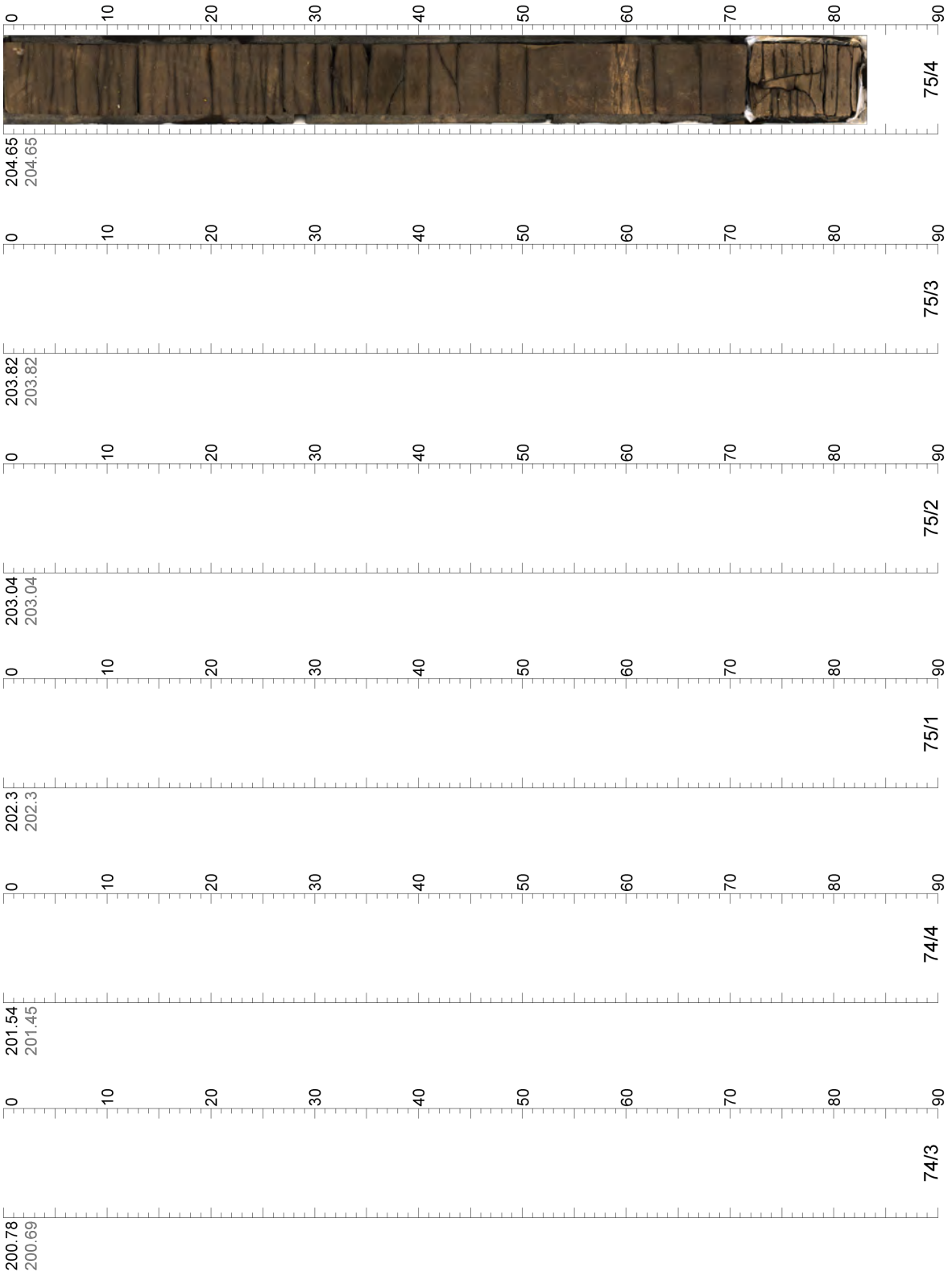
0
10
20
30
40
50
60
70
80
90
75/4
204.65
204.65
75/3
203.82
203.82
75/2
203.04
203.04
75/1
202.3
202.3
74/4
201.54
201.45
74/3
200.78
200.69

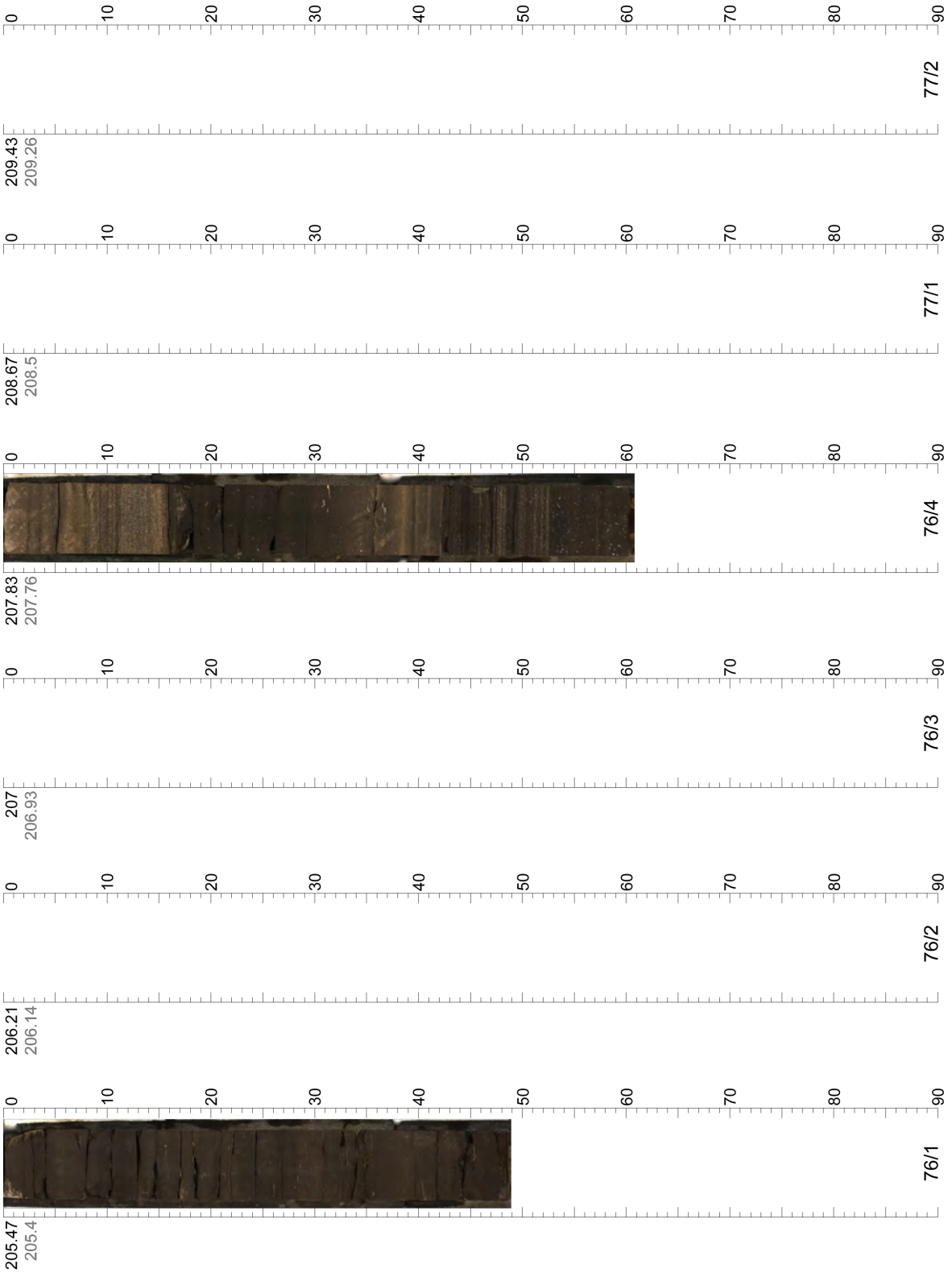
77/2
209.43
209.26
77/1
208.67
208.5
76/4
207.83
207.76
76/3
207
206.93
76/2
206.21
206.14
76/1
205.47
205.4

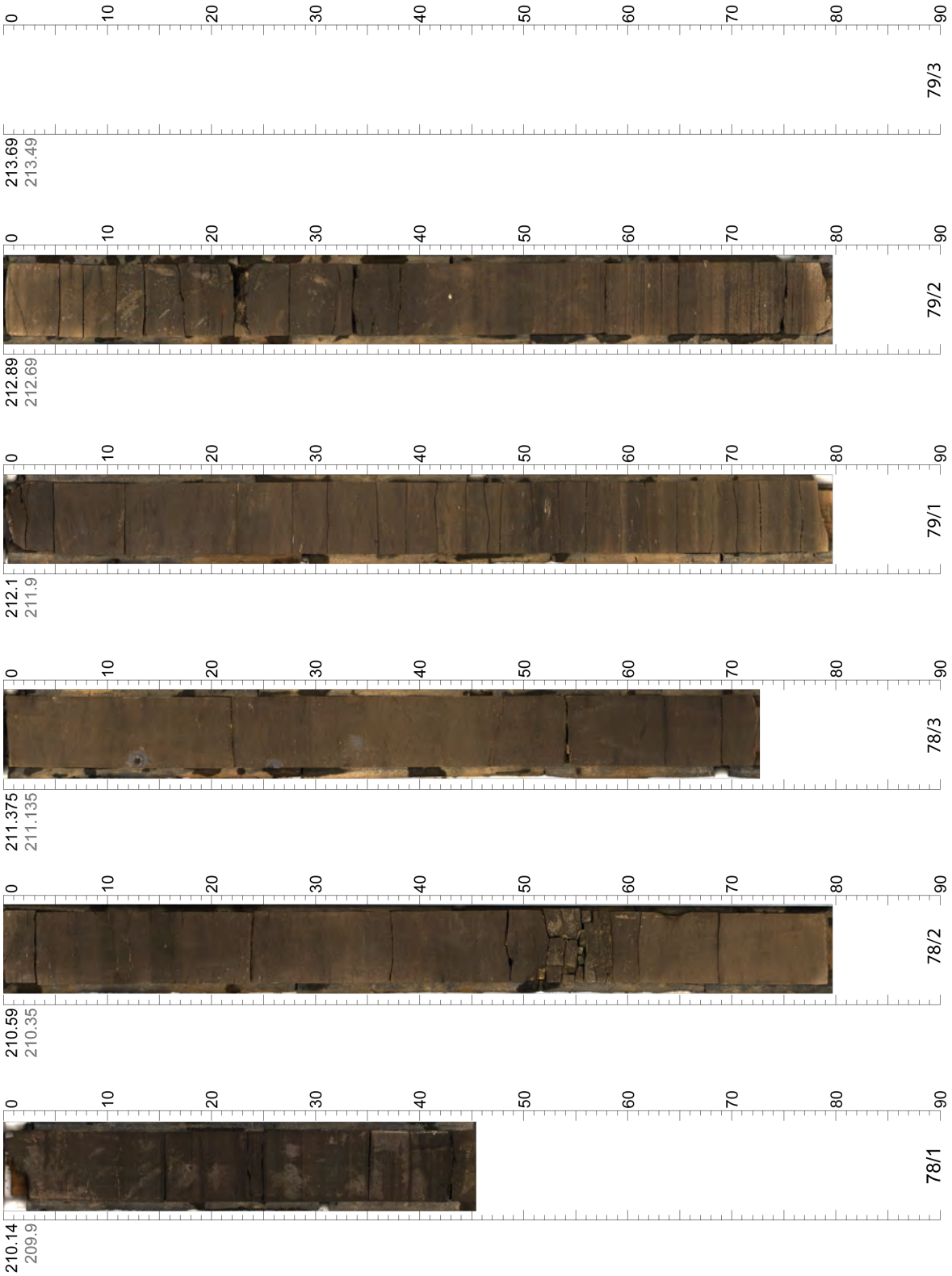
0
10
20
30
40
50
60
70
80
90
79/3
213.69
213.49
79/2
212.89
212.69
79/1
212.1
211.9
78/3
211.375
211.135
78/2
210.59
210.35
78/1
210.14
209.9

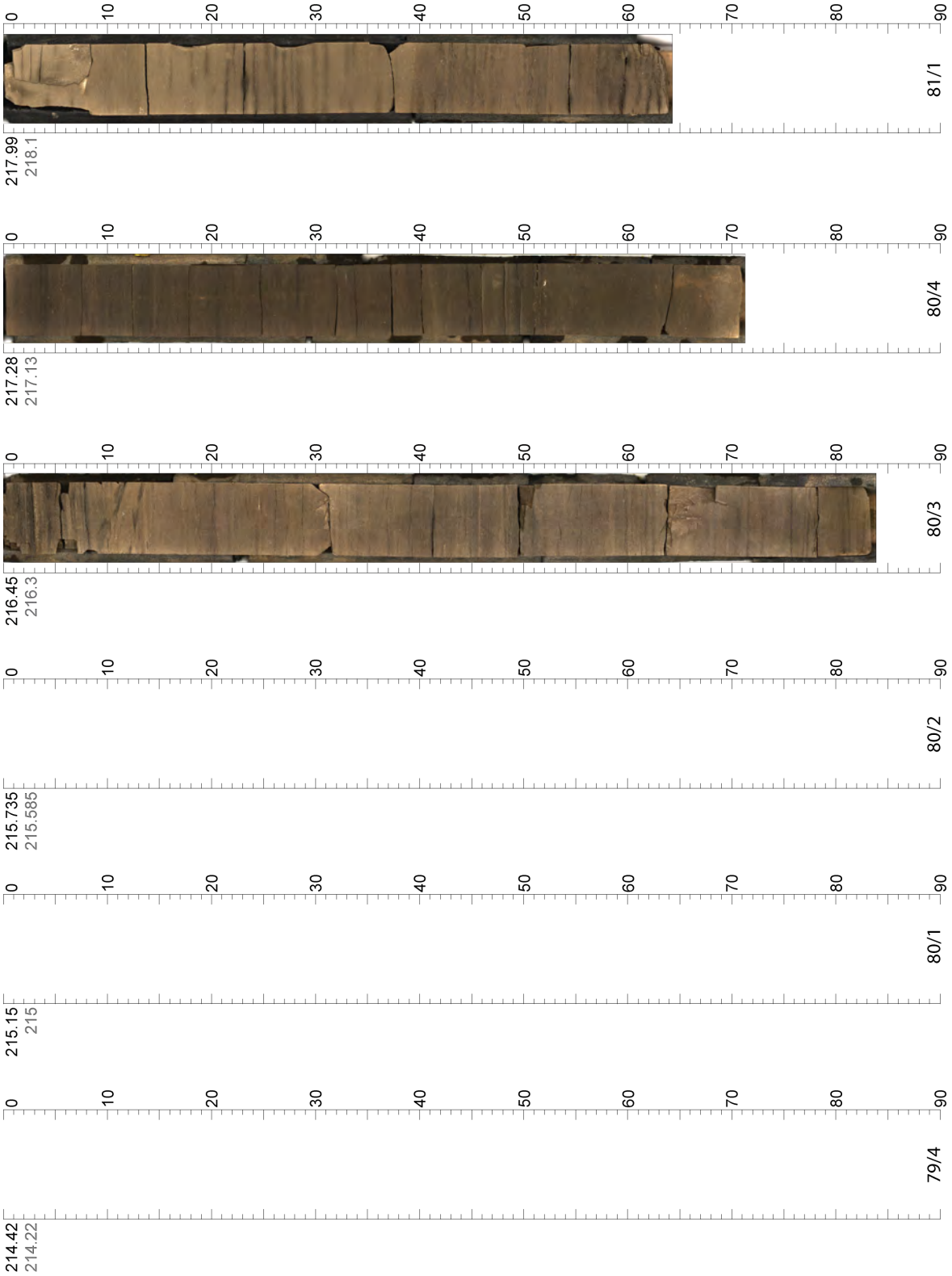
0
10
20
30
40
50
60
70
80
90
81/1
217.99
218.1
80/4
217.28
217.13
80/3
216.45
216.3
80/2
215.735
215.585
80/1
215.15
215
79/4
214.42
214.22

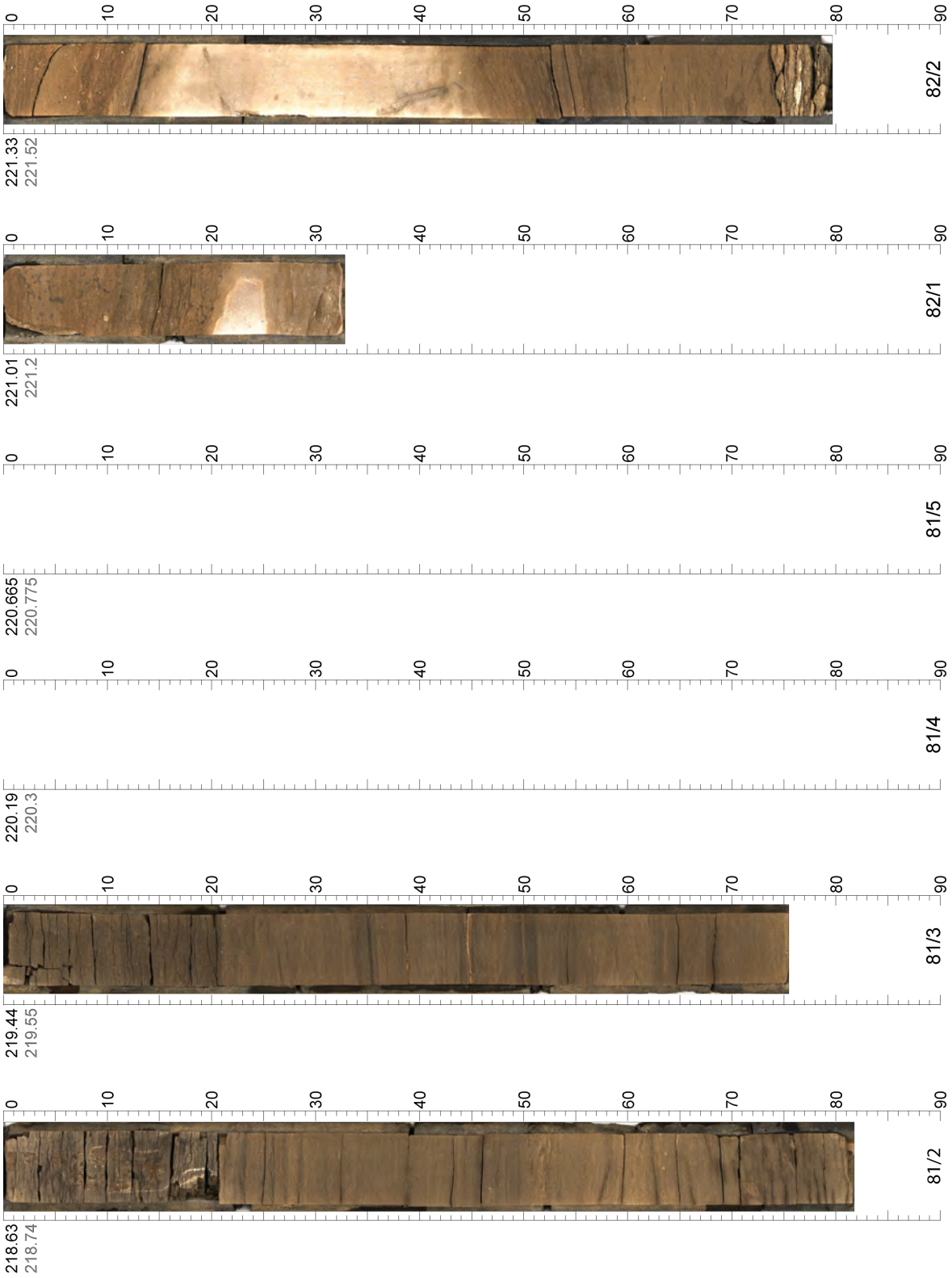
0
10
20
30
40
50
60
70
80
90
82/2
221.33
221.52
82/1
221.01
221.2
81/5
220.665
220.775
81/4
220.19
220.3
81/3
219.44
219.55
81/2
218.63
218.74

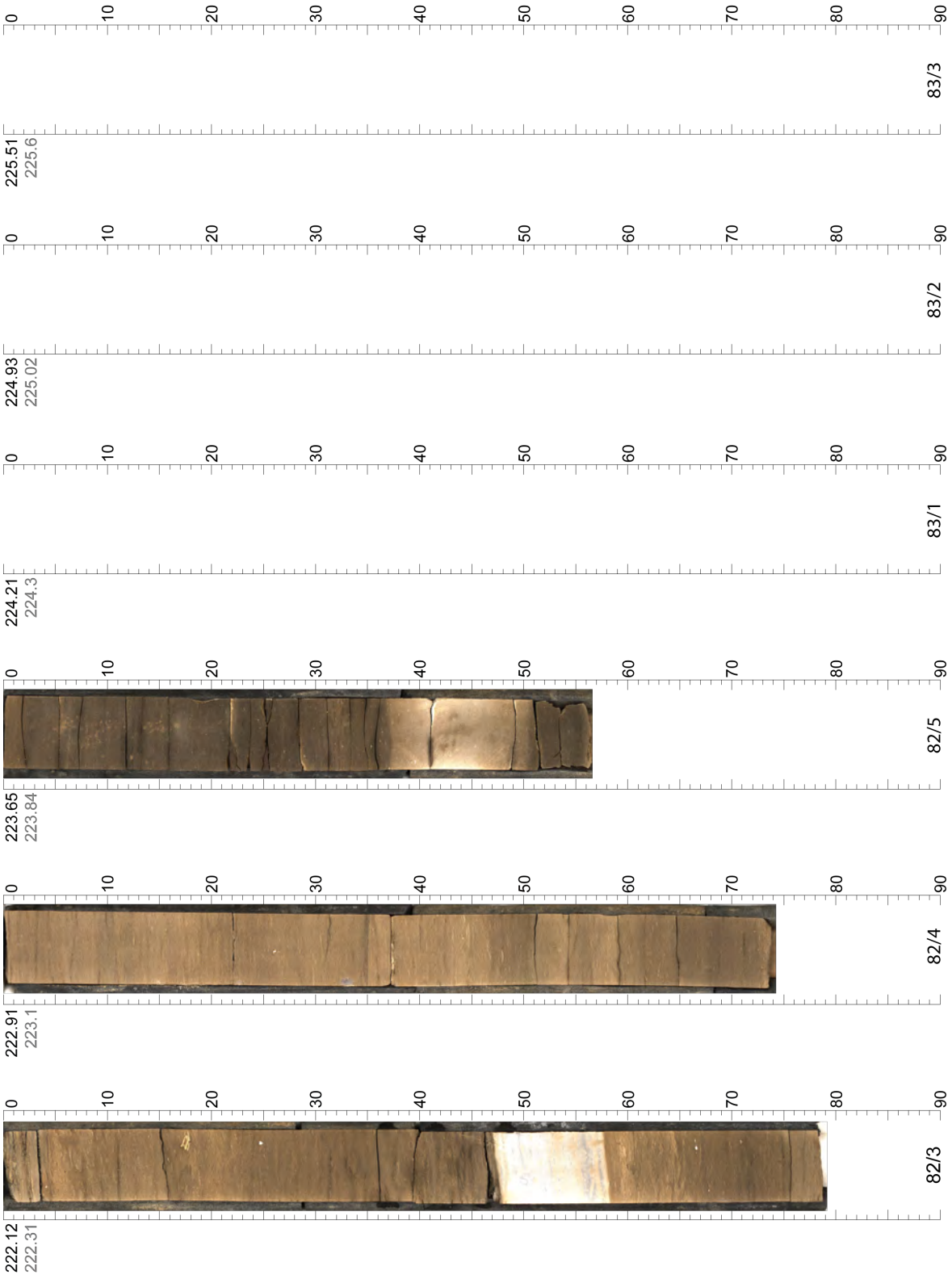
0
10
20
30
40
50
60
70
80
90
83/3
225.51
225.6
83/2
224.93
225.02
83/1
224.21
224.3
82/5
223.65
223.84
82/4
222.91
223.1
82/3
222.12
222.31

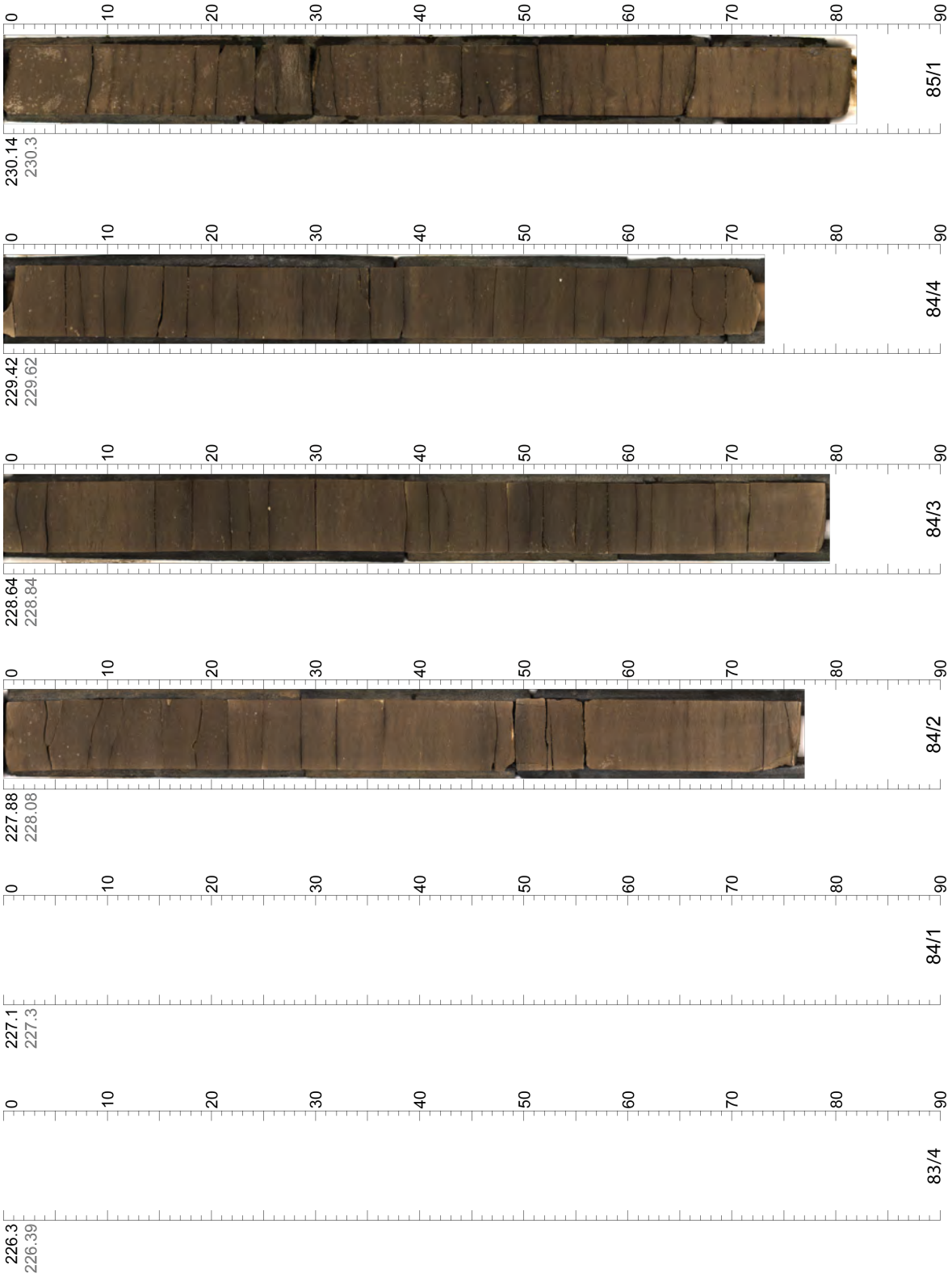
0
10
20
30
40
50
60
70
80
90
85/1
230.14
230.3
84/4
229.42
229.62
84/3
228.64
228.84
84/2
227.88
228.08
84/1
227.1
227.3
83/4
226.3
226.39

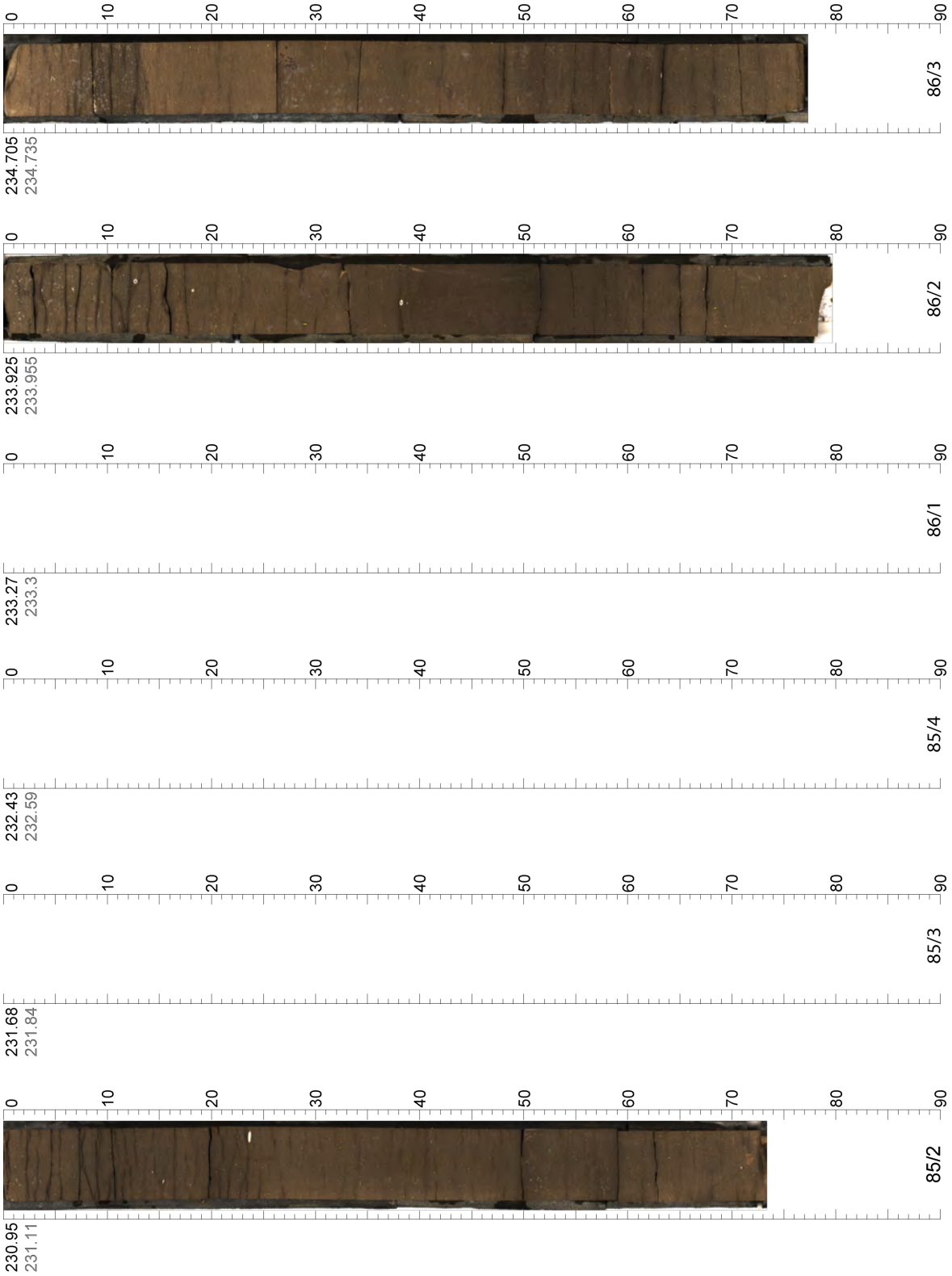
0 10 20 30 40 50 60 70 80 90
86/3
234.705
234.735
0 10 20 30 40 50 60 70 80 90
86/2
233.925
233.955
0 10 20 30 40 50 60 70 80 90
86/1
233.27
233.3
0 10 20 30 40 50 60 70 80 90
85/4
232.43
232.59
0 10 20 30 40 50 60 70 80 90
85/3
231.68
231.84
0 10 20 30 40 50 60 70 80 90
85/2
230.95
231.11

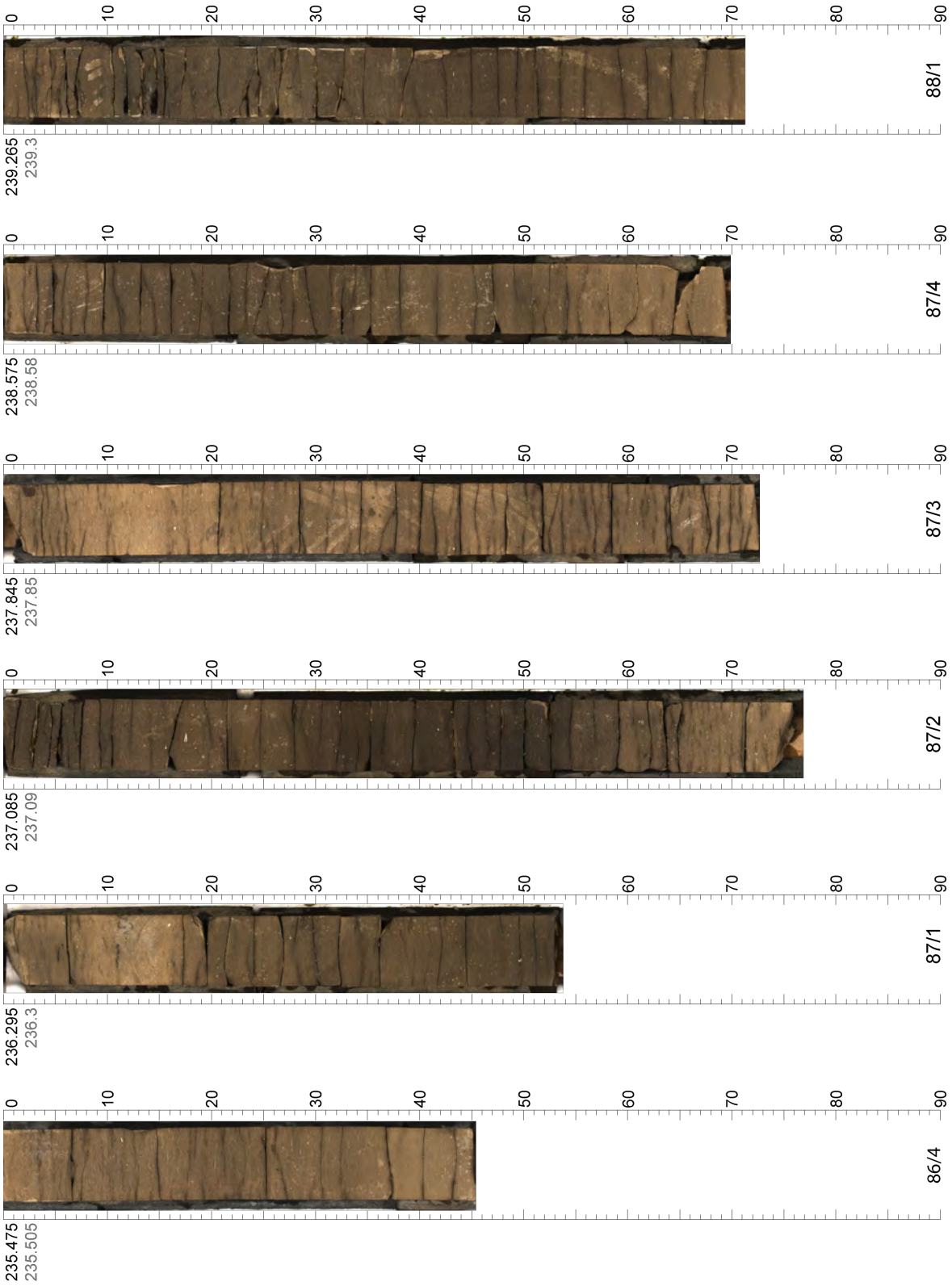
0
10
20
30
40
50
60
70
80
90
88/1
239.265
239.3
87/4
238.575
238.58
87/3
237.845
237.85
87/2
237.085
237.09
87/1
236.295
236.3
86/4
235.475
235.505

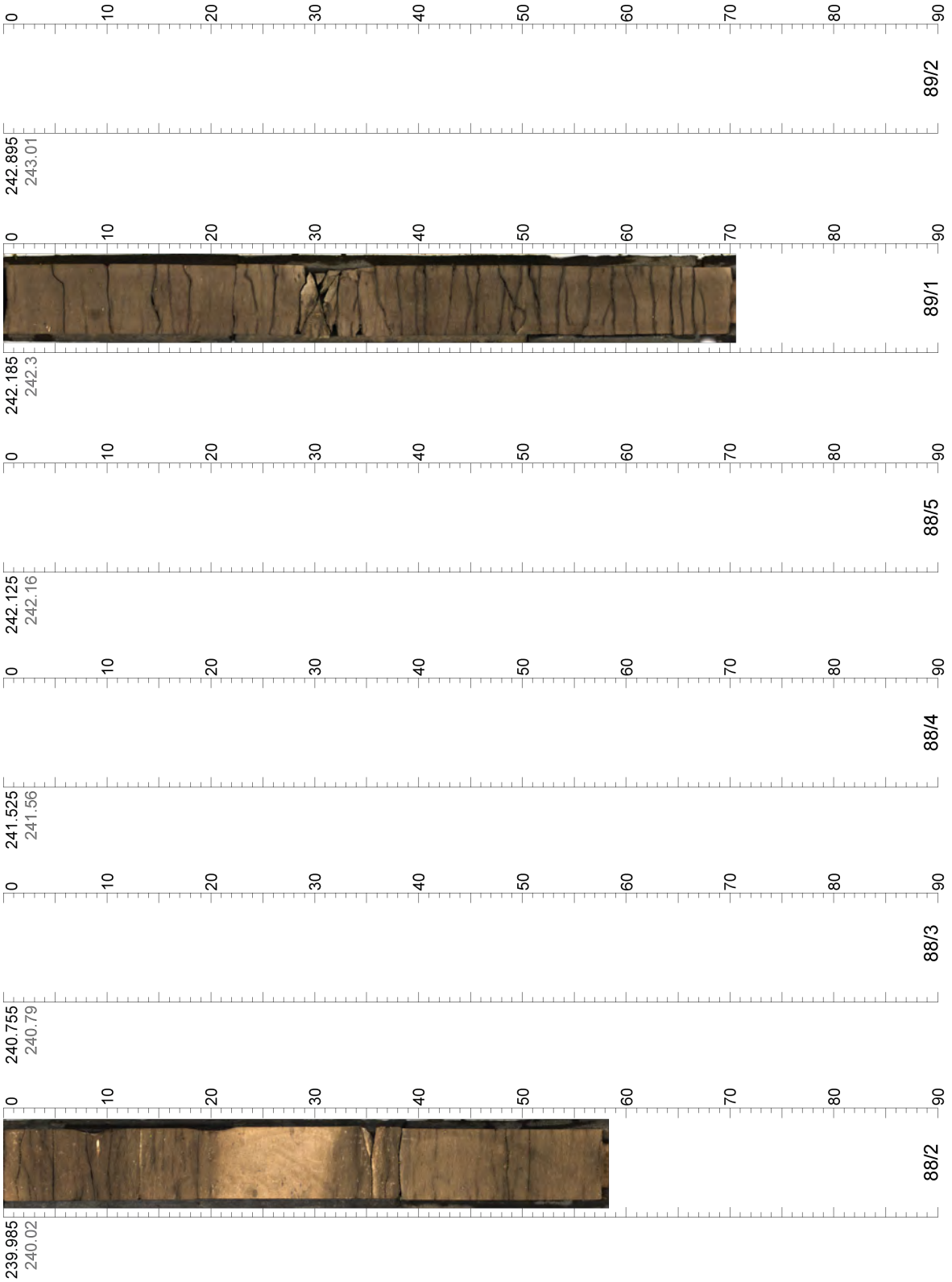
0
10
20
30
40
50
60
70
80
90
89/2
242.895
243.01
89/1
242.185
242.3
88/5
242.125
242.16
88/4
241.525
241.56
88/3
240.755
240.79
88/2
239.985
240.02

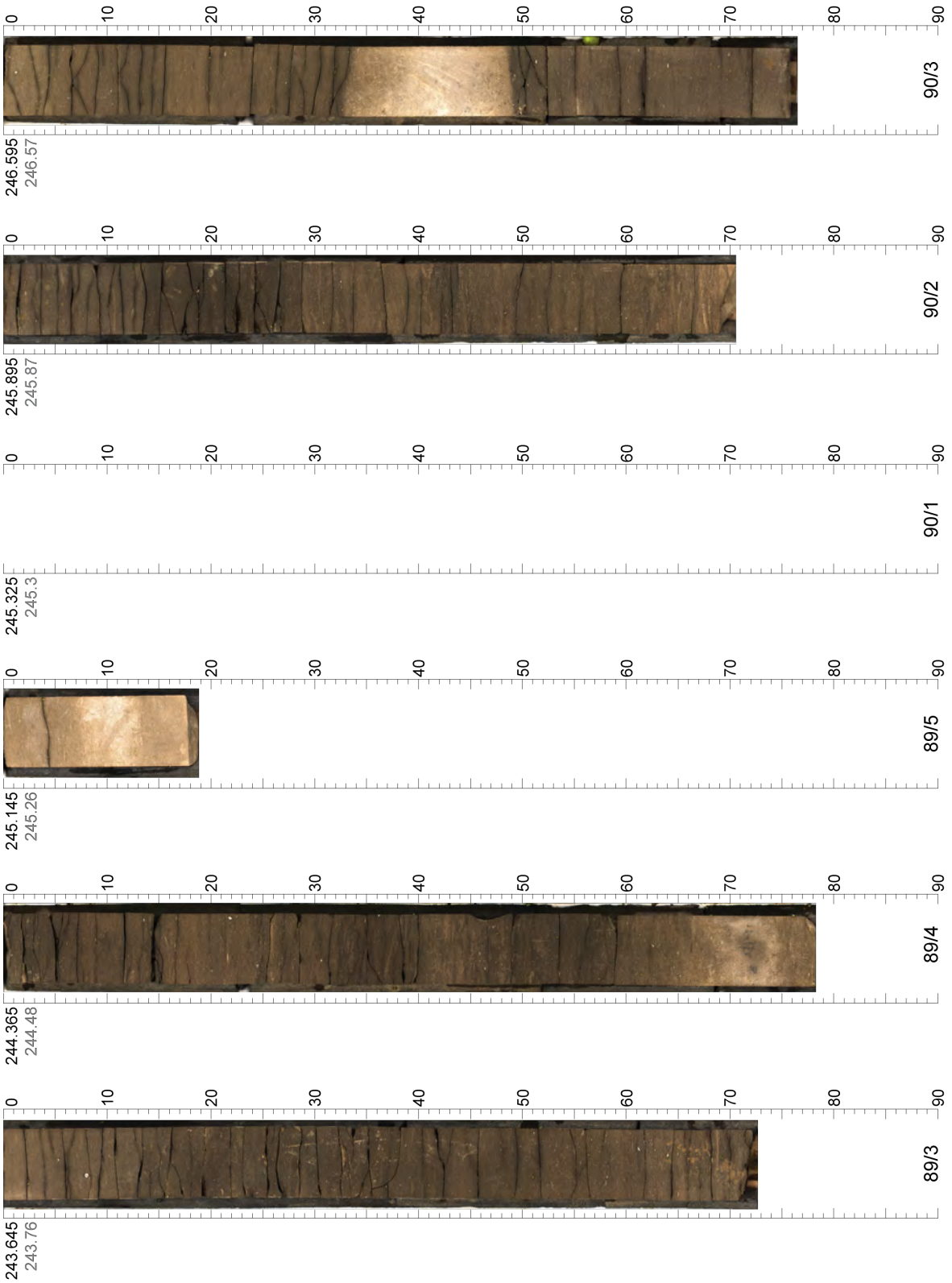
90/3
246.595
246.57
90/2
245.895
245.87
90/1
245.325
245.3
89/5
245.145
245.26
89/4
244.365
244.48
89/3
243.645
243.76

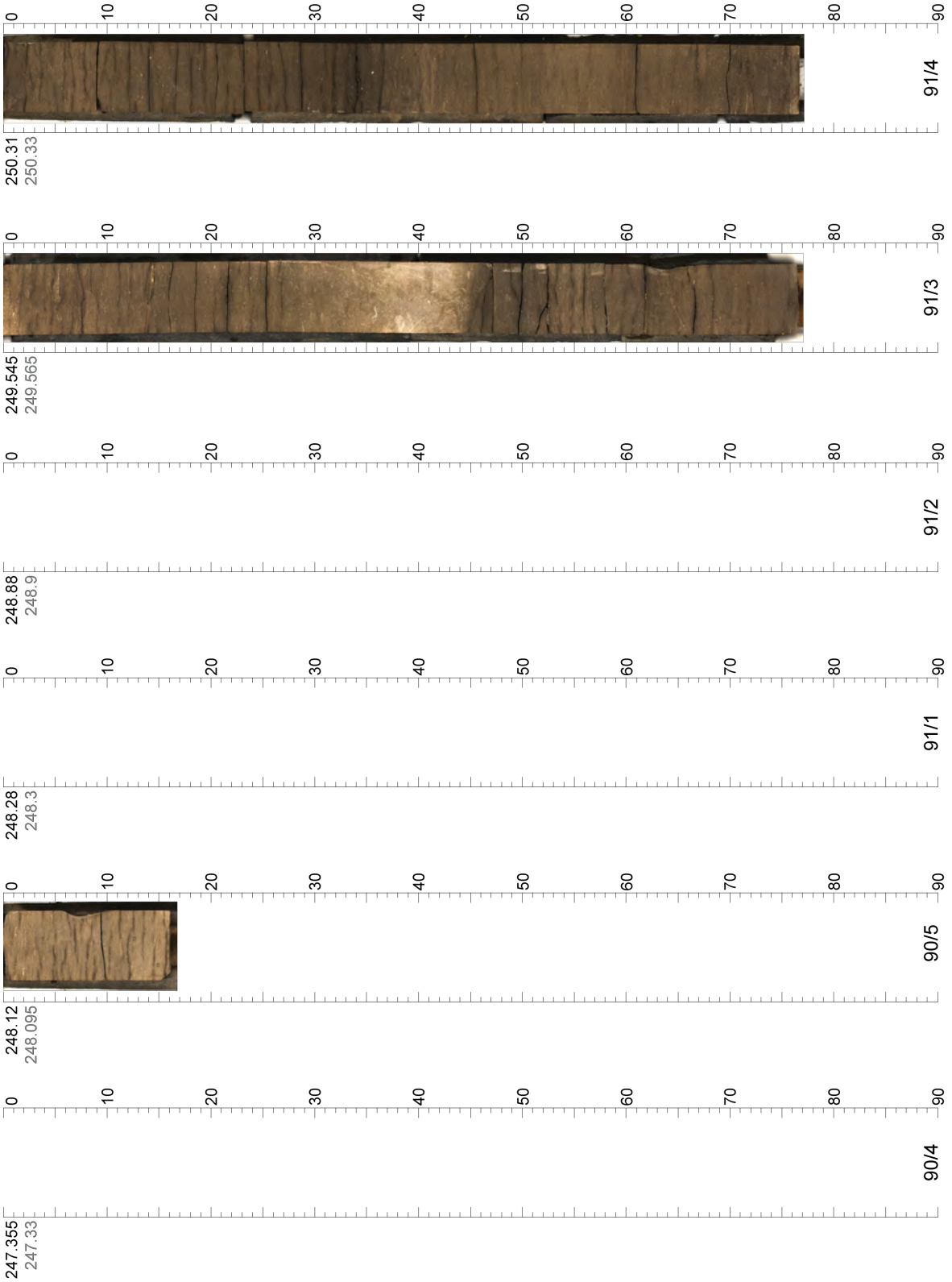
0
10
20
30
40
50
60
70
80
90
91/4
250.31
250.33
91/3
249.545
249.565
91/2
248.88
248.9
91/1
248.28
248.3
90/5
248.12
248.095
90/4
247.355
247.33

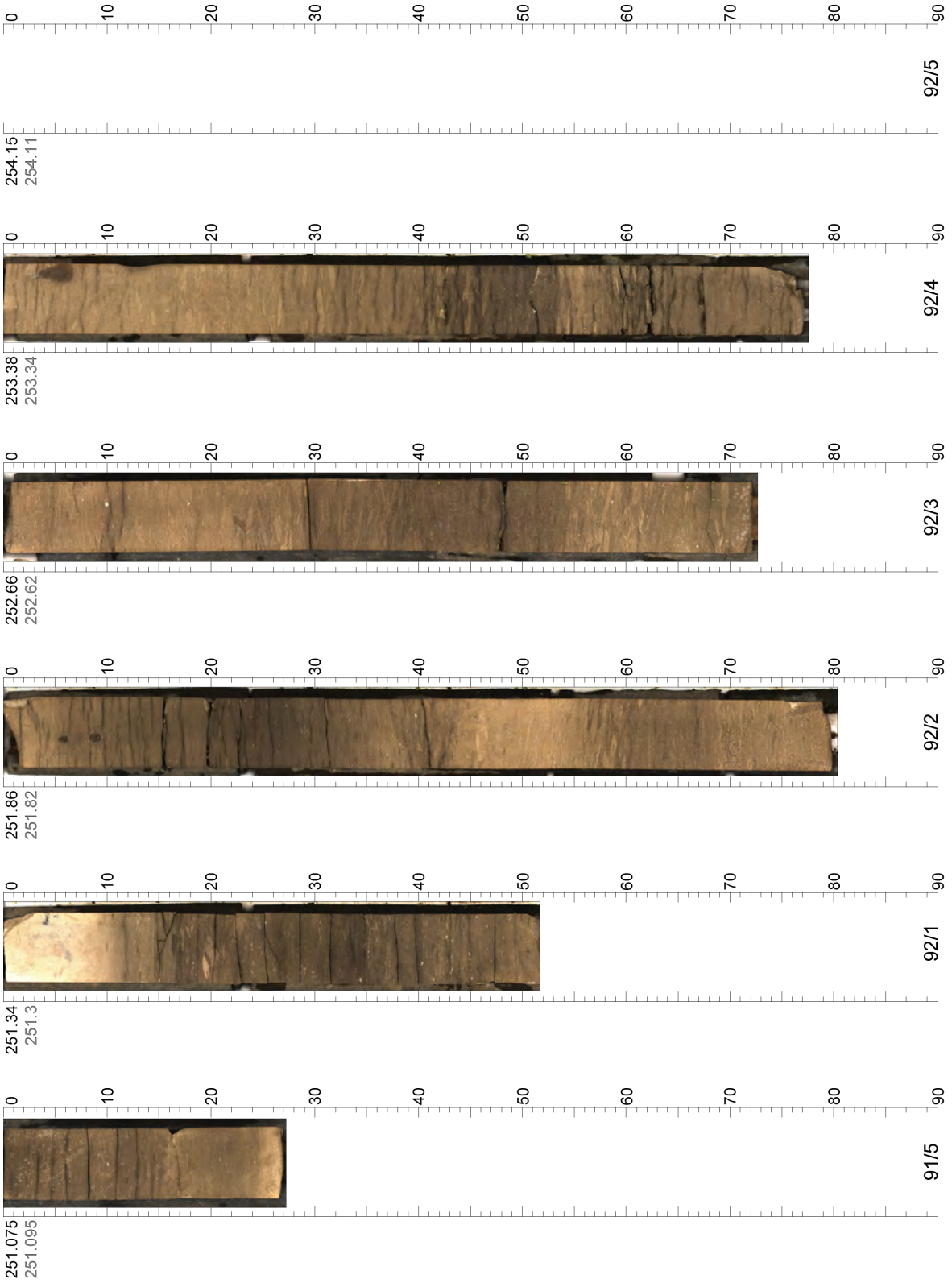
0
10
20
30
40
50
60
70
80
90
92/5
254.15
254.11
92/4
253.38
253.34
92/3
252.66
252.62
92/2
251.86
251.82
92/1
251.34
251.3
91/5
251.075
251.095

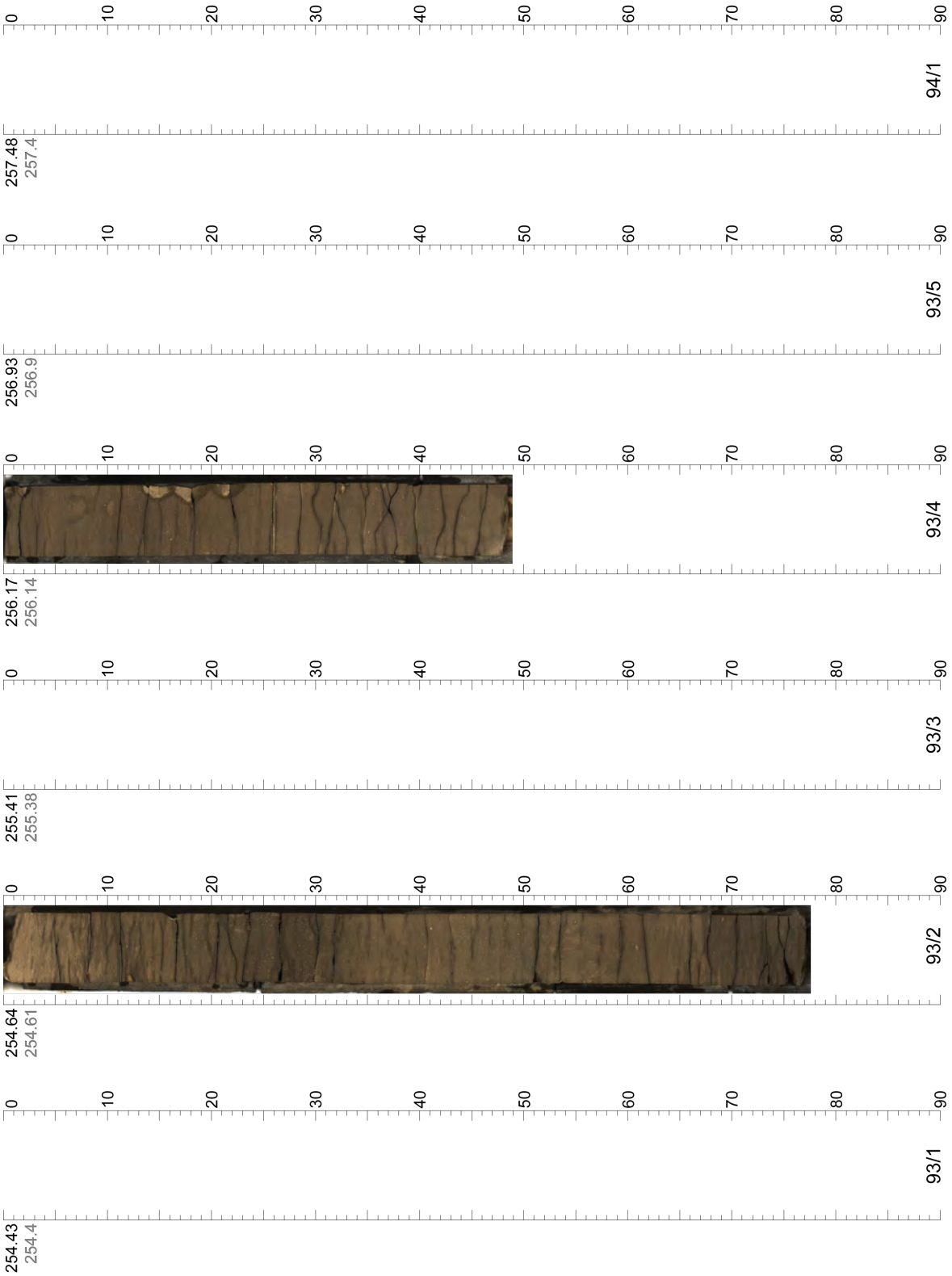
94/1
257.48
257.4
93/5
256.93
256.9
93/4
256.17
256.14
93/3
255.41
255.38
93/2
254.64
254.61
93/1
254.43
254.4

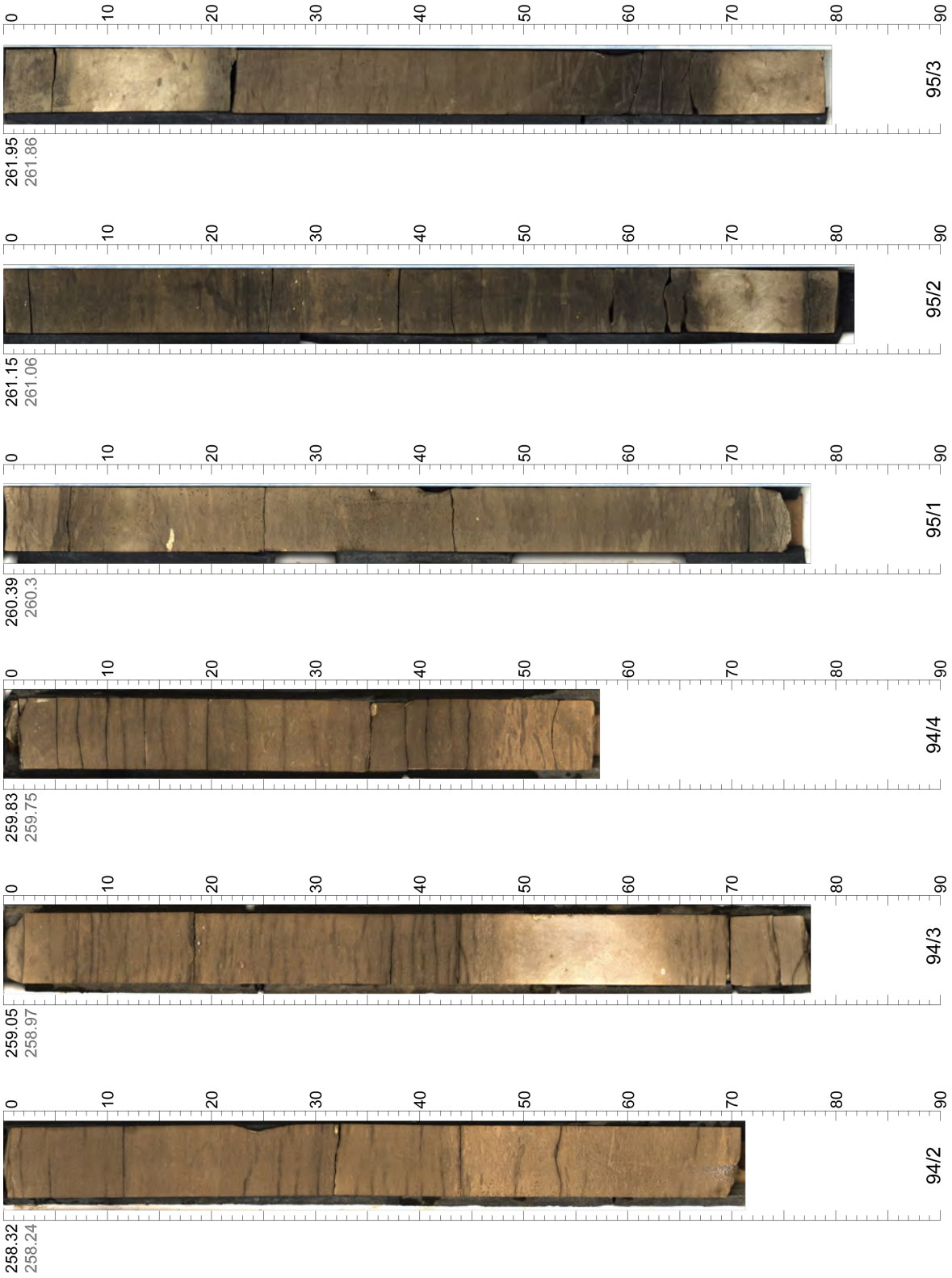
0 10 20 30 40 50 60 70 80 90
95/3
261.95
261.86
0 10 20 30 40 50 60 70 80 90
95/2
261.15
261.06
0 10 20 30 40 50 60 70 80 90
95/1
260.39
260.3
0 10 20 30 40 50 60 70 80 90
94/4
259.83
259.75
0 10 20 30 40 50 60 70 80 90
94/3
259.05
258.97
0 10 20 30 40 50 60 70 80 90
94/2
258.32
258.24

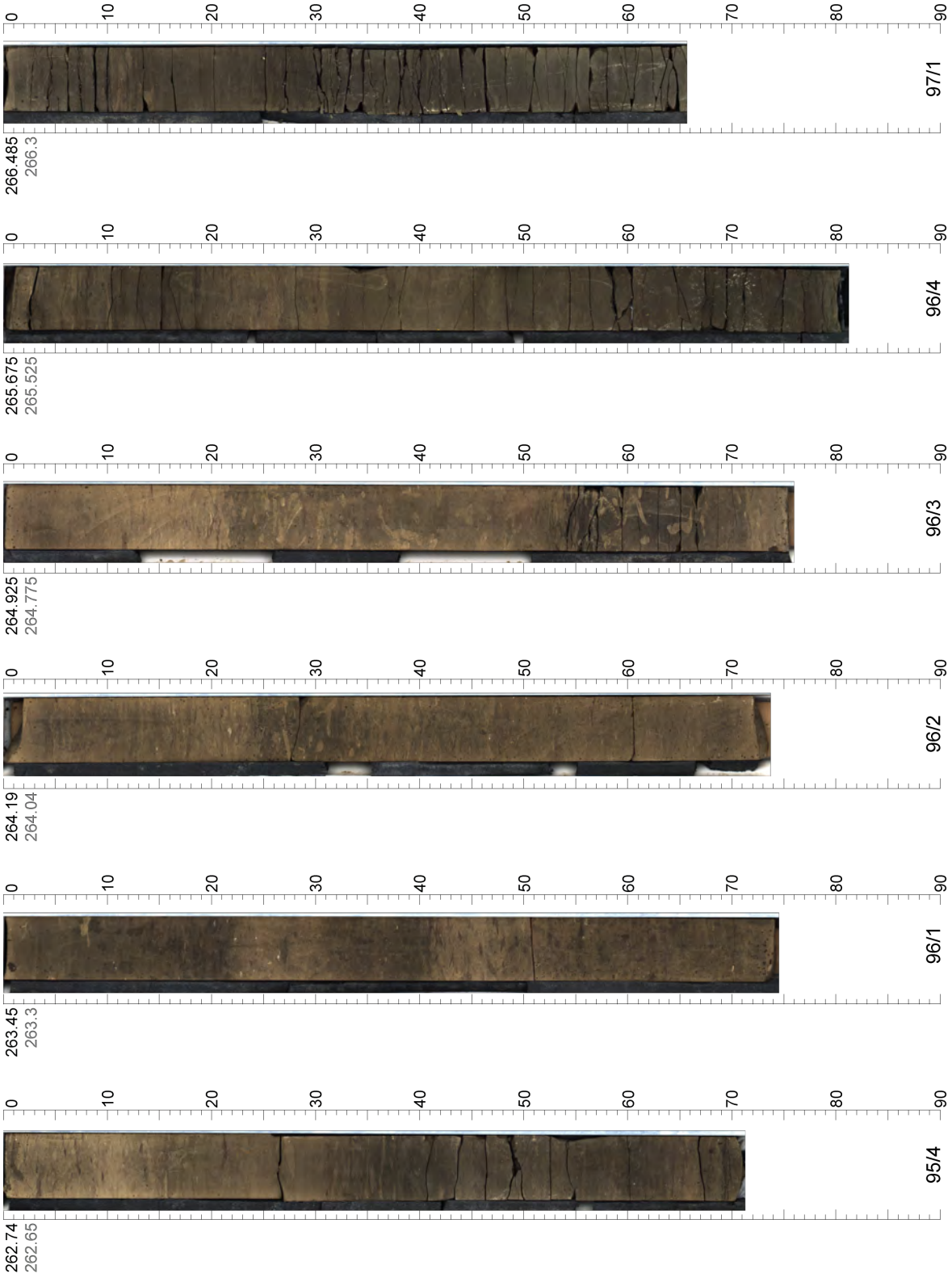
0
10
20
30
40
50
60
70
80
90
97/1
266.485
266.3
96/4
265.675
265.525
96/3
264.925
264.775
96/2
264.19
264.04
96/1
263.45
263.3
95/4
262.74
262.65

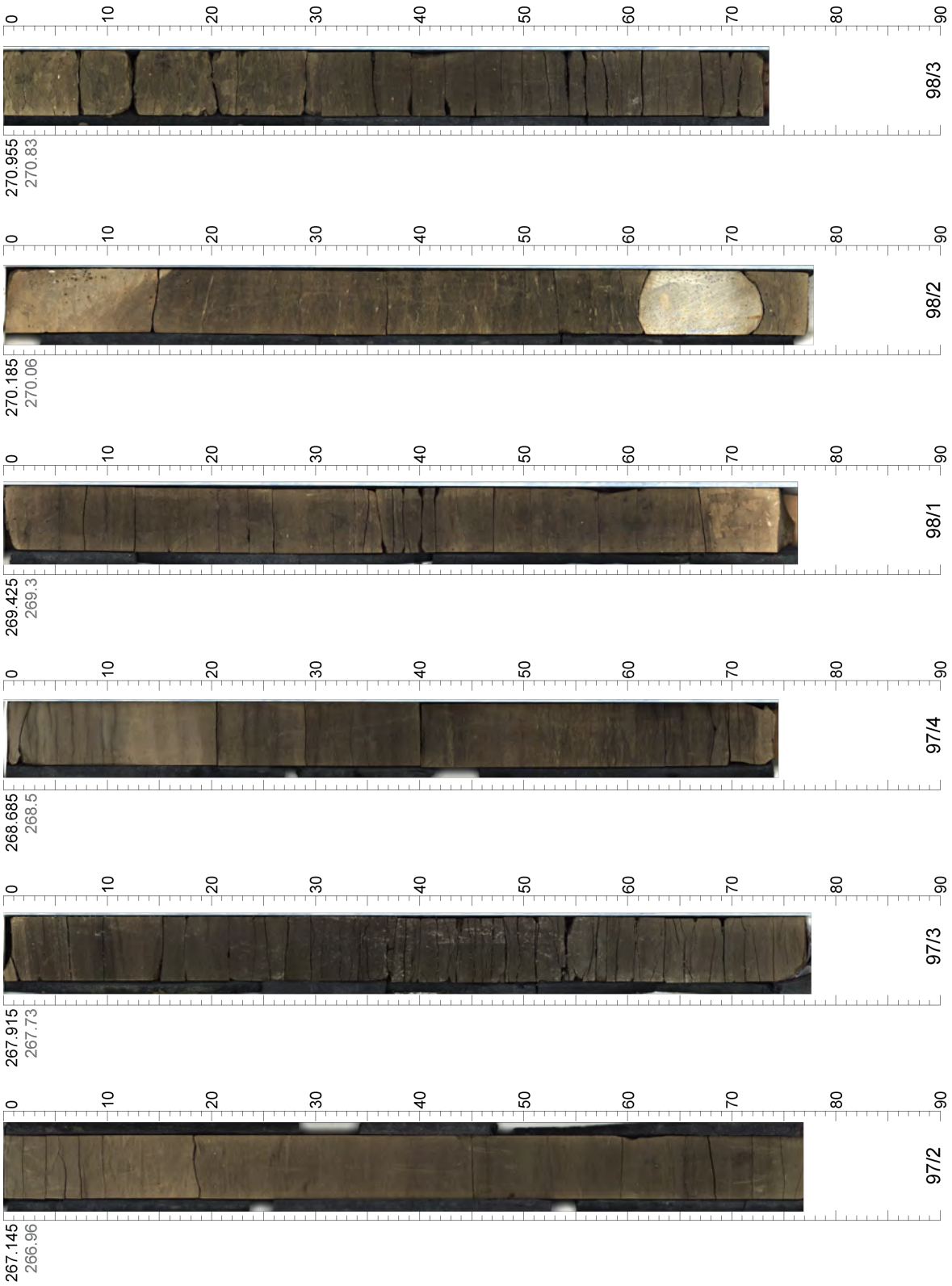
0
10
20
30
40
50
60
70
80
90
98/3
270.955
270.83
98/2
270.185
270.06
98/1
269.425
269.3
97/4
268.685
268.5
97/3
267.915
267.73
97/2
267.145
266.96

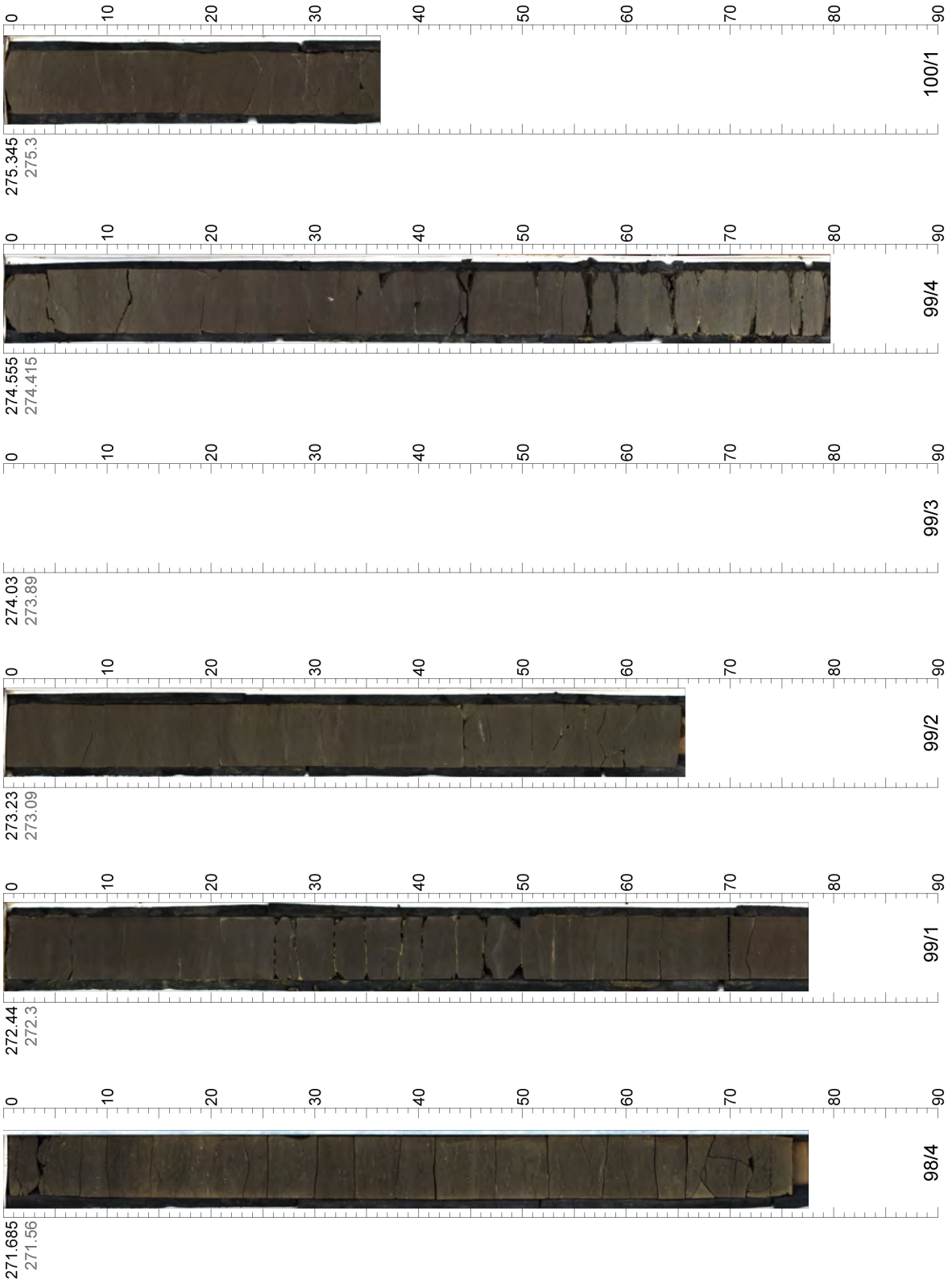
0
10
20
30
40
50
60
70
80
90
100/1
275.345
275.3
99/4
274.555
274.415
99/3
274.03
273.89
99/2
273.23
273.09
99/1
272.44
272.3
98/4
271.685
271.56

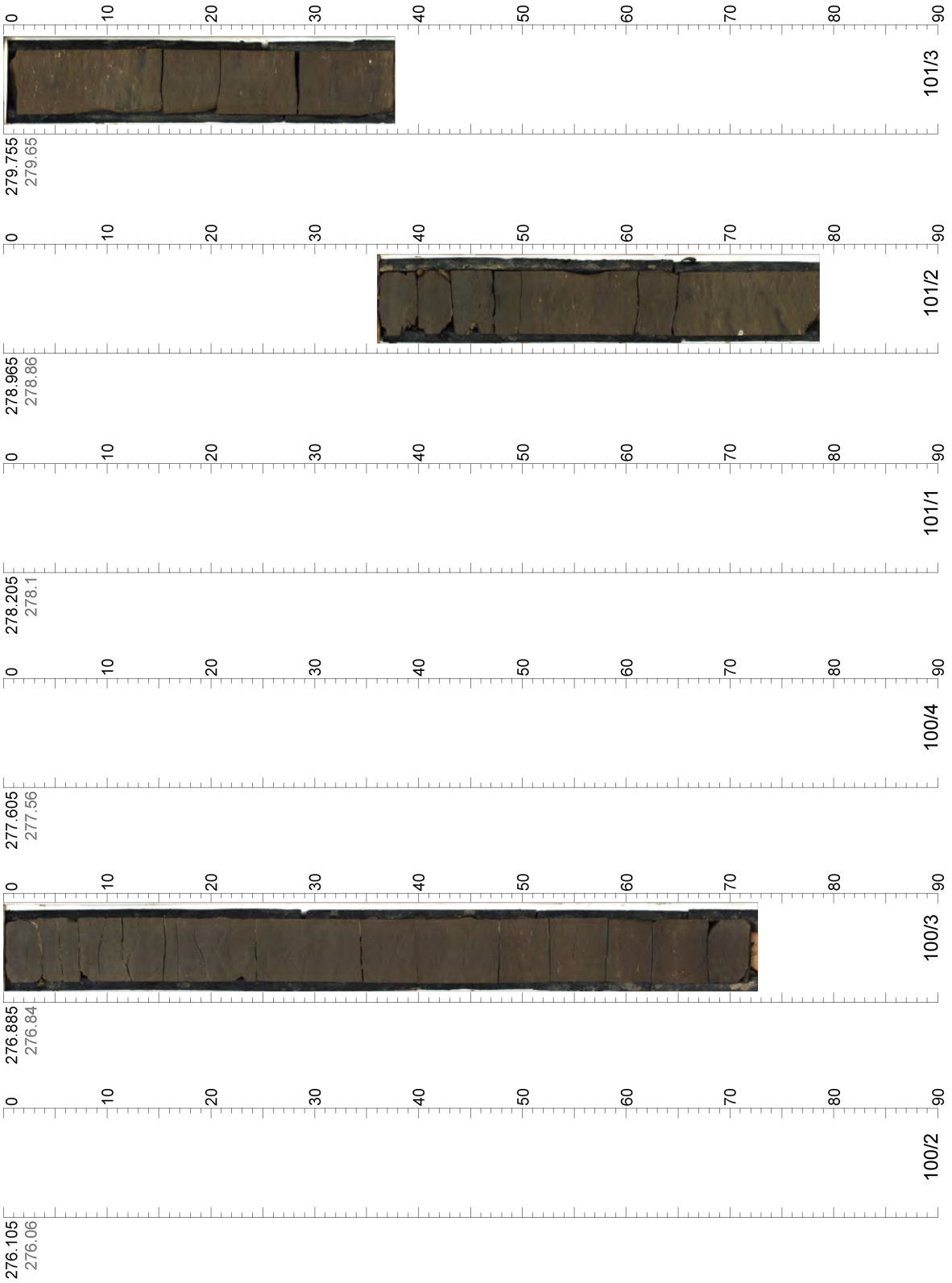
101/3
279.755
279.65
101/2
278.965
278.86
101/1
278.205
278.1
100/4
277.605
277.56
100/3
276.885
276.84
100/2
276.105
276.06

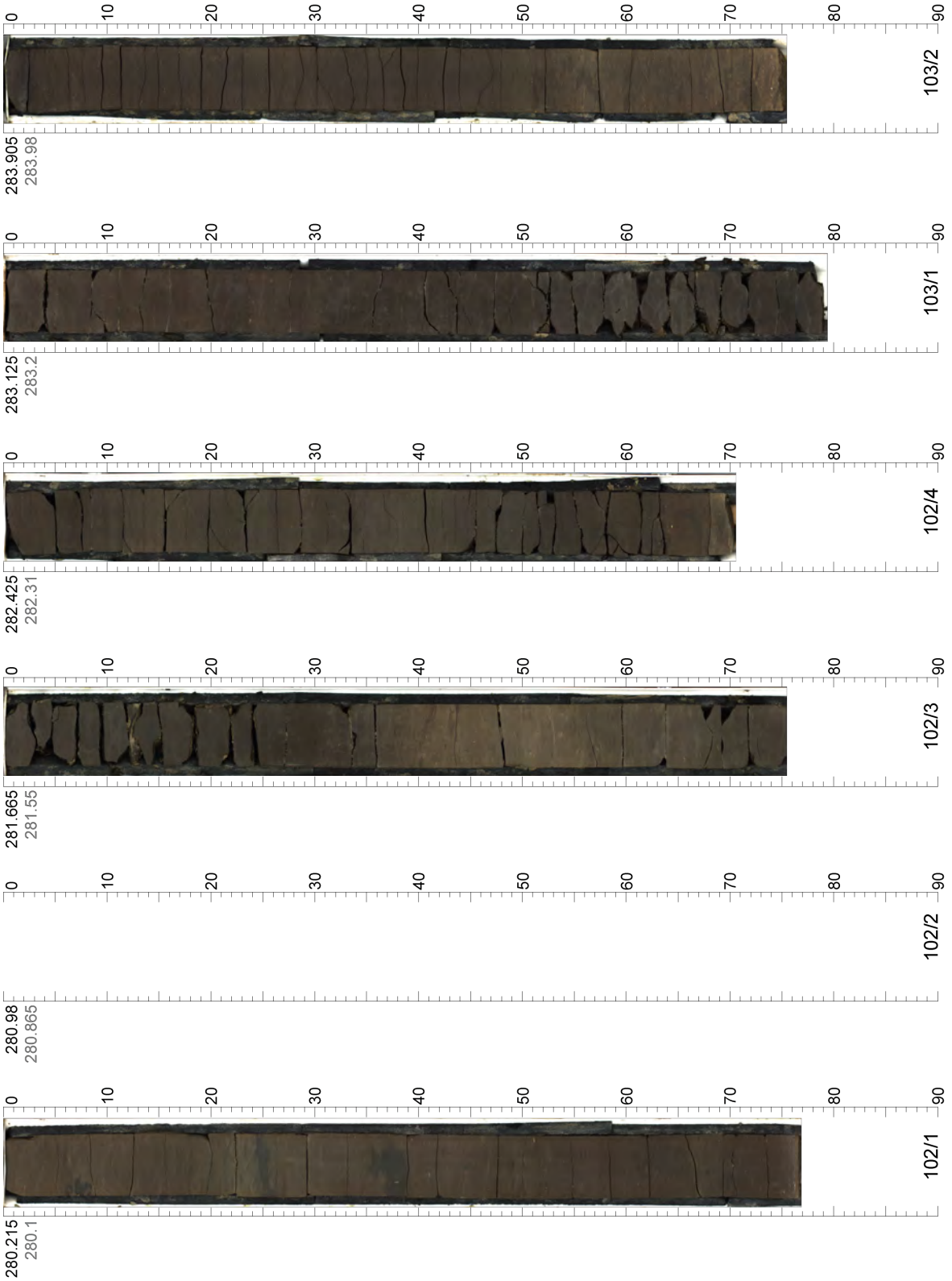
0 10 20 30 40 50 60 70 80 90
103/2
283.905
283.98
0 10 20 30 40 50 60 70 80 90
103/1
283.125
283.2
0 10 20 30 40 50 60 70 80 90
102/4
282.425
282.31
0 10 20 30 40 50 60 70 80 90
102/3
281.665
281.55
0 10 20 30 40 50 60 70 80 90
102/2
280.98
280.865
0 10 20 30 40 50 60 70 80 90
102/1
280.215
280.1

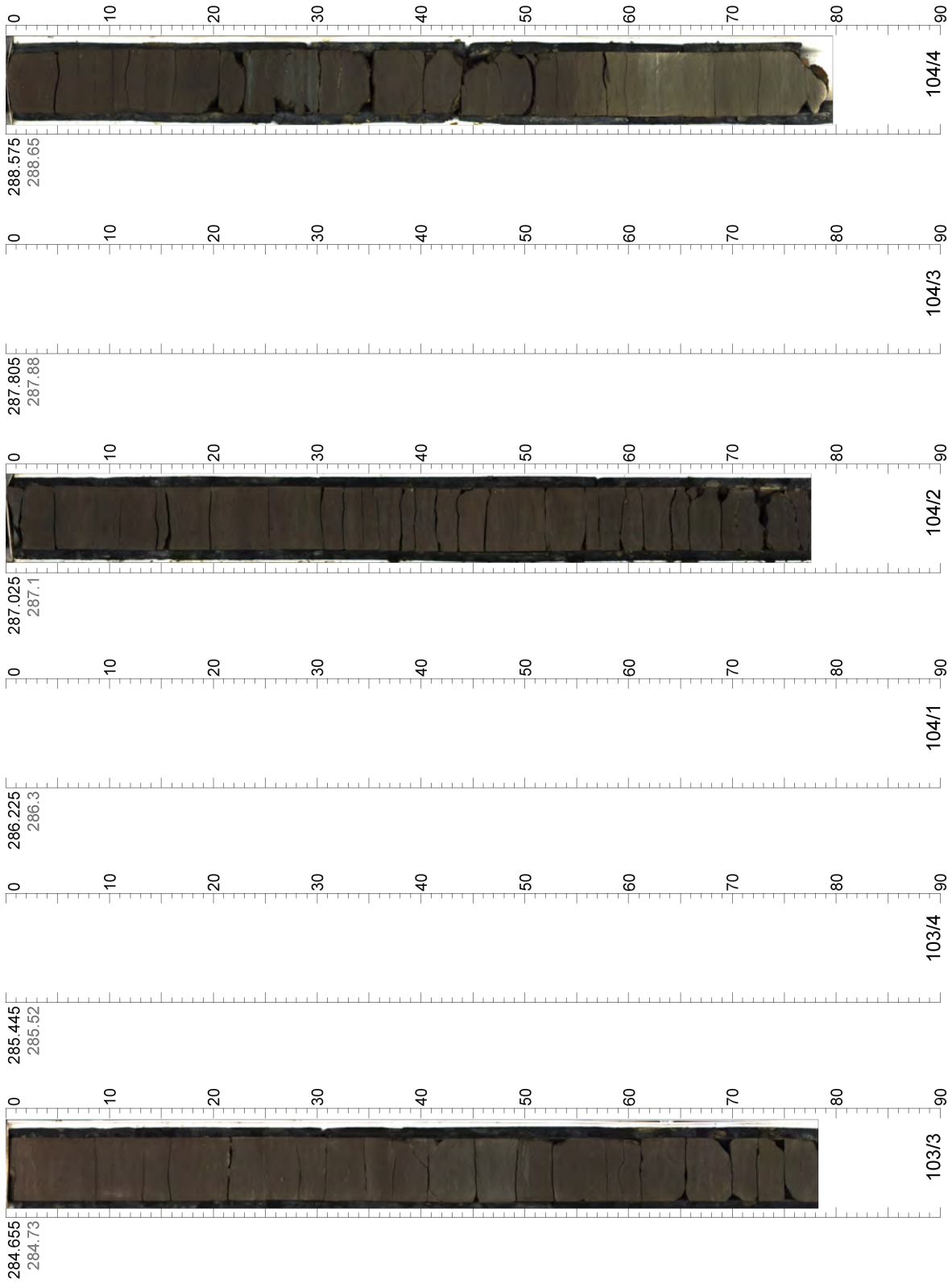
104/4
288.575
288.65
104/3
287.805
287.88
104/2
287.025
287.1
104/1
286.225
286.3
103/4
285.445
285.52
103/3
284.655
284.73

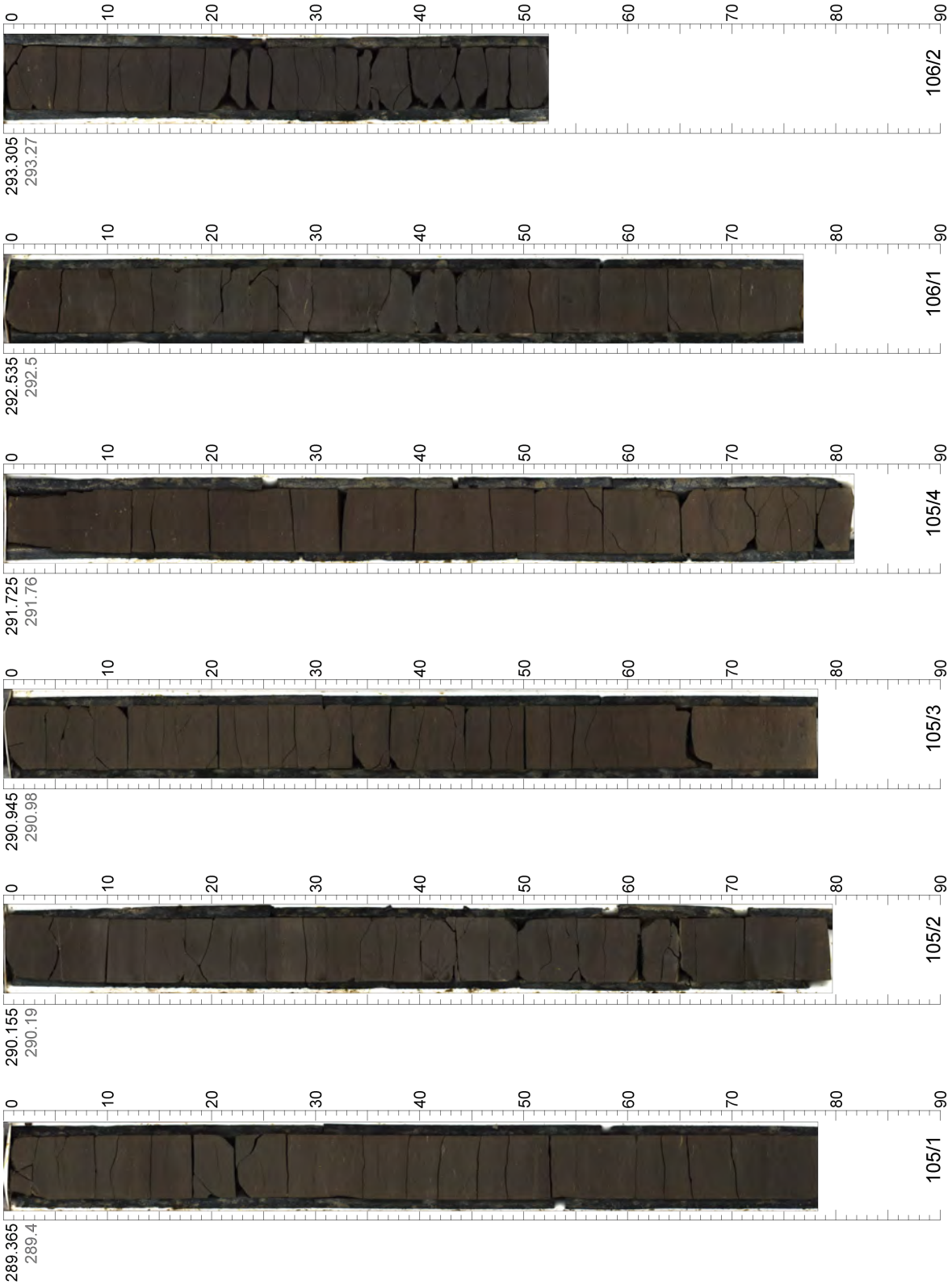
106/2
293.305
293.27
106/1
292.535
292.5
105/4
291.725
291.76
105/3
290.945
290.98
105/2
290.155
290.19
105/1
289.365
289.4

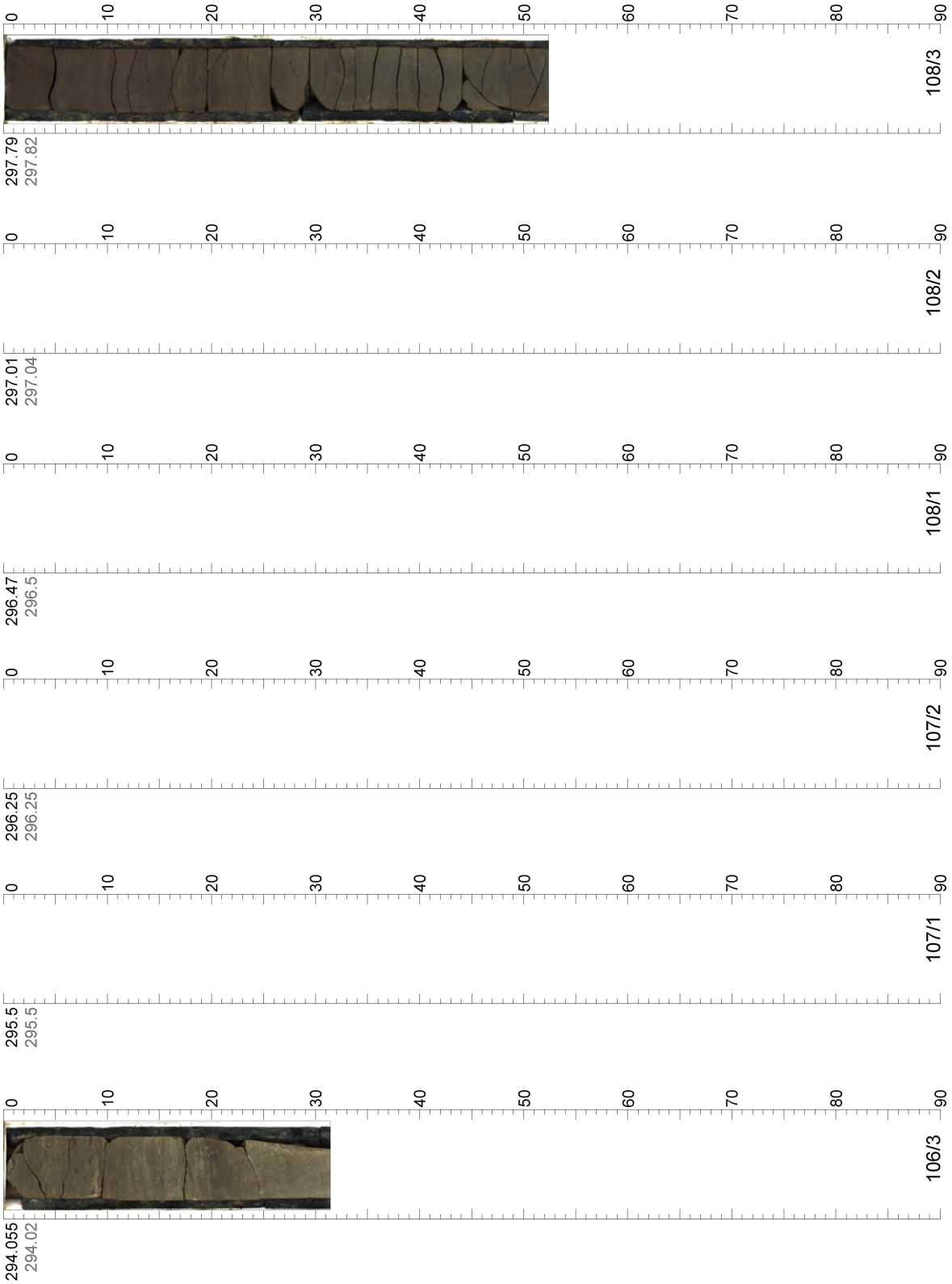
0
10
20
30
40
50
60
70
80
90
108/3
297.79
297.82
108/2
297.01
297.04
108/1
296.47
296.5
107/2
296.25
296.25
107/1
295.5
295.5
106/3
294.055
294.02

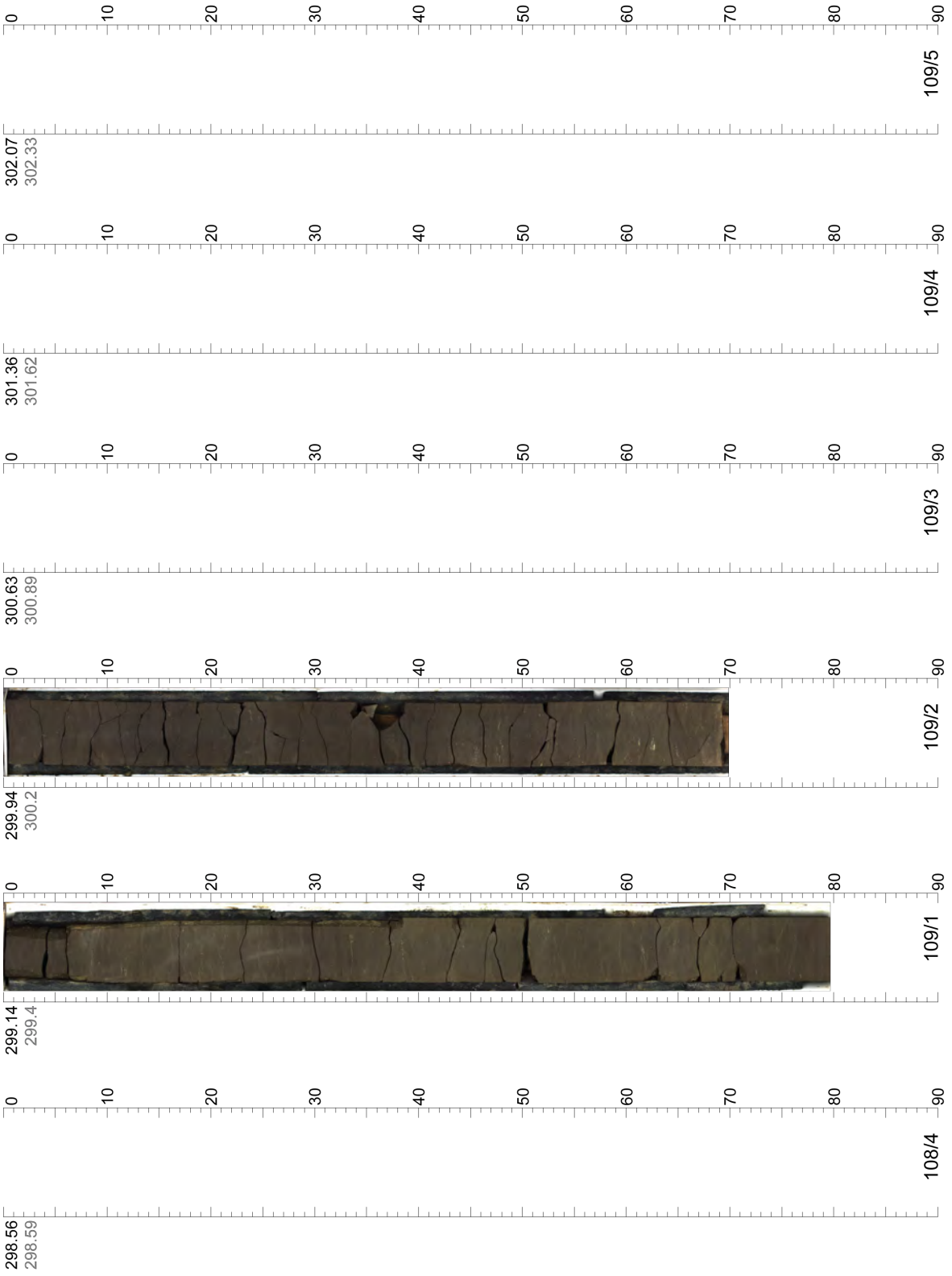
0
10
20
30
40
50
60
70
80
90
109/5
302.07
302.33
109/4
301.36
301.62
109/3
300.63
300.89
109/2
299.94
300.2
109/1
299.14
299.4
108/4
298.56
298.59

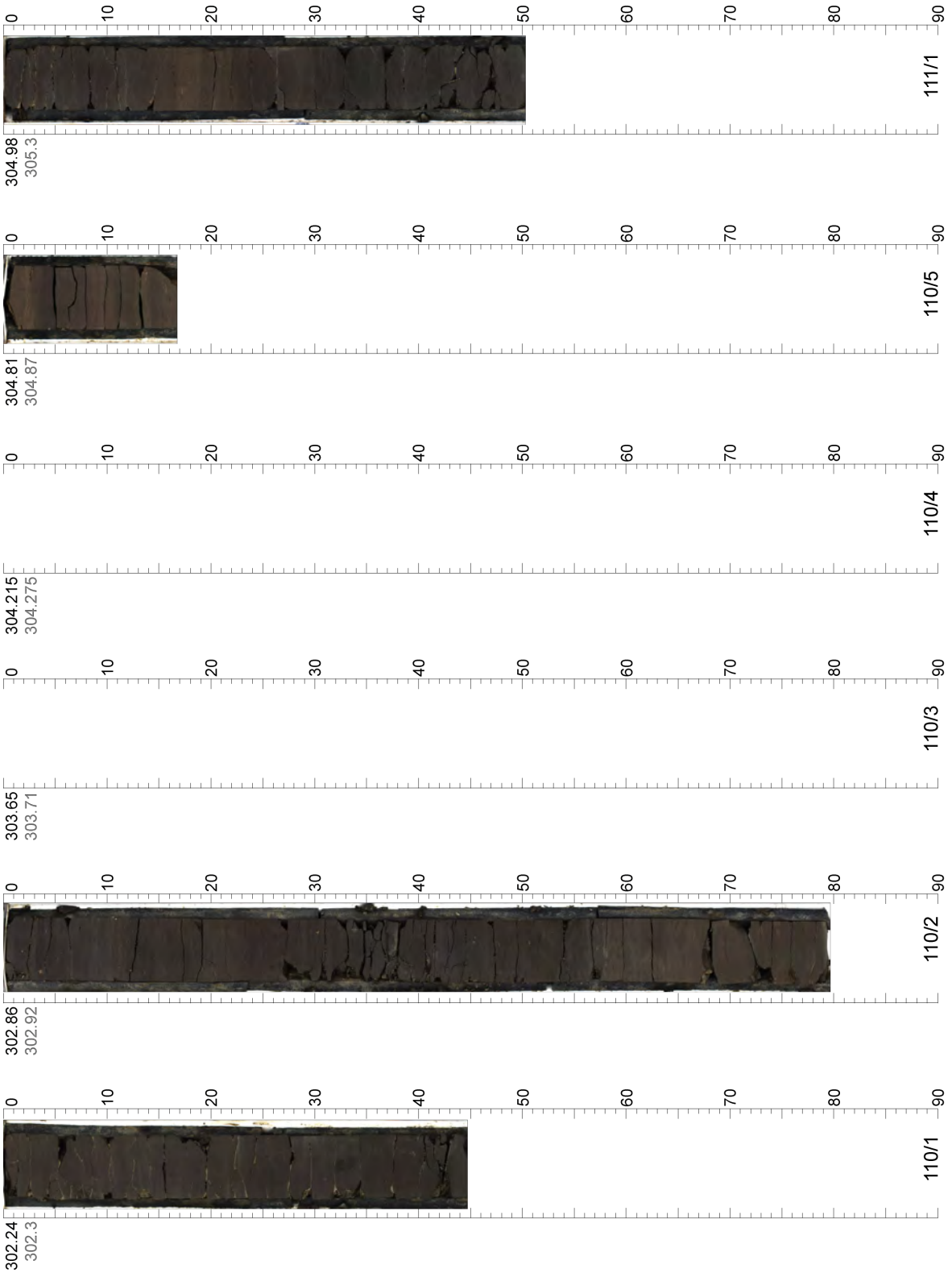
111/1
304.98
305.3
110/5
304.81
304.87
110/4
304.215
304.275
110/3
303.65
303.71
110/2
302.86
302.92
110/1
302.24
302.3

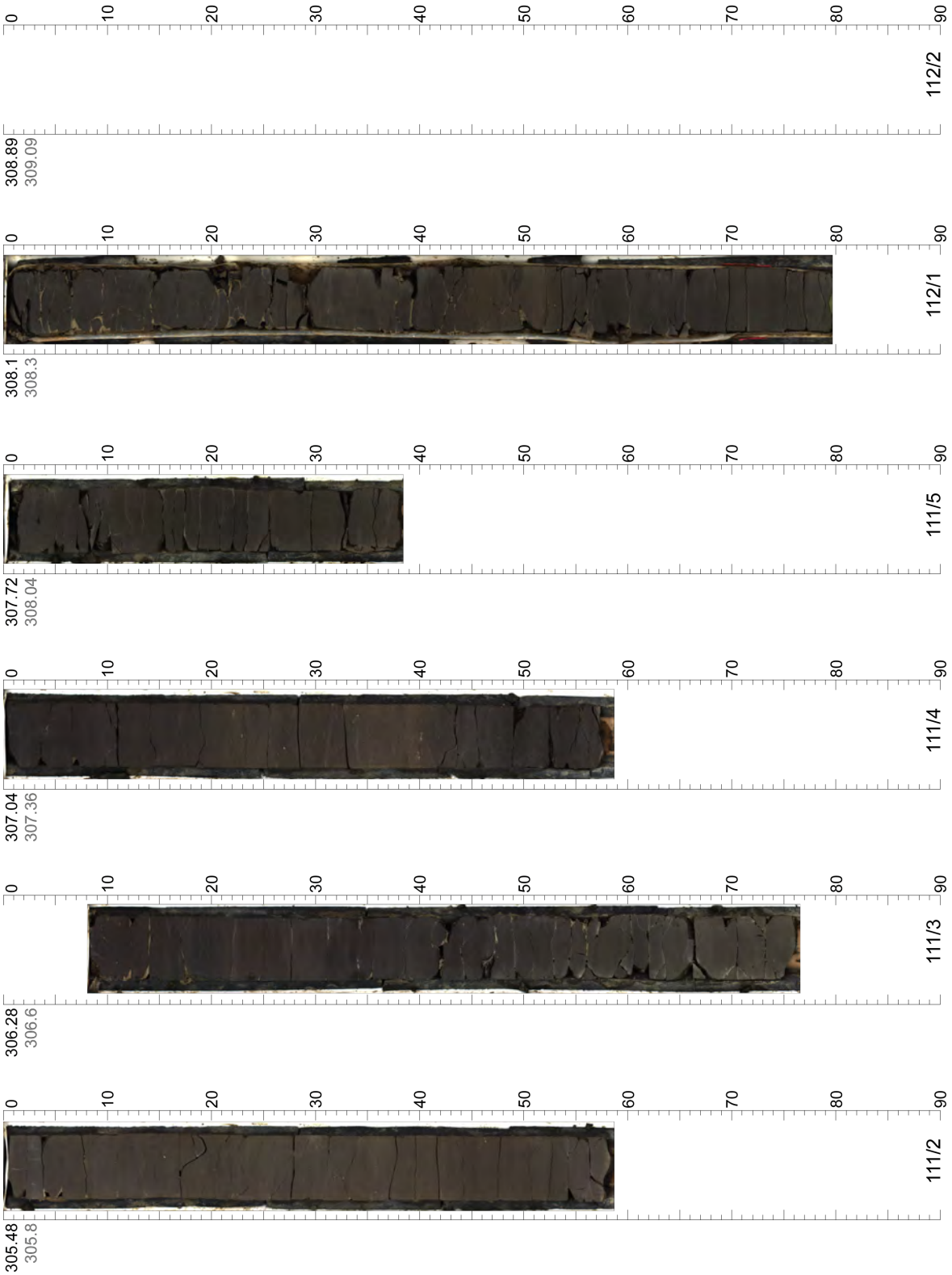
0
10
20
30
40
50
60
70
80
90
112/2
308.89
309.09
112/1
308.1
308.3
111/5
307.72
308.04
111/4
307.04
307.36
111/3
306.28
306.6
111/2
305.48
305.8

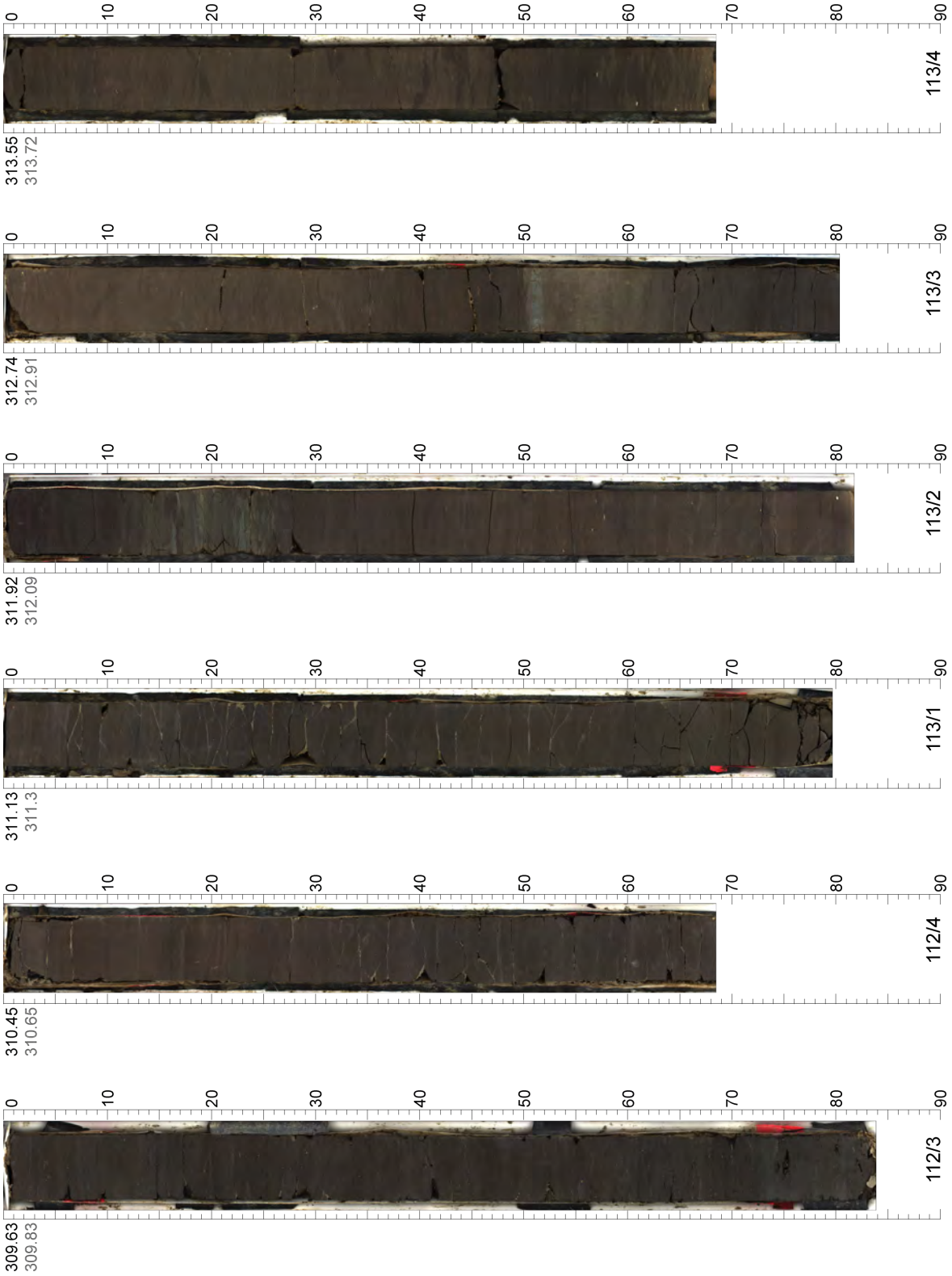
0
10
20
30
40
50
60
70
80
90
113/4
313.55
313.72
113/3
312.74
312.91
113/2
311.92
312.09
113/1
311.13
311.3
112/4
310.45
310.65
112/3
309.63
309.83

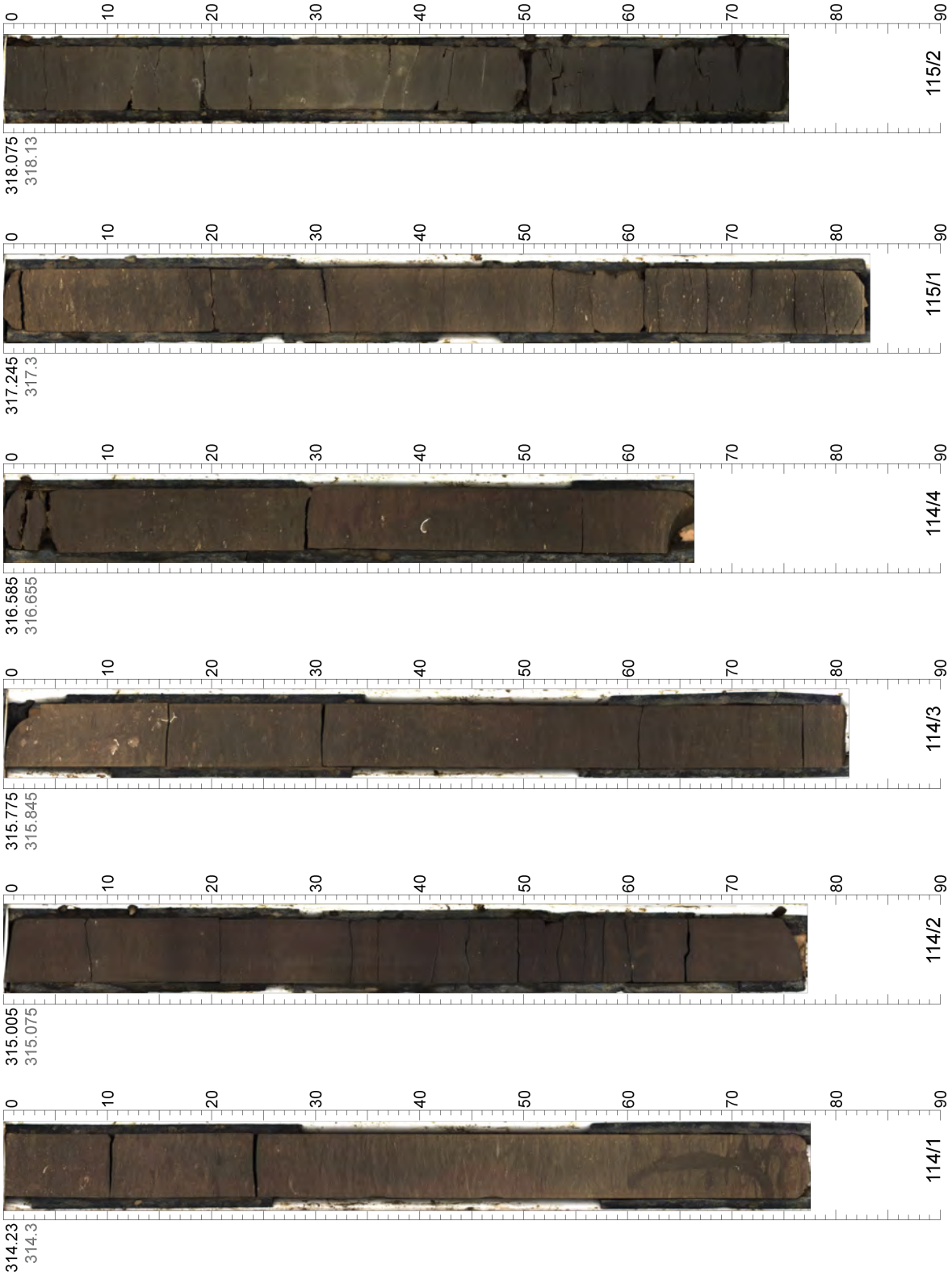
0
10
20
30
40
50
60
70
80
90
115/2
318.075
318.13
115/1
317.245
317.3
114/4
316.585
316.655
114/3
315.775
315.845
114/2
315.005
315.075
114/1
314.23
314.3

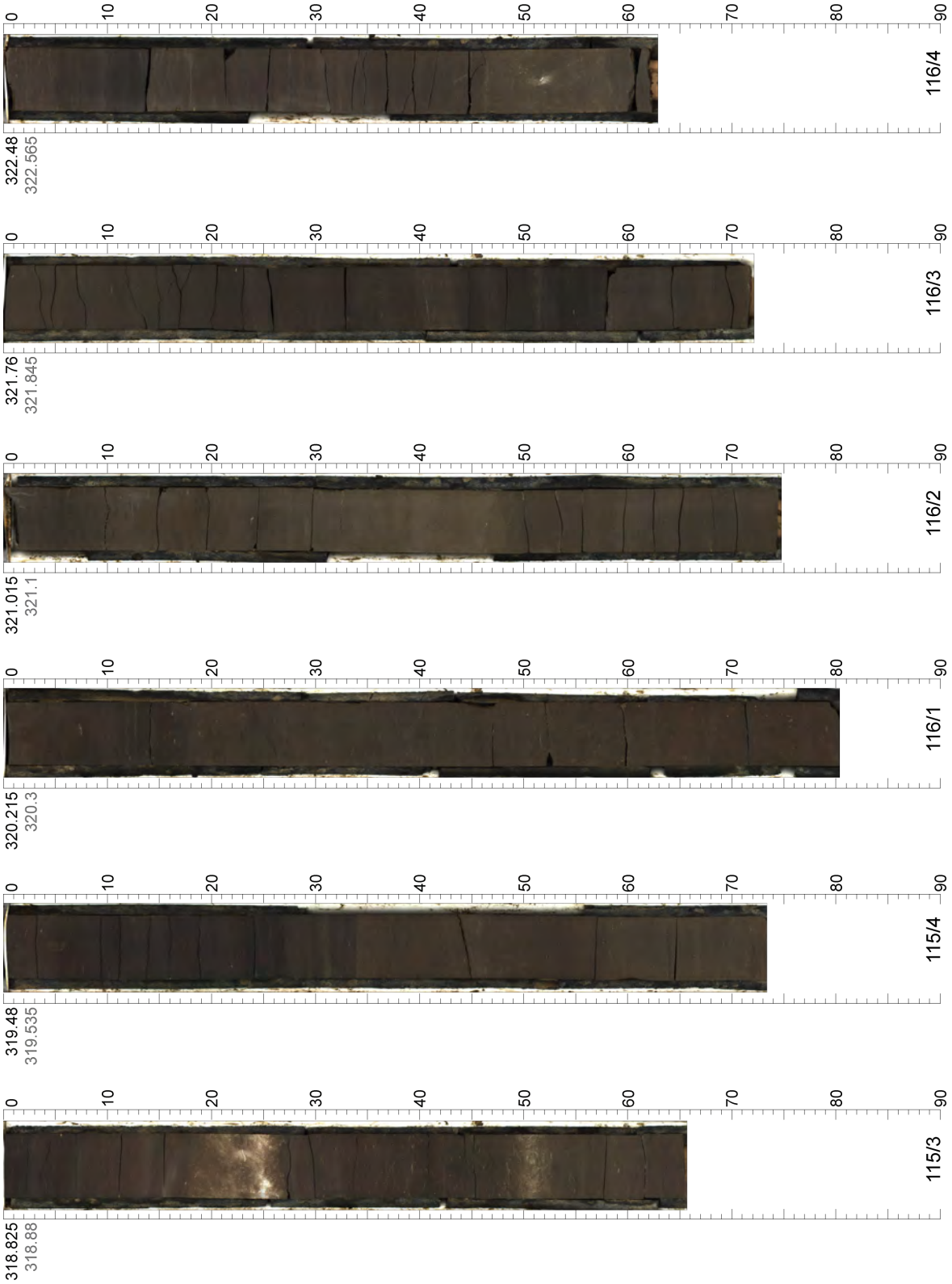
0
10
20
30
40
50
60
70
80
90
116/4
322.48
322.565
116/3
321.76
321.845
116/2
321.015
321.1
116/1
320.215
320.3
115/4
319.48
319.535
115/3
318.825
318.88

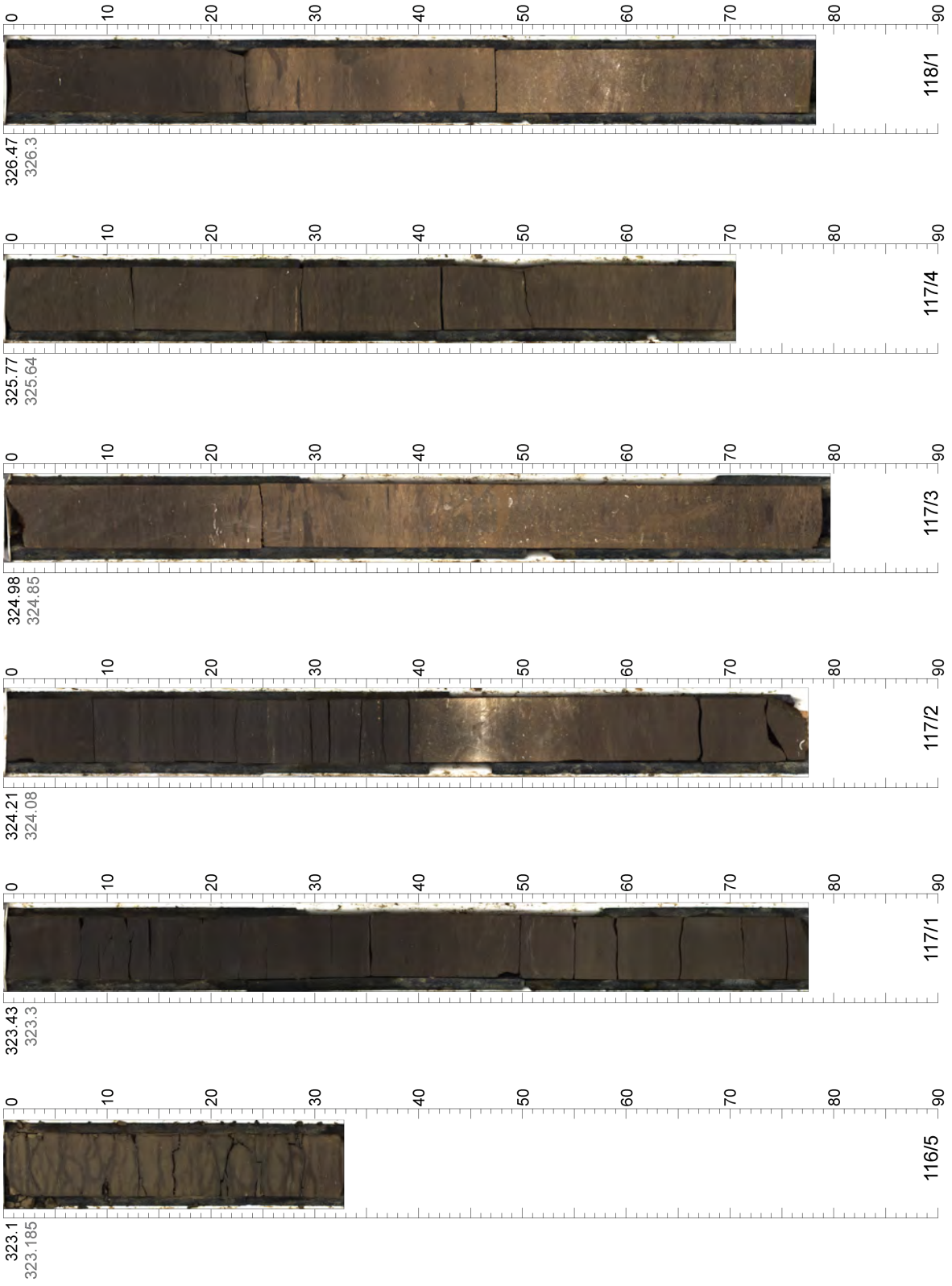
0
10
20
30
40
50
60
70
80
90
118/1
326.47
326.3
117/4
325.77
325.64
117/3
324.98
324.85
117/2
324.21
324.08
117/1
323.43
323.3
116/5
323.1
323.185

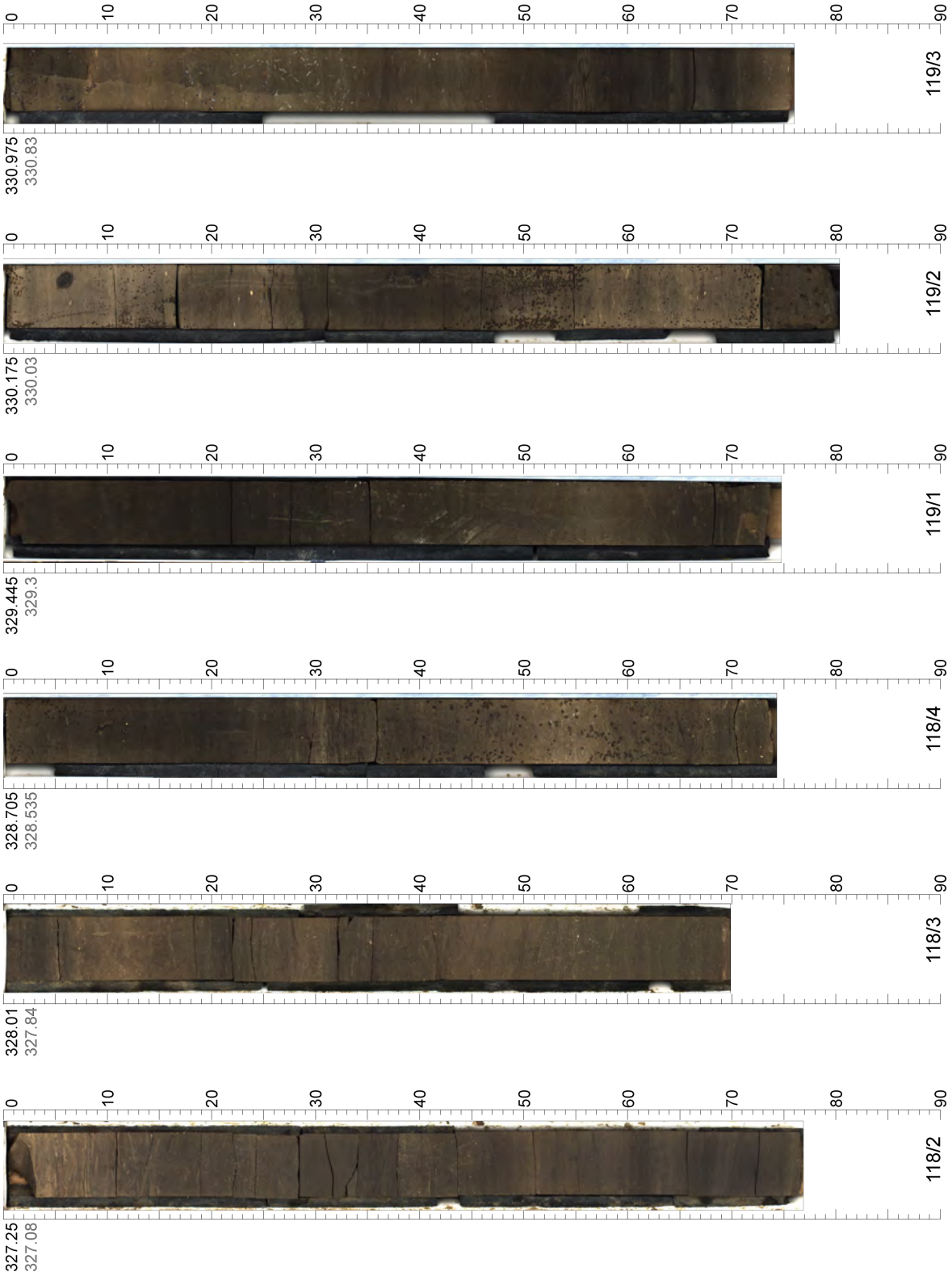
0
10
20
30
40
50
60
70
80
90
119/3
330.975
330.83
119/2
330.175
330.03
119/1
329.445
329.3
118/4
328.705
328.535
118/3
328.01
327.84
118/2
327.25
327.08

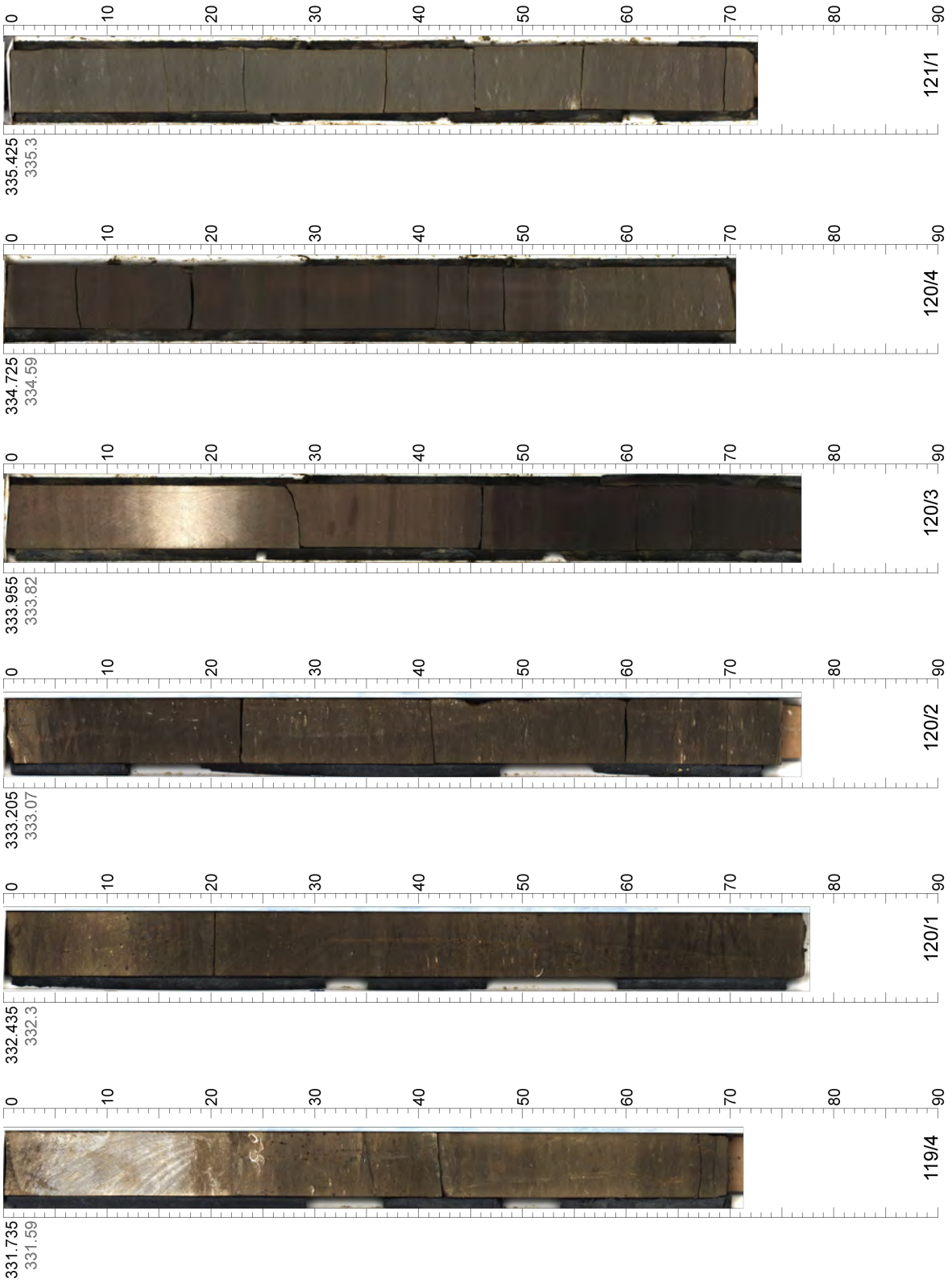
0
10
20
30
40
50
60
70
80
90
121/1
335.425
335.3
120/4
334.725
334.59
120/3
333.955
333.82
120/2
333.205
333.07
120/1
332.435
332.3
119/4
331.735
331.59

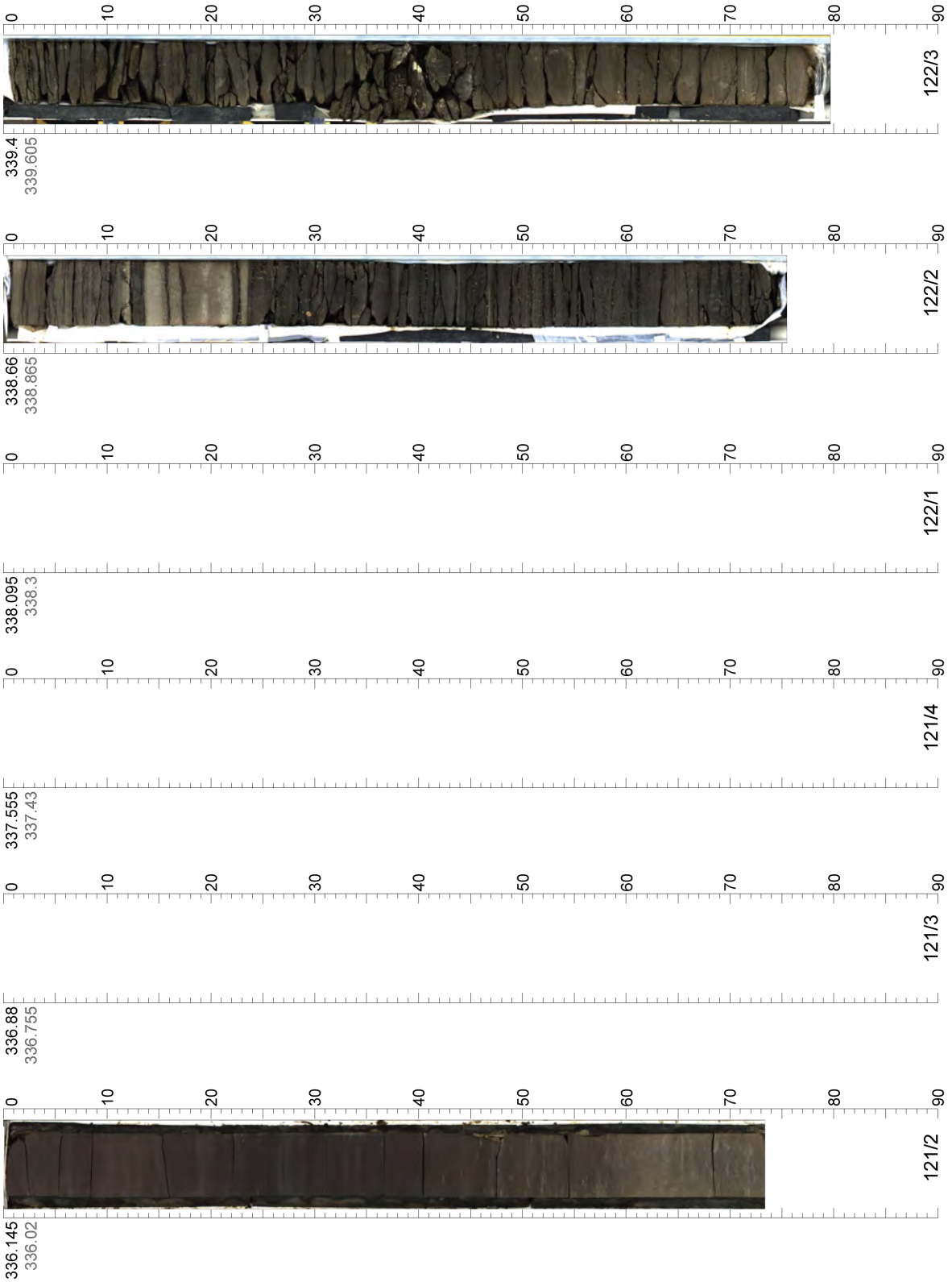
0
10
20
30
40
50
60
70
80
90
122/3
339.4
339.605
122/2
338.66
338.865
122/1
338.095
338.3
121/4
337.555
337.43
121/3
336.88
336.755
121/2
336.145
336.02

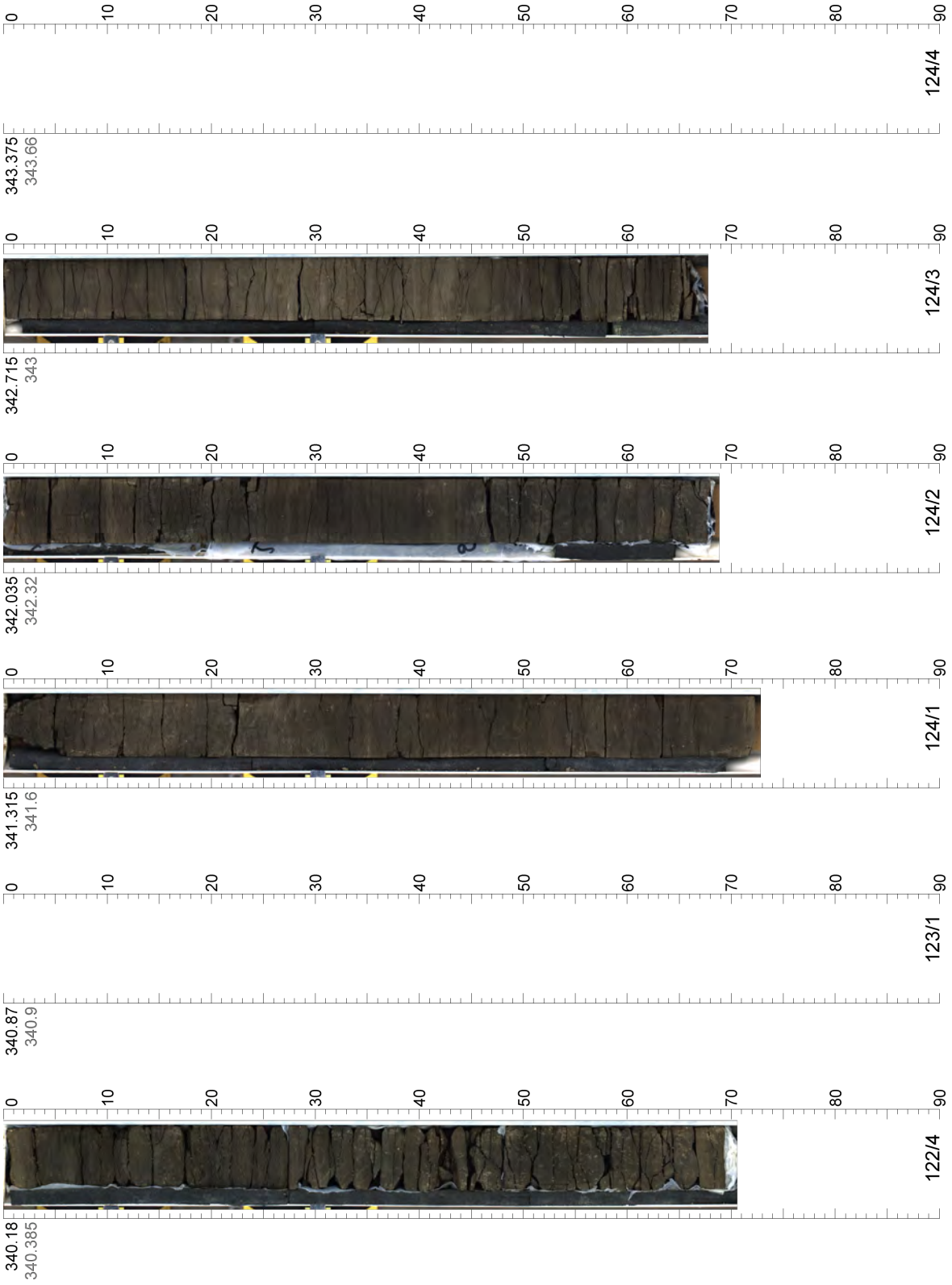
0
10
20
30
40
50
60
70
80
90
124/4
343.375
343.66
124/3
342.715
343
124/2
342.035
342.32
124/1
341.315
341.6
123/1
340.87
340.9
122/4
340.18
340.385


0
10
20
30
40
50
60
70
80
90
126/1
347.16
347.1
125/5
346.785
346.955
125/4
346.205
346.375
125/3
345.575
345.745
125/2
344.885
345.055
125/1
344.13
344.3

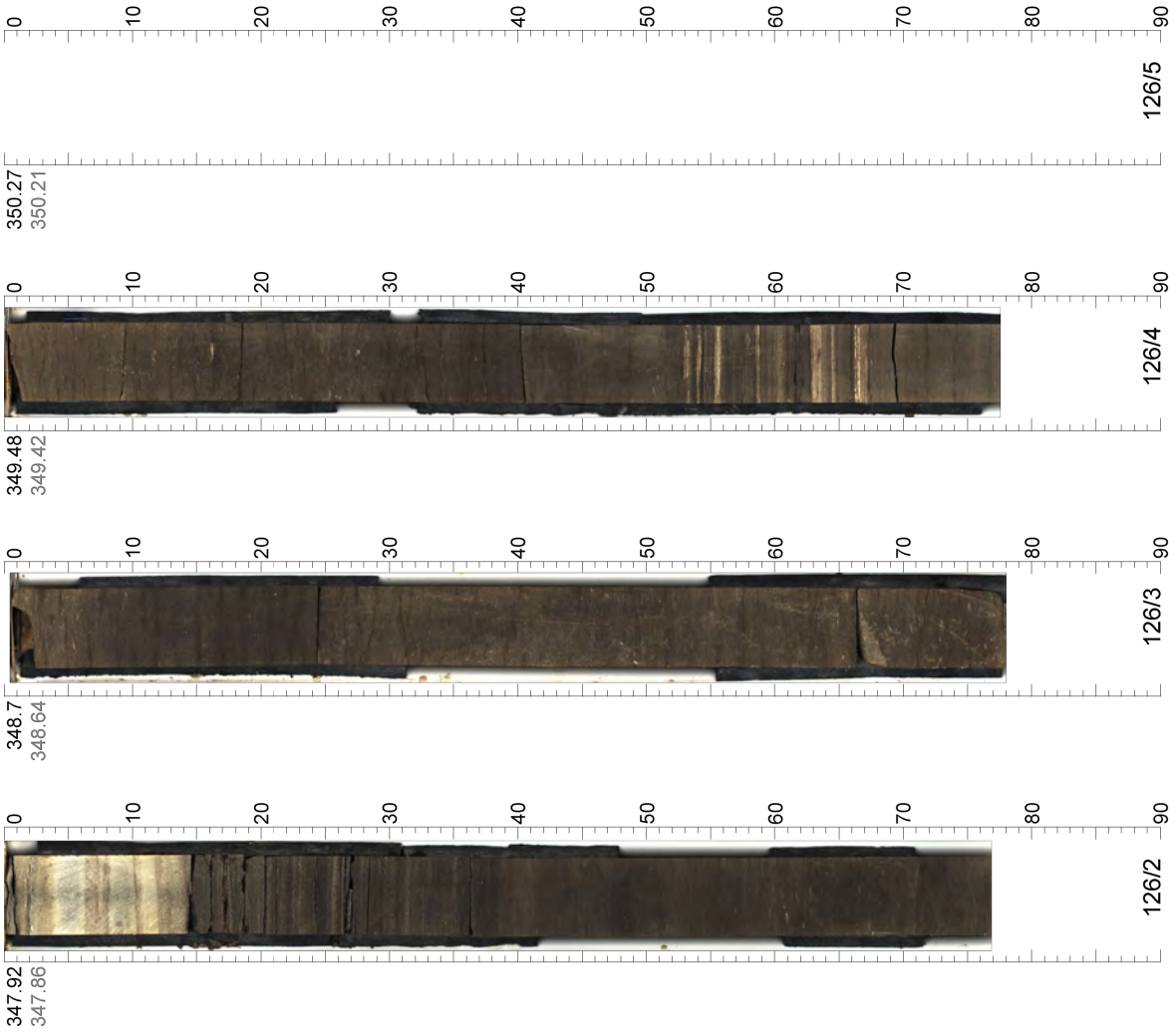
0
10
20
30
40
50
60
70
80
90
126/5
350.27
350.21
126/4
349.48
349.42
126/3
348.7
348.64
126/2
347.92
347.86